Growth of metal and semiconductor nanostructures for nonlinear optical applications

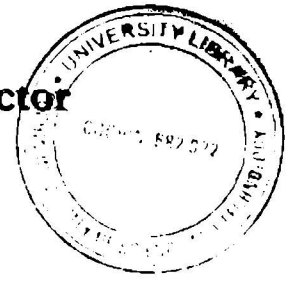

Thesis submitted to
COCHIN UNIVERSITY OF SCIENCE AND TECHNOLOGY
in partial fulfillment of the requirements
for the award of the degree of
DOCTOR OF PHILOSOPHY

Sreeja. R

Department of Physics
Cochin University of Science and Technology
Kochi - 682 022, Kerala, India

July 2011

Growth of metal and semiconductor nanostructures for nonlinear optical applications

Ph.D. thesis in the field of Materials Science

Author:

Sreeja. R
Optoelectronic Devices Laboratory
Department of Physics
Cochin University of Science and Technology
Kochi - 682 022, Kerala, India
E-mail: sreekrishna07@gmail.com

Supervisor:

Dr. M.K. Jayaraj
Professor
Optoelectronic Devices Laboratory
Department of Physics
Cochin University of Science and Technology
Kochi – 682 022, Kerala, India
E-mail: mkj@cusat.ac.in

Front cover: Gold nanoparticles attached Multi walled carbon nanotubes
Back cover: Block diagram of Z-scan setup

July 2011

Dr. M.K. Jayaraj
Professor
Department of Physics
Cochin University of Science and Technology
Kochi – 682 022, India.

6th July 2011

Certificate

Certified that the work presented in this thesis entitled **"Growth of metal and semiconductor nanostructures for nonlinear optical applications"** is based on the authentic record of research carried out by Ms. Sreeja. R under my guidance in the Department of Physics, Cochin University of Science and Technology, Kochi – 682 022 and has not been included in any other thesis submitted for the award of any degree.

Dr. M. K. Jayaraj
(Supervising Guide)

Phone : +91 484 2577404 extn 33 Fax: 91 484 2577595 E-mail: mkj@cusat.ac.in

Declaration

Certified that the work presented in this thesis entitled **"Growth of metal and semiconductor nanostructures for nonlinear optical applications"** is based on the original research work done by me under the supervision and guidance of Dr. M. K. Jayaraj, Professor, Department of Physics, Cochin University of Science and Technology, Kochi– 682 022 and has not been included in any other thesis submitted previously for the award of any degree.

Kochi – 22
6th July 2011

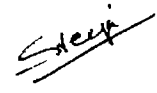

Sreeja. R

The one who was my first and best listener
The one who was my first and best teacher
Who taught me how to be humane, kind and fearless
Who struggled the most for me to be here
And this is for your love and patience my mom.....
And I love you the most in the world.....

Acknowledgements

I am deeply indebted to my supervising guide, Dr. M. K. Jayaraj, for making the last four years of research a pleasant experience who never put any limit to the students in suggesting new ideas and offered maximum freedom to think and work in their own ways. I express my deep sense of gratitude for his selfless support, excellent guidance, timely advice, keen observations and persistent encouragement as well as willingness to share his knowledge and experience during the entire course of work, without which the successful completion of this thesis would not have been possible. Throughout my academic as well as research career, I will be nourished with the virtues and goodness that I gained from his positive attitude towards colleagues and students, stubbornness in decisions and unparalleled patience in achieving a goal. Anything I may become in my academic or research career, its solid roots came from the fertile soil that his affection and support created in our research environment as a supervising guide. I heartfully thank him for making it possible for me to start a research career and thereafter the successful completion of research work.

I express my sincere thanks to Prof. M.R.Anantharaman, Head of the Department of Physics and all the former Heads of the Department – Prof.V. C. Kuriakose, Prof. Ramesh Babu Thayyullathil and Prof. Godfrey Louis, - for permitting me to use the research facilities in the Department. I gratefully acknowledge the help and inspiration from all my teachers at the Department of Physics for the help and guidance right from the beginning of my research work. Special mention goes to my doctoral committee member Dr.S.Jayalakshmi for her innate love and selfless support. She was indeed a bright candle in my student life who always filled my heart through her lovely smile, soft words, extreme sincerity and immense care from

whom I learned how a teacher shall be to her students. Special thanks to Prof. T..Pradeep. IIT Madras for TEM measurements and Dr. Shibu Eappen at SAIF STIC for ICP-AES measurements.

It is my special pleasure that I acknowledge Dr.Reji Philip, RRI, Bangalore for the valuable suggestions and discussions throughout this work. Without any hesitation he was there always along with me just a mail away to constantly encourage and, clarify my doubts and ideas. Special mention to Suchand Sandeep and Kishore Shridharan, research students under Dr.Reji Philip who offered maximum support in taking measurements at Raman research institute.

I am thankful to all the office and library staff of the Department of Physics for all the help and cooperation.

I am deeply thankful to the KSCSTE -Kerala State Council for Science Technology and Environment, Government of Kerala for initially supporting me during this research endeavour. Also I express my sincere gratitude to CSIR -Council for Scientific and Industrial Research- for financially assisting me in the due course of my research work. I sincerely acknowledge the academic and financial support of SPIE - The international Society for Optical Engineering -during the period of my research work.

I remember with gratitude the sincere support of Mr. Manu George, Dr.K.J.Saji and Dr. R.S.Ajimsha for all the support and encouragements they offered during the very initial stages of my research.

I gratefully acknowledge the helps and supports received from my senior researchers in the lab Dr.Manoj, Dr.Aldrin Antony, Dr.Nisha, Dr.Asha, Dr.Anila, Dr. Anoop Menon, Dr. Mini Krishna, Dr.Joshy and Vanaja madam.

I would like to express my sincere appreciation to my colleagues in the optoelectronic devices laboratory Aneesh, Ratheesh, Arun, Krishna Prasad, Sanal, Sasank, James sir, Sathish Bhai and Saritha chechi. It was very enjoyable in working with the younger generation of the lab- Vikas, Hasna, Rakhy, Navaneeth and Majesh.

I am also thankful to Jem, Jobina, Anlin and Jerin for their valuable help during various stages of my work. I remember my happiest moments with Vineetha during the very early stage of my research life in OED. I treasure my friendship with Anuraj, Shitha, Shonima, Najila, Jijin, Vinod, Shijeesh, Jafar, Christie, Sarathlal and Aeby.

I remember my friends Nijo, Priyesh, Tharanath and Vivek who were along with us in conducting programmes and scientific exhibitions in the Department. Special mention to Poornima, Rajeshmon, Rajesh CS with whom I cherished a part of my joyous moments in the Department. I express my sincere thanks to my MSc. friends Sajitha, Linthish, Pradeep, Manikandan and Shinoj and Sarath.

I thank Amritha Institute of Medical Sciences who gave me a wonderful opportunity to teach M.Tech. students with extreme confidence in my abilities. Special thanks to Mansoorettan, Avinashettan, Subhramanian Sir and Shanthi Sir for their support and encouragements. Special thanks to Renjusha, Asha, Anu and Jayesh; my friends at Amritha Institute.

I treasure my moments of adichupoli and thamazhas in hostel with Anila, Subha chechi, Anu Philip, Bindu chechi, Soumya, Vijutha chechi, Anisha, Joyni, Sini chichi, Chitra chichi and Geetha chechi. Indeed Subha chechi is one of the best supporter and promoter that I ever met who showered her self less love upon me and tried her level best to lift me up from failures and sufferings and filled me with confidence in moments where I was in true need and she is a true Chechi in that sense and I will miss her a lot in my life time.

Special mention to Reshmi chechi and Subha who were not just my colleagues but my sisters. We cherished and enjoyed our good days and shared the shadow of the bad days with equal heart. Throughout my life I cannot forget the lovely and homely days with them.

I remember with extreme pleasure the support and love extended by my best friends and deep most well wishers who gave a big hand to me in the path I travelled. They came to my life at different times, from my Nursery classes to my PhD life and even lost the contacts with a few of them but the glee and love that their memories arouse in my heart are all equal. They are those who understood me well and loved me deep and enjoyed my success and prayed for me in my falls. With a heart full of joy and with eyes wet I thank you my most dear friends Ajitha, Suja, Sreeja, Sari, Ragu, Chandu, Bhavya and Maya; the words of thanks has little relevance as far as they are concerned since it cannot pay for the patience and love they extended to me.

Now it is time to remember my Ravi sir and Pattazhi sir who were indeed two light houses in the student life of a twelve year old village girl from a very ordinary back ground. It is them who taught me that I have nothing else other than bright dreams and a mind filled with fire. Throughout my life I will be thankful to them who gave

the strong foundation to my academic life and taught me to dream the maximum and work restlessly for achieving the goal.

I express my deep sense of gratitude to Achan and Amma of my husband's family for the self less support, love, care and inspiration they extended towards me at the very final stages of my thesis work. I am blessed to be a part of such family who can fill my mind with love and encouragement at the moment of submitting my PhD thesis.

I record my deep and utmost gratitude to my Amma, Achan and Kuttan for the motivation, encouragements, patience and tolerance during the entire period of my life. They tried their level best and suffered alot in fulfilling their girl's hopes and dreams a reality.

Now it is time to thank Arunettan, my dearmost caretaker and well wisher who walked with the music of my mind throughout every moment after the Great Lord sent him to my life. The very final stages of the thesis involve his full contribution. When I became weak at certain times, never did he allow me to be alone in my research endeavour. He proved the role of a true life partner through his deep most love, care, support and encouragement.

Above all, I bend my head in humble gratitude before the Omnipotent God Almighty for kindly allowing me to make my research endeavour a reality.

Sreeja

Contents

Chapter 3- Fabrication of an automized Z-scan setup for nonlinear optical studies

Chapter 7- Linear and nonlinear optical properties of gold nanoparticle attached MWCNTs

Chapter 8- Summary and scope for future work

Preface

Nanotechnology is the science of building machines at a subatomic level. Nanotechnology encompasses those materials with morphological features on the nanoscale, and especially those that have special properties stemming from their nanoscale dimensions. Practical nanotechnology is essentially the increasing ability to manipulate (with precision) matter on previously impossible scales, presenting possibilities which many could never have imagined. Today's nanotechnology harnesses current progress in chemistry, physics, material science and biotechnology to create novel materials that have unique properties because their structures are determined on the nanometer scale. The products of advanced nanotechnology that will become available in coming decades promise even more revolutionary applications than the products of current and near-term nanotechnology. The very important aspect of nanotechnology is the vastly increased surface to volume ratio which makes possible new quantum mechanical effects, for example the "quantum size effect" where the optical and electrical properties of solids are altered with great reductions in particle size. The enhancement in the optical parameters in the nano regime found wide applications in fabricating optical devices of the current era.

Nonlinear optics has been a rapidly growing field in recent decades since the invention of lasers. The systematic progress in the laser technology increases our efficiency in the generation and control of coherent optical radiations. Nonlinear optics is based on the study of effects and phenomena related to the interaction of intense coherent light radiation with matter. Compared to other light sources laser

radiation can provide high directionality, high monochromaticity, high brightness and high photon degeneracy. At such a very intense incident beam, the matter responds in a nonlinear manner to the incident radiation fields, which endows the media a characteristic to change the refractive index or absorption coefficient of the media or the wavelength, or the frequency of the incident electromagnetic waves. This thesis encompasses the fabrication of nonlinear optical devices based on semiconductor and metal nanostructures. The presented work focus on the experimental and theoretical discussions on nonlinear optical effects especially nonlinear absorption and refraction exhibitted by metal and semiconductor nanostructures.

Chapter 1 gives a very short introduction to behavior and applications of semiconductor and metal nanoparticles while coming to the nano regime. It includes the fundamental aspects of the quantum confinement in nanostructures. Among the semiconductor nanoparticles, the materials of our choice are ZnO and ZnS. Among the metal nanoparticles, the gold and silver are selected as NLO material. A brief review on the nature of these materials is given in this chapter.

Chapter 2 describes in detail the growth techniques and characterization tools employed for the fabrication of nanostructures. Different types of physical and chemical synthesis techniques of quantum dots, especially liquid phase laser ablation (LP-PLA) technique and wet chemical methods are described in detail. Nanostructures grown were characterized by various analytical techniques; thickness measurement of the thin films using stylus profiler, structural characterization using X-ray diffraction method, microstructure analysis using transmission electron microscopy (TEM), composition analysis by inductively

coupled plasma atomic emission spectroscopy (ICP-AES) analysis and Atomic Absorption Spectra (AAS), determination of band gap by UV-visible absorption for colloids and diffused reflectance spectra for powder samples. Photo luminescent (PL) investigations helped to analyze the luminescence mechanism of the nanostructures prepared.

Chapter 3 describes in detail the major nonlinear optical effects, including physical principles and theoretical back ground and current or potential applications. The theoretical background to the Z-scan technique is well detailed in the chapter. And towards the end of the chapter describes the fabrication of an automised Z-scan setup for the nonlinear optical studies.

Chapter 4 deals with the synthesis and characterization of ZnO nanoparticles embedded in PMMA matrix. The ZnO nanoparticles of various sizes were prepared by wet chemical methods. The particle size, band gap, photoluminescence emission peak position and the nonlinear optical characteristics are found to be varying with the NaOH concentration in the precursor solution. It is observed that the band gap of the samples shows a decrease with increase in concentration of NaOH in the reaction mixture indicating an increase in particle size. The nonlinear absorption studies using Nd:YAG laser (532nm,7ns) shows that the ZnO:PMMA shows an optical limiting type nonlinearity. The nonlinear refraction in the ZnO:PMMA shows a negative value of n_2. The value of nonlinear coefficients is found to be increasing with increase in nanoparticle's size. The mechanical properties of the ZnO:PMMA polymer films enable its use for device fabrication compared to quantum dots dispersed in a solution.

Chapter 5 deals with the synthesis of luminescent ZnS:Cu nanoparticles through wet chemical route in aqueous media and their further characterization. The structural analysis of the nanoparticles was made by XRD and TEM analysis. The ZnS:Cu nanoparticles displayed a systematic increase in the band gap with increase in the copper doping concentration as found from the diffused reflectance spectra. A strong photoluminescence emission band was observed in the green region for copper doped ZnS. The open aperture Z-scan traces taken at 800nm (pulse width = 100 fs) of the ZnS:Cu nanoparticles embedded in PVA matrix showed optical limiting. The increase in the value of the nonlinear absorption coefficient with increase in the doping concentration was observed. Thus Cu doped ZnS nanoparticles in the polymer matrix found an effective material for optical limiting applications.

Chapter 6 deals with the characterization of gold and silver nanoparticles in water synthesized by LP-PLA. The optical properties of the Au and Ag nanoparticles were found to be varying with the size of the particles due to quantum confinement effect. It was observed that the particle size and particle concentration can be tuned by varying the laser fluence and duration of laser ablation. The lower sized Ag nanoparticles showed more stability compared to higher sized Ag nanoparticles. Stable and flexible nonlinear optical device was fabricated by incorporating the Au and Ag nanocrystals in a poly vinyl alcohol matrix. The optical absorptive nonlinearity taken with Nd:YAG laser (532nm, 7ns) in gold and silver nanoclusters showed optical limiting type nonlinearity. The efficiency of optical limiting was found to be increasing with decrease in particle size. The Au nanoclusters showed negative value of nonlinear refraction indicating self defocusing type nonlinearity. The size of the silver nanoparticles decreased with increase of the duration of

ablation for a fixed incident laser ablation fluence.

Chapter 7 deals with the homogenous attachment of Au-NPs produced by LP-PLA in water on to the walls of MWCNTs. The uniform distribution of the Au-NPs on the walls of MWCNTs was studied by XRD and TEM characterization. The optical limiting studies of the Au NPs attached MWCNTs were performed using Nd:YAG laser (532nm,7ns). The optical limiting properties increased with increasing the concentration of Au-NPs. Thus a highly stable and flexible optical limiting device was fabricated using MWCNT's with attached Au-NPs in a polymer matrix.

Chapter 8 Summarizes the important results in the thesis and recommends the scope for future work.

Part of the thesis has been published in internationally referred journals

1. Size dependent optical nonlinearity of Au nanocrystals, R. Sreeja, P. M. Aneesh, Arun Aravind, R. Reshmi, Reji Philip and M. K. Jayaraj, Journal of Electrochemical society, 156 (10), K167 (2009)
2. Linear and nonlinear optical properties of luminescent ZnO nanoparticles embedded in PMMA matrix, R. Sreeja, Jobina John, P. M. Aneesh and M. K. Jayaraj, Optics Communications 283 (2010) 2908–2913
3. Linear and Nonlinear Optical Properties of Gold Nanoparticle Attached MWCNTs, R. Sreeja, R. Reshmi,P. M. Aneesh and M. K. Jayaraj (Under revision Journal of Electrochemical Society)

4. Liquid phase pulsed laser ablation of metal nanoparticles for nonlinear optical applications, R. Sreeja, R. Reshmi, P. M. Aneesh and Dr. M. K. Jayaraj (In press Advanced Solid state physics)
5. Optical properties of wet chemically grown Copper doped ZnS nanoparticles, R. Sreeja, Kishore Sreedharan, Reji Philip and M. K. Jayaraj (Under review Applied Physics B : Lasers and optics)

Other publications to which the author has contributed

1. Linear and nonlinear optical properties of rare earth doped of BST thin films, R. Reshmi, R. Sreeja, M. K. Jayaraj, J. James and M. T. Sebastian, Applied Physics B: Lasers and Optics, 96, 433 (2009)
2. Determination of third-order optical absorptive nonlinearity of ZnO nanoparticles by Z-scan technique, R. Sreeja, R. Reshmi, Manu George and M. K. Jayaraj, Proceedings of SPIE - The International Society for Optical Engineering 7155, art. no. 715521 (2008)
3. Growth of silver nanoparticles in SiO_2 matrix by co-sputtering technique, K. C. Sanal, R. Sreeja, K. Anlin Lazar and M. K. Jayaraj, Proc. of SPIE, 7393, 73930J (2009)
4. Electrical and optical characteristics of surface treated ZnO nanotubes, R. Renjusha, R. Sreeja, A. M. Anu, K. R. V. Subramanian, Santhikumar V. Nair and A. Balakrishnan (Under Review, Materials Science and Engineering B)

Conference proceedings

1. Determination of third-order optical absorptive nonlinearity of ZnO nano particles by Z-scan technique, Sreeja. R, Reshmi. R, Manu George, M. K.

Jayaraj (Presented at 9th International Symposium on Laser Metrology on 30 June - 2 July 2008 at SMU Conference Centre, Singapore)

2. Size dependent optical absorptive nonlinearity of Au nano clusters in water, R. Sreeja, P. M. Aneesh, Arun Aravind, R. Reshmi, M. K. Jayaraj (Presented in International Conference on Fiber Optics and Photonics on 9-11 December 2008 at New Delhi, India)
3. Gold nanoparticles by liquid phase pulsed laser ablation for biological and optical limiting applications, P. M. Aneesh, R. Sreeja, Arun Aravind, R. Reshmi, M. K. Jayaraj (Presented at 2nd BANGALORE NANO on 11-13 December 2008 at Bangalore, India)
4. Fabrication of an automized Z-scan setup for nonlinear optical studies, R. Sreeja, Jobina John, V. L. Anuraj, K. Saritha, M. K. Jayaraj (Presented in International Seminar at PSGRKC on Mathematical &Experimental Physics on 18-19 December 2008 at Coimbatore, India)
5. Synthesis of gold nanoparticles by laser ablation in liquid media, P. M. Aneesh, Arun Aravind, R. Sreeja, R. Reshmi and M. K. Jayaraj (Presented at Second International Conference on Frontiers in Nanoscience and Technology on 3-6 January 2009 at Kochi, India)
6. Linear and nonlinear optical properties of pulsed laser deposited $Zn_{(1-x)}Mn_xO$ thin films, R. Sreeja, Arun Aravind, E. K. Ragitha, M. K. Jayaraj (Presented at International conference on electro ceramics on 13-17 January 2009 at Delhi , India)

Chapter 1

Introduction to nanostructured materials

1.1. Introduction

Nanotechnology is the expected future manufacturing technology that will make most products lighter, stronger, cleaner, less expensive and more precise. Nanoscale materials can be defined as those whose characteristic length scale lies within the nanometric range, i.e. in the range between one and several hundreds of nanometers. Encompassing nanoscale science, engineering and technology, nanotechnology involves imaging, measuring, modelling and manipulating matter at this length scale. Unusual physical, chemical and biological properties can emerge in materials at the nanoscale. These properties may differ in important ways from the properties of bulk materials and single atoms or molecules. Even more popular than "Nanoscience" has become the term "Nanotechnology" which relates to the ability to build functional devices based on the controlled assembly of nanoscale objects for specific technological applications. The importance of both nanoscience and nanotechnology has been confirmed by a number of national and international initiatives to promote their study. Funding agencies in the USA, Europe, Australia and Japan are spending a significant part of their funds for the development of nanoscience and nanotechnology.

Nanotechnology can be defined as the synthesis and engineering at the molecular level for the possible device applications. Nanoscience deals with the investigations of phenomena and properties exhibited by materials at the nano level. A nanostructure is an object of intermediate size between

molecular and microscopic (micrometer-sized) structures. Nanoparticles made of semiconducting material may also be labeled as quantum dots if they are small enough (typically < 10nm) that quantization of electronic energy levels occurs. Nanoparticles are of great scientific interest as they are effectively a bridge between bulk materials and atomic or molecular structures. A bulk material should have constant physical properties regardless of its size, but at the nano-scale this is often not the case. Size-dependent properties are observed such as quantum confinement in semiconductor particles, surface plasmon resonance in some metal particles and super paramagnetism in magnetic materials. Nanostructured materials have gathered great interest worldwide due to their unique size-dependent properties for chemical, electronic, structural, medical and consumer applications.

Nanoscience and nanotechnology is the science and technology of ultrafine particles. The trend in device oriented manufacturing towards smaller and smaller dimensions has led to the development of nano fabrication techniques as well as understanding the physics of nanometer scale materials [1]. Materials when reduced to nano scale shows entirely different chemical, physical, electrical and optical properties as compared to what they exhibit on the macro scale. At these dimensions the surface to volume ratio becomes very large which determines the properties of the material in the nanoregime. The percentage of atoms at the surface of a material becomes significant as the size of that material approaches the nano scale. Suspensions of nanoparticles are possible because the interaction of

the particle surface with the solvent is strong enough to overcome differences in density, which usually result in a material either sinking or floating in a liquid. Nanoparticles often have unexpected visible properties because they are small enough to scatter visible light rather than absorbing it. For example gold nanoparticles appear deep red to black in solution.

The ultimate motive of nanotechnology is to manipulate and control the individual atoms and such a definition may be extended to the organization of objects having nano dimension. The properties of materials change as their size approaches the nanoscale. Nanoparticles behave quite differently due to the high surface to volume ratio. The more loosely bound surface atoms constitute a significant fraction of the sample whose properties influence the sample's behaviour. For example, the bending of bulk copper (wire, ribbon, etc.) occurs with movement of copper atoms/clusters at about the 50 nm scale. Copper nanoparticles smaller than 50 nm are considered super hard materials that do not exhibit the same malleability and ductility as bulk copper. The melting point of gold is dramatically reduced when the particle diameter drops below 5nm, it changes its state from solid to liquid at room temperature. Optical properties are modified because of the quantum size effect on the band structure. Optical energy band gap is blue shifted for ultrafine materials. Nano sized copper is blue in colour, this gives scope to a variety of applications in the semiconductor industry.

Two main approaches are used in nanotechnology: one is a "bottom-up" approach where materials and devices are built up atom by atom, the

other a "top-down" approach where they are synthesized or constructed by removing existing material from larger entities. A unique aspect of nanotechnology is the vastly increased surface area to volume ratio present in many nanoscale materials, which opens new possibilities in surface-based science, such as catalysis. This catalytic activity also opens potential risks in their interaction with biomaterials.

In describing nanostructures, it is necessary to differentiate between the number of dimensions on the nanoscale. Nanotextured surfaces have one dimension on the nanoscale, i.e., only the thickness of the surface of an object is between 0.1 and 100 nm. Nanotubes have two dimensions on the nanoscale, i.e., the diameter of the tube is between 0.1 and 100 nm. Finally, spherical nanoparticles have three dimensions on the nanoscale, i.e., the particle is between 0.1 and 100 nm in each spatial dimension. The dimensionality [2D-0D] refers to the number of directions in which the carriers of the material can act as the free carriers. In the case of a bulk material, the electronic carriers are free to move in all the three directions [2]. The nanoparticles discussed in this thesis work belong to two major categories; **(i).** Semiconductor nanoparticles and **(ii).** Metal nanoparticles.

1.2. Semiconductor nanoparticles

Nanomaterials can be of various shapes and therefore their properties may change according to their size and/or shape. These materials may be metals, semiconductors, metal oxides, organic materials or biomaterials. Thus there is a tremendous scope to design new materials with

unusual properties. Amongst the various types of nanomaterials, semiconductor nanoparticles have been widely investigated. Semiconductor nanoparticles constitute a bigger sector of the nanotechnology due to their wide range of applications in optics including nonlinear optical device fabrications, luminescent display technology as well as biological applications. Semiconductors have been useful in making electronic as well as optical devices. The drive towards miniaturization of electronic components and integration to accommodate huge number of them in small volume has been there for decades. This has enabled the evolution of very compact digital watches, calculators, computers, laptops etc. Electronic structure of nanomaterials may be different as compared to corresponding bulk material. This has led to interesting devices like single electron transistors, tunnel junctions, magnetic spin valves etc. which do not have bulk counterparts [3].

Besides this, at nano scale, semiconductor materials like silicon that are not optoelectronic materials due to indirect band gap have showed strong luminescence in visible range [4]. Moreover they exhibit emission which is size dependent luminescence. Some groups have showed [5, 6], for II-VI and III-V semiconductors, the change in band gap with particle size. Doped semiconductors such as CdSe, CdS has been used over a long term due to their good luminescent nature. But these quantum dots are found to be quite poisonous in nature so we are in survey of quantum dots which are non poisonous and highly trustworthy. This leads to the choice of ZnO and ZnS as the new nanostructured materials for the biological applications.

1.2.1. Quantum dot

Quantum dots are a non-traditional type of semiconductor with limitless applications as an enabling material across many industries. A quantum dot is a semiconductor nanostructure that confines the motion of conduction band electrons, valence band holes or excitons (pairs of conduction band electrons and valence band holes) in all three spatial directions.

A quantum dot has a discrete quantized energy spectrum [7]. The corresponding wave functions are spatially localized within the quantum dot, but extend over many periods of the crystal lattice. Larger quantum dots have more energy levels which are more closely spaced. This allows the quantum dot to absorb photons containing less energy, i.e. those closer to the red end of the spectrum. Larger dots have more closely spaced energy levels in which the electron-hole pair can be trapped. Therefore, electron-hole pairs in larger dots live longer causing larger dots to show a longer life time. A quantum dot contains a small finite number (of the order of 1-100) of conduction band electrons, valence band holes, or excitons, i.e., a finite number of elementary electric charges. Small quantum dots, such as colloidal semiconductor nanocrystals, can be as small as 2 to 10 nanometers, corresponding to 10 to 50 atoms in diameter and a total of 100 to 100,000 atoms within the quantum dot volume.

One of the optical features of small excitonic quantum dots immediately noticeable to the unaided eye is coloration. While the material which makes up a quantum dot defines its intrinsic energy signature, more

significant in terms of coloration is the size. The larger the dot, the redder (the more towards the red end of the spectrum) the florescence. The smaller the dot, the bluer (the more towards the blue end) it is. The coloration is directly related to the energy levels of the quantum dot. Quantitatively speaking, the band gap energy that determines the energy (and hence color) of the fluoresced light is inversely proportional to the square of the size of the quantum dot. Recent articles in nanotechnology and other journals have begun to suggest that the shape of the quantum dot may also be a factor in the colorization, but as yet not enough information has become available. Furthermore, it was shown [8] that the life time of fluorescence is determined by the size of the quantum dot.

Quantum dots found application as light emitting diodes in sign displays, cell staining for life science observation, even as inks that can aid in spotting counterfeits. Another security application that could soon be realized is luminescent dust, which could be used to track trespassers in restricted areas. Much like fiber optics, quantum dots may also be used to transmit data. Some estimates suggest that data transfer using quantum dots could be a million-fold efficient over standard ethernet connections. While these are some of the cutting edge applications, there are also more mundane ones as well. Quantum dots could be used as a light source in buildings, or even as illumination for computer screens.

1.2.2. Quantum well

A quantum well is a thin layer which can confine quasiparticles (typically electrons or holes) in the dimension perpendicular to the layer

surface, whereas the movement in the other dimensions is not restricted. That means it is a potential well that confines particles, which were originally free to move in three dimensions in to two dimensions, forcing them to occupy a planar region. The confinement is a quantum effect. The effects of quantum confinement take place when the quantum well thickness becomes comparable to the de-Broglie wavelength of the carriers (generally electrons and holes), leading to energy levels called "energy sub bands", i.e., the carriers can only have discrete energy values [8, 9]. It has profound effects on the density of states for the confined particles. For a quantum well with a rectangular profile, the density of states is constant within certain energy intervals.

A quantum well is often realized with a thin layer of a semiconductor medium, embedded between other semiconductor layers of wider band gap (examples: GaAs quantum well embedded in AlGaAs [10], or InGaAs in GaAs [11]). The thickness of such a quantum well is typically < 5–20□nm. Such thin layers can be fabricated with molecular beam epitaxy (MBE) or metal–organic chemical vapor deposition (MOCVD). In optically pumped semiconductor lasers, most pump radiation may be absorbed in the layers around the quantum wells, and the generated carriers are captured by the quantum wells thereafter.

If a quantum well is subject to strain, as can be caused by a slight lattice mismatch (e.g., for InGaAs quantum wells in GaAs), the electronic states are further modified, which can even be useful in laser diodes. Because of their quasi-two dimensional nature, electrons in quantum wells

have a sharper density of states than bulk materials. Therefore semiconductor quantum wells are often used in the active regions of laser diodes [12], where they are sandwiched between two wider layers with higher band gap energy. These cladding layers function as a waveguide, while electrons and holes are efficiently captured by the quantum well, if the difference in band gap energies is sufficiently large.

Quantum wells are also used as absorbers in semiconductor saturable absorber mirrors (SESAMs) and in electro absorption modulators. They are also used to make High Electron Mobility Transistors (HEMTs) [13], which are used in low-noise electronics. Quantum well infrared photo detectors [14] are also based on quantum wells and are used for infrared imaging. If a large amount of optical gain or absorption is required, multiple quantum wells (MQWs) can be used, with a spacing typically chosen large enough to avoid overlap of the corresponding wave functions.

1.2.3. Quantum wire

A quantum wire is an electrically conducting wire, in which quantum effects are affecting transport properties. Due to the confinement of conduction electrons in the transverse direction of the wire, their transverse energy is quantized into a series of discrete values E_0 ("ground state" energy, with lower value), E_1, E_2 etc (like particle in a box, quantum harmonic oscillator). An exact calculation of the transverse energies of the confined electrons has to be performed to calculate the wire resistance. Following from the quantization of electron energy, the resistance is also found to be quantized. The importance of the quantization is inversely

proportional to the diameter of the nanowire for a given material. From material to material, it is dependent on the electronic properties, especially on the effective mass of the electrons. In simple words, it means that it will depend on how conduction electrons interact with the atoms within a given material. In practice, semiconductors show clear conductance quantization for large wire transverse dimensions (100 nm) because the electronic modes due to confinement are spatially extended. As a result, their fermi wavelengths are large and thus they have low energy separations. This means that they can only be resolved at cryogenic temperature (few Kelvins) where the thermal excitation energy is lower than the inter-mode energy separation.

The electron transport properties in quantum wires were investigated and a quantum wire resonant tunnelling transistor, which works as a kind of multi channel rotational switch, was proposed in an earlier report [15]. Also there are reports on the ZnO nanowires based gas sensors for ethanol-sensing [16]. The quantum wire based dye sensitised solar cells [17] are now widely used in photovoltaics. It is possible to make quantum wires out of metallic carbon nanotubes [18], at least in limited quantities. The advantages of making wires from carbon nanotubes include their high electrical conductivity (due to a high mobility), light weight, small diameter, low chemical reactivity and high tensile strength. The major drawback of carbon nanotube based quantum wires is the high cost.

1.2.4. Confinement regimes

In a bulk materials, the carriers can exist in nearly continuous band, but in quantum dot structures due to the confinement of charges in all the

three directions, the carriers are restricted to a specific set of completely quantised energy states. The effect of confinement on the resulting energy state of the system can be obtained by solving for the eigen energies of the Schrodinger wave equation for the carriers in a confined space [19].

Different energy state equation can be obtained depending upon the confinement regimes. Depending upon the ratio between the nanocrystal radius a, and the bulk exciton radius a_x, three different confinement regimes can occur [20]. (1).Strong confinement regime (2).Weak confinement regime (3). Intermediate stage

The strong and weak states are determined by the degree of coupling between the electron and hole in the exciton.

(a).Strong confinement regime:

When the quantum dot radius a_0 is smaller than the excitonic bohr radius a_B, it corresponds to the strong confinement state.

$$\text{ie; } a_0 \ll a_B ,$$

which means that as the degree of confinement is increased in a smaller dot, the exciton can no longer exist and therefore an electron and a hole can be treated as independent particles [2]. In this situation the coulomb effects are small compared with the quantization of the kinetic energy of the carriers (confinement energies). When these conditions are present, the carriers are said to be strongly confined and the electron and hole wave functions are uncorrelated. Therefore the approach of solving the energy states in a strong confinement regime is similar to that in a weak confinement regime; but the only exception is that in the case of strong

confinement, the electron and hole have independent Bessel function and therefore the resulting energy shift expression can be written as,

$$E = E_g + \frac{\hbar^2 \pi^2}{2eR^2 \mu^*} - \frac{1.786e}{4\pi\varepsilon_0 \varepsilon_r R} - 0.248E_{ex} \qquad (1.1)$$

where E is the band gap of the dots, E_g is the band gap of the bulk material, R is the dot size, μ^* gives the effective reduced mass as $\frac{1}{\mu^*} = \frac{1}{m_e^*} + \frac{1}{m_h^*}$ and the last term represents the correlation energy which can be expressed in terms of the excitonic binding energy E_{ex}. m_e^* and m_h^* are the individual electron and hole masses respectively.

(b). Weak confinement regime:

When the quantum dot radius, a_0 is few times greater than the excitonic bohr radius, a_B; the confinement corresponds to the weak confinement regime.

$$\text{ie; } a_0 \rangle\rangle a_B$$

which means that coulomb interaction energy is on the order of the electron and hole sublevel separations and it has to be taken into account. Here the electron and hole motions are strongly correlated via coulomb interaction and the nanocrystal energy spectra are determined by the quantization of the motion of the exciton center of mass [2]. Expression for energy quantization in a spherical 0D structure is,

$$E = \frac{\hbar^2 \pi^2}{2em^* R^2} + E_g - E_{ex} \qquad (1.2)$$

where m^* is the translational mass of the exciton which is the algebraic sum of the electron and hole masses (effective exciton mass : $m^* = m_e^* + m_h^*$) and R is the mean dot size. The eqn. (1.2) gives the shift in energy that occurs when a bulk solid exciton is confined in 3D in the range of 3-10 times the exciton bohr radius. ie; a blue shift in energy results as the size of the crystal decreases.

(c). Intermediate stage

In the intermediate stage, the energy structures of nanocrystals are determined by a complex interplay between quantum confinement and the coulomb electron-hole interaction. Due to the relatively large exciton bohr radius II-IV nanocrystals are convenient systems for the studies of the strong, weak and intermediate regimes [20]. The coulomb interaction scales with the nanocrystal radius as a^{-1} where as the confinement energies are proportional to a^{-2}. Therefore in the strong confinement regime the coulomb term in the Hamiltonian can be ignored which leads to a problem of independent quantization of electron and hole energies. Effective mass approximation (EMA) has proven to be a powerful tool for describing energy structures in semiconductors, but it fails in the limit of very small nanocrystals [20].

1.2.5. Particles at the nano level

Semiconductor nanocrystallites are known to exhibit unique size dependent optical properties, which render them attractive from the view point of integrated photonic devices. Quantum confinement effects are

particularly important, if the crystalline dimension is less than a critical size known as the exciton bohr radius of the material.

Controlled variation of nanocrystalline size results in remarkable changes in the properties from molecular to bulk. Blue shift in the optical absorption spectrum, size dependent luminescence, enhanced oscillator strength and nonlinear optical effects are some examples of the interesting properties exhibited by these nanocrystals.

Due to the small size of the nanocrystals and hence their relatively large surface to volume ratio, the effect of nanocrystal surface on the charge carriers cannot be neglected [20]. In practice the surface properties must be modified in some way in order to control nanocrystal growth and reduce or prevent the charge carriers interacting with the surface, thus realizing effective quantum confinement. Surface passivation with various organic ligands or epitaxial over coating with a wide band gap semiconductor can be used to enable efficient radiative recombination of charge carriers.

1.2.6. Physical concepts of nanocrystals

Electronic states and probabilities of optical transitions in molecules and crystals are determined by the properties of the atom and their spatial arrangement. An electron in an atom possesses a discrete set of states, resulting in a corresponding set of narrow absorption and emission lines [19]. In semiconductors, broad bands of the allowed electron and hole states separated by a forbidden gap give rise to characteristic absorption and emission features completely dissimilar to atomic spectra. The evolution of

the properties of the matter from an atom to a crystal can be described in terms of the two steps,

(i) From the atom to cluster

(ii) From cluster to crystal

As the particle size grows, the properties can be described in terms of the particle size and shape. When the particle size becomes comparable to the de-Broglie wavelength of the elementary excitations, they are often called "Quantum crystallites", "Quantum dots" or "Quasi zero dimensional structures". As the size of these crystallites ranges from one to tens of nanometers, the word "Nanocrystals" is widely used [19].

From the view point of the solid state physics, nanocrystals are just a kind of a low dimensional structure complementary to quantum well (two dimensional structure) and quantum wire (one dimensional structure). Quantum wires and quantum wells possess translational symmetry in one or two dimensions and statistically a large number of electronic excitations can be created. In nanocrystals translational symmetry is totally broken, and only a finite number of electrons and holes can be created within the same nanocrystal. Therefore the concepts of electron-hole gas and quasi momentum are not applicable to nanocrystals [19]. Additionally a finite number of atoms in nanocrystal promotes a variety of photo induced phenomena like persistent and permanent photo physical and photo chemical phenomena that are known in atomic and molecular physics but do not occur in solids.

From the view point of molecular physics, a nanocrystal can be considered as a kind of large molecule. Every nanocrystal ensemble has inhomogeneously broadened absorption and emission spectra due to their distribution of sizes, defect concentration, shape fluctuation, environmental inhomogeneities and other features.

Also, as the size of crystallites and their concentration grow, the heterogeneous medium "matrix-crystallites" becomes a subject of the optics of ultra disperse media, thus introducing additional aspects to the optical properties of nanocrystal ensembles [20]. The matrices coloured with semiconductor nanocrystal have been known for centuries as stained glasses. Because of these features, studies of the optical properties of the nanocrystals form a new field of bordering solid state physics, optics, molecular physics and chemistry.

1.2.7. Electron states in crystal

A nanocrystal can be considered as a three dimensional potential box in which photon absorption and emission result either in creation or in annihilation of some elementary excitation in an electron sub system. These excitations are described in terms of quasi particles (electron, holes and excitons) known for bulk crystals [19]. Features connected with absorption and emission of light in nanocrystals can be understood in terms of the quantum confinement approach.

(a). Particle in a potential well

In order to consider electrons in a crystal, we start with a particle in a one dimensional potential well. The relevant time-independent Schrödinger equation is given as,

$$-\frac{\hbar^2}{2m}\frac{\partial^2}{\partial x^2}\psi(x)+U(x)\psi(x)=E\psi(x) \tag{1.3}$$

where m is the particle size and E is the particle energy. The potential U(x) is considered as a rectangular well with infinite walls and is given as,

$$U(x)=\begin{cases}0\ for|x|\le a/2\\ \infty for|x|\ge a/2\end{cases} \tag{1.4}$$

where a denotes the well width.

From elementary quantum mechanics, it is known that the Schrödinger equation stated above has the solutions of both even and odd types and is given as,

$$\psi^{(-)}=\sqrt{\frac{2}{a}}\frac{\cos}{\hbar}\sqrt{2mE} \quad \text{for n=1, 3, 5.....} \tag{1.5}$$

$$\psi^{(+)}=\sqrt{\frac{2}{a}}\frac{\sin}{\hbar}\sqrt{2mE} \quad \text{for n=2, 4, 6.....} \tag{1.6}$$

The most important result of the problem is a discrete set of energy values given by,

$$E_n=\frac{\hbar^2\pi^2n^2}{2ma^2} \tag{1.7}$$

where n takes values 1, 2, 3, etc. This equation gives values of kinetic energy. The minimum energy a particle can have (for n=1) is given by,

$$E_1 = \frac{\hbar^2 \pi^2}{2ma^2} \tag{1.8}$$

This energy is called the particle's zero point energy.

(b). Electron in a coulomb potential

The coulomb potential is given by the following eqn,

$$U(r) = -\frac{e^2}{r} \tag{1.9}$$

The equation for the radial part of the wave unction can be written as,

$$\left[\frac{d^2}{d\rho} + \varepsilon + \frac{2}{\rho} - \frac{l(l+1)}{\rho}\right] U(\rho) = 0 \tag{1.10}$$

The dimensionless argument $\rho = \frac{r}{a^0}$ and energy, $\varepsilon = \frac{E}{E^0}$ are expressed in terms of the so called atomic length unit a^0 and atomic energy unit E^0 as given by,

$$E^0 = \frac{e^2}{2a^0} \cong 13.6eV \tag{1.11}$$

where $a^0 = \frac{\hbar^2}{m_0 e^2} \cong 5.292 \times 10^{-2}\, nm$ with m_0 being the electron mass.

As a solution for the radial part of the wave function, the energy levels obeys a series, $\varepsilon = -\frac{1}{(n_r + l + 1)^2} = -\frac{1}{n^2}$, where the number $n = (n_r + l + 1)$ is called the "principal quantum number". Here n_r

determines the quantity of nodes of the corresponding wave function and is called the "radial quantum number".

For every n value, exactly n states exist differing in l, which varies from 0 to (n-1) and additionally for every l value, $(2l+1)$ degeneracy occurs with respect to $m = 0,\pm1,\pm2.....$

Therefore the total degeneracy is $\sum_{l=0}^{n-1}(2l+1) = n^2$

For n=1, $l=0$ (1s state), the wave function obeys a spherical symmetry with radius a^0 corresponding to the most probable distance where an electron can be found [19]. The relevant term a^0 in real atom like structures is called "Bohr radius". The problem of a particle in a spherical potential well is used to model an electron and a hole in a nanocrystal and the hydrogen atom model is essential to model for excitons in a bulk crystal and in nanocrystals.

(c). Electron in a periodic potential

Consider a particle in a potential of type U(x) = U(x+a) which shows the translation invariance. Then the Schrödinger equation takes the form,

$$-\frac{\hbar^2}{2m}\nabla^2\psi(x+a)+U(x)\psi(x+a)=E\psi(x+a) \qquad (1.12)$$

ie; the wave functions $\psi(x)$ and $\psi(x+a)$ satisfy the same schrodinger equation with the same eigen value E.

ie; $|\psi(x+a)|^2 = |\psi(x)|^2$

Wave function that satisfy the schorindger equation with a periodic potential can be written as, $\psi(x) = e^{ikx} u_k(x)$ where,

$$u_k(x) = u_k(x + a)$$

which means that the eigen functions of the Hamiltonian with a periodic potential is a plane wave modulated with the same period as the potential. This statement is known as the "Bloch's theorem". The wave numbers k_1 and k_2 differ by a value $k_1 - k_2 = \frac{2\pi n}{a}$, where n = ±1, ±2, ± 3..... Each of these intervals contains the full set of non equivalent k values and is called the "Brillouin zone". The dispersion curve has discontinuities at points $k_n = \frac{\pi n}{a}$ for every k_n value. The value $P = \hbar k$ is called "quasi-momentum". It differs from the momentum by a specific conservation law. Although the E(k) relation in the case under consideration differs noticeably from that for a free particle, it can be expressed as,

$$E(k) = \frac{\hbar^2 k^2}{2m^*(k)} \tag{1.13}$$

where m*(k) is a function referred to as "effective mass". For every periodic potential there exist extrima in the band structure and energy expression can be of the form,

$$E(k) = E_0 + (k - k_0)\left.\frac{dE}{dk}\right|_{k=k_0} + \frac{1}{2}(k - k_0)^2 \left.\frac{d^2E}{dk^2}\right|_{k=k_0} + \ldots\ldots\ldots \tag{1.14}$$

Neglecting the contributions from terms higher than k^2 we get the simplified expression analogous to above energy value expression. Therefore the effective mass m* is given by the relation,

$$m^{*-1} = \frac{1}{\hbar^2}\frac{d^2E}{dk^2}\bigg|_{k=k_0} = cons\tan t \qquad (1.15)$$

where as for a free particle m*= m.

To summarize the properties of a particle in a periodic potential, we can conclude with the following results

(i) A particle is described with a plane wave modulated with a period of the potential.

(ii) The particle state is characterized by the quasi momentum.

(iii) The energy spectrum consists of a wide continuous bands separated from each other by forbidden gaps.

As a plane wave, a particle in a periodic potential exhibits quasi free motion without acceleration. With respect to the external force the particle behaviour is described in terms of the effective mass.

1.2.8. Concept of quasi particles: Electron, Hole and Exciton

Electrons in the conduction band of a crystal can be described as particles with charge –e, spin ½, mass m_e^* and quasi momentum $\hbar k$ with respect to the conservation law. From the above mentioned parameters only the charge and the spin remain the same for an electron in a vacuum and in a crystal.

Quasi particles are described as the elementary excitations of the system consisting of a number of real particles. Under this consideration an

electron in the conduction band is the primary elementary excitation of the electron subsystem of a crystal. The further elementary excitation is a hole, which is a quasi particle relevant to an ensemble of electrons in the valence band from which one electron is removed. This excitation is characterized by the positive charge +e, spin ½, effective mass m_h^* and a proper quasi momentum.

If a photon of energy comparable to the band gap energy is incident on a semiconductor, then they can be absorbed by the electrons forming atomic bonds between neighboring and so provide them with enough energy to break free and move around in the body of the crystal. Within the band theory of solids this would be described as "exciting an electron from the valence band across the band gap into the conduction band". If the energy of the photon is larger than the band gap, a free electron is created and an empty state is left within the valence band. This empty space behaves very much like an air bubble in a liquid and rises to the top of the lower energy state. This hole behaves as though it was positively charged and hence forms a bond with the conduction band electrons. The attractive potential leads to the reduction in potential energy of the electron and hole. This bound electron-hole pair is known as exciton.

1.2.9. ZnO: An outlook

ZnO is a versatile material and has been used considerably for its catalytic, electrical, optical and photochemical properties [21]. Due to its wide band gap of 3.37eV and large exciton binding energy of 60meV at room temperature, ZnO is recognized as a promising optoelectronic

material in the blue-ultraviolet (UV) region and as an excellent candidate for dye sensitized oxide semiconductor solar cell, gas sensors or field emitter. ZnO is a direct II-IV semiconductor that crystallizes in the wurtzite structure at 300K with lattice constants of a=3.25Å and c=5.21 Å. The energy gap at room temperature is E_g=3.37eV and the free exciton binding energy equals 60meV [7, 21].

The Zn atoms are tetrahedrally coordinated to four O atoms and the Zn d-electrons hybridize with O p-electrons. The crystal structure of ZnO can be rock salt, zinc blende and wurtzite. From the calculations of ground state total energy of ZnO for different crystal structures by using a first principle periodic Hartree-Fock linear combination of atomic orbital theory, the wurtzite structure appears to be the most thermodynamically stable phase. Wurtzite zinc oxide has a hexagonal structure (space group *C6mc*) with lattice parameters a = 0.3296 and c = 0.52065 nm. The structure of ZnO can be simply described as a number of alternating planes composed of tetrahedrally coordinated O^{2-} and Zn^{2-} ions, stacked alternately along the c-axis (figure 1.1).

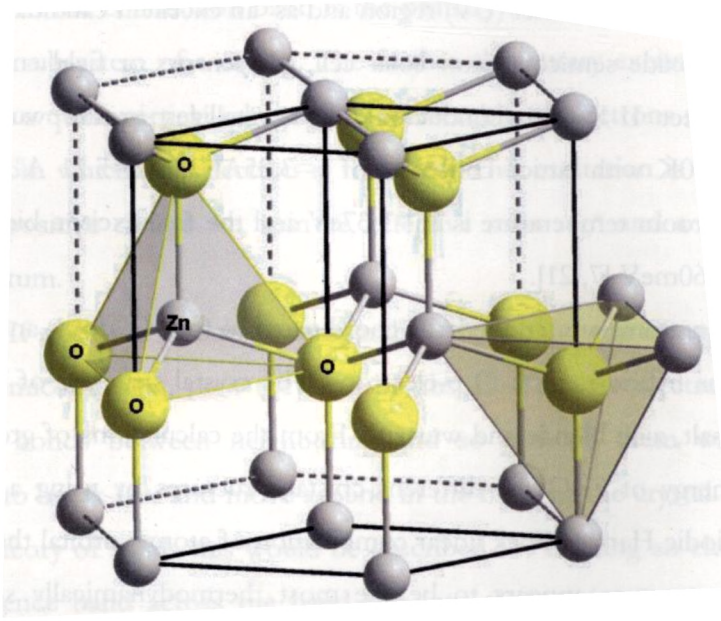

Figure 1.1. Wurtzite Crystal structure of ZnO.

It is predicted that the gas sensing, photon to electron conversion efficiency and photonic performance would be enhanced by reducing the dimensions of ZnO because of the surface area increase and the quantum confinement effect. Therefore, extensive research on the fabrication of ZnO nanostructures, such as nanowires, nanobelts, nanocables and nanotubes, has been carried out recently [7]. The fabrication method of the 1D ZnO nanostructures are mainly focused on the vapour transport including chemical vapor deposition (CVD), metal organic chemical vapour deposition (MOCVD), metal organic vapor phase epitaxy (MOVPE) or pulsed laser deposition. The growth of ZnO nanorods on Au-coated ITO substrates using a low temperature wet chemical process has been reported earlier [22].

The solution phase method at moderate temperature was recently reported to produce flower like ZnO nanocone and nanowire arrays on a Zn foil [21]. While most research to date has focused on vapour deposition, solution methods offer advantages of low temperature processing, large area uniformity, benign chemistry and potentially inexpensive manufacturing. Photoluminescence and cathodo luminescence spectra of the solution-grown ZnO nanorods were actively studied earlier [23].

In nanocrystals, the quantum confinement effect becomes a predominant investigation field which gives rise to many interesting optical and electronic properties [24]. The phenomenon concerning the quantum confinement effect in ZnO nanocrystals were rarely studied due to large electron effective mass caused by the large band gap (3.37eV) of this material. The large exciton binding energy of this material makes it an attractive candidate for room temperature lasing application. Additionally, the Coulomb interaction of electron and hole has reduced the exciton confinement energy partly due to the small dielectric constant in this system, which is also related to large band gap. Thus, the ZnO binary semiconductor material will have a small quantum confinement effect in quantum dot and quantum well structures.

The structural, morphological and luminescence properties of ZnO nanostructured films are usually influenced by the preparation techniques. Different types of ZnO nanostructures such as nanowires [24], nanorods [25], nanobelts [26], nanonails [27] and nanowalls [28] are reported in the literature. Among the various hierarchical structures, ZnO nanowires and

nanorods are widely studied on account of their suitability for various device applications. Usually one-dimensional nanorods are synthesized using thermal evaporation, chemical vapour deposition and molecular beam epitaxy techniques which are high temperature processes requiring costly equipment.

In recent years, the preparation of ZnO nanostructures through wet chemical methods has attracted a great deal of interest. The solution approach to the synthesis of ZnO nanorods is a viable low temperature simple process. Vayssieres *et al* developed a low temperature wet chemical process to produce arrays of ZnO nanorods [29] on various substrates. Wang *et al* synthesized arrays of obelisk-like ZnO nanorods [30] using an aqueous solution deposition method. Lee *et al* studied the fabrication of ZnO nanorod arrays on Si and Zn foil [31] using a low temperature aqueous solution method. Eventhough several methods are available for ZnO nanorod synthesis, systematic studies on the effect of precursor concentrations and deposition parameters on the growth of ZnO nanorods are only rarely reported in the literature.

The tetrahedral coordination in ZnO results in noncentro symmetric structure and consequently piezoelectricity [32] and pyroelectricity [33]. Here in our work we demonstrate the wet chemical route method for the synthesis of ZnO nanoparticles. This bottom up approach is motivated due to the considerable interest in the fabrication of optoelectronic devices.

1.2.10. Nanophosphors: An overview

Luminescence or 'weak glow' [34] is the radiation emitted by a material excessive in comparison to thermal radiation. It results from the transition of an excited electronic state to a ground state or another state lower in energy, the duration of which is much longer than the period of light vibrations (10^{-10} sec). The competing radiationless transitions results from interactions with the lattice or a transfer of energy to other ions. Luminescence, depending on the mode of excitation, is reflected in expressions such as photo-, electro-, chemi-, thermo-, sono-, or tribo luminescence. In practice, most often the excitation is via X-rays, cathode rays or UV emission of a gas discharge. The position of the band in the luminescence spectrum is independent of the method of excitation and is determined only by the inter-level spacing. Two other terms quite often used to classify luminescent materials are fluorescence ($\tau < 10$ ms) and phosphorescence ($\tau > 100$ms). As the mechanism of luminescence is associated with the duration of glow, the decay law of luminescence is exponential in fluorescence and hyperbolic or still more complicated for phosphorescence. The luminescent emission from the mineral "barite" on exposure to sunlight was identified as 'photoluminescence' (PL) first by Vincenzo Cascariolo. A material photoluminesces when excited by monochromatic light or by UV radiation with a spectrum broad enough to overlap the ion absorption bands. The phenomenon is pictorially illustrated using either a one-dimensional diagram of energy levels (in the form of

straight lines) or a bidimensional pattern (energy versus interionic distance) of the same levels in the form of configuration curves [35].

The three elementary processes between ion's states are: excitation, emission and radiationless transitions. If the interaction between the ion and the lattice is weak, the wavelength of the emission band matches that of the absorption band. For example, the f electrons in trivalent rare-earth (RE^{3+}) ions are shielded from the interactions with the lattice. If the interaction is fairly strong, as in transition metal ions, the emission band shifts towards longer wavelength with respect to the absorption band – a relation known as the empirical Stoke's law [36].

Excitation and emission are separated by a time interval i.e., by the life time of the excited state (~ 10^{-8} sec or more). This time interval is sufficient for the system to adapt itself to the given excited electronic state which includes shifting of the surrounding (ligand) ions to a new equilibrium position, rearranging the interionic distance and transition to the lowermost of the vibrational levels (~10^{-12} sec) i.e., to the excited electronic level. If a transition occurs between the levels, say, m (excited electronic state) and n (ground state or state of lower energy), the life time τ_m is expressed as,

$$\tau_m = \frac{1}{(\sum A_{mn} + \sum C_{mn})} \tag{1.16}$$

where, A_{mn} and C_{mn} denote the probability for radiative and nonradiative transitions between the levels. The summation is relevant whenever the transition occurs not over a single but over several sub-

adjacent levels. The fraction of emission transitions with respect to the sum total of emission and radiationless transitions gives the quantum yield η,

$$\eta = \frac{\sum A_{mn}}{(\sum A_{mn} + \sum C_{mn})} \tag{1.17}$$

If there are N_m photons in the excited state initially, the exponential law of luminescence decay states that after a time t,

$$N(t) = N_m e^{-t/\tau_m} \tag{1.18}$$

A direct relation exists between the emission intensity and the probability A_{mn} of emission transition given by,

$$I_{em} = N_m h\nu_{mn} A_{mn} \tag{1.19}$$

Thus, shorter the life time of the excited state i.e. time for photon emission, more intensive shall be the glow. Conversely, the greater the probability C_{mn} of radiationless transition, the lesser the intensity of glow and hence the quantum yield. The greater the oscillator strength for a given transition, higher shall be the intensity of the emission, provided radiation fewer transitions are absent. Photoluminescence is divided into two major kinds: intrinsic and extrinsic depending on the nature of electronic transition producing it.

(a). Intrinsic luminescence

The luminescence shown by the pure material itself is called the intrinsic luminescence. There are three kinds of intrinsic luminescence: band-to-band luminescence, exciton luminescence and cross luminescence.

(1). Band-to-band luminescence

The recombination of an electron in the conduction band with a hole in the valance band generates band-to-band luminescence. This kind of luminescence is observed in pure crystals at relatively high temperatures. For example Si, Ge and IIIb-Vb compounds such as GaAs. The light emission from bright light emitting diodes and semiconductor lasers is usually due to band-to-band transition process.

(2). Exciton luminescence

An exciton moves in a crystal conveying energy and produces luminescence owing to the recombination of the electron and the hole. There are two kinds of excitons: Wannier exciton and Frenkel exciton. The Wannier exciton model expresses an exciton as composed of an electron in the conduction band and a hole in the valence band bound together by the Coulomb interaction. The expanse of the wave function of the electron and hole is much larger than the lattice constant. This kind of luminescence is observed in inorganic semiconductors such as IIIb-Vb and IIb-VIb compounds. Wannier excitons are stable only at relatively low temperatures where the binding energies of excitons are higher than the thermal energy. At higher temperatures, excitons are no longer stable and band-to-band luminescence appears instead.

The Frenkel exciton model is used in cases where the expanse of the electron and hole wave function is smaller than the lattice constant. Typical examples are organic molecular crystals and inorganic complex salts. In these materials, the excited state of an isolated molecule or a complex ion

transfers from molecule to molecule or from complex ion to ion usually, owing to dipole-dipole interactions. It is therefore regarded as the exciton state. Luminescence characteristics are similar to those of isolated molecules or complex ions.

(3). Cross luminescence

Cross luminescence is produced by the recombination of an electron in the valance band with a hole created in the outer most core band [37]. This is observed in a number of alkali and alkaline earth halides and double halides. This occurs only when the energy difference between the top of valance band and that of the outermost core band is smaller than the band gap energy. Or else, an auger process occurs selectively. The shape of the spectra reflects the grouping of the molecular orbitals in the clusters involving cations with a hole in the core shell and nearest neighbour halide ions. For crystals with more than one type of cation, the spectrum reveals information about the 'active' cation which contains the core hole and also about the other cations. A notable characteristic of cross luminescence is that the decay time is very fast, of the order of nanoseconds or less, and hence such luminescent systems are used as scintillators [38].

(b). Extrinsic luminescence

Luminescence caused by intentionally incorporated impurities (or activators) is classified as extrinsic luminescence. Most of the observed types of luminescence that have practical applications belong to this category. Extrinsic luminescence in ionic crystals and semiconductors is classified into two types: unlocalized and localized.

(1). Unlocalized type

In the unlocalized type, the electrons and holes of the host lattice, i.e., free electrons in the conduction band and free holes in the valence band, participate in the luminescence process. This includes two kinds of luminescence transitions, namely the transition of a free carrier to a bound carrier and the transition of a bound electron at a donor to a bound hole at an acceptor. These kinds of luminescence lines and bands are usually observed in compound semiconductors such as IIIb-Vb and IIb-VIb compounds.

(2). Localized type

Here, the luminescence excitation and emission process are confined in a localized luminescence centre. Various kinds of metallic impurities intentionally incorporated in ionic crystals and semiconductors often create efficient localized luminescence centres. Localized type centres are classified into allowed and forbidden transition type in terms of electric dipole transitions. The electric dipole transition can take place between energy levels only with different parities ie. $\Delta l = \pm 1$, l being the azimuthal quantum number. When atoms and ions are incorporated in crystals, the forbidden character of the dipole transition is altered by the perturbation of the crystal electric field, so that the forbidden transition becomes allowed to some degree.

1.2.11. Development of ZnS based nanophosphors

Huge amount of research is being expanded during the recent years in order develop nanophosphors that come under the category of doped

nanocrystals (DNC) [39]. To utilize the phenomena of quantum confinement further, device fabrication with nano dimensions is being done world wide. The challenge is great but will be equally rewarding. Materials that convert absorbed energy to visible light without going to high temperatures i.e. incandescence are known as luminescent materials and also referred as phosphors. Such materials find applications in displays like television i.e. cathode ray tubes (CRT), plasma display panels (PDP), Electroluminescence (EL) based displays and field emission displays; in light sources like fluorescent tubes, compact fluorescent lamps and cold cathode lamps; as detectors for X-rays, temperature and pressure sensors. Phosphors are generally in crystalline powder form with size ranging from 1-100 μm. Phosphors with one dimension <100 nm are called nanophosphors, possess strikingly different absorption and emission characteristics with improved efficiency and life times [40].

Out of the generally used luminescent nanophosphors, ZnS based phosphors are widely used as one of the best candididate. ZnS occurs in two common polytypes, zinc blende (also called sphalerite) and wurtzite. The two types have these features in common: Zinc blende/sphalerite is based on a fcc lattice of anions whereas wurtzite is derived from an hcp array of anions. In both structures, the cations occupy one of the two types of tetrahedral holes present. The mineral crystallizes in the cubic crystal system. In the crystal structure, zinc and sulfur atoms are tetrahedrally coordinated. The structure is closely related to the structure of diamond. The lattice constant for zinc sulfide in the zinc blende crystal structure is 0.596 nm,

calculated from geometry and ionic radii of 0.074 nm (Zinc) and 0.184 nm (Sulfide). It forms ABCABC layers. The hexagonal analog is known as the wurtzite structure.

In either structure, the nearest neighbor connections are similar, but the distances and angles to further neighbors differs. Zinc blende has 4 asymmetric units in its unit cell whereas wurtzite has 2. To recap, zinc blende is best thought of as an fcc array of anions and cations occupying one half of the tetrahedral holes. Each ion is 4-coordinate and has local tetrahedral geometry. Unlike wurtzite, zinc blende has its own antitype, that means we can switch the anion and cation positions in the cell and it doesn't matter (as in NaCl). In fact, replacement of both the Zn and S with C gives the diamond structure. In Figure 1.2 shown below for the Sphalerite structure, notice that how only half of the tetrahedral sites (i.e. four of the eight octants of the cube) are occupied by Zn^{2+} (Blue).

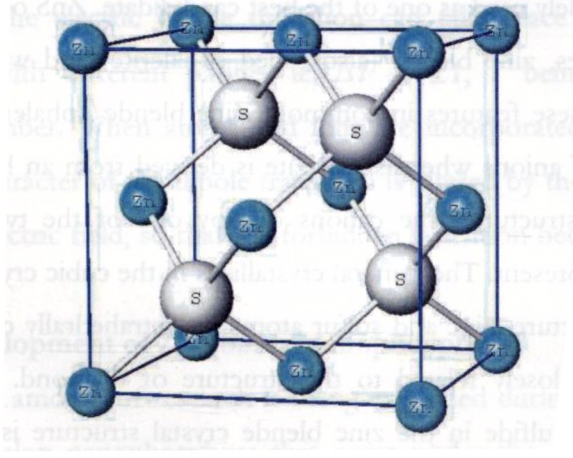

Figure 1.2. Shalerite structure of ZnS.

The first report on doped nanocrystals (DNCs) that showed all features such as increased band gap, shift of excitation and emission spectra of nanosized semiconductor was by Bhargava *et al* [41] in 1994. They synthesised manganese doped nanocrystals of zinc sulfide. Following the encouraging results of Bhargava *et al* on Mn doped ZnS nanophosphor, Khosravi *et al* [42] reported synthesis of manganese doped ZnS nanoparticles by aqueous method and synthesis of copper doped zinc sulphide quantum particles [43]. Method used by Weller *et al* [44] for the synthesis of CdS was employed for the purpose. Yu *et al* [45] prepared zinc sulfide nanoparticles with homogeneous Mn distribution and studied optical properties along with other characteristics. Stanic *et al* [46] reported in 1997 the sol–gel synthesis of nanosized ZnS, a key material to a large number of phosphors.

Yang *et al* [47] in 2001 synthesised ZnS nanocrystals co-activated with Cu and rare-earth metals like Ce, Y, Nd, Er and Tb. Doped zinc sulfide nanoparticles were made by precipitation from homogeneous solution. Ebenstein *et al* [48] in 2002 reported fluorescence quantum yield of CdSe/ZnS core/shell nanophosphors synthesised by them. Nandakumar *et al* [49] in 2002 synthesised CdS quantum dots in polymer matrix Nafion following ion exchange reaction. Synthesis and photoluminescent properties ZnS nanocrystals doped with Cu and halogen was reported by Manzoor *et al* [50] in 2003. For undoped ZnS, emission is reported to be peaked at 434 nm with a shoulder at 464 nm on excitation with 319 nm. The emission called self-activated emission and is attributed to sulfur vacancies contrary to Zn

vacancy related activated luminescence in bulk ZnS. The authors have studied undoped ZnS and some other ZnS:Cu,F samples with variation in stoichiometry. Lee *et al* [51] studied in 2004, the effect of synthesis temperature on particle size/shape of ZnS:Cu nanocrystals. The band diagram for copper doped ZnS nanophosphors is shown in figure 1.3. The additional sets of energy levels created due to the presence of defects are displayed clearly in the diagram.

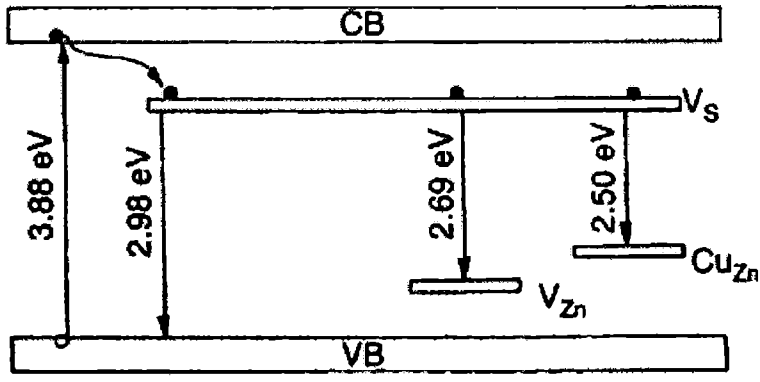

Figure 1.3. The energy band diagram of Cu doped ZnS (V_{Zn} is the zinc vacancy, Cu_{Zn} is the interstitial zinc and V_S is the sulphur vacancy.

Luminescence properties are characterised by studying excitation and emission spectra.

1.3. Metal nanoparticles

In recent years, researchers in the field of nanotechnology found that metal nanoparticles have all kinds of unexpected benefits in both the conventional and medical technology. Metal nanoparticles have served a variety of functions over time; gold and silver nanoparticles occupy the most popular position among the conventionally used metal nanoparticles in science and technology. They are non-toxic and appear to have endless medical applications; it has also been found that ingesting liquid gold nanoparticles has extremely beneficial effects on human health. Nanotechnology is fairly new to our civilization, but it turns out that colloidal gold has been in existence since ancient times and it was originally used to stain glass. It was rediscovered by Michael Faraday in the 1850s and almost immediately became one of science's favorite substances.

1.3.1. Surface plasmon resonance

Nanoparticle metal colloidal solutions of the noble metals of copper, silver and gold exhibit very intense colour which is absent in the bulk materials as well as for the individual atoms. This colouration is due to the collective oscillation of the free conduction electrons in metal nanoparticles induced by the interacting electromagnetic fields [52-55]. These resonances are called surface plasmon resonances (SPR). SPR originates from the field of plasmonics which constitutes the larger portion of nanophotonics. Nanophotonics is quite simply the study of the optical behaviour of nanometer scale objects [56].

Plasmonics is concerned with conduction electrons at metal surfaces and their interaction with electromagnetic radiation [57]. The quantization of the collective oscillations of electrons in the conduction band of a metal produces the plasmon. There are three types of plasmons: volume plasmons, surface plasmon polaritons and localized surface plasmons. Surface plasmons (SPs) are basically the quanta of plasma oscillations at a metal surface. When a surface plasmon couples with a photon, a quasiparticle called the surface plasmon polariton (SPP) is formed. Volume plasmons are the excitation of the conduction electron sea that occurs in bulk metals and localized surface plasmons are the excitations (non-propagating) of conduction electrons in metallic nanostructures coupled to the electromagnetic field.

Classical mechanics [58] and the Drude model can be used to describe plasmons and predict their behaviour [59, 60]. Surface plasmons (SPs) are coherent electron oscillations that exist at the interface between any two materials where the real part of the dielectric function changes sign across the interface (e.g. a metal-dielectric interface such as a metal sheet in air). The surface plasmon polariton (SPP) can propagate along the surface of a metal until energy is lost either via absorption in the metal or radiation into free-space. The existence of SPs was first predicted in 1957 by Ritchie *etal* [61]. Although a mathematical prediction of SPR was developed in the late 1890's, the SPR phenomenon was first physically witnessed in the early 20th century by Wood *etal* at Johns Hopkins University [62].

In detail, the surface plasmons (surface plasmon polaritons) are surface electromagnetic waves that propagate in a direction parallel to the metal/dielectric (or metal/vacuum) interface as shown in figure 1.4. Since the wave is on the boundary of the metal and the external medium (air or water for example), these oscillations are very sensitive to any change of this boundary, such as the adsorption of molecules on to the metal surface. SPs have lower energy than bulk (or volume) plasmons which quantise the longitudinal electron oscillations about positive ion cores within the bulk of an electron gas (or plasma). The charge density oscillations and associated electromagnetic fields are called surface plasmon-polariton waves. These waves can be excited very efficiently with light in the visible range of the electromagnetic spectrum. The excitation of a surface plasmon is one of the energy loss interactions that take place within the energy levels.

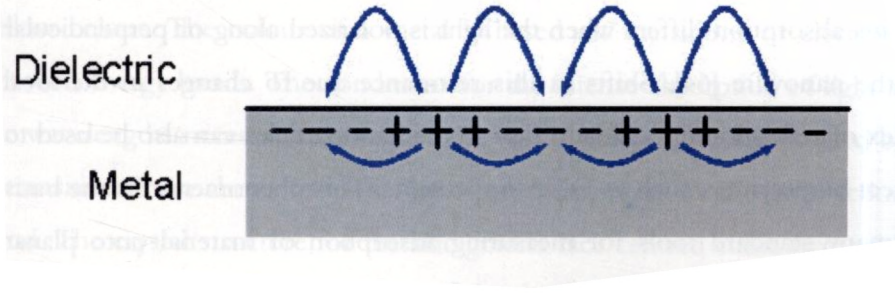

Figure 1.4. Schematic representation of an electron density wave propagating along a metal-dielectric interface.

The energy of the surface plasmon E_p may be estimated using the free electron model (eqn.(1.20), where n is the conduction electron density, e

is the elementary charge, m is the mass of an electron, and ϵ_0 is the permittivity of free space) which brought together the Drude model and the Fermi-Dirac statistics from quantum mechanics.

$$E_p = \hbar\sqrt{\frac{ne^2}{m\varepsilon_0}} \tag{1.20}$$

The excitation of SPs by light is denoted as an SPR for planar surfaces or a localized surface plasmon resonance (LSPR) for nanometer-sized metallic structures. For nanoparticles, localized surface plasmon oscillations can give rise to the intense colours of suspensions or sols containing the nanoparticles. Nanoparticles or nanowires of noble metals exhibit strong absorption bands in the ultraviolet-visible light regime that are not present in the bulk metal. This extraordinary absorption increase has been exploited to increase light absorption in photovoltaic cells by depositing metal nanoparticles on the cell surface [63]. The energy (colour) of this absorption differs when the light is polarized along or perpendicular to the nanowire [64]. Shifts in this resonance due to changes in the local index of refraction upon adsorption to the nanoparticles can also be used to detect biopolymers such as DNA or proteins. This phenomenon is the basis of many standard tools for measuring adsorption of material onto planar metal (typically gold and silver) surfaces or onto the surface of metal nanoparticles. It is behind many colour based biosensor applications and different lab-on-a-chip sensors.

SPR relies on the ability of a "source" to excite the SPs that reside in the conduction band of a noble-type metal thin film. Standard excitation

sources are electromagnetic radiation and electron beams. If a light source is used, it must be p-polarized (parallel to the plane of incidence). Wood's early work demonstrated that using s-polarized light would not produce the same excitation (in electronic surface plasmons) outcome as p-polarized light [61]. Common light sources can be in the far-infrared (10-1000 μm), mid-infrared (2.5-10 μm), near-infrared (750 nm-2.5 μm), or visible light ranges (400-700 nm). Lasers that operate at the desired wavelength are often used since they are monochromatic and coherent. The major class of metal nanoparticles discussed in the present thesis are gold and silver nanoparticles.

1.3.2. Gold nanoparticles

Gold is a chemical element with the symbol Au (Latin: *aurum*, "shining dawn") and an atomic number of 79. The atomic mass of the gold atom is 196.967amu and the atomic radius is 0.1442nm. The arrangement of outer electrons around the gold nucleus is related to gold's characteristic yellow colour. The colour of a metal is based on transitions of electrons between energy bands. The conditions for the intense absorption of light at the wavelengths necessary to produce the typical gold colour are fulfilled by a transition from the d band to unoccupied positions in the conduction band. The crystal structure for metallic gold is face centred cubic (fcc) with lattice parameter a=0.40788nm (see figure 1.5). This crystal structure contributes to gold's very high ductility since fcc lattices are particularly suitable for allowing the movement of dislocations in the lattice. Such dislocation movement is essential for achieving high ductility.

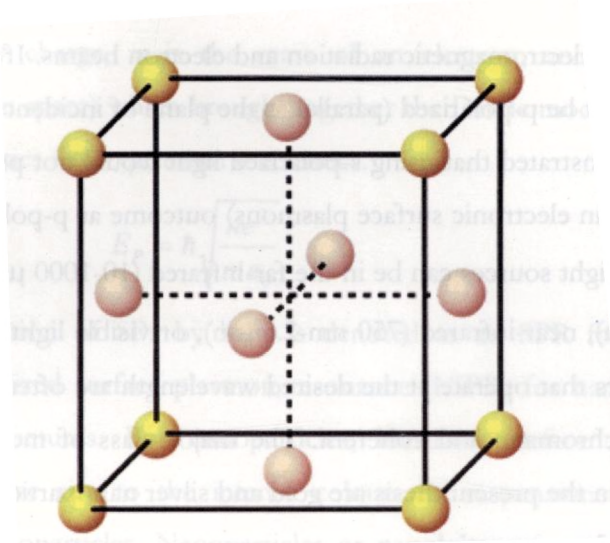

Figure 1.5. fcc crystal structure of gold.

The melting point of pure gold is 1064°C, although when alloyed with other elements such as silver or copper, the gold alloy will melt over a range of temperatures. The boiling point of gold, when gold transforms from the liquid to gaseous state is 2860°C. Gold is dense, soft, shiny and the most malleable and ductile pure metal known. Pure gold has a bright yellow colour and lustre traditionally considered attractive, which it maintains without oxidizing in air or water. Chemically, gold is a transition metal and can form trivalent and univalent cations in solutions. Compared with other metals, pure gold is chemically least reactive, but it is attacked by aquaregia (a mixture of acids), forming chloroauric acid, but not react with the individual acids and with alkaline solutions. Gold dissolves in mercury, forming amalgam alloys, but does not react with it. Gold demonstrates excellent biocompatibility within the human body (the main reason for its

use as a dental alloy), and as a result there are a number of direct applications of gold as a medical material.

Gold also possesses a high degree of resistance to bacterial colonisation and because of this; it is the material of choice for implants that are at risk of infection, such as the inner ear. It is important to draw a distinction between the properties of gold in the bulk form and those properties it exhibits when present in the form of nanoparticles. The unique properties of gold at the nanoscale lead to its use in a growing number of applications including colloids for optical limiting applications, biomedical applications and as catalysts in chemical processing and pollution control.

Colloidal gold, also known as "nanogold", is a suspension (or colloid) of sub-micrometer sized particles of gold in a fluid (usually water). The liquid is usually of either an intense red color (for particles less than 100 nm), or a dirty yellowish color (for larger particles). Properties and applications of colloidal gold nanoparticles depend upon shape. For example, gold nanorods have both transverse and longitudinal absorption peak and anisotropy of the shape affects their self-assembly [65]. The colour of the colloidal gold solution changes with the increase in the size of the nanoparticles dispersed in the media. The figure 1.6 shows how the colour of the colloidal gold nanoparticles solution shifts form wine red to blue color as the particle size is gradually increasing.

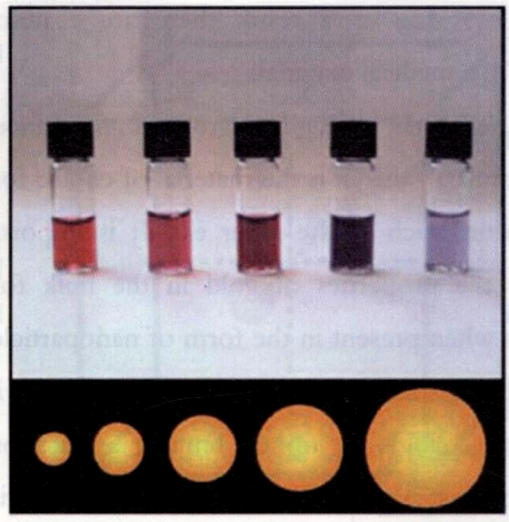

Figure 1.6. Shift in the colour of the gold colloid with increase in the nanoparticle size [66].

The property of SPR in the metal nanoparticles causes enhanced light absorption at frequencies very close to the SPR frequency which comes under the category of nonlinear absorption that find application in "optical limiting". The nonlinear absorption may be of multi photon absorption type occurring in a single step or may be an excited state absorption process which is a multi step process. That means the nonlinearity may be a spontaneous nonlinearity or a cascaded nonlinearity. Gold nanoparticles in a colloidal form or gold nanoparticles embedded dielectric matrices were selected widely for optical limiting application. Optical limiters are those materials whose transmittance falls with increase in incident light fluence

[67]. The fundamental mechanisms of optical limiting, their applications and their theoretical background are detailed well in chapter 3.

Among the commercially used optical limiting materials gold nanoparticles occupy a superior position. At the surface plasmon resonance (SPR) position the electric field inside the metal nanoparticle is much larger than the applied electric field. The ratio of the electric field inside the particle to the applied field is called the local field factor, $f(\omega)$. For a spherical particle with a radius that is very small compared to the wavelength of light, the local field factor is given by eqn.(1.21) [68, 69],

$$E_l = \frac{3\varepsilon_h}{\varepsilon_m + 2\varepsilon_h} E_0 = fE_0 \qquad (1.21)$$

where ε_h the dielectric constant of the host medium and ε_m is is the complex dielectric constant of the metal. The local field factor becomes large when the real part of the denominator ($\varepsilon_m + 2\varepsilon_h$) goes to zero.

Even when the inherent third order susceptibility $\chi_m^{(3)}$ of the metal inside the particle is very low, because of the local field enhancement the $\chi_m^{(3)}$ value could be very large. The third order optical nonlinearities of the materials are generally determined by the single beam method called Z-scan technique [70], the theory and experimental of the Z-scan setup are described in detail in chapter 3.

In addition to the nonlinear optical applications, colloidal gold has been successfully used as a therapeutic agent for rheumatoid arthritis in rats [71]. In a related study, [72] the implantation of gold beads near arthritic hip joints in dogs has been found to relieve pain. In cancer research, colloidal

gold can be used to target tumours and provide detection using SERS (surface enhanced Raman spectroscopy) in-vivo. Gold nanorods are being investigated as photo thermal agents for in-vivo applications. Gold nanorods are rod shaped gold nanoparticles whose aspect ratios tune the surface plasmon resonance (SPR) band from the visible to near infrared wavelength. Gold nanoparticles are promising probes for biomedical applications because they can be easily prepared and unlike other fluorescent probes such as quantum dots or organic dyes, they do not burn out after long exposure to light [73]. Gold nanoparticles are highly useful for a wide range of processes including general nanotechnology, electronics manufacturing and the synthesis of rare materials.

1.3.3. Silver nanoparticles

Silver is a metallic chemical element with the chemical symbol Ag (Latin: argentum, from the Indo-European root arg- for "white" or "shining") and atomic number 47. A soft, white, lustrous transition metal, it has the highest electrical conductivity than any element and the highest thermal conductivity than any metal. Metallic silver has an fcc lattice (shown in figure 1.7) with lattice parameter a=0.408626nm. Its electronic configuration is [Kr] $4d^{10}$ $5s^{1}$.

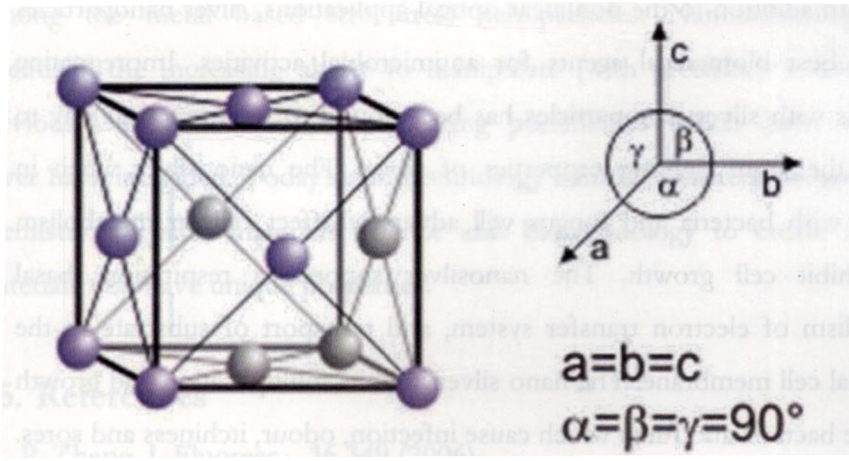

Figure 1.7. fcc structure of silver.

One nanomaterial that is having an early impact in healthcare products is nano-silver. Nanoparticles are used because they obviously exhibit enhanced or different properties when compared with the bulk material. Nano-silver is: highly efficacious, fast acting, non poisonous, non stimulating, non allergic, tolerance free and hydrophilic. Sharp surface plasmon absorption of silver nanoparticles [74] makes them very attractive for optics and bioscience applications. Silver nanoparticles are advantageous compared with nanoparticles of other noble metals (in particular, gold and copper) because the energy of the surface plasmon resonance (SPR) of silver lies far from the energy corresponding to inter band transitions. The latter means that, in composite materials with silver nanoparticles, it becomes possible to study optical nonlinearities associated with the SPR of silver.

In addition to the nonlinear optical applications, silver nanoparticles are the best biomedical agents for antimicrobial activities. Impregnating materials with silver nanoparticles has been found to be a practical way to exploit the germ fighting properties of silver. The nano silver when in contact with bacteria and fungus will adversely affect cellular metabolism and inhibit cell growth. The nanosilver suppresses respiration, basal metabolism of electron transfer system, and transport of substrate in the microbial cell membrane. The nano silver inhibits multiplication and growth of those bacteria and fungi which cause infection, odour, itchiness and sores. Their very small size results in particles having a large surface area relative to their volume. In the case of silver nanoparticles, this allows them to easily interact with other particles and thus increases their antibacterial efficiency. Nano silver can be applied to a range of other healthcare products such as dressings for burns, scald, skin donor and recipient sites; plasters for surgical and trauma wounds and aqueous gel for spots.

1.4. Conclusions

A brief introduction to the principles, theoretical back ground and applications of semiconductor and metal nanoparticles is given. Such nanotechnologically enhanced materials will enable a weight reduction accompanied by an increase in stability and improved functionality of optical, luminescent and biological devices. Among the various types of nanostructured materials presented, a special attention is given to ZnO and ZnS (among the semiconductor based nanomaterials) and gold and silver

(among the metal based structures) nanoparticles. Nanotechnology is essentially the increasing ability to manipulate (with precision) matter on previously impossible scales, presenting possibilities which many could never have imagined. Today's nanotechnology harnesses current progress in chemistry, physics, materials science and biotechnology to create novel materials that have unique properties.

1.5. References

1. P. Zhang, J. Fluoresc. **16** 349 (2006)
2. T. J. Bukowsk and J. H. Simmons, Crit. Rev. in Solid State Mater. Sci. **27** 119 (2002)
3. M. Bangal, S. Ashtaputre, S. Marathe, A. Ethiraj, N. Hebalkar and S. W. Gosavi, J. Urban and S. K. Kulkarni, Semiconductor Nanoparticles Hyperfine Interactions **160** 81 (2005)
4. L. T. Canham, Appl. Phys. Lett. **57** 1046(1990)
5. L. E. Brus, J. Chem. Phys. **80** 4403 (1984)
6. Y. Wang and N. Herron, J. Phys. Chem. **95** 525 (1991)
7. M. A. Reed, J. N. Randall, R. J. Aggarwal, R. J. Matyi, T. M. Moore and A. E. Wetsel, Phys. Rev. Lett. **60** 535 (1988)
8. A. F. Van Driel, Phys. Rev. Lett. **95** 236804 (2005)
9. C. T. Giner and J. L. Gondar, Physica B+C **138** 287(1986)
10. H. H. Tan, J. S. Williams, C. Jagadish, P. T. Burke and M. Gal, Appl. Phys. Lett. **68** 2401 (1996)

11. W. B. Peng, W. D. Hai, N. H.Qiao, H. S. Song, Z. Feng, X. Y. Hua, X. Y. Qiang and N. Z. Chuan, Chin. Phys. Lett. **24** 3543 (2007)
12. S. Nakamura, M. Senoh, S. Nagahama, N. Iwasa, T. Yamada, T. Matsushita, H. Kiyoku and Y. Sugimoto, Jpn. J. Appl. Phys. **35** L74 (1996)
13. M. Behet, K. V. Zanden, G. Borghs and A. Behres, Appl. Phys. Lett.**73** 2760 (1998)
14. B. F. Levine, Semicond. Sci. Technol. **8** S400 (1993)
15. J. Sone, Semicond. Sci. Technol. **7** 8210 (1992)
16. Q. Wan, Q. H. Li, Y. J. Chen, T. H. Wang, X. L. He, J. P. Li and C. L. Lin, Appl. Phys. Lett. **84** 3654 (2004)
17. M. Law, L. E. Greene, J. C. Johnson, R. Saykally and P. Yang, Nature Mater. Lett. **4** 455 (2005)
18. L. Guan, K. Suenaga, S. Okubo, T. Okazaki and S. Iijima, J. Am. Chem. Soc. **130** 2162 (2008)
19. S. V. Gaponenko, Optical properties of semiconductor nano crystals, Cambridge University Press, Cambridge (1998)
20. K. E. Gonsalves, S. P. Rangarajan and J. Wang edited by H. S. Nalwa, Nanostructured Materials and Nanotechnology; Academic Press USA (2002)
21. G. H. Du, F. Xu, Z. Y. Yua and G. V. Tendeloo, Appl.Phys. Lett. **88** 243101 (2006)
22. T. Mahalingam, K. M. Lee, K. H. Park, S. Lee, Y. Ahn, J. Y. Park and K. H. Koh, Nanotechnology **18** 035606 (2007)

23. J. W. P. Hsu, D. R. Tallant, R. L. Simpson, N. A. Missert and R. G. Copeland, Appl.Phys. Lett. **88** 252103 (2006)

24. C. Y. Lee, T. Y. Tseng, S. Y. Li and P. Lin, J. Sci. Eng. **6** 127 (2003)

25. H. Yu, Z. Zhang, M. Han, X. Hao and F. Zhu, J. Am.Chem. Soc. **127** 2378 (2005)

26. Y. X. Chen, X. Q. Zhao, B. Sha and J. H. Chen, Mater. Lett. **62** 2369 (2008)

27. X. Song, Y. Zhang, J. Zheng and X. Li , J. Phys. Chem. Solids **68** 1681 (2007)

28. J. Y. Lao, J. Y. Huang, D. Z. Wang, Z. F. Ren, D. Steeves, B. Kimball and W. Porter, Appl. Phys. A: Mater. Sci. Process. **78** 539 (2004)

29. L. Vayssieres, N. Beermann, S. E. Lindquist and A. Hagfeldt, Chem. Mater. **13** 233 (2001)

30. Z. Wang, X. F. Qian, J. Yin and Z. K. Zhu, J. Solid State Chem. **177** 2144 (2004)

31. J. H. Lee, I. C. Leu and M. H. Hon, J. Cryst. Growth **275** 2069 (2005)

32. K. M. Zhang, Y. P. Zhao, F. Q. He and D. Q. Liu, Chin. J. Chem. Phys. **20** 721 (2007)

33. G. Heiland and H. Ibach, Solid State Commun. 4 353 (1966)

34. G. Wiedemann, Ann. Phys. Chem. **34** 446 (1888)

35. A. S. Marfunin, Spectroscopy, Luminescence and Radiation Centers in Minerals, translated by V. V. Schiffer, Springer-Verlag, New York (1979)

36. D. R. Vij (Ed.), Luminescence of Solids, Plenum Press, New York (1998)

37. C. W. E. van Eijk, J. Lumin. **60** 936 (1994)

38. H. B. Dietrich and R. B. Murray, J. Lumin. **5** 155 (1972)

39. H. Chander, Mater. Sci. Eng. R **49** 113 (2005)

40. M. W. Blair, L. G. Jacobsohn, S. C. Tornga, O. Ugurlu, B. L. Bennett, E. G. Yukihara and R. E. Muenchausen, J. Lumin. **130** 825 (2010)

41. R. N. Bhargava, D. Gallagher, X. Hong and A. Nurmikko, Phys. Rev. Lett. **72** 416 (1994)

42. A. A. Khosravi, M. Kundu, B. A. Kuruvilla, G. S. Shekhawat, R. P. Gupta, A. K. Sharma, P. D. Vyas and S. K. Kulkarrni, Appl .Phys. Lett. **67** 2506 (1995)

43. A. A. Khosravi, M. Kundu, L. Jatwa, S. K. Deshpande, U. A. Bhagwat, M. Sastry and S. K. Kulkarni, Appl. Phys. Lett. **67** 2702 (1995)

44. H. Weller, Angew. Chem. Int. Ed. Engl. **32** 41 (1993)

45. I. Yu, T. Isobe and M. Senna, J. Phys. Chem. Solids **57** 373 (1996)

46. V. Stanic, T. H. Etsell, A. C. Pierre and R. J. Mikula, Mater. Lett. **31** 35 (1997)

47. P. Yang, M. Lu, D. Xu and G. Zhou, J. Lumin. **93** 101 (2001)

48. Y. Ebenstein, T. Mokari and U. Banin, Appl. Phys. Lett. **80** 4033 (2002)

49. P. Nandakumar, C. Vijayan and Y. V. G. S. Murti, J. Appl. Phys. **91** 1509 (2002)

50. K. Manzoor, S. R. Vadera, N. Kumar and T. R. N. Kutty, Mater. Chem. Phys. **82** 718 (2003)

51. S. Lee, D. Song, D. Kim, J. Lee, S. Kim, I. Y. Park and Y. D. Choi, Mater. Lett. **58** 342 (2003)

52. A. Cottey, J. Phys. C: Solid State Phys. 4 1734 (1971)

53. G. C. Papavassiliou, Prog. Solid State Chem. **12** 185 (1979)

54. B. S. Yilbas, R. Davies, Z. Yilbas and A. Koc, Pramana **34** 473 (1990).

55. F. Bohren and D. R. Huffman, Absorption and Scattering of Light by Small Particles, Wiley, New York (1983)

56. V. M. Shalaev and S. Kawata, Nanophotonics with Surface Plasmons; Elsevier, Amsterdam (2007)

57. S. A. Maier, Plasmonics: Fundamentals and Applications, Springer, New York (2007)

58. A. J. Haes, S. Zou, G. C. Schatz, R. P. V. Duyne, J. Phys. Chem. B **1008** 109 (2004)

59. P. Drude, Ann. Phys. **1** 566 (1900)

60. P. Drude, Theory of Optics, Longmans, Green *& Co.*, New York (1922)

61. R. H. Ritchie, Phys. Rev. **874** 106(1957)

62. R. W. Wood, Phil. Magm. 4 396(1902)

63. S. Pillai, K. R. Catchpole, T. Trupke and M. A. Green, J. Appl. Phys. **101** 093105(2007)

64. K. Locharoenrat, H. Sano and G. Mizutani, Sci. Technol. Adv. Mater. **8** 277 (2007)

65. S. Vivek, P. Kyoungweon and S. Mohan, Mater. Sci. Eng. Reports **65** 1(2009)

66. http://www.webexhibits.org/causesofcolor/images/content/9_diameter_of_gold.jpg

67. L. W. Tutt and T. F.Boggess, P. Quant. Electron. **17** 299 (1993)

68. D. Ricard, P. H. Roussignol and C. H. R. Flytzanis, Opt. Lett. **10** 511(1985)

69. F. Hache, J. Opt. Soc. Am. B **3** 1647 (1986)

70. M. Sheik-Bahae, A. A. Said and E. W. Van Stryland, Opt. Lett. **14** 955 (1989)

71. C. Y. Tsai , A. L. Shiau , S. Y. Chen, Y. H. Chen , P. C. Cheng , M. Y. Chang, D. H. Chen, C. H. Chou, C. R. Wang and C. L. Wu, Arthritis Rheum. **56** 544 (2007)

72. G. T. Jaeger, S. Larsen, N. Soli and L. Moe, Acta Vet Scand. **23** 49 (2007)

73. H. Xie, H. Alves and A. F. Morpurgo, J. Am. Chem. Soc. **80** 245305 (2009)

74. R. A. Ganeev, M. Baba, A. I. Ryasnyanski, M. Suzuki and H. Kuroda, Opt. Commun. **240** 437 (2004)

Chapter 2

Experimental techniques and tools used for the synthesis and characterization of the nanomaterials

2.1. Introduction

Nanotechnology is a very diverse field, ranging from extensions of conventional device physics to completely new approaches based upon molecular self-assembly. It is orienting at developing new materials with dimensions on the nanoscale and investigating whether we can directly control matter on the atomic scale. Nanotechnology has the potential to create many new materials and devices with a vast range of applications, such as in medicine, electronics and energy production. As particle size drop from microns to tens of nanometers, nanoparticles cease to behave as bulk and begin exhibiting quantum mechanical behaviour similar to that of individual atoms. Ten hydrogen atoms stacked side-by-side measure only a single nanometer. The lure of nanotechnology is not just making small devices; but to construct the smallest physical structures possible.

The goal of molecular manufacturing is to manipulate atoms individually and place them in a pattern to produce a desired structure. Experts sometimes disagree about what constitutes the nanoscale; but in general, you can think of nanotechnology dealing with anything measuring between 1 and 100 nm. Unusual physical, chemical and biological properties can emerge in materials at the nanoscale. These properties may differ in important ways from the properties of bulk materials or single atoms or molecules. A single atom is only a tenth of a nanometer in diameter.

Nanotechnology is, in a very literal sense, an opportunity to play with,

(1) Physical methods and

(2) Chemical methods to synthesise nanostructures.

Several different physical methods are currently in use for the synthesis and commercial production of nanostructured materials. The first and the most widely used technique involve the synthesis of single-phase metals and ceramic oxides by the inert-gas evaporation technique [1]. The generation of atom clusters by gas phase condensation [2] proceeds by evaporating a precursor material, either a single metal [3] or a compound [4], in a gas maintained at a low pressure, usually below 1 atm. The evaporated atoms or molecules undergo a homogeneous condensation to form atom clusters via collisions with gas atoms or molecules in the vicinity of a cold-powder collection surface. The clusters once formed must be removed from the region of deposition to prevent further aggregation and coalescence of the clusters. These clusters are readily removed from gas condensation chamber either by natural convection of the gas or by forced gas flow.

Sputtering is another technique used to produce nanostructured materials clusters as well as a variety of thin films [5]. This method involves the ejection of atoms or clusters of designated materials by subjecting them to an accelerated and highly focused beam of inert gas such as argon or helium. The third physical method involves the generation of nanostructured materials via severe mechanical deformation [6, 7]. In this method nanostructured materials are produced not by cluster assembly but

rather by structural degradation of coarser-grained structures induced by the application of high mechanical energy. The nanometer-sized grains nucleate within the shear bands of the deformed materials converting a coarse-grained structure to an ultrafine powder. The heavy deformation of the coarser materials is affected by means of a high-energy ball mill or a high-energy shear process. Although this method is very useful in generating commercial quantities of the material, it suffers from the disadvantage of contamination problems resulting from the sources of the grinding media.

Self-assembled quantum dots nucleate spontaneously under certain conditions during molecular beam epitaxy [MBE] [8] and metallorganic vapour phase epitaxy [MOVPE] [9], when a material is grown on a substrate to which it is not lattice matched. The resulting strain produces coherently strained islands on top of a two dimensional "wetting layer". This growth mode is known as Stranski-Krastanov growth [10]. The islands can be subsequently burried to form the quantum dot. This fabrication method has potential applications in quantum cryptography [11] (i.e. single photon sources) and quantum computation [12]. The main limitations of this method are the cost of fabrication and the lack of control over positioning of individual dots. The major two methods involved in the present thesis for the synthesis of nanostructured materials are liquid phase pulsed laser ablation (LP-PLA) and wet chemical methods. Controllable growth of flexible nanoparticles embedded polymeric optical devices can be fabricated at a very low cost through these two methods.

2.2. Liquid phase pulsed laser ablation (LP-PLA)

Formation of nanoparticles using pulsed laser ablation of solids, either in gas or in vacuum, has been extensively explored during the last decade for nanofabrication such as nanostructured thin films, nanorods [13], quantum wells and quantum dots [14]. Being performed in a controllable contamination-free environment this method makes possible the production of nanomaterials without impurities. Precise control over the size of the nanostructures could be attained by tuning various deposition parameters like substrate temperature, substrate to target distance, gaseous atmosphere in the chamber and laser energy density during the pulsed laser deposition [15].

Recently liquid phase-pulsed laser ablation technique (LP-PLA) has been evolved as a synthesis technique for the preparation of nanoparticles [16]. Liquid phase pulsed laser ablation (LP-PLA) involves the focusing of high intense laser beam (UV nanosecond pulsed laser source such as the frequency tripled (355 nm) or quadrupled (266 nm) solid state Nd:YAG laser or the KrF (248 nm) or ArF (193 nm) excimer laser) onto the surface of a solid target, which is submerged beneath a liquid (in the present work water) as shown in figure 2.1.

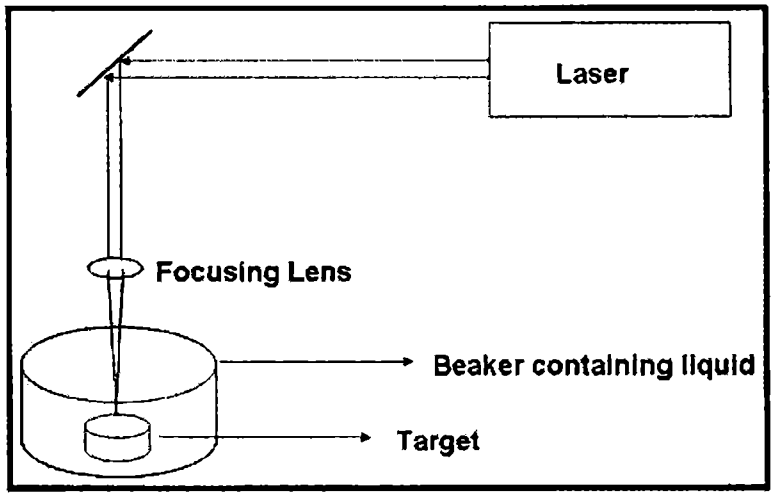

Figure 2.1. The setup of liquid phase pulsed laser ablation.

The very first process of liquid phase pulsed laser ablation is the interaction of laser with the solid target surface submerged below the liquid layer and subsequent vaporisation of the solid target as well as a very small amount of surrounding liquid. At sufficiently high incident flux densities and short pulse duration, all elements in the target are rapidly heated up to their evaporation temperature due to pulsed laser irradiation. It leads to the congruent evaporation of the target irrespective of the evaporating point of the constituent elements or compounds of the target. Materials are dissociated from the target surface and ablated out with the same stoichiometry as the target leading to plasma plume formation from the surface of the material. The species in the plasma plume will undergo rapid collision with the molecules of the surrounding liquid and react them,

producing new compounds containing atoms from both the original target and the liquid.

Since the ejected species are in highly excited state, there is strong chance for the chemical reactions between the ablated species and molecules in the liquid [17]. Typically the reaction products are nanoparticles consisting of atoms from both the target and the liquid, which will form nanoparticle suspension in the liquid. These nanoparticles accumulate homogenously in the surrounding liquid thus forming a colloidal solution. Therefore there is a chance for the prolonged interaction of this nanocolloidal suspension with the laser radiation leading to further changes in the nanoparticle's composition, size or morphology [18].

Thus we can see that the process of laser interaction with the target is similar for both laser ablation in vacuum and ablation at the solid-liquid interface. In both process plasma plume will be generated and create a strong confinement of the emission species, resulting in an efficient electron-ion recombination. The major difference is that when the plasma begins to expand, which occurs freely in vacuum in normal PLA where as it is confined by a liquid layer in LP-PLA. The liquid layer causes delay to the expansion of the plasma that will lead to a very high plasma pressure and temperature thus allowing the formation of novel materials.

Fabbro *et al* [19] reported that at the very initial stage of interaction of the high energy laser with the interface between the solid and the liquid, species ejected from the solid target surface have a large initial kinetic energy. The liquid surroundings will generate a covering effect to these

ejected species and the species will form a dense region in the vicinity of the solid-liquid interface. This stage is similar to that which occurs in vacuum or low pressure gas, where the laser generates a plasma 'plume'. In LP-PLA, the plasma is confined in the liquid and expansion process happens adiabatically at supersonic velocity generating a shock-wave in front of it. This shock-wave will cause an additional instantaneous pressure as it passes through the liquid. This 'laser-induced pressure' will result in the temperature increase in the plasma [20, 21]. This is another reason for the higher pressure and higher density in the case of plasma formed in LP-PLA compared with PLA plasma formed in gas or vacuum.

Detailed studies regarding the mechanisms involved in the nucleation and phase transition of nanocrystals upon LP-PLA are not reported yet. The nucleation thermodynamics, the phase transition and the growth kinetics of nanocrystals by laser ablation of liquids is explained well in a recent review by Yang *et al* [22]. It is proposed that LP-PLA is very fast and far from equilibrium process. Hence all metastable and stable phases forming at the initial, intermediate and final stages of the transformation must be reserved in the final products especially for any metastable intermediate phases [23]. It has been recently demonstrated [24, 25] that the nanoparticle size can be drastically reduced by the use of aqueous solutions. Gold as well as ZnO nanoparticles [26, 27] dispersed water can be prepared by this method using third harmonic Nd: YAG laser.

One of the advantages of LP-PLA is that both the solid target and the liquid are vaporised, so the product will contain atoms from the target

material and the liquid. The generation of various nanoparticles by LP-PLA is an alternative to the well-known chemical vapour deposition (CVD) method and is characterized by its relative simplicity and the low cost of the experimental setup. The very special advantage of LP-PLA is that nanoparticles produced by laser ablation of solid targets in a liquid environment are free of any counter-ions or surface-active substances because quantum dots can be directly dispersed in liquid medium without the play of much chemistry [28]. However, physical aspects of laser ablation in liquids still remain unclear and relative contributions of the physical and chemical factors of particle reduction are to be still evaluated.

2.2.1. Water Confined Regime (WCR) model

The plasma production in LP-PLA is associated with the shock wave emission [29]. It has been reported that the ablation rate is high in the water confined regime as compared to the ambient conditions [22]. In the WCR configuration water confined plasma exerts a much stronger pressure. This enhanced pressure has significant effects on the mechanical response of solid surfaces immersed in the liquid. This high-pressure, high-temperature plasma results in a much higher ablation rate. The duration of the shock wave is two to three times longer than that in the direct regime for the same laser intensity.

Here the target material is put in a glass jar with a water layer with an appropriate thickness above the target. It has been reported that the ablation rate could be highly enhanced in the WCR regime by a 1.1 mm water layer above the solid substrates as reported on Si substrate in water media [30].

The energy absorbed by the target material decreases quickly with the increase of the water layer thickness. Therefore, the plasma generated in water is weaker and the ablation rate decreases accordingly. With the increase of water layer thickness, the plasma became weaker and finally almost disappeared. Hence the thickness of the water layer should be minimum for efficient ablation rate.

Also the thickness of the water layer must not fall very low since it may lead to ablative piston effect. The removal of the material during laser ablation will lead to a rapid rise in the local particle density, which results in a rapid rise in the pressure of the materials' surface. This process is usually accompanied by plasma generation and the high pressure is released as a shock wave. After emitting into air, the shock wave will decay into acoustic waves by air friction, which is called the "ablative piston" effect [31]. When there is a water layer above the surface of the target, the shock wave generated during laser ablation will be emitted into the water layer first and the plasma will produce an explosion in water. Afterwards, the shock wave will decay into acoustic waves as a direct result of air friction. Therefore when the water layer thickness above the surface of the target is very small, the material removal rate will be very large and the ablative piston effect will be predominant in the ablation process.

We know that the pressure developed in the liquid confined ablation mode will be very high. An analytical model was previously introduced for the prediction of laser-induced pressures in the confined ablation mode [32]. According to this model there exist three different phases for the plasma;

laser heating, adiabatic cooling and final expansion. This model helps in the direct estimation of the pressure inside the confined plasma. This maximum pressure generated by the laser plasma in the WCR is given by the following relation [32],

$$P(GPa) = 0.01\sqrt{\frac{\alpha}{\alpha+3}} \times \sqrt{Z(gcm^{-2}s^{-1}} \times \sqrt{I_0(GW/cm^2)} \quad (2.1)$$

where I_0 the incident power intensity, α is the fraction of internal energy devoted to thermal energy (typically α=0.25) and Z the reduced shock impedance between target and the confining water defined by the relation,

$$\frac{2}{Z} = \frac{1}{Z_{water}} + \frac{1}{Z_{target}} \quad (2.2)$$

where Z_{water} and Z_{target} are the shock impedances of the water and the target respectively. The maximum pressure obtained in the water confined regime can be compared to the value obtained in the direct ablation regime. In the direct ablation regime under ambient conditions, the ablation pressure is given by the relation,

$$P_d(GPa) = 0.4 I_0^{0.7}(GW/cm^2)\lambda^{-0.03}(\mu m)\tau^{-0.05}(ns) \quad (2.3)$$

where λ is wavelength and τ pulse duration. The relation between the saturated vapour pressure P and plume temperature T is given by [33],

$$P(T) = P_0 \exp\left[-\frac{\Delta G_{lv}}{RT}\right] \quad (2.4)$$

where P_0 is the ambient pressure, ΔG_b and R are constants. Here, the surface temperature of substrate T_s is equal to plume temperature T at thermal equilibrium. The ablation rate v can be written as [34],

$$v = v_0 \exp\left(-\frac{T_a}{T_s}\right) \tag{2.5}$$

where v_0 is of the order of the sound velocity within the target material and T_a the activation temperature. From eqn.(2.4) it is obvious that the substrate surface temperature T_s increases with plasma pressure. Also from eqn.(2.5), it is observed that higher T_s results in higher ablation rate. Also the laser ablation in the water confined regime is a dynamic positive feedback process because the higher ablation rate of material will enhance the confined plasma pressure. Therefore, we can conclude that the ablation rate will be very much enhanced by WCR.

2.3. Chemical methods

Recent advances in the synthesis of various nanoparticles using colloidal chemical approaches involve either rapid injection of reagents into hot surfactant solution followed by ageing at high temperature or the mixing of reagents at a low temperature and slow heating under controlled conditions. The advantage of chemical synthesis is its versatility in designing and synthesizing new materials that can be refined into a final product. The primary advantage of the chemical processes over other methods is its good chemical homogeneity, as chemical synthesis offers mixing at the molecular level. Molecular chemistry can be designed to prepare new materials by

understanding how matter is assembled on an atomic or molecular level and the consequent effects on the desired material macroscopic properties. A basic understanding on the principles of crystal chemistry, thermodynamics and phase equilibrium and reaction kinetics is important to take advantage of the many benefits that chemical processing has to offer.

There are certain difficulties in general chemical processing. In some preparations, the chemistry is complex and hazardous. Contamination can also result from the byproducts being generated or side reactions in the chemical process. This should be minimized or avoided to obtain desirable properties in the final product. Agglomeration can also be a major cause of concern at any stage in a synthetic process and it can dramatically alter the properties of the materials. Agglomeration frequently makes it more difficult to consolidate nanoparticles to a fully dense and compact structure. Finally, although many chemical processes are scalable for economical production, it is not always straight forward for all systems.

Solution chemistry is used sometimes to prepare the precursor, which is subsequently converted to the nanophase particles by non-liquid phase chemical reactions. Precipitation of a solid from a solution is a common technique for the synthesis of fine particles. The general procedure involves reactions in the aqueous or non-aqueous solutions containing the soluble or suspended salts [1]. Once the solution becomes super saturated with the product, the precipitate is formed by either homogeneous or heterogeneous nucleation. The formation of a stable material with or without the presence of a foreign species is referred to as heterogeneous or

homogeneous nucleation respectively. The growth of the nuclei after formation usually proceeds by diffusion, where concentration gradients and reaction temperatures are very important in determining the growth rate of particles, for example to form monodispersed particles. For instance, to form unagglomerated particles with a very narrow size distribution, all the nuclei must be formed at nearly the same time and the subsequent growth must occur without further nucleation or agglomeration of particles.

Nanostructured materials are also prepared by chemical vapour deposition (CVD) [35] or chemical vapour condensation (CVC) [36] which are used to produce high-purity, high-performance solid materials. That means a chemical precursor is converted to the gas phase and it then undergoes decomposition at either low or atmospheric pressure to generate the nanostructured particles. Precursor gases (often diluted in carrier gases) are delivered into the reaction chamber at approximately ambient temperatures. As they pass over or come into contact with a heated substrate, they react or decompose forming a solid phase and are deposited onto the substrate. The process is often used in the semiconductor industry to produce thin films.

Chemical vapour deposition (CVD) is a generic name for a group of processes that involve depositing a solid material from a gaseous phase and is similar in some respects to physical vapour deposition (PVD). In a typical CVD process, the wafer (substrate) is exposed to one or more volatile precursors, which react and/or decompose on the substrate surface to produce the desired deposit. Frequently, volatile byproducts are also

produced, which are removed by gas flow through the reaction chamber. CVD is an extremely versatile process that can be used to process almost any metallic or ceramic compound. Some of these include elements, metals, alloys, carbides, nitrides, borides, oxides and intermetallic compounds. It has applications in coatings for a variety of applications such as wear resistance, corrosion resistance, high temperature protection, erosion protection etc. They also find applications in integrated circuits, sensors and optoelectronic devices, production of novel powders and fibres and optical fibres for telecommunications. The clusters prepared by these methods have poorly defined surfaces and a broad size distribution, which is detrimental to the properties of semiconductor materials. A more detailed discussion on nanomaterial preparation and nanostructure fabrication can be found in the recent literature [1].

2.3.1. Wet chemical methods

Wet chemical method is a recently introduced method which is a simple, room temperature method for the synthesis of nanostructures. Wet chemistry is a term that represents a number of scientific techniques that involve direct experimentation with liquids. Because it is a broad industry term, the exact definition will vary from business to business. A general rule that can be applied is that if it involves a scientist working with liquids by hand and physically observing the results of the experiment, it is wet chemistry. The use of robotics in the laboratory, however, has even challenged this definition to some extent.

Wet chemistry includes basic experimentation techniques like measuring, mixing and weighing chemicals, as well as testing concentration, conductivity, density, pH, specific gravity, temperature, viscosity and other aspects of liquids. Analytical techniques in wet chemistry are usually qualitative in nature, meaning that they attempt to determine the presence of a specific chemical rather than the exact amount. However, some quantitative techniques are used in wet chemistry, and they include gravimetric (weighing) and volumetric analysis (measuring).

Bench chemistry is sometimes used as a synonym for wet chemistry. The terms differ in two primary ways: first, bench chemistry can involve dry chemicals, while wet chemistry always involves at least one substance in the liquid phase; second, wet chemistry sometimes involves hightech equipment, while bench chemistry only includes techniques that use simple devices in keeping with the classical chemistry spirit. Both types of chemistry, however, do share many of the same techniques and equipment.

A large number of techniques have been used for the synthesis of semiconductor nanostructures, such as electrochemical deposition technique, sputter deposition, hydrothermal methods and vapour methods. The above said methods require reaction conditions such as high reaction temperature or accurate gas concentration, gas flow rate or scarce raw materials or complex processes and so on. Hence the wet chemistry offers simple, low temperature and environment protective method for the synthesis of the semiconductor nanoparticles.

NASA's Phoenix Mars Lander had a wet chemistry lab abroad when it landed on the red planet in 2008. As one of its experiments, Phoenix scooped up small amounts of soil, then dissolved the samples in water. The soil solutions then had various aspects tested, including conductivity, pH and redox potential. The instruments also tested for the presence of bromide anions, carbon, chloride anions, magnesium cations, oxygen, sodium cations and sulfate anions.

2.4. Characterisation tools

2.4.1. Structural characterisation

(a). X-ray diffraction studies (XRD)

Electrical and optical properties of the materials are influenced by their crystallographic nature. X-ray diffraction (XRD) studies were carried out to study the crystallographic properties of the nanostructures prepared. A given substance always produces a characteristic X-ray diffraction pattern, whether that substance is present in the pure state or as one constituent of a mixture of substances. This fact is the basis for the diffraction method of chemical analysis. The particular advantage of X-ray diffraction analysis is that it discloses the presence of a substance but not in terms of its constituent chemical elements. Diffraction analysis is useful whenever it is necessary to know the state of chemical combination of the elements involved or the particular phase in which they are present. Compared with ordinary chemical analysis, the diffraction method has the advantage that it

is much faster, requires only very small amount of sample and is non destructive [37, 38].

The basic law involved in the diffraction method of structural analysis is the Bragg's law. When monochromatic X-rays impinge upon the atoms in a crystal lattice, each atom acts as a source of scattering. The crystal lattice acts as series of parallel reflecting planes. The intensity of the reflected beam at certain angles will be maximum when the path difference between two reflected waves from two different planes is an integral multiple of λ. This condition is called Bragg's law and is given by the relation,

$$n\lambda = 2d\sin\theta \tag{2.6}$$

where n is the order of diffraction, λ is the wavelength of the X-rays, d is the spacing between consecutive parallel planes and θ is the glancing angle (or the complement of the angle of incidence) [39]. The schematic diagram of XRD is shown in figure 2.2.

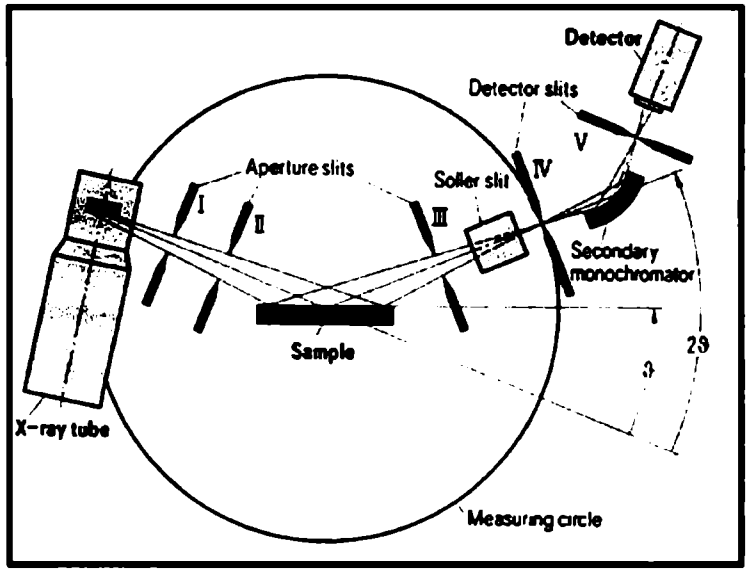

Figure 2.2. Schematic of an X-ray diffractometer.

X-ray diffraction studies give a whole range of information about the crystal structure, orientation, average crystalline size and stress in the sample material. Experimentally obtained diffraction patterns of the sample are compared with the standard powder diffraction files published by the international centre for diffraction data (ICDD). The average grain size D of the sample can be calculated using the Scherrer's formula [37],

$$D = \frac{0.9\lambda}{\beta \cos\theta} \tag{2.7}$$

where, λ is the wavelength of the X-ray and β is the full width at half maximum intensity in radians. The lattice parameter values for different

crystallographic systems can be calculated from the following equations using the (hkl) parameters and the interplanar spacing d_{hkl}.

For cubic system,

$$d_{hkl} = \frac{a}{\sqrt{h^2 + k^2 + l^2}} \qquad (2.8)$$

X-ray diffraction measurements of the different nanostructures were done using Rigaku automated X-ray diffractometer. The filtered copper K_α (λ=1.5418A^0) radiation was used for recording the diffraction pattern.

(b). Transmission electron microscopy (TEM)

Transmission electron microscopy (TEM) is an imaging technique whereby a beam of elecrons is focused onto a specimen causing an enlarged version to appear on a fluorescent screen or layer of photographic film or to be detected by a CCD camera. The first practical transmission electron microscope was built by Albert Prebus and James Hillier at the University of Torondo in 1938 using concepts developed earlier by Max Knoll and Ernst Ruska. Electrons are generated by a process known as thermionic emission in the same manner as the cathode in a cathode ray tube, or by field emission; they are then accelerated by an electric field and focused by electrical and magnetic fields onto the sample. The electrons can be focused onto the sample providing a resolution far better than that is possible with light microscopes and with improved depth of vision. Figure 2.3 shows a schematic outline of a TEM instrument. A TEM contains four parts:

Electron source

The electron source consists of a cathode and an anode. The cathode is a tungsten filament which emits electrons when heated. A negative cap confines the electrons into a loosely focused beam (Figure 2.2). The beam is then accelerated towards the specimen by the positive anode. Electrons at the rim of the beam will fall onto the anode while the others at the center will pass through the small hole of the anode. The electron source works like a cathode ray tube.

Electromagnetic lens system

After leaving the electron source, the electron beam is tightly focused using electromagnetic lens and metal apertures. The system only allows electrons within a small energy range to pass through, so the electrons in the electron beam will have a well-defined energy.

Sample holder

The sample holder is a platform equipped with a mechanical arm for holding the specimen and controlling its position.

Imaging system

The imaging system consists of another electromagnetic lens system and a screen. The electromagnetic lens system contains two lens systems, one for refocusing the electrons after they pass through the specimen and the other for enlarging the image and projecting it onto the screen. The screen has a phosphorescent plate which glows when being hit by electrons. Image forms in a way similar to photography.

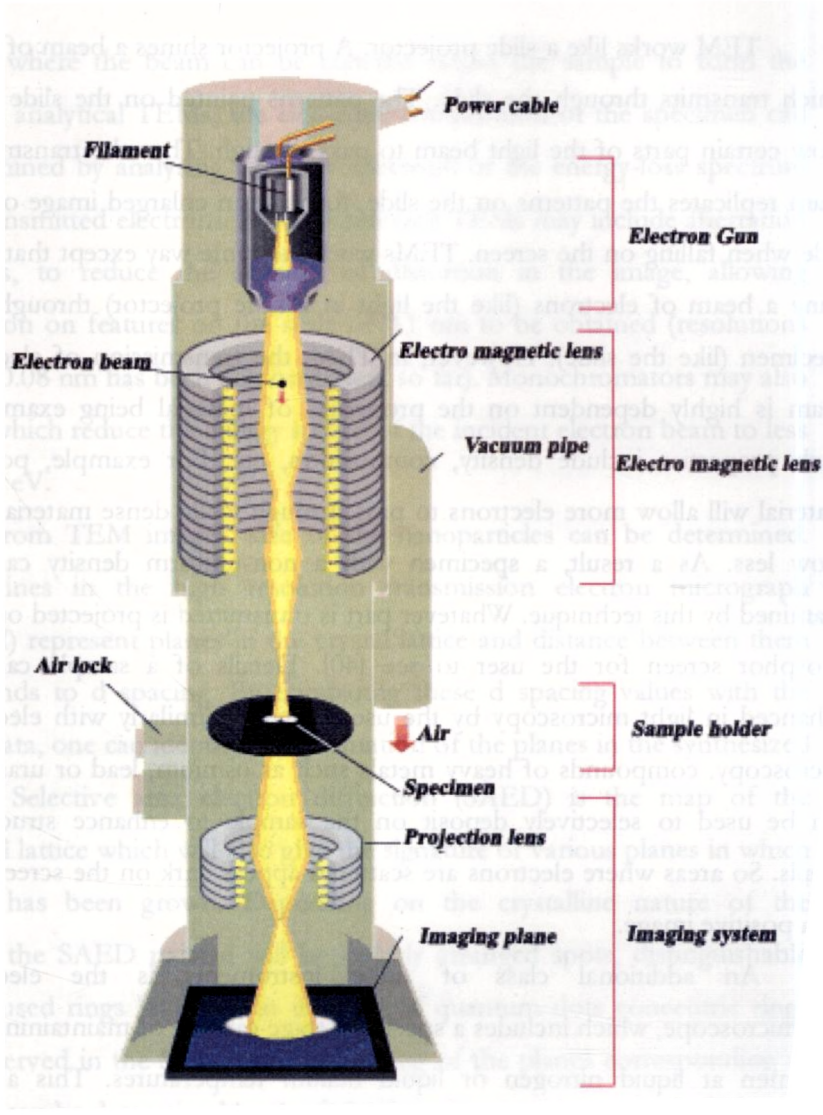

Figure 2.3. Schematic of a transmission electron microscope.

TEM works like a slide projector. A projector shines a beam of light which transmits through the slide. The patterns painted on the slide only allow certain parts of the light beam to pass through. Thus the transmitted beam replicates the patterns on the slide, forming an enlarged image of the slide when falling on the screen. TEMs work the same way except that they shine a beam of electrons (like the light in a slide projector) through the specimen (like the slide). However, in TEM, the transmission of electron beam is highly dependent on the properties of material being examined. Such properties include density, composition, etc. For example, porous material will allow more electrons to pass through while dense material will allow less. As a result, a specimen with a non-uniform density can be examined by this technique. Whatever part is transmitted is projected onto a phosphor screen for the user to see [40]. Details of a sample can be enhanced in light microscopy by the use of stains. Similarly with electron microscopy, compounds of heavy metals such as osmium, lead or uranium can be used to selectively deposit on the sample to enhance structural details. So areas where electrons are scattered appear dark on the screen, or on a positive image.

An additional class of these instruments is the electron cryomicroscope, which includes a specimen stage capable of maintaining the specimen at liquid nitrogen or liquid helium temperatures. This allows imaging specimens prepared in vitreous ice, the preferred preparation technique for imaging individual molecules or macromolecular assemblies. Another type of TEM is the scanning transmission electron microscope

(STEM), where the beam can be rastered across the sample to form the image. In analytical TEMs, the elemental composition of the specimen can be determined by analysing its X-ray spectrum or the energy-loss spectrum of the transmitted electrons. Modern research TEMs may include aberration correctors, to reduce the amount of distortion in the image, allowing information on features on the scale of 0.1 nm to be obtained (resolutions down to 0.08 nm has been demonstrated, so far). Monochromators may also be used which reduce the energy spread of the incident electron beam to less than 0.15 eV.

From TEM images, size of the nanoparticles can be determined. Parallel lines in the high resolution transmission electron micrograph (HRTEM) represent planes in the crystal lattice and distance between them corresponds to d spacing. By comparing these d spacing values with the JCPDS data, one can identify the orientation of the planes in the synthesized material. Selective area electron diffraction (SAED) is the map of the reciprocal lattice which will also give the signature of various planes in which material has been grown. Depending on the crystalline nature of the material, the SAED pattern will be orderly arranged spots, distinguishable ring or fused rings [41]. But in the case of quantum dots concentric rings were observed in the SAED. The d spacing of the planes corresponding to the rings can be determined by the following equation,

$$dD = CL\lambda \tag{2.9}$$

where L is the effective camera length, λ is the de Broglie wavelength of the accelerated electrons, D is the ring diameter of the electron diffraction

(STEM), where the beam can be rastered across the sample to form the image. In analytical TEMs, the elemental composition of the specimen can be determined by analysing its X-ray spectrum or the energy-loss spectrum of the transmitted electrons. Modern research TEMs may include aberration correctors, to reduce the amount of distortion in the image, allowing information on features on the scale of 0.1 nm to be obtained (resolutions down to 0.08 nm has been demonstrated, so far). Monochromators may also be used which reduce the energy spread of the incident electron beam to less than 0.15 eV.

From TEM images, size of the nanoparticles can be determined. Parallel lines in the high resolution transmission electron micrograph (HRTEM) represent planes in the crystal lattice and distance between them corresponds to d spacing. By comparing these d spacing values with the JCPDS data, one can identify the orientation of the planes in the synthesized material. Selective area electron diffraction (SAED) is the map of the reciprocal lattice which will also give the signature of various planes in which material has been grown. Depending on the crystalline nature of the material, the SAED pattern will be orderly arranged spots, distinguishable ring or fused rings [41]. But in the case of quantum dots concentric rings were observed in the SAED. The d spacing of the planes corresponding to the rings can be determined by the following equation,

$$dD = CL\lambda \tag{2.9}$$

where L is the effective camera length, λ is the de Broglie wavelength of the accelerated electrons, D is the ring diameter of the electron diffraction

pattern and d is the interplanar spacing [40]. The term in the right hand side of the eqn.2.9 is referred to as the camera constant. TEM, JEOL operating at an accelerating voltage of 200 kV was used for the determination of the particle size and crystalline nature of the nanoparticles in the present work.

2.4.2. Optical studies

In the present study, diffuse reflectance spectroscopy and optical absorption spectroscopy were the optical characterization tools to determine the band gap of powder and solution samples respectively.

(a). Diffuse reflectance spectroscopy (DRS)

Diffuse reflection is the reflection of light from an uneven or granular surface such that an incident ray is seemingly reflected at a number of angles. Diffuse reflected rays from a sample do not obey the Snell's law as do the ordinary mirror-like specular reflections. The measurement of radiation diffusely reflected from a surface constitutes the area of spectroscopy known as diffuse reflectance spectroscopy (DRS). Specular reflection is due to the reflection at the surface of single crystallites while diffuse reflection arises from the radiation penetrating into the interior of the solid and re-emerging to the surface after being scattered numerous times. Thus, the DRS spectra will exhibit both absorbance and reflectance features due to contributions from transmission, internal and specular reflectance components as well as scattering phenomena in the collected radiation.

Based on the optical properties of the sample, several models have been proposed to describe the diffuse reflectance phenomena. The Kubelka-

Munk (KM) model put forward in 1931 [42, 43] is widely used and accepted in DRS. The KM theory is based on a continuum model where reflectance properties are described by differential equations for infinitesimally small layers. When the depth of the sample is infinite, the theory is solved to arrive at the remission function or the so-called KM function $f(r_\alpha)$,

$$f(r_\alpha) = \frac{(1-r_\alpha)^2}{2r_\alpha} = \frac{k}{s} \qquad (2.10)$$

where, $r_\alpha = \frac{R_\alpha(Sample)}{R_\alpha(S\tan dared)}$, R_α denotes the diffuse reflectance. Here the standard used is $BaSO_4$. R (standard) is taken as unity. The intensity of the diffusely reflected light therefore depends on the scattering coefficient s and the absorption coefficient k. The band gap is estimated from the plot of $\{(k/s).h\nu\}^2$ versus $h\nu$.

(b). Optical absorption spectroscopy

Intrinsic optical absorption of a single photon across the band gap is the dominant optical absorption process in a semiconductor. The absorption/ transmission of thin films as well as colloidal solutions in the present study were recorded using Jasco V570 spectrophotometer. The block diagram of the spectrophotometer while taking the absorption of a solution is shown in figure 2.4. The spectrophotometer uses two light sources, a deuterium (D2) lamp for ultraviolet light and a tungsten (W) lamp for visible light. After bouncing off a mirror (mirror 1), the light beam passes through a slit and hits a diffraction grating. The grating can be rotated allowing for a specific wavelength to be selected. At any specific orientation

of the grating, only monochromatic light (single wavelength) successfully passes through a slit. A filter is used to remove unwanted higher orders of diffraction. The light beam hits a second mirror before it gets split into half (half of the light is reflected, the other half passes through). One of the beams is allowed to pass through a reference cuvette (which contains the solvent only), the other passes through the sample cuvette. The intensities of the reference light beam (I_0) as well as the transmitted beam (I) are then measured at the end using detector 1 and 2. From the value of I_0 and I the absorption coefficient (α) and band gap (E_g) of the sample material can be found out.

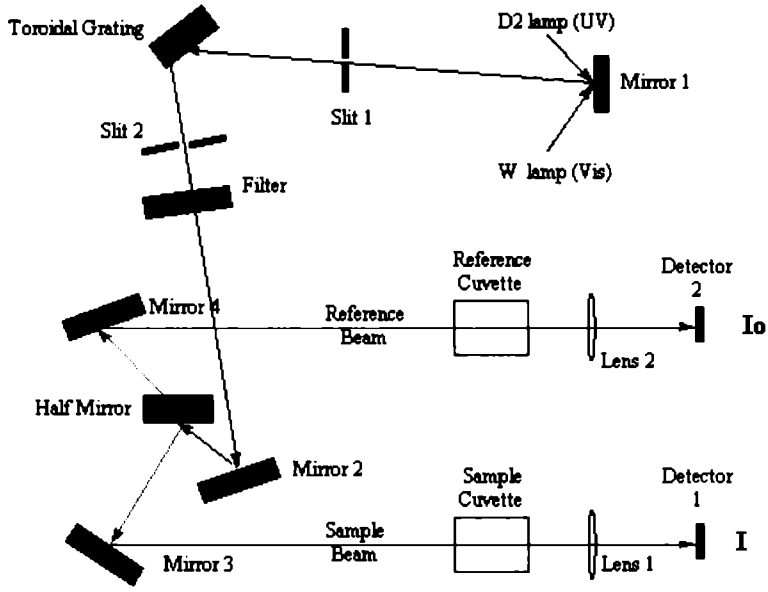

Figure 2.4. The schematic diagram of UV-visible spectrophotometer.

When the energy of the incident photon ($h\nu$) is larger than the band gap energy, the excitation of electrons from the valence band to the empty states of the conduction band occurs. The light passing through the material is then absorbed and the number of electron hole pairs generated depends on the number of incident photons $S_0(\nu)$ (per unit area, unit time and unit energy). The frequency ν is related to the wavelength λ by the relation, $\lambda = \frac{c}{\nu}$, where c is the velocity of light.

The photon flux $S(x,\nu)$ decreases exponentially inside the crystal according to the relation,

$$S(x,\nu) = S_0(\nu) \exp(-\alpha x) \tag{2.11}$$

where, the absorption coefficient α, ($\alpha(\nu) = 4\pi k\nu/c$) is determined by the absorption process in semiconductors and k is the extinction coefficient. For the parabolic band structure, the relation between the absorption coefficient (α) and the band gap of the material is given by [44],

$$\frac{\alpha h\nu}{A} = (h\nu - E_g)^r \tag{2.12}$$

where, r = 1/2 for allowed direct transitions, r = 2 for allowed indirect transitions, r = 3 for forbidden indirect transitions and r = 3/2 for forbidden direct transitions. "A" is the parameter which depends on the transition probability. The absorption coefficient can be deduced from the absorption or transmission spectra using the relation,

$$\alpha = \frac{1}{t}\ln(\frac{I}{I_0}) \qquad (2.13)$$

where, I is the transmitted intensity and I_0 is the incident intensity of the light and t is the thickness of the film. In the case of direct transition, from eqn. 2.12, $(\alpha h\nu)^2$ will show a linear dependence on the photon energy ($h\nu$). A plot of $(\alpha h\nu)^2$ against $h\nu$ will be a straight line and the intercept on energy axis at $(\alpha h\nu)^2$ equal to zero will give the band gap energy. Thus UV-visible absorption is a simpler method of measuring the band gap of the sample material.

2.4.3. Photoluminescence studies (PL)

Photoluminescence spectroscopy is a contactless, non-destructive method of probing the electronic structure of materials [45]. Photoluminescence (PL) is the emission of light when a substance is irradiated with a shorter wavelength light. Quantum mechanically, photo-excitation causes electrons within the material to move into permissible excited states. When these electrons return to their equilibrium states, the excess energy is released radiatively or non radiatively. The radiative emission on photo-excitation is referred to as photoluminescence.

The energy of the emitted light relates to the difference in energy levels between the two electronic states involved in the transition. The quantity of the emitted light is related to the relative contribution of the radiative process. The intensity and spectral content of the luminous output is a direct measure of various important material properties. Radiative transitions in semiconductors also involve localized defect levels. The

photoluminescence energy associated with these levels can be used to identify specific defects and the amount of photoluminescence can be used to determine their concentration.

Two types of luminescence spectra can be distinguished: excitation and emission. The excitation spectrum gives the intensity variations of the exciting radiation over a range for a fixed emission wavelength. It gives information on the position of excited states just as the absorption spectrum does, except that the former reveals only the absorption bands that result in the emission of light. The observed differences between the absorption and excitation spectra can yield useful information. An emission spectrum provides information on the spectral distribution of the light emitted by a sample for a given excitation wavelength. The time resolved PL measurement is a powerful tool for the determination of the radiative efficiency that specifies the fraction of excited states which de-excite by emitting photons.

The schematic block diagram showing the components of spectroflurometer is shown in figure 2.5. The emission and excitation spectra of the samples are recorded using Fluoromax -3 spectroflurometer consisting of 150W Xenon arc lamp, monochromator and a detector. A continuous source of light shines on to an excitation monochromator, which selects a band of wavelengths. This monochromatic excitation light is directed onto a sample, which emits luminescence. The luminescence is directed to a second emission monochromator which selects a band of wavelengths and shines them onto a photon counting detector (R928P

PMT) ranging from 180-850nm. The reference detector monitoring the Xenon lamp - a UV enhanced Si photodiode - requires no external bias and has good response from 190-980nm. The signal from the detector is reported to a system controller and host computer where the data can be manipulated and presented using special software.

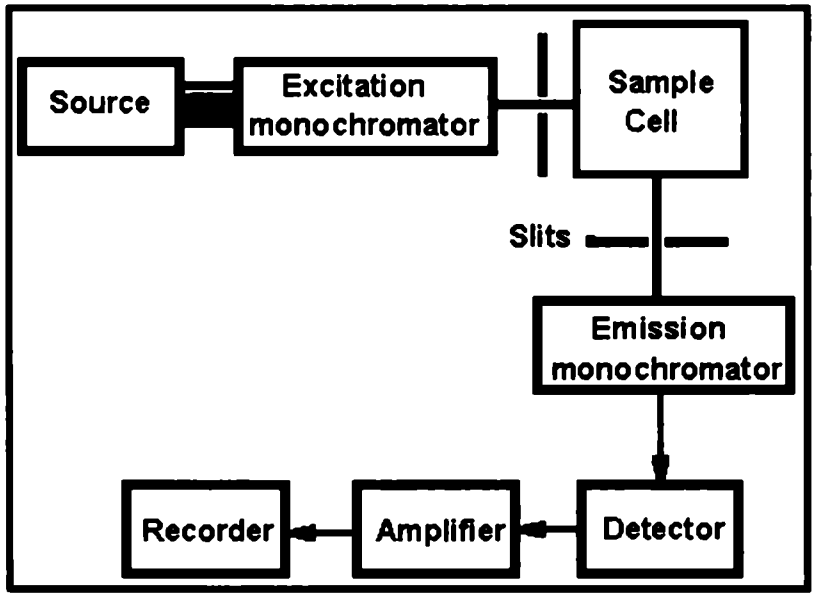

Figure 2.5. The schematic block diagram showing the components of spectroflurometer.

2.4.4. Inductively coupled plasma - Atomic emission spectroscopy (ICP-AES)

Inductively coupled plasma atomic emission spectroscopy (ICP-AES), also referred to as inductively coupled plasma optical emission spectrometry (ICP-OES), is a spectrophotometric technique, exploiting the fact that excited electrons emit energy at a given wavelength as they return to ground state [46]. This technique uses plasma called inductively coupled plasma to produce excited atoms. The fundamental characteristic of this process is that each element emits energy at specific wavelengths peculiar to its chemical character. Although each element emits energy at multiple wavelengths, in the ICP-AES technique it is most common to select a single wavelength (or a very few) for a given element. The intensity of the energy emitted at the chosen wavelength is proportional to the amount (concentration) of that element in the analyzed sample. Thus, by determining which wavelengths are emitted by a sample and by determining their intensities, the analyst can quantify the elemental composition of the given sample relative to a reference standard. ICP -AES measurement was done in the present work using Thermo Electron IRIS INTREPID II XSP DUO.

2.4.5. Raman spectroscopy

Raman spectroscopy is a technique that can detect both organic and inorganic species and measure the crystallanity of solids. Raman spectroscopy is based on the Raman effect, first reported by Raman in 1928 [47]. If the incident photon imparts part of it's energy to the lattice in the

form of a phonon it emerges as a lower energy photon. This down converted frequency shift is known as Stokes-shifted scattering. Anti-Stokes shifted scattering results when the photon absorbs a phonon and emerges with higher energy. The anti-Stokes mode is much weaker than the Stokes mode so the Stokes-mode scattering is usually monitored. In Raman spectroscopy, a laser beam, referred to as the pump, is incident on the sample. The weak scattered light or the Raman signal is passed through a double monochromator to reject the Raleigh scattered light and the Raman shifted wavelengths are detected by a photodetector. Various properties of the semiconductors, mainly composition and crystal structure can be determined. The Stokes line shifts and broadenings becomes asymmetric for microcrystalline Si with grain sizes below 10 nm [48]. The lines become very broad for amorphous semiconductors, allowing distinction to be made between single crystal, polycrystalline, and amorphous materials. Raman spectroscopy is used to study the vibrational properties of nanostructured materials. The information about structure, phase, grain size, phonon confinement etc can be obtained from Raman spectroscopy. The extent of phonon confinement in a material can be observed as the shift in Raman line frequencies. Acoustic modes are not observed by Raman measurements in bulk systems because of their low frequencies. But in nanostructured materials, they appear in the measurable frequency range (below 100 cm^{-1}) [49, 50]. The frequency of the acoustic mode is inversely proportional to the size of the nanoparticles and this can be used to determine the size of the particles. Confinement of optical phonons results in the frequency shift and

asymmetrical broadening of longitudinal optical (LO) and transverse optical (TO) mode line shape [51]. The information about the structure and quality of the low dimensional structures can be obtained from Raman spectroscopy. In the present work, Raman studies were carried out with micro Raman (Renishaw) with He- Ne Laser (632.8 nm) as the excitation source.

2.4.6. Atomic absorption spectroscopy (AAS)

In analytical chemistry, atomic absorption spectroscopy is a technique for determining the concentration of a particular metal element in a sample [52]. The technique can be used to analyze the concentration of over 70 different metals in a solution. Although atomic absorption spectroscopy dates to the nineteenth century, the modern form was largely developed during the 1950s by a team of Australian chemists. They were led by Alan Walsh and worked at the CSIRO (Commonwealth Science and Industry Research Organisation) Division of Chemical Physics in Melbourne, Australia.

The technique makes use of absorption spectrometry to assess the concentration of an analyte in a sample. It relies therefore heavily on Beer-Lambert law. In short, the electrons of the atoms in the atomizer can be promoted to higher orbitals for a short amount of time by absorbing a set quantity of energy (i.e. light of a given wavelength). This amount of energy (or wavelength) is specific to a particular electronic transition in a particular element, and in general, each wavelength corresponds to only one element. This gives the technique its elemental selectivity. As the quantity of energy

(the power) put into the flame is known and the quantity remaining at the other side (at the detector) can be measured, it is possible, from Beer-Lambert law, to calculate how many of these transitions took place, and thus get a signal that is proportional to the concentration of the element being measured. The schematic of an atomic absorption spectrometer is shown in figure 2.6. The components are described below.

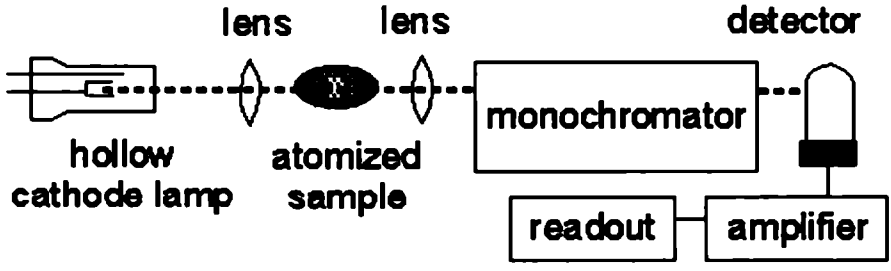

Figure 2.6. The schematic of an atomic absorption spectrometer.

Light source: The light source is usually a hollow-cathode lamp of the element that is being measured. The radiation source chosen has a spectral width narrower than that of the atomic transitions. Inside the lamp, filled with argon or neon gas, is a cylindrical metal cathode containing the metal for excitation and an anode. When a high voltage is applied across the anode and cathode, gas particles are ionized. As voltage is increased, gaseous ions acquire enough energy to eject metal atoms from the cathode. Some of these atoms are in an excited state and emit light with the frequency characteristic

to the metal [53]. Many modern hollow cathode lamps are selective for several metals.

Atomizer: AAS requires that the analyte atoms be in the gas phase. Ions or atoms in a sample must undergo desolvation and vaporization in a high-temperature source such as a flame or graphite furnace. Flame AAS can only analyze solutions, while graphite furnace AAS can accept solutions, slurries, or solid samples. A liquid sample is normally turned into an atomic gas in three steps:

1. Desolvation (Drying) – The liquid solvent is evaporated and the dry sample remains.

2. Vaporization (Ashing) – The solid sample vaporises to a gas.

3. Atomization – The compounds making up the sample are broken into free atoms.

Flame: AAS uses a slot type burner to increase the path length, and therefore to increase the total absorbance (Beer-Lambert law). Sample solutions are usually aspirated with the gas flow into a nebulizing/mixing chamber to form small droplets before entering the flame. The technique typically makes use of a flame to atomize the sample [54], but other atomizers such as a graphite furnace [55] or plasmas (primarily inductively coupled plasmas) are also used [56]. When a flame is used, it is laterally long (usually 10 cm) and not deep. The height of the flame above the burner head can be controlled by adjusting the flow of the fuel mixture. A beam of light passes through this flame at its longest axis (the lateral axis) and hits a detector. The graphite furnace has several advantages over a flame. It is a

much more efficient atomizer than a flame and it can directly accept very small absolute quantities of sample. It also provides a reducing environment for easily oxidizing elements. Samples are placed directly in the graphite furnace and the furnace is electrically heated in several steps to dry the sample, ash organic matter and vaporize the analyte atoms.

Light separation and detection: AAS use monochromators and detectors for UV and visible light. The main purpose of the monochromator is to isolate the absorption line from background light due to interferences. Simple dedicated AAS instruments often replace the monochromator with a band pass interference filter. Photomultiplier tubes are the most common detectors for AAS.

Excitation: A flame provides a high-temperature source for desolvating and vaporizing a sample to obtain free atoms for spectroscopic analysis. For atomic emission spectroscopy, the flame excites the atoms to higher energy levels.

The narrow bandwidth of hollow cathode lamps makes spectral overlap rare. That is, it is unlikely that an absorption line from one element will overlap with another. Molecular emission is much broader, so it is more likely that some molecular absorption band will overlap with an atomic line. This can result in artificially high absorption and an improperly high calculation for the concentration in the solution. Three methods are typically used to correct for this:

(a). Zeeman correction: A magnetic field is used to split the atomic line into two side bands on the basis of Zeeman effect. These side bands are

close enough to the original wavelength to still overlap with molecular bands, but are far enough not to overlap with the atomic bands. The absorption in the presence and absence of a magnetic field can be compared, the difference being the atomic absorption of interest.

(b). Smith-Hieftje correction: The hollow cathode lamp is pulsed with high current, causing a larger atom population and self-absorption during the pulses. This self-absorption causes a broadening of the line and a reduction of the line intensity at the original wavelength [57].

(c). Deuterium lamp correction: In this case, a separate source (a deuterium lamp) with broad emission is used to measure the background emission. The use of a separate lamp makes this method the least accurate, but its relative simplicity (and the fact that it is the oldest of the three) makes it the most commonly used method.

2.4.7. Thin film thickness

Thickness is one of the most important thin film parameter to be characterised, since it plays an important role in the film properties unlike a bulk material. Microelectronic applications generally require the maintenance of precise and reproducible film metrology (i.e., thickness as well as lateral dimensions). Various techniques are available to characterise the film thickness which are basically divided into optical and mechanical methods, and are usually non-destructive but sometimes destructive in nature.

Film thickness may be measured either by in-situ monitoring at the rate of deposition or after the film deposition. The thicknesses of the thin films prepared for the work presented in this thesis were measured by a

stylus profiler (Dektak 6M). The stylus profiler takes measurements electromechanically by moving the sample beneath a diamond tipped stylus. The high precision stage moves the sample according to a user defined scan length, speed and stylus force. The stylus is mechanically coupled to the core of a linear variable differential transformer (LVDT). The stylus moves over the sample surface. Surface variations cause the stylus to be translated vertically.

Electrical signals corresponding to the stylus movement are produced as the core position of the LVDT changes. The LVDT scales an ac reference signal proportional to the position change, which in turn is conditioned and converted to a digital format through a high precision, integrating, analog-to-digital converter [58]. The film whose thickness has to be measured is deposited with a region masked. This creates a step on the sample surface. Then the thickness of the sample can be measured accurately by measuring the vertical motion of the stylus over the step. The stylus profiler (Dektak 6M) is shown in figure 2.7.

Figure 2.7. Picture of automised Dektak stylus profiler.

The major factors which limit the accuracy of stylus measurements are [59]:

1. Stylus penetration and scratching of films (makes problem in very soft films).

2. Substrate roughness: Excessive noise is introduced into the measurement as a result of substrate roughness and this creates uncertainty in the position of the step.

3. Vibration of the equipment: Proper shock mounting and rigid supports are essential to minimise background vibrations.

In modern instruments, the levelling and measurement functions are computer controlled. The vertical stylus movement is digitized and data can be processed to magnify areas of interest and yield best-profile fits. Calibration profiles are available for standardization of measurement.

2.5. References

1. K. E. Gonsalves, S. P. Rangarajan and J. Wang edited by H. S. Nalwa, Nanostructured Materials and Nanotechnology, Academic Press, Newyork (2002)
2. A. Fernandez, E. P. Reddy, T. C. Rojas and J. C. S. Lopez, Vacuum **52** 83(1999)
3. S. L. Gafner and Y. Y. Gafner, J. Exp. Theor.Phys. **107** 712(2008)
4. V. M. Jimenez, A. R. G. Elipe, J. P. Espinos, A. Justo and A. Fernandez, Sensors and Actuators B: Chemical **31** 29(1996)
5. C. Johnson, R. Gemmen and N. Orlovskaya, Composites Part B: Eng. **35** 167(2004)
6. C. C. Koch, Nanostructured Mater. **9** 13(1997)
7. T. L. Brown, S. Swaminathan, S. Chandrasekar, W. D. Compton, A. H. King and K. P. Trumble, J. Mater. Res. **17** 2484 (2002)
8. D. Spirkoska, C. Colombo, M. Heiss, G. Abstreiter and A. F. I. Morral, J. Phys. Condens. Matter. **20** 454225 (2008)
9. O. Kryliouk, H. J. Park, Y. S. Won, T. Anderson, A. Davydov, I. Levin, J. H. Kim and J. A. Freitas Jr, Nanotechnology **18** 135606 (2007)

10. J. A. Venables, Introduction to Surface and Thin Film Processes. Cambridge University Press, Cambridge (2000)
11. B. Alloing, C. Zinoni, V. Zwiller, L. H. Li, C. Monat, M. Gobet, G. Buchs, A. Fiore, E. Pelucchi and E. Kapon, Appl. Phys. Lett. **86** 101908 (2005)
12. L. Pan, S. Li, J. Liu, Z. Niu, S. Feng and H. Zheng, Science in China Series A: Mathematics **45** 666 (2002)
13. Y. Ishikawa, Y. Shimizu, T. Sasaki and N. Koshizaki, J. Colloid Interface Sci. **300** 612 (2006)
14. R. S. Ajimsha, G. Anoop, A. Aravind and M. K. Jayaraj, Electrochem. Solid-State Lett. **11** K14 (2008)
15. A. Rahm, M. Lorenz, T. Nobis, G. Zimmermann, M. Grundmann, B. Fuhrmann and F. Syrowatka, Appl. Phys. A **88** 31 (2007)
16. H. B. Zeng, W. P. Cai, B. Q. Cao, J. L. Hu, Y. Li and P. S. Liu, Appl. Phys. Lett. **88** 181905 (2006)
17. T. Sakka, S. Iwanaga, Y. H. Ogata, A. Matsunawa and T. Takemoto, J. Chem. Phys. **112** 8645 (2000)
18. A. V. Simakin, V. V. Voronov, N. A. Kirichenko, G. A. Shafeev, Appl. Phys. A **79** 1127 (2004)
19. L. Barther, R. Fabbro, P. Peyre, L. Tollier, E. Bartinicki, J. Appl. Phys. **89** 2836 (1997)
20. S. Zhu, Y. F. Lu, M. H. Hong, X. Y. Chen, J. Appl. Phys. **89** 2400 (2001)
21. S. Zhu, Y. F. Lu, M. H. Hong, Appl. Phys. Lett. **79** 1396 (2001)
22. G. W. Yang, J. Prog. Mater. Sci. **52** 648 (2007)

23. G. W. Yang, J. B. Wang, Appl. Phys. A **72** 475 (2001)

24. J. Zheng, Z. Zheng, W. Gong, X. Hu, W. Gao, X. Ren and H. Zhao, Chem. Phys. Lett. **465** 275 (2008)

25. Y. Ishikawa, Y. Shimizu, T. Sasaki and N. Koshizaki, J. Colloid Interface Sci. **300** 612 (2006)

26. F. Mafune, J. Y. Kohno, Y. Takeda and T. Kondow, J. Phys. Chem. B **105** 5114 (2001)

27. S. C. Singh and R. Gopal, Physica E: Low-dimensional Systems and Nanostructures **40** 724 (2008)

28. J. B. Wang, C. Y. Zhang, X. L. Zhong and G. W. Yang, Chem. Phys. Lett. **86** 361 (2002)

29. L. Berthe, R. Fabbro, P. Peyre, L. Tollier and E. Bartinicki, J. Appl. Phys. **82** 2826(1997)

30. S. Zhu, Y. F. Lu, M. H. Hong and X. Y. Chen, J. Appl. Phys. **89** 2400 (2001)

31. W. P. Leung and A. C. Tam, Appl. Phys. Lett. **60** 23 (1992)

32. M. V. Allmen and A. Blatter, Laser-Beam Interactions with Material:Physical Principles and Applications, Springer, Berlin (1995)

33. R. Fabbro, J. Fournier, P. Ballard, D. Devaux and J. Virmont, J. Appl. Phys. **68** 775 (1990)

34. Bauerle, Laser Processing and Chemistry, Springer, Berlin (1996)

35. G. Che, B. B. Lakshmi, C. R. Martin and E. R. Fisher, Chem. Mater. **10** 260 (1998)

36. D. W. Lee, J. H. Yu, T. S. Jang and B. K. Kim, Mater. Lett. **59** 2124(2005)

37. B. D. Cullity and S. R. Stock, Elements of X-ray diffraction, Third edition, Prentice Hall, New Jersey (2001)

38. M. J. Buerger, X-ray Crystallography, John Wiley & Sons, New York (1962)

39. C. Kittel, Introduction to Solid State Physics, Seventh edn, Wiley Eastern Limited, USA (1996)

40. P. E. J. Flewitt and R. K. Wild, Physical methods for materials characterisation, IOP Publishing Ltd, London (2003)

41. L. A. Bendersky and F.W. Gayle, J. Res. Natl. Inst. Stand. Technol. **106** 997 (2001)

42. P. Kubelka and F. Munk, Zh. Tekh. Fiz. **12** 593 (1931)

43. P. Kubelka, J. Opt. Soc. Am. **38** 448 (1948)

44. A. Goswami, Thin Film Fundamentals, New Age International (P) Limited, New Delhi (1996)

45. D. R. Vij (Ed.), Luminescence of solids, Plenum Press, New York (1998)

46. A. Stefnsson, I. Gunnarsson and N. Giroud. Anal. Chim. Acta, **582** 69 (2007)

47. C. V. Raman and K. S. Krishna, Nature **121** 501 (1928)

48. H. Richter, Z. P. Wang, and L. Ley, Solid State Commun. **39** 625 (1981)

49. M. Rajalakshmi, T. Sakunthala and A. K. Arora, J. Phys.: Condens. Matter **9** 9745 (1997)

50. A. Tanaka, S. Onari and T. Arai, Phys. Rev. B **47** 1237 (1993)

51. A. Tanaka, S. Onari and T. Arai, Phys. Rev. B **45** 6587 (1992)
52. M. Sperling and B. Welz, Atomic Absorption Spectrometry, Wiley-VCH, Weinheim (1999)
53. D. Skoog, J. Holler, S. Crouch, Principles of Instrumental Analysis, 6th edn, Thomson Books/Cole, Belmont (2007)
54. C. T. J. Alkemade, T. Hollander, W. Snelleman and P. J. T. Zeegers, Metal Vapours in Flames, Pergamon Press, Oxford (1982)
55. B. V. Lvov, Spectrochim. Acta B **52** 1239 (1997)
56. J. A. C. Broekaert, Analytical Atomic Spectrometry with Flames and Plasmas, Third Edition, Wiley-VCH, Weinheim (1998)
57. S. B. Smith Jr and G. M. Hieftje, Appl. Spectrosc. **37** 419 (1983)
58. Veeco Dektak 6M Manual 2004
59. M. Ohring. Materials Science of Thin Films: Deposition and Structure. Academic Press, New York (2001)

Chapter 3

Fabrication of an automized Z-scan setup for nonlinear optical studies

3.1. Introduction to nonlinear optics

Nonlinear optics (NLO) is the branch of optics that describes the behaviour of light in nonlinear media [1], that is, media in which the dielectric polarization **P** responds nonlinearly to the electric field **E** of the light. This branch of science explores the coherent coupling of two or more electromagnetic fields in a nonlinear medium. It is expected to have a major role in the technology of photonics. Photonics is the analogue of electronics in that it describes the technology in which photons instead of electrons are used to acquire, store, transmit and process information. This nonlinearity is typically only observed at very high light intensities such as those provided by lasers. With the advent of lasers which provide high intensity coherent light, the strong oscillating electric field produces a polarization response that is nonlinear in character and that can act as a source of new optical fields with altered properties. Since the size of the spot of light is inversely proportional to its wavelength, second harmonic generation [2] can increase the capacity of stored information on optical disks immensely. Using nonlinear phenomena one can build devices such as frequency mixers that can act as new light sources or as amplification schemes, light modulators for controlling the phase amplitude of a light beam [3], optical switches [4], optical limiters [5] and numerous ways of processing the information content of data or images. Nonlinear optical devices are found to be best suite for transistor and optical bistable devices. NLO devices with ultrafast switching times have found wide application in the field of optical

processing of information where a gain in certain types of switching functions and reconfigurable connectivity of light sources and detectors with a rare chance of interference or cross talk between adjacent channels is required. Femto second photonic switching enables a gain in the switching speed many orders of magnitude higher than electronic switching. Tremendous gains in the band width of information processing, ultra weak interference with electric and magnetic sources of optical processing techniques are far better to electronic processing techniques.

Basically all materials including all forms of matter gases, liquids and solids shows nonlinear behaviour, but the amplitude of optical field required to observe these effects varies over different orders depending on the detailed nature of the electronic structure of the atomic and molecular constituents of the medium, their dynamical behaviour as well as the symmetry and their geometrical arrangement in the medium. From device point of view, solid materials are found to have more application and they must meet some important requirements such as high stability in the ambient conditions and high withstandability to intense light sources. In the molecular materials, the optical nonlinearity is primarily derived from the molecular structure. The expression for the nonlinearity is highly dependent on the geometrical arrangement of the molecules in the case of second order nonlinear process but much less so far for third order nonlinear process.

The second major class of nonlinear materials is the bulk materials where the origin of nonlinearity stems from the electrons and not associated with the nuclei such as those in metals and semiconductors. The optical

nonlinearity is decided by the electronic characteristic of the bulk medium and it requires detailed theoretical frame work to account for the nonlinearity. The major examples are quantum well structures arising from GaAs [6] and II–IV semiconductors such as CdSe [7]. Inorganic crystals such ads KDP and KTP are considered as bulk materials since no single molecular unit in the ionic lattice is identified. But in these systems the nonlinear behaviour is surely related to the individual bond polarisabilities. Organic and other molecular materials are increasingly being recognized as the materials of the future because their molecular nature combined with the versatility of synthetic chemistry can be used to alter and optimize molecular structure to maximize nonlinear response and other properties. Another advantage is the ease of fabrication that are available or under development for building thin film structures. Many organic materials have excellent mechanical strength as well as environmental and thermal stability.

3.2. Progress of NLO

Before 1960's, in the area of conventional optics many basic mathematical equations or formulae manifested a linear feature. The important physical quantity of interest in order to interpret various optical phenomena like reflection, refraction, dispersion, birefringence of light propagating through a medium, is the electric polarization induced in the medium. Observation of the second harmonic generation (SHG) by P.A. Franken in 1961 marked the birth of nonlinear optics as a new discipline in the area of laser-matter interaction [2]. Franken observed that light of

wavelength 347.1nm could be generated when a quartz crystal was irradiated with light of wavelength 694.2nm obtained from ruby laser. He attributed this novel result to the coherent mixing of two optical fields at 694.1nm in the crystal to produce 347.1nm [8].

Though the discovery of SHG marked the birth of nonlinear optics as a new branch of experimental investigation, SHG was not the first optical effect to be observed. Optical pumping is a nonlinear optical phenomenon, which was known prior to the invention of laser [9]. After the discovery of the SHG, several other optical mixing processes were introduced depending on the way of application of laser radiation which include sum frequency generation [10] (1962), difference frequency generation [11] (1963), optical third harmonic generation [12] (1962), optical rectification [13] (1962), optical parametric amplification and oscillation [14] (1965). These inventions provide a theoretical background to the existence of nonlinear polarization as well as provide an alternative approach to generate optical coherent radiation.

The discovery of stimulated Raman scattering [15] (1962) is the second milestone to the history of nonlinear optics. Novelty of this discovery is that the "stimulated nature" of light scattering excited by an intense laser radiation was revealed. Simulated Raman scattering is an alternative physical method to generate coherent optical radiation [16] without the need of population inversion.

The stimulated Brillowin scattering [17, 18] (1965) was introduced next which is caused by the interaction of the intense monochromatic

optical field with the hypersonic field in a scattering medium through a phenomenon called electrostriction mechanism [19]. After the discovery, this has been introduced as an efficient technique to generate or amplify a coherent optical radiation with a small frequency shift [20].

Followed by this, the self focussing mechanisms [21, 22, 23] was introduced which included the refractive index modification of a material medium when intense radiation pass through it and the further impact of this refractive index shift on the shape of the laser beam itself. This effect is very significant since it causes optical damage in a solid state lasing materials or optical elements. Another effect is that the dramatic increase in the local field intensity inside a medium causes anomalous threshold decrease of certain nonlinear processes such as stimulated Raman scattering. Detailed studies on self focusing lead the scientists to the discovery of self phase modulation and spectral self broadening effects [24] which found application in the generation of ultrashort pulses and continuum radiation with a super broad spectral band.

The studies on the transient optical effects such as photon echoes [25] (1964), self induced transparency [26] (1965) and optical nutation [27] (1969) provide an approach to the relaxation mechanism of the resonant excitation in an absorbing media. The saturable absorption and two photon absorption (TPA) are two fundamental nonlinear effects which are known before the invention of the laser. The saturable absorption observed early in the radio frequency spectroscopy was the key factor to the discovery of population inversion and which later lead to the discovery of lasers and

masers [28 20]. Saturable absorbing dyes found application in mode locking [29] and Q-switching [30] applications later. Although the theoretical explanation to the TPA was done earlier in the 1930's itself, first experimental demonstration with TPA induced fluorescence with laser radiation was done only in 1961 [31].

The 1970's started the second era of nonlinear optics. In this period various new nonlinear techniques were introduced such as coherent anti stokes Raman spectroscopy (CARS) [32], Doppler free TPA spectroscopy [33] (1971), inverse Raman spectroscopy [34], Raman gain spectroscopy [35] and laser polarization spectroscopy [36] (1976). All these nonlinear spectroscopic techniques require two beams, at least one of which must be tunable. In this, one beam is used as a pump beam to excite a selected set of atoms or molecules and the other beam called the probe beam is used to detect the specific changes in the optical properties of the samples for the selected excitation.

Later optical phase conjugation was observed in 1972 by Russian researchers as an experimental observation of wave front reversal of back ward stimulated Brillowin scattering [37]. The physical understanding of the optical phase conjugation phenomena is unknown for a long term and the effect became significant only after the introduction of three wave and four wave mixing for the generation of phase conjugated waves (1977) [38]. The optical phase conjugation found wide application in high brightness lasing or amplification through a distorted gain medium, the aberration compensation in a disturbing propagation medium, the real time optical

holographic wave front reconstruction and the optical data storage and processing.

Therefore, the study of nonlinear effects is very important. It helps us to understand the mechanism of nonlinearity as well as its spatial and temporal evolution. Besides, detailed knowledge of NLO processes and their dynamics is also essential for the implementation of these techniques in appropriate areas of technology such as optical switching, optical communication, passive optical power limiting, data storage and design of logic gates.

3.3. Interaction of light with matter

Light is a magical phenomenon that provides visual information about the world and it seems to flow or propagate through empty space, as well as through material objects. The familiar visual effects of reflection, refraction, diffraction, absorption and scattering common to us can be explained by assigning a small set of optical parameters to materials. These parameters will be constants independent of the intensity of light that causes the observed optical phenomena. This sets the classic foundation to the so called linear optics [39]. Light is basically an electromagnetic wave consisting of electric and magnetic fields. These fields are real quantities, but are rapidly time variant. For most of optics, the optical wave may be characterized by defining its electric fields. Let we assume that light beams are propagating through an unbounded linear medium. The interaction of light wave with

linear media can be explained by using Maxwell's electromagnetic theory [40]. For linear isotropic media,

$$\vec{B} = \mu \vec{H} \tag{3.1}$$

$$\vec{D} = \varepsilon \vec{E} \tag{3.2}$$

$$\vec{J} = \sigma \vec{E} \tag{3.3}$$

in which μ, ε and σ are the permeability, permittivity and conductivity of the material of choice. These constants are independent of the field variables, although they do depend on frequency [41]. Since the light is transverse electromagnetic (EM) wave, when a theoretical formulation for the interaction of light with matter is generated, the effect of the electric field $\vec{E}$ and magnetic field $\vec{B}$ as well as their directional nature should be considered. Also more specifically spoken, spatial and temporal variation of $\vec{E}$ and $\vec{B}$ are to be taken into account [42]. But in the case of the nonmagnetic materials, light-matter interaction is described in terms of the electric field $\vec{E}$ only and the contribution from $\vec{B}$ is neglected [43]. Generally we know that the magnitude of $\vec{B}$ is less than that of $\vec{E}$. We can relate the $\vec{B}$ to $\vec{E}$ through the velocity of light, c, by the following relation,

$$c = \frac{\vec{E}}{\vec{B}} \tag{3.4}$$

3.3.1. Linear polarization

In the case of a linear media the interaction with light can generally be regarded within the framework of a dielectric subjected to an electric field [44]. The applied optical field E(t) polarizes the molecules in the medium and interact with charged particles in the matter, mainly electrons and hence distort the equilibrium charge distribution, which results in the separation of unlike charges to produce an electric polarization. The polarization thus generated is related to externally applied electric field through a characteristic property of the medium, called optical susceptibility (χ). It determines the magnitude as well as the direction of induced electric polarization for a given field strength, at a particular wavelength. The magnitude of optical susceptibility depends on various factors such as molecular and atomic structure of the materials, wavelength of excitation and intensity of light. The strength of electric field inside the medium is lowered by the polarization that opposes the externally applied field. If the applied field strength is relatively low, the polarization in the medium behaves linearly with the applied field and the linear polarization is expressed in terms of a susceptibility χ as,

$$P(t) = \varepsilon_0 \chi \; E(t) \tag{3.5}$$

where χ is linear susceptibility of the medium and is related to dielectric constant (ε) of the medium by the relation,

$$\varepsilon = 1 + \chi \tag{3.6}$$

The susceptibility χ is a second-rank tensor which connects the polarization vector components to the electric field vector components. This linear susceptibility is related to the refractive index of the medium through the following relation,

$$\chi = n^2 - 1 \tag{3.7}$$

The electric field associated with conventional light sources such as xenon lamp and mercury lamp is very low in comparison with interatomic electric field. Such low electric field strength light sources cannot appreciably perturb the molecular charge distribution in the material media. For instance, atomic field is of the order of 10^8 or 10^9 V/cm, whereas electric field strength associated with conventional sources is of the order of 10^2–10^5 V/cm. Such a very low electric field when acted upon the atoms, electrons bound to the nucleus are displaced only by about 10^{-18}m, which is very small in comparison with interatomic distance which is of the order of 10^{-10}m [41]. Therefore while the conventional light sources interact with the atoms, it can be said that the displacement produced is very small which is within the elastic limit and therefore there is no anharmonicity in the oscillations of induced polarization. Hence, measurements using conventional light sources gave a polarization P, which is linearly dependent on electric field strength. This domain of interactions of electric field with matter is referred to as linear optics. Linear effects; also called first order effects include linear optical properties such as linear refractive index, linear absorption and birefringence. This is not the case when intense light such as laser beams

interact with the medium where in the induced polarization doesn't behave linearly with the strength of applied optical field; however it behaves some what nonlinear.

3.3.2. Nonlinear polarization

It has been found that when excitation intensity is increased, induced polarization becomes a nonlinear function of applied electric field strength [45]. The consequence of the nonlinear relationship between E and P is that at very high value of incident intensity, a number of new and interesting phenomena begin to manifest macroscopically. In this situation, it is highly advantageous to analyse the field strength $\vec{E}$ associated conventional sources used for excitation and compare the same with interatomic field.

With invention of lasers, which has high degree of spectral purity, coherence and directionality, it has become possible to irradiate atoms and molecules with an $\vec{E}$ that is comparable to interatomic field. This is achieved because lasers can be focused to very small spot size (of the order of its wavelength) producing very large intensity and consequently extremely high electric field strength at the focal region. This extremely high optical field at the focal region produces a considerable distortion of the equilibrium charge distribution in the medium, which gives rise to a large displacement of electrons from their equilibrium position. As a result of this, electrons vibrate quite anharmonically. There exists another significant fact that when the incident laser beam is tightly focused, photon density at the focal region approaches atomic density. In this situation, the potential experienced by the electrons cannot be approximated to a parabolic one. The final consequence

of this anharmonicity is that unlike in eqn.(3.5), induced polarization becomes a function of higher powers of electric field too, that is nonlinear dependence of polarisation on applied electric field strength. The nonlinear polarization is expressed as a power series in the applied field as [46],

$$\vec{P}_{NL} = \varepsilon_0(\chi^{(1)}E + \chi^{(2)}E^2 + \chi^{(3)}E^3 + \ldots\ldots\ldots \quad (3.8)$$

Here $\chi^{(1)}$ and $\chi^{(2)}$ and $\chi^{(3)}$ correspond to first order, second order and third order susceptibilities of the medium respectively. For example, we suppose that the incident laser beam has the form,

$$E = E_0 \cos(\omega t) \quad (3.9)$$

On substituting the above expression in eqn(3.8) and performing some numerical manipulations will lead to the final expression for the polarisation in the nonlinear media,

$$\vec{P}_{NL} = \frac{1}{2}\varepsilon_0\chi^{(2)}E_0^2 + \varepsilon_0(\chi^1 + \frac{3}{4}\chi^{(3)}E_0^2)E_0\cos(\omega t) + \frac{1}{2}\varepsilon_0\chi^{(2)}E_0^2\cos(2\omega t) + \frac{1}{4}\varepsilon_0\chi^{(3)}E_0^3\cos(3\omega t) + \ldots\ldots\ldots \quad (3.10)$$

The very first term in the above equation is a constant and it is meant for the dc field across the medium. The second term is the first or fundamental harmonic of polarisation. The third contribution will have a frequency of oscillation 2ω and is called the second harmonic of polarisation and the fourth contribution is called the third harmonic of polarisation.

In the nonlinear optical regime, a number of interesting phenomena that are absent in the linear regime emerge out. One of the major differences between linear and nonlinear optical interactions is that, in nonlinear optical processes two light beams can interact and exchange their

optical energy through induced nonlinear polarization of the medium. If the laser beam is highly intense, even air itself can act as nonlinear medium. It is a well known fact that femto second laser pulses get self-focused in air. A very important nonlinear process having scientific and technological relevance is the generation of super continuum [47] (white light), which occurs when some materials are irradiated with terra watts of power.

3.4. Some important nonlinear effects

All the nonlinear effects can be broadly classified into two categories; one is concerned with frequency conversion [48] and the other one is concerned with optical modulation [49]. Examples of frequency conversion processes are sum and difference frequency generations. Processes concerned with optical modulation include Kerr effect [50], self phase modulation [51] etc. In optical modulation processes, light modulates some property of the medium like refractive index. Generation of new frequencies in frequency conversion processes is due to the oscillations of induced nonlinear polarization at appropriate frequencies. Obviously, frequency conversion processes are instantaneous and take place in a time scale as short as the inverse of the frequencies involved ($\sim\upsilon^{-1}$). However, common practice is to broadly classify the NLO effects on the basis of the susceptibility term involved like second order, third order etc. All the non linear optical interactions consist of two successive processes;

(1) Intense light beam induces a nonlinear response (that is nonlinear polarization) in the medium.

(2) The medium reacts on the light, which induces the nonlinear polarization, and modifies the light in a nonlinear way [46].

The first process is governed by the constitutive equations, which are general equations between external field and induced polarization, written in terms of optical susceptibility $\chi^{(n)}$. The second process is governed by Maxwell's equations, which describes the generation of new frequencies in presence of nonlinear polarization. It is to be noted that the nonlinear polarization acts as a source term in Maxwell's equation.

3.4.1. Second-Harmonic Generation

Second-harmonic generation (SHG; also called frequency doubling) is a nonlinear optical process, in which photons interacting with a nonlinear material are effectively "combined" to form new photons with twice the energy, and therefore twice the frequency and half the wavelength of the initial photons. In the SHG, a polarization oscillating at a frequency 2ω radiates an electromagnetic wave of the same frequency which propagates with the same velocity as the incident wave [52]. The output wave thus emerged from the medium will have the same property of directionality and monochromaticity, as the incident wave and is emitted in the same direction.

Now we can have a relation for the second order nonlinear polarization in a medium. The nonlinear polarizability in crystalline materials depends on the direction of propagation of the light beam, polarization of electric field and orientation of optic axis of the crystal. Therefore we can observe that in crystalline materials, the vectors $\vec{P}$ and $\vec{E}$ need not

necessarily be parallel and hence the coefficient χ must be treated as tensors. The second order polarization P_i^2 can therefore be represented by the relation,

$$P_i^2 = \varepsilon_0 \sum_{j,k} \chi_{ijk}^{(2)} E_j E_k \tag{3.11}$$

where i, j, k represents the coordinates x, y, z. It must be noted that the second harmonic generation represented by (3.11) occur in certain type of crystal only. For example, consider an isotropic crystal, for which χ_{ijk} is a constant. If the direction of the axis is reversed $(x \to -x, y \to -y, z \to -z)$ leaving electric field and dipole moment unchanged in direction, the sign of these two must change,

$$\therefore -P_i^{(2)} = \varepsilon_0 \sum_{j,k} \chi_{ijk}^{(2)} (-E_j)(-E_k) = +P_i^{(2)} \tag{3.12}$$

which happens only when the nonlinear polarisation $P_i^{(2)} = 0$. This means that $\chi_{ijk}^{(2)} = 0$, so second harmonic generation cannot occur in an isotropic medium such as liquids or gases or in non centro symmetric crystals.

The detailed research on the mechanism of harmonic generation indicates that there exists an important phase relation between the fundamental and generated frequencies, as they are passing through the crystal having optical dispersion [53, 54]. It was also found that the efficiency of harmonic generation depends not only on the intensity of the

exciting radiation, but also on its direction of propagation in crystal. The relevance of a phase relation is as described below.

Let we consider that an incident beam of frequency ω passes through a nonlinear medium of thickness L which can generate second harmonic waves. Now the incident plane wave at frequency ω and the second harmonics at frequency 2ω driven by it are propagating in the z-direction through a material. In this case the expression for the intensity of SHG signal at the exit surface of the material can be derived to be [52],

$$I = \frac{\sin^2\left(\frac{2k_1 - k_2}{2}\right)}{\left(\frac{2k_1 - k_2}{2}\right)^2} L \tag{3.13}$$

where k_1 the wave is number of fundamental frequency and k_2 is the wave number of second harmonic. From the eqn.(3.13), it is clear that output intensity is sharply peaked about,

$$\left(\frac{2k_1 - k_2}{2}\right)L = 0 \tag{3.14}$$

That is when,

$$k_2 = 2k_1 \tag{3.15}$$

Therefore for efficient frequency doubling, this relation must be satisfied. This requirement for efficient frequency doubling is called as phase matching criterion. The wave numbers are also related to the refractive indices through the following relations,

$$k_2 = \frac{2\omega\eta_{2\omega}}{c} \quad \text{and} \quad k_1 = \frac{\omega\eta_{\omega}}{c} \tag{3.16}$$

where $\eta_{2\omega}$ and η_{ω} are the refractive indices of the material with the second harmonic and fundamental frequency respectively. Therefore we can write that,

$$\eta_{2\omega} = \eta_{\omega} \tag{3.17}$$

Thus phase matching criterion reduces to refractive index criterion. Second harmonic generation was first successfully generated in quartz crystal. The major crystals showing SHG are potassium dihydrogen phosphate (KDP), barium titanate and lithium iodate. The major relevance of the SHG is that it is the principal method for the conversion of infrared laser radiation into visible and then to ultraviolet laser radiation.

3.4.2. Sum-and Difference-Frequency Generation

When multiple waves interact in a nonlinear medium the phenomenon of wave mixing (frequency mixing) happens leading to the generation some new frequencies. The principle is that optical beams interact in a medium to generate a mixture of the frequencies. Frequency mixing is a more general process and usually involves light at three different frequencies: ω_1, ω_2 and ω_3, where $\omega_1 + \omega_2 = \omega_3$. Sum and difference frequency generation corresponds to the frequency mixing processes.

In sum frequency generation the frequency of the generated wave is the sum of the frequencies of the applied fields; $\omega_1 + \omega_2 = \omega_3$. In the sum frequency generation we are allowing an optical field consisting of two

distinct frequency components ω_1 and ω_2 being incident upon a nonlinear optical medium characterized by a nonlinear susceptibility $\chi^{(2)}$. It can generate a nonlinear polarization at $P^{(2)}$ ($\omega_3 = \omega_1 + \omega_2$). In sum frequency generation, for effective energy transfer from the pump wave at ω_1 and ω_2 to the generated wave at ω_3, conservation of both energy and momentum must be satisfied. The energy conservation requires $\omega_3=\omega_1+\omega_2$; while momentum conservation requires $k_3=k_1+k_2$.

On the other hand, beams at frequencies ω_3 and ω_2 can mix to generate a beam at frequency $\omega_1 = \omega_3 - \omega_2$. This is called difference frequency generation (DFG). The process of difference-frequency generation is described by a nonlinear polarization term $P^{(2)}$ ($\omega_3=\omega_1-\omega_2$). In this process, the conservation of energy requires that for every photon that is created at the difference frequency $\omega_3=\omega_1-\omega_2$, a photon at the higher input frequency (ω_1) must be destroyed and a photon at the lower input frequency (ω_2) must be created. Thus, the lower frequency input field is amplified by the process of difference-frequency generation. For this reason, the process of difference-frequency generation is also known as parametric amplification.

3.4.3. Self focusing of light

Self focusing is a nonlinear optical phenomenon produced by the change in refractive index of materials when they are exposed to intense electromagnetic radiation like laser source [55]. Such a medium whose refractive index increases with the applied electric field intensity acts as a focusing lens for an electromagnetic wave such as laser beam. The phenomenon of self-focusing is often observed when high intensity

radiation such as those generated by femtosecond lasers propagates through solids, liquids and gases. Depending on the type of material and on the intensity of the radiation, several mechanisms produce variations in the refractive index which result in self-focusing: the main case of interest is Kerr-induced self-focusing. The origin of the Kerr induced self lensing lies in the optical Kerr effect, which produces a variation of the refractive index n (when a media is exposed to intense radiation) as given by the formula $n = n_0 + n_2 I$, where n_0 and n_2 are the linear and nonlinear components of the refractive index, and I is the intensity of the incident radiation. In most materials, n_2 is positive and this leads to increased value of the refractive index in the areas where the incident intensity is higher, usually at the centre of the incident beam, creating a focussed intensity profile which will potentially leading to the collapse of a beam on itself [56, 57].

The theoretical basis to the shift in the refractive index due to Kerr induced self focussing is given below.

The refractive index (n) of a material is related to the susceptibility (χ) by the following relation,

$$n = \sqrt{1 + \chi} \tag{3.18}$$

In a nonlinear media, the susceptibility χ is a function of the applied field strength E as said above in the eqn(3.10) for the total polarisation in a nonlinear media. Therefore the value of n will depend on E. In fact the process of self focusing does not alter the frequency of light waves. We need, therefore, consider only the second term in the relation (3.10) which describes the fundamental harmonic,

$$P^{(1)} = \varepsilon_0(\chi^{(1)} + \frac{3}{4}\chi^{(3)}E_0^{\,2})E \tag{3.19}$$

Therefore now the expression for the refractive index will change to,

$$n = \sqrt{1 + (\chi^{(1)} + \frac{3}{4}\chi^{(3)}E_0^{\,2})} \tag{3.20}$$

We can represent this equation as,

$$n = \sqrt{\varepsilon_l + \varepsilon_{nl}} \tag{3.21}$$

where we made the substitutions,

$$\varepsilon_l = 1 + \chi^{(1)} \tag{3.22}$$

$$\varepsilon_{nl} = \frac{3}{4}\chi^{(3)}E_0^{\,2} \tag{3.23}$$

where ε_l and ε_{nl} as the dielectric permittivity of the linear medium and a nonlinear increment in dielectric permittivity respectively. The expression for the refractive index can be rewritten as,

$$n = \sqrt{\varepsilon}\sqrt{1 + \frac{\varepsilon_{nl}}{\varepsilon_l}} \approx \sqrt{\varepsilon_l}(1 + \frac{\varepsilon_{nl}}{2\varepsilon_l}) \qquad (\text{Since } \varepsilon_{nl} \le \varepsilon_l) \tag{3.24}$$

$$= n_l(1 + \frac{\varepsilon_{nl}}{2n_l^{\,2}}) = n_l\left(1 + \frac{3\chi^{(3)}E_0^2}{8n_l^2}\right)$$

$$\text{Or} \quad n = n_l(1 + n_{nl}E_0^{\,2}) \tag{3.25}$$

where $n_l = \sqrt{\varepsilon_l}$ is the refractive index of the nonlinear medium, and

$$n_l n_{nl} E_0^{\,2} = \frac{\varepsilon_{nl}}{2\sqrt{\varepsilon_l}} \frac{3\chi^{(3)}E_0^{\,2}}{8\sqrt{1+\chi^{(1)}}} = n_2 I \tag{3.26}$$

is the nonlinear increment in the expression for the refractive index and $E_0^2=I$, the intensity of the incident radiation.

The expression (3.26) tells us that the effective refractive index of the nonlinear medium is proportional to the square of the amplitude of the field, that is to the intensity. We know that the intensity of the laser beam is not constant over the cross section. It has peak value along the axis of the beam and decreases gradually away from the axis. Also the velocity of the light wave is given by the relation, $v = \frac{c}{n}$.

The decrease in the value of n (owing to the falling of the intensity of the light beam) causes the velocity to increase with distance away from the axis. The very direct result is that a plane wave front incident on the medium becomes concave as it propagates through the medium and contracts towards the axis as shown in figure 3.1. That means, the light beam self focuses, after which it propagates as a narrow light beam.

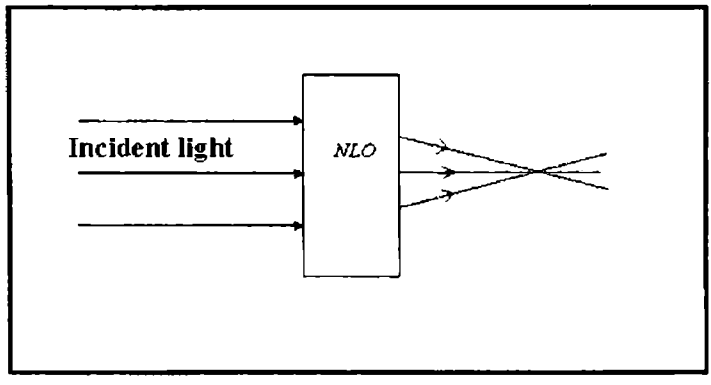

Figure 3.1. Self focusing in a Kerr media.

There exists a maximum distance L_0 over which the beam self-focuses which is approximately estimated using the formula,

$$L_0 = \frac{D}{\sqrt{n_{nl} E_0^2}} \tag{3.27}$$

where D is the diameter of the beam. Also another important parameter is the threshold intensity value for self focussing to happen which is estimated from the formula,

$$I_{thresh} = \frac{\lambda^2}{n_l^2 n_{nl} D^2} \tag{3.28}$$

From the formula we can see that for higher frequencies and for materials with greater nonlinear susceptibilities, the threshold intensity for self focussing will be lower.

3.4.4. Multi photon process

The very fundamental definition of the multi photon process is that the excitation of an atom or other microscopic system to a higher quantum state by simultaneous absorption of two or more photons which together provide the necessary energy for transition. Such multi photon processes were introduced even during the first years of development of quantum mechanics. But the experimental techniques available at that time were not that much adequate to observe the predicted phenomena. The major two photon processes that could be observed experimentally before the invention of lasers were Rayleigh [58] and Raman scattering [59].

Transformation of a coherent light wave with frequency ω into a coherent light wave with frequency 2ω or 3ω cannot take place through

interaction among photons. The transformation can be brought about only through an intermediary - a quantum system such as an atom or molecule characterized by a system of discrete energy levels. An atom or a molecule can absorb or emit photon and in the process may undergo a transition from one energy level to the other. When simultaneous absorption of multiple photons happens, an atom will proceed to an intermediate state corresponding to a characteristic eigen state or to a "virtual state." These virtual states are not eigen states; they do not correspond to any specific principal quantum number (n) or orbital quantum number (l) state and these states are in the actual sense merely superposition of waves. Compared to the eigen states, the life time of a virtual state is short. The closer the virtual state is to an actual eigen state, the longer will be the life time of the virtual state. Multi photon absorption processes include two photon absorption, three photon absorption processes etc.

3.4.5. Two-Photon Absorption

Two-photon absorption (TPA) is the phenomenon in which two photons of identical or different frequencies are absorbed simultaneously such that a molecule from one state (usually the ground state) will be excited to a higher electronic energy state. In this process the absorption of two photons by the electron happens at approximately the same time (or within less than a nanosecond) and achieves an excited state that corresponds to the sum of the energy of the incident photons. The difference in the energy between the lower and upper states of the molecule is equal to the sum of the energies of the two incident photons. The intermediate level is a virtual

state in this case. The two step absorption involving real intermediate state is called excited state absorption. Two photon absorption will occur with significant rates only at very high optical intensities, since the value of the two-photon absorption coefficient is proportional to the light intensity.

The phenomenon of two photon absorption was originally predicted by Maria Goeppert-Mayer in 1931 [60] and the first experimental verification of the TPA was done when two-photon-excited fluorescence was detected in a europium-doped crystal just after the invention of laser [61]. What makes it different from the ordinary (linear) light absorption is that the strength of absorption depends on the square of the light intensity, thus it is a nonlinear optical process. The two-photon absorption enables us to populate high energy levels that are otherwise unreachable by single photon transitions from the ground state.

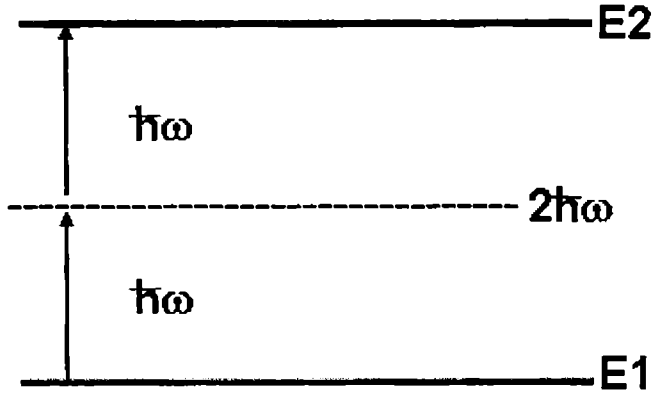

Figure 3.2. Two-Photon Absorption.

Two photon absorption can be broadly classified into two types, one is called the resonant TPA and the other one belongs to non resonant TPA. The non resonant TPA is the process in which two photons combine to bridge an energy gap larger than the energies of individual photons. When there exists an intermediate state in the gap, the transition happen through two separate one-photon transitions and the process is now described as "resonant TPA (sequential TPA). In non resonant TPA there need not be an intermediate state for the atom to reach before arriving at the final excited state (as if it were moving up two stair steps by stepping one at a time). Instead, the atom is excited to a "virtual state" which need not correspond to any electronic or vibrational energy eigen state.

The selection rules for TPA are entirely different from one-photon absorption (OPA), which is dependent on the first-order susceptibility. For example, in a centrosymmetric molecule, one- and two-photon allowed transitions are mutually exclusive. Quantum mechanically speaking, this difference between the selection rules for OPA and TPA results from the need to conserve angular momentum. Since photons have spin of ± 1, one-photon absorption requires such an excitation in which an electron changes its molecular orbital to one with an angular momentum different by ± 1 from the initial orbital. Two-photon absorption requires an angular momentum change of +2, 0, or −2. The Beer's law for OPA is given by eqn.(3.29) :

$$I(x) = I_0 e^{-\alpha c x} \tag{3.29}$$

where output optical intensity I is expressed as a function of path length x, concentration c and the initial light intensity I_0 and α is the linear absorption coefficient. However while coming to the TPA case eqn(3.29) changes to eqn.(3.30) as,

$$I(x) = \frac{I_0}{1 + \beta c x I_0} \tag{3.30}$$

Here β is the TPA coefficient. The molecular two-photon cross-section is usually quoted in the units of Goeppert-Mayer (**GM**) (after its discoverer, Nobel laureate Maria Goeppert-Mayer), where 1 GM is 10^{-50} cm^4 s $photon^{-1}$. Now towards special attention, the fact is that, this TPA transition or any multi photon transition, cannot, in principle, be divided into a temporal sequence of events. That means both photons are absorbed simultaneously during the transition. Two very relevant features of two-photon absorption which needs our special attention are:

(a) OPA occurs between states of opposite parity. In nonlinear medium a TPA occurs between states of same parity. The point is that a transition that is forbidden for one photon absorption is allowed for two photon absorption.

(b) Also the probability of two-photon absorption is proportional to the fourth power of the electric field, i.e., to the square of the intensity. The propagation equation for a TPA absorber is given by,

$$\frac{dI}{dZ} = -\alpha I - \beta I^2 \tag{3.31}$$

where α is the linear absorption coefficient and β is the two photon absorption coefficient. For a centrosymmetric system and linearly polarised light β is related to the imaginary part of third order susceptibility $\mathrm{Im}\,\chi^{(3)}$ by,

$$\beta = \frac{3\pi}{\varepsilon_0 n^2 c\ \lambda} \mathrm{Im}\,\chi^{(3)} \tag{3.32}$$

β is related to the intrinsic TPA cross section through,

$$\sigma_2 = \frac{\omega\beta\hbar}{N} \tag{3.33}$$

where N is the number density of molecules in the system and ω is the incident radiation frequency.

The phenomena of two photon absorption have very relevant applications in present science and technology. Some of them are in 3D optical data storage, microscopy and imaging, 3D micro fabrication and optical power limiting.

3.4.6. Three-Photon Absorption

Three photon absorption is the simultaneous absorption of three photons by a system in the ground state from an incident radiation field so as to reach an excited state which is not possible by single photon absorption. It is a fifth order nonlinear process. The propagation equation for a three photon absorber is given by,

$$\frac{dI}{dZ} = -\alpha I - \gamma I^3 \tag{3.34}$$

where α is the linear absorption coefficient and γ is the three photon absorption coefficient. For a centrosymmetric system and linearly polarised light, γ is related to the imaginary part of fifth order susceptibility $\mathrm{Im}\,\chi^{(5)}$ by,

$$\gamma = \frac{5\pi}{\varepsilon_0^2 n^3 c^2 \lambda} \mathrm{Im}\,\chi^{(5)} \tag{3.35}$$

3.5. Application of NLO

There are a number of highly relevant and desirable applications for NLO effects in various fields of technology and basic research. The main parameters determining the application side are its (1) sign (2) response time and (3) nature (real and imaginary) of the nonlinearity at the wavelength of excitation apart from the magnitude of nonlinearity. Major applications of the nonlinear optical phenomena include frequency mixing, optical limiting, optical switching, nonlinear wavelength conversion, optical parametric processes, frequency mixing, stimulated scattering, self- and cross-phase modulation, continuum generation, filamentation and optical solitons. Some of the very important applications are described below.

3.5.1. Frequency mixing

One of the very important applications of sum-frequency generation is the production of tunable radiation in the ultraviolet spectral region [52]. Difference-frequency generation can be used to produce tunable infrared radiation by mixing the output of a frequency-tunable visible laser with that of a fixed-frequency visible laser. Second harmonic of Nd:YAG laser (which

has a fundamental output at 1064 nm) is at 532nm and this laser is the most popular source of green light. Frequency tripled YAG laser is used for fusion applications. Optical parametric oscillators, which work on the principle of parametric wave mixing, are now used to get continuously tunable laser output from 400nm to 2000nm.

3.5.2. Optical short pulse generation and measurement

Optical pulses having pulse width less than nanosecond can be obtained only by using nonlinear techniques. Picosecond pulses can be obtained by mode locking technique [62]. Among different mode locking techniques, passive mode locking using nonlinear saturable absorbers [63] is preferred due to intrinsic speed limit of active mode locking techniques using acousto-optic & electro-optic modulators. Organic films, dye jets, bulk semiconductor quantum wells are some of the nonlinear media used for this purpose. Pulse width of less than one picosecond is usually measured by autocorrelation technique, which utilizes SHG. Frequency resolved optical grating (FROG) is a nonlinear optical technique used for measuring the time dependent intensity and phase of a femtosecond pulse [64]. Thus, generation and characterization of ultrashort pulses is possible only with appropriate nonlinear processes.

3.5.3. Nonlinear optical effects in optical communications

In communication, stimulated Brillioun scattering [65], stimulated Raman scattering, etc are detrimental effects, as they can cause optical loss and also frequency shift during propagation of laser beams through fibers [66, 67]. Raman amplification can be obtained by using stimulated Raman

scattering (SRS), which actually is a combination between Raman processes and stimulated emission. It is interesting for application in telecommunication fibers to amplify signal inside the standard material with low noise. Fiber amplifiers [68] are used to compensate the attenuation. Stimulated Brillouin scattering is one effect by which optical phase conjugation can take place. Stimulated Brilliouin scattering is particularly important in single mode fibers. New and remarkable image transformation properties of self phase modulation (even in the presence of a distorting optical element) open the door to many potential applications in optical communications; optical fibers etc.

3.5.4. Optical switching

The optical switch is the one that helps in the selective switching of signals in optical fibers or integrated optical circuits (IOCs) from one circuit to another. The switches that perform this function by physically switching light are called as photonic switches, independent of the way in which the switching of the light is achieved. Optical switches have a very important role in advanced optical fiber communication systems [69] and optical fiber sensor systems [70]. Many kinds of non mechanical optical switches using electro optic, magneto optic and acousto optic effects have been reported.

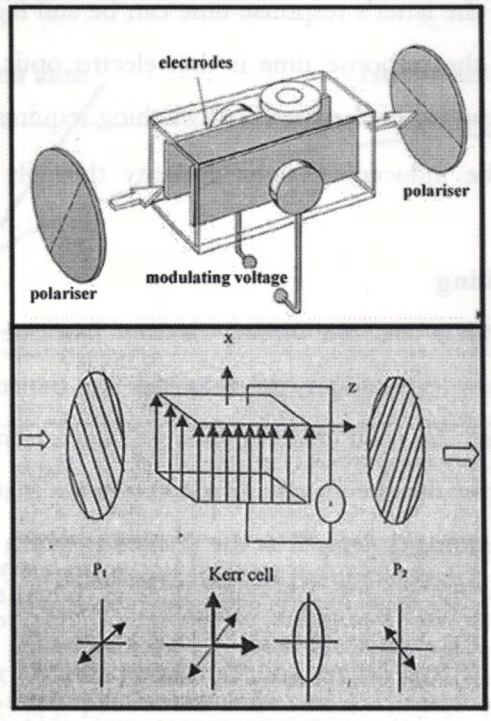

Figure 3.3. Working of an optical switch.

Generally speaking, an optical switch is the unit that actually switches light between fibers and a photonic switch is one that does this by using nonlinear optical properties of the material to steer light. Usually refractive nonlinearity is responsible for photonic switching [71]. The response time of the nonlinearity depends on the mechanism of evolution of nonlinearity. Optical switching by third order effects such as optical Kerr effect (as shown in figure 3.3) has special advantages over the linear electro optic effect. The former has instantaneous response (response time around

picoseconds) while the latter's response time can be still higher. The reason for this change in the response time is that electro optic effects includes charge separation and hence the speed of switching requires a phase shift of more than π to be induced by light intensity through refractive index modulation.

3.5.5. Optical limiting

Optical limiters are the optical devices fabricated to have high transmittance for low level inputs while blocking the transmittance for high intensity laser beams. An ideal optical limiter will have a linear transmission up to threshold input fluence I_{th}, which will vary from material to material. The threshold of limiting is defined as the fluence at which the transmission decreases to half of the value at low input fluence. When the magnitude of incident fluence is increased beyond I_{th}, transmittance of the limiting medium remains constant [72]. Just after the development of the first lasers in the late 60's, passive optical limiters have been introduced and analysed to protect optical sensors against laser-induced damage. The need for protection of eyes and different types of optical sensors from highly intense laser pulses lead to the search for optical limiting devices which have the superior qualities of being transparent at low intensity of light but non-transparent towards high intensity of light.

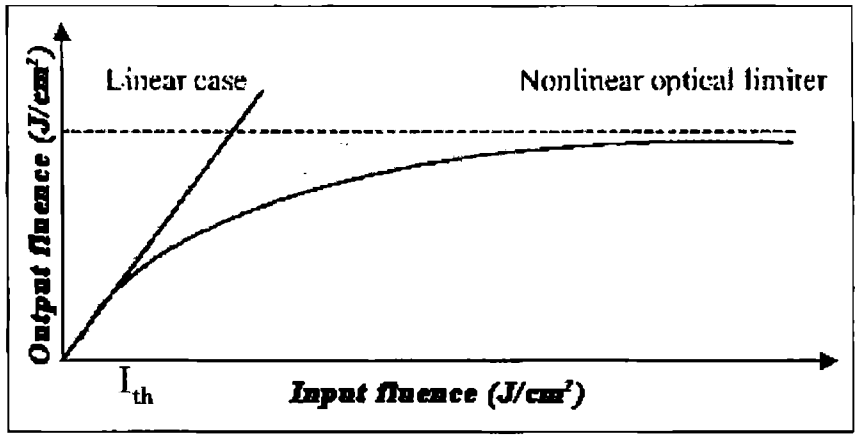

Figure 3.4. Ideal optical limiting plots.

The efficiency of optical limiting is related to the imaginary part of third order susceptibility. The major mechanisms contributing to the process of optical limiting are two photon absorption (TPA) [73], reverse saturable absorption (RSA) [74], free carrier absorption (FCA) [75], excited state absorption (ESA) [76] and nonlinear scattering [77]. Nowadays, molecules exhibiting reverse saturable absorption (RSA) have been the subject of intense research because of their strong limiting behavior, principally for nanosecond pulses. This type of absorption mechanism occurs in materials where the excited-state absorption cross section is larger than that of the ground state. In metal nanoparticles such as gold and silver nanoparticles, the optical limiting can be attributed to multi photon absorption processes enhanced by the surface plasmon absorption processes in the nanoparticles. In semiconductors, the optical limiting is attributed to the multi photon absorption processes occurring across the band gap.

3.6. Z-scan technique for the analysis of nonlinear absorption and refraction

Z-scan technique is a single beam method for measuring the sign and magnitude of nonlinear refractive index that has a sensitivity compared to interferometric methods [78]. Thus it provides direct measurement of nonlinear absorption coefficient. Previous measurements of nonlinear refraction have used a variety of techniques including nonlinear interferometry [79, 80], degenerate four wave mixing [81], nearly degenerate three wave mixing [82], ellipse rotation [83] and beam distortion measurements [84]. The first three methods namely nonlinear interferometry and wave mixing are potentially sensitive techniques, but all require complex experimental apparatus. Beam distortion measurements on the other hand are relatively insensitive and require detailed wave propagation analysis.

The Z-scan technique is based on the principle of spatial beam distortion which offers simplicity as well as high sensitivity. Theoretical analysis of the Z-scan measurements is given in section 3.6.1 for a "thin" nonlinear medium. Nonlinear refraction and its sign can be obtained from a simple relationship between the observed transmittance changes and the induced phase distortion without the need of performing detailed calculations.

3.6.1. The Z-scan technique

Using a single Gaussian laser beam in tight focus geometry as depicted in figure 3.5, we measure the transmittance of a nonlinear medium through a finite aperture in the far field as a function of the sample position

z measured with respect to the focal plane. The following example will qualitatively elucidate how such a trace (Z-scan) is related to nonlinear refraction of the sample. Assume, for instance, a material with a negative nonlinear refractive index and thickness smaller than the diffraction length of the focused beam (a thin medium). This can be regarded as a thin lens of variable focal length. Starting the scan from a distance far away from the focus (negative z), where the beam irradiance is low and therefore only negligible nonlinear refraction occurs; hence, the transmittance (D_2/D_1 in figure 3.5) remains relatively constant.

As the sample is brought closer to focus, the beam irradiance increases, leading to self-lensing in the sample. A negative self-lensing prior to focus will tend to collimate the beam, causing a beam narrowing at the aperture, which results in an increase in the measured transmittance. As the scan in z continues and sample passes the focal plane to the right (positive z), the same self defocusing increases the beam divergence, leading to beam broadening at the aperture, and thus a decrease in transmittance. This suggests that there is a null as the sample crosses the focal plane. This is analogous to placing a thin lens at or near the focus, resulting in a minimal change of the far-field pattern of the beam. The Z-scan is completed as the sample is moved away from the focus (positive z) such that the transmittance becomes linear since the irradiance is again low.

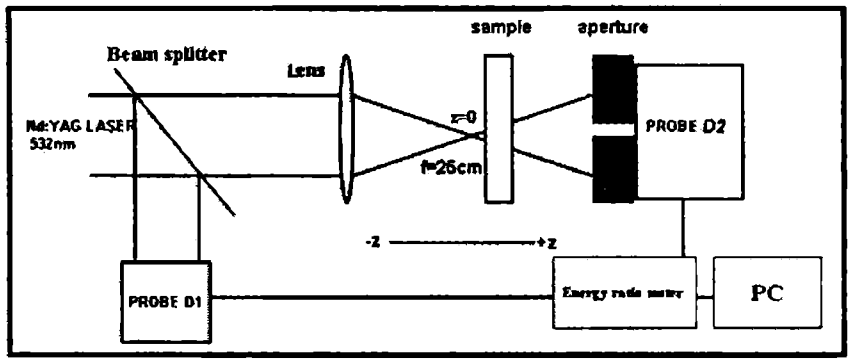

Figure 3.5. The schematic of the Z-scan setup.

A prefocal transmittance maximum (peak) followed by a post focal transmittance minimum (valley) is, therefore the Z-scan signature of a negative refractive nonlinearity. Positive nonlinear refraction, following the same analogy gives rise to an opposite valley-peak configuration. It is an extremely useful feature of the Z-scan method that the sign of the nonlinear index is immediately obvious from the data and the magnitude can also be easily estimated using a simple analysis for a thin medium. In the above picture describing the Z-scan, one must bear in mind that a purely refractive nonlinearity was considered assuming that no absorptive nonlinearities (such as multi photon absorption or saturation of absorption) are present.

3.6.2. Theory

(a).Purely refractive case

Considering the geometry given in figure 3.5, we will formulate and discuss a simple method for analyzing the Z-scan data based on modifications of existing theories. In general, nonlinearities of any order can

be considered; however, for simplicity, we first examine only a cubic nonlinearity where the index of refraction n is expressed in terms of nonlinear index n_2 (esu) or γ (m^2/W) through,

$$n = n_0 + \frac{n_2}{2}|E|^2 = n_0 + \gamma I \tag{3.36}$$

where n_0 is the linear index of refraction, E is the peak electric field (CGS) and I denote the irradiance (MKS) of the laser beam within the sample. n_2 and γ are related through the conversion formula,

$$n_2(esu) = \frac{cn_0}{40\pi}\gamma(m^2/W) \tag{3.37}$$

where c (m/s) is the speed of light in vacuum. Assuming a TEM_{00} Gaussian beam of beam waist radius w_0 travelling in the +z direction, we can write E as,

$$E(z,r,t) = E_0(t)\left[\frac{w_0}{w(z)}\right].Exp\left\{\frac{-r^2}{w^2(z)} - \frac{ikr^2}{2R(z)}\right\}.e^{-i\varphi(z,t)} \tag{3.38}$$

where $w^2(z) = w_0^2\left(1 + \frac{z^2}{z_0^2}\right)$ is the square of beam radius at z, $R(z) = z\left(1 + \frac{z_0^2}{z^2}\right)$ is the radius of curvature of the wave front at z, $z_0 = k\frac{w_0^2}{2}$ is the diffraction length of the beam, k = $2\pi/\lambda$ is the wave vector and λ is the laser wavelength, all in free space. $E_0(t)$ denotes the radiation electric field at the focus and contains the temporal envelope of the laser pulse. The $e^{-i\phi(z,t)}$ term contains all the radially uniform phase variations. As

we are only concerned with calculating the radial phase variations $\Delta\phi(r)$, the slowly varying envelope approximation (SVEA) applies, and all other phase changes that are uniform in r are ignored.

If the sample length is small enough that changes in the beam diameter within the sample due to either diffraction or nonlinear refraction can be neglected, the medium is regarded as "thin", in which case the self–refraction process is referred to as "external self–action" [85]. For linear refraction this implies that the sample length $L << z_0$, while for nonlinear refraction, $L << \frac{z_0}{\Delta\phi_0}$. In most experiments using the Z-scan technique, we find that the second criterion is automatically met since $\Delta\phi$ is small. Additionally, it is found that the first criterion for linear diffraction is more restrictive than it need be and it is sufficient to replace it with $L < z_0$. We have determined this empirically by measuring n_2 in the same material using various z_0's and the same analysis and have obtained the same value for n_2. Such an assumption simplifies the problem considerably, and amplitude I and the phase ϕ of the electric field as a function of z' are now governed in the slowly varying envelop approximation by a pair of simple equations:

$$\frac{d\Delta\phi}{dz} = \Delta n(I)k \tag{3.39a}$$

and

$$\frac{dI}{dz} = -\alpha(I)I \tag{3.39b}$$

where z' is the propagation depth in the sample and $\alpha(I)$, in general includes linear and nonlinear absorption terms. Note that z' should not be confused with the sample position z. In the case of a cubic nonlinearity and negligible nonlinear absorption (3.39a) and (3.39b) are solved to give the phase shift $\Delta\phi$ at the exit surface of the sample, which simply follows the radial variation of the incident irradiance at a given position of the sample z. Thus,

$$\Delta\phi(z,r,t) = \Delta\phi_0(z,t)\exp\left\{\frac{-2r^2}{w^2(z)}\right\} \tag{3.40a}$$

with,

$$\Delta\phi_0(z,t) = \frac{\Delta\phi_0(t)}{\left(1+\frac{z^2}{z_0^2}\right)} \tag{3.40b}$$

$\Delta\phi_0(t)$, the on–axis phase shift at the focus is defined as,

$$\Delta\phi(t) = k\Delta n_0(t)L_{eff} \tag{3.41}$$

where $L_{eff} = \frac{(1-e^{-\alpha L})}{\alpha}$, with L the sample length and α the linear absorption coefficient. Here, $\Delta n_0 = \gamma I_0(t)$ with $I_0(t)$ being the on-axis irradiance at the focus (i.e; z=0). Ignoring the Fresnel reflection losses such that, for example, $I_0(t)$ is the irradiance within the sample. The complex electric field existing in the sample, E_e now contains the nonlinear phase distortion.

$$E_e(z,r,t) = E(z,r,t)e^{-\frac{\alpha L}{2}} e^{i\Delta\phi(z,r,t)} \tag{3.42}$$

By virtue of Huygen's principle, one can obtain the far-field pattern of the beam at the aperture plane through a zeroth-order Hankel transformation of E_e [86]. By following a more convenient treatment applicable to Gaussian input beams which is referred to as the "Gaussian decomposition" (GD) method given by Weaire *et al*, in which the complex electric field at the exit plane of the sample is decomposed into a summation of Gaussian beams through a Taylor series expansion of the nonlinear phase term $e^{i\Delta\phi(z,r,t)}$ in eqn.(3.42). That is,

$$e^{i\Delta\phi}(z,r,t) = \sum_{m=0}^{\infty} \frac{[i\Delta\phi_0(z,t)]^m}{m!} e^{-2mr^2/w^2(z)}$$

Each Gaussian beam can now be simply propagated to the aperture plane where they will be resumed to reconstruct the beam. When including the initial beam curvature for the focused beam, we derive the resultant electric field pattern at the aperture as,

$$E_a(r,t) = E(z,r=0,t)e^{-\alpha L/2}\sum_{m=0}^{\infty}\frac{[i\Delta\phi_0(z,t)]^m}{m!}\frac{w_{m0}}{w_m}.\exp(-\frac{r^2}{w_m^2}-\frac{ikr^2}{2R_m}+i\theta_m) \tag{3.43}$$

Defining d as the propagation distance in free space from the sample to the aperture plane and $g = \left(1+\frac{d}{R(z)}\right)$, the remaining parameters in eqn. (3.43) are expressed as,

$$w_{mo}^2 = \frac{w^2(z)}{(2m+1)} \tag{3.44}$$

$$d_m = \frac{kw_{mo}^2}{2} \tag{3.45}$$

$$w_m^2 = w_{m0}^2\left[g^2 + \frac{d^2}{d_m^2}\right] \tag{3.46}$$

$$R_m = d\left[1 - \frac{g}{\left(g^2 + \frac{d^2}{d_m^2}\right)}\right]^{-1} \tag{3.47}$$

$$\theta_m = \tan^{-1}\left[\frac{\left(\frac{d}{d_m}\right)}{g}\right] \tag{3.48}$$

The expression given by eqn.(3.43) is a general case of that derived by Weaire *et al* where for a collimated beam (R=∝) for which g =1. This GD method is very useful for the small phase distortions detected with the Z-scan method since only a few terms of the sum in eqn.(3.43) are needed. The method is also easily extended to higher order nonlinearities. The transmitted power through the aperture is obtained by spatially integrating $E_a(r, t)$ up to the aperture radius r_a giving,

$$P_T(\Delta\phi_0(t)) = c\varepsilon_0 n_0 \Pi \int_0^{r_a} |E_a(r,t)|^2 r dr \tag{3.49}$$

where ϵ_0 is the permittivity of vacuum. Including the pulse temporal variation, the normalized Z-scan transmittance T(z) can be calculated as,

$$T(z) = \frac{\int_{-\infty}^{+\infty} P_i(\Delta\phi_0(t))dt}{S\int_{-\infty}^{+\infty} P_i(t)dt} \tag{3.50}$$

where $P_i(t) = \frac{\pi w_0^2 I_0(t)}{2}$ is the instantaneous input power (within the sample) and $S = 1 - \exp\left(\frac{-2r_a^2}{w_a^2}\right)$ is the aperture linear transmittance with w_a denoting the beam radius at the aperture in the linear regime.

First consider an instantaneous nonlinearity and a temporally square pulse to illustrate the general features of the Z-scan. This is equivalent to assuming CW radiation and the nonlinearity has reached the steady state. The normalized transmittance T(z) in the far field is shown in figure 3.6 for $\Delta\phi_0 = \pm$ 0.25 and a small aperture (S= 0.01). They exhibit the expected features, namely a valley-peak (v-p) for the positive nonlinearity and a peak-valley (p-v) for the negative one. For a given $\Delta\phi_0$, the magnitude and shape of T(z) do not depend on the wavelength or geometry as long as the far field condition for the aperture plane ($d >> z_0$) is satisfied. The aperture S, however is an important parameter since a large aperture reduces the variations in T(z). This reduction is prominent in the peak where beam narrowing occurs and can result in a peak transmittance which cannot exceed (1-S). Needless to say, for very large aperture or no aperture (S=1), the effect vanishes and

T(z) =1 for all z and $\Delta\phi_0$. For small $|\Delta\phi_0|$, the peak and valley occur at the same distance with respect to focus, and for a cubic nonlinearity, this distance is found to be $\cong 0.86z_0$. With larger phase distortions ($|\Delta\phi_0| > 1$), numerical evaluation of eqn.(3.43) – eqn.(3.50) shows that this symmetry no longer holds and peak and valley both move toward ± z for the corresponding sign of nonlinearity ($\Delta\phi_0$) such that their separation remains nearly constant, given by,

$$\Delta Z_{p\text{-}v} \cong 1.7\ z_0 \tag{3.51}$$

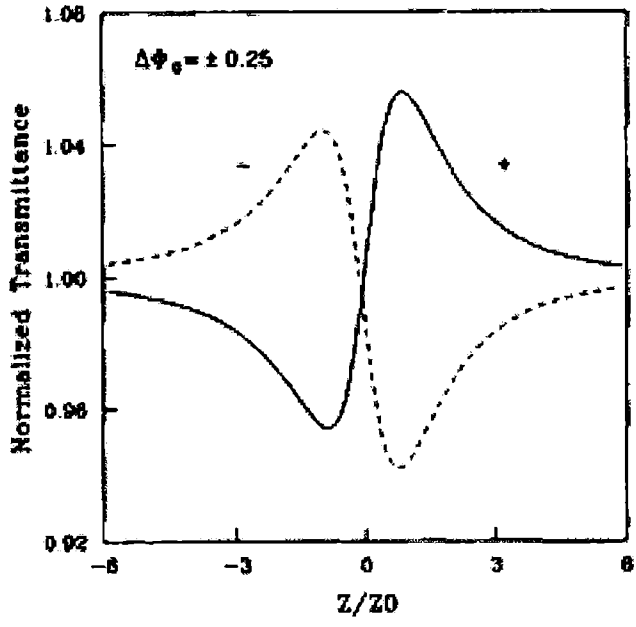

Figure 3.6. Calculated Z-scan transmittance curves for a cubic nonlinearity with either polarity and a small aperture (S=0.01).

The quantity ΔT_{p-v} is defined as the difference between the normalized peak and valley transmittance: T_p- T_v. The variation of this quantity as a function of $|\Delta\phi_0|$, as calculated for various aperture sizes, is illustrated in figure 3.7. These curves are independent of the laser wavelength, geometry (as long as the far field condition is met), and sign of nonlinearity. Secondly, for all aperture sizes, the variation of ΔT_{p-v} is found to be almost linearly dependent on $|\Delta\phi_0|$. For small phase distortion and small aperture (S≅0),

$$\Delta T_{p-v} = 0.406\,|\Delta\phi_0| \tag{3.52a}$$

Numerical calculations show that this relation is accurate to within 0.5% for $|\Delta\phi_0| \leq \pi$. Based on a numerical fitting, the following relationship can be used to include such variations within a ±2 % accuracy.

$$\Delta T_{p-V} \cong 0.406\,(1-S)^{0.25}|\Delta\phi_0| \qquad \text{for } |\Delta\phi_0| \leq \pi \tag{3.52b}$$

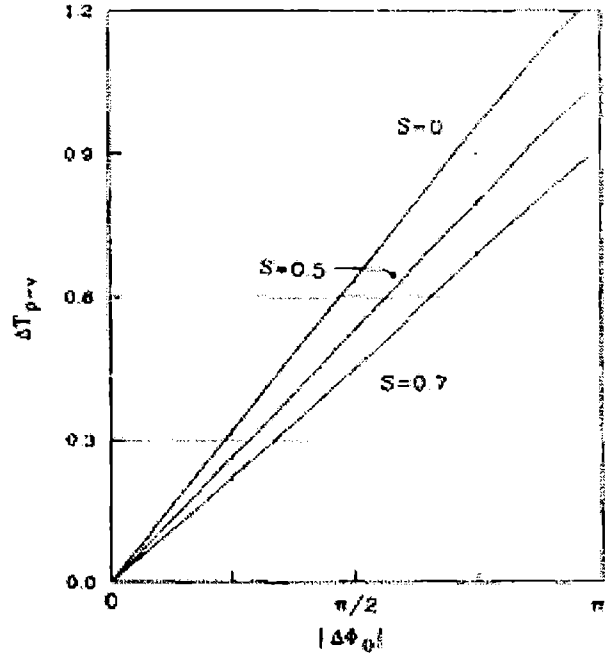

Figure 3.7. Calculated ΔT_{P-V} as a function of the phase shift ($\Delta\phi_0$) at the focus.

The sensitivity, as indicated by the slope of the curves, decreases slowly for larger aperture sizes (S>0). The implications of eqn.(3.52a) and eqn.(3.52b) are quite promising in that they can be used to readily estimate the nonlinear index (n_2) with good accuracy after a Z-scan is performed. To achieve high sensitivity we need high optical quality materials.

(b). Both absorption and refraction are present

A method by which the Z-scan technique can be used to determine both the nonlinear refractive index and the nonlinear absorption coefficient

for materials that show such nonlinearities simultaneously is described below. Large refractive nonlinearities in materials are commonly associated with a resonant transition, which may be of single, or multi photon nature. The nonlinear absorption in such materials arising from either direct multi photon absorption, saturation of the single photon absorption, or dynamic free-carrier absorption has strong effects on the measurements of nonlinear refraction using the Z-scan technique. Clearly, even with nonlinear absorption, a Z-scan with fully open aperture (S=1) is insensitive to nonlinear refraction (thin sample approximation). Such Z-scan traces with no aperture are expected to be symmetric with respect to focus (z=0) where they have a minimum transmittance (e.g, multi photon absorption) or maximum transmittance (e.g., saturation of absorption). In fact, coefficients of nonlinear absorption can be easily calculated from such transmittance curves.

Here we analyze two photon absorption (2PA), which we have studied in semiconductors with $E_g<2\hbar\omega<2E_g$ where E_g is the band gap energy and ω is the optical frequency [87]. The third order nonlinear susceptibility is now considered to be a complex quantity:

$$\chi^{(3)} = \chi_R^{(3)} + i\chi_I^{(3)} \tag{3.53}$$

where the imaginary part is related to the 2PA coefficient β through,

$$\chi_I^{(3)} = \frac{n_0^2 \varepsilon_0 c^2 \beta}{\omega} \tag{3.54a}$$

and the real part is related to γ through,

$$\chi_R^{(3)} = 2n_0^2\varepsilon_0 c\gamma \tag{3.54b}$$

Here, we are concerned with the low excitation regimes where the free-carrier absorption (refractive and absorptive) can be neglected. In view of this approximation eqn.(3.39a) and eqn.(3.39b) will be re-examined after the following substitution:

$$\alpha(I) = \alpha + \beta I \tag{3.55}$$

This yields the irradiance distribution and phase shift of the beam at the exit surface of the sample as,

$$I_e(z,r,t) = \frac{I(z,r,t)e^{-\alpha L}}{1+q(z,r,t)} \tag{3.56}$$

and

$$\Delta\varphi(z,r,t) = \frac{k\gamma}{\beta}\ln\left[1+q(z,r,t)\right] \tag{3. 57}$$

where $q(z,r,t) = \beta I(z,r,t)L_{eff}$ (again, z is the sample position). Combining eqn.(3.56) and eqn.(3.57), we obtain the complex field at the exit surface of the sample to be [88],

$$E_e = E(z,r,t)e^{\frac{-\alpha l}{2}}(1+q)^{\frac{ik\gamma}{\beta}-\frac{1}{2}} \tag{3.58}$$

Eqn.(3.62) reduces to eqn.(3.46) in the limit of no two photon absorption. In general, a zeroth order Hankel transform of (3.57) will give the field distribution at the aperture which can then be used in eqn.(3.49) and (3.50), to the yield the transmittance. For $|q| < 1$, following a binomial series expansion in powers of q, equation eqn.(3.58) can be expressed as an

infinite sum of Gaussian beams similar to the purely refractive case as follows;

$$E_e = E(z,r,t)e^{-\alpha L/2}\sum_{m=0}^{\infty} q(z,r,t)^m / m![\prod_{n=0}(\frac{ik\gamma}{\beta} - \frac{1}{2} - n + 1)] \qquad (3.59)$$

where the Gaussian spatial profiles are implicit in q(z,r,t) and E(z,r,t). The complex field pattern at the aperture plane can be obtained in the same manner as before. The result can again be represented by eqn.(3.43) if we substitute the $i\frac{\Delta\phi_0(z,t)^m}{m!}$ terms in the sum given below,

$$f_m = i\frac{\Delta\phi_0(z,t)^m}{m!}\prod_{n=0}^{m}\left(1 + i(2n-1)\frac{\beta}{2k\gamma}\right) \qquad (3.60)$$

with $f_0 = 1$. Note that the coupling factor $\frac{\beta}{2k\gamma}$ is the ratio of the imaginary to real parts of the third order susceptibility $\chi^{(3)}$.

The Z-scan transmittance variations can be calculated following the same procedure previously. As is evident from eqn.(3.60), the absorptive and refractive contributions to the far field beam profile and hence to the Z-scan transmittance is coupled. When the aperture is removed, however, the Z-scan transmittance is insensitive to beam distortion and is only a function of the nonlinear absorption. The total transmitted fluence in that case (S=1) can be obtained by spatially integrating eqn.(3.56) without having to include the free- space propagation process. On integrating we get,

$$P(z,t) = P_i(t)e^{-\alpha L}.[\ln(1 + q_0(z,t))/ q_0(z,t)] \qquad (3.61)$$

where $q_0(z,t) = \frac{\beta I_0(t) L_{eff}}{\left(1 - \frac{z^2}{z_0^2}\right)}$ and $P_i(t)$ was defined in eqn(3.51).

For a temporally Gaussian pulse, eqn.(3.61) can be time integrated to give the normalized energy transmittance.

$$T(z, S=1) = \frac{1}{\sqrt{\pi} q_0(z,0) \cdot \int \ln\left[1 + q_0(z,0) e^{-\tau^2}\right] d\tau} \tag{3.62}$$

For $|q_0| < 1$, this transmittance can be expressed in terms of peak irradiance in a summation form more suitable for numerical evaluation:

$$T(z, S=1) = \sum_{m=0}^{\infty} \left[\frac{(-q_0(z,0))^m}{(m+1)^{\frac{3}{2}}} \right] \tag{3.63}$$

Thus once an open aperture (S=1) Z-scan is performed, the nonlinear absorption coefficient β can be unambiguously deduced. With β known, the Z-scan with aperture in place (S<1) can be used to extract the remaining unknown, namely, the coefficient γ.

3.6.3. Automated Z-scan setup for nonlinear optical studies

An automated Z-scan setup was fabricated in our laboratory for nonlinear optical studies. The picture of the fabricated Z-scan setup we used for nonlinear optical studies is shown in the figure 3.8.

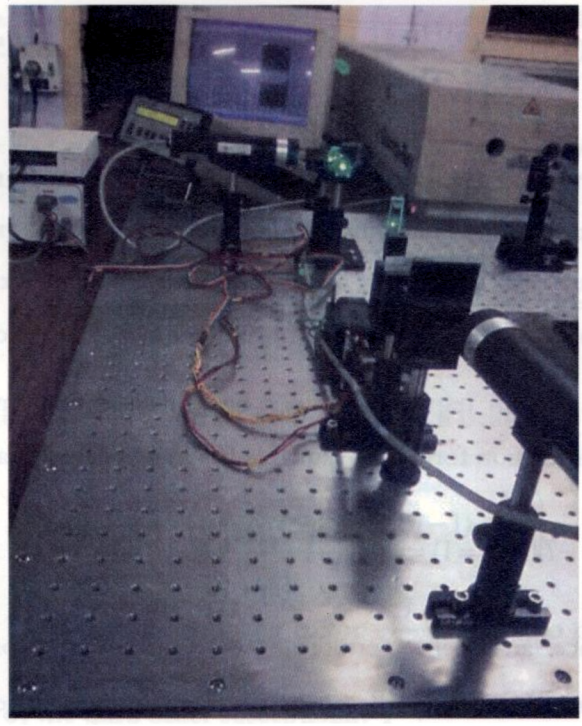

Figure 3.8. Photograph of automised Z-scan setup.

The automised Z-san set-up contains the following major components.

1. Nd:YAG Laser

The pulsed laser used here for the experiment is an electro-optically Q-switched Nd:YAG laser having a fundamental output of 1.06μm (Quanta Ray GCR 150). Nd:YAG is the acronym used for Neodymium doped Yttrium Aluminum Garnet. The diffraction coupled resonator cavity delivers a 'doughnut' shaped beam profile at energies of the order of 650 mJ at ≈ 8-

9ns pulse width with a power stability <2%. It has second harmonic generator (KDP crystal) which can be placed in the path of the fundamental beam to provide the second harmonic output at 532nm (300mJ) at 6-7ns pulse width with a conversion efficiency of ≈ 50%. Figure 3.9 shows the schematic of the Nd:YAG laser. Higher order harmonics at 355 nm can be obtained by introducing the appropriate crystal in the beam path.

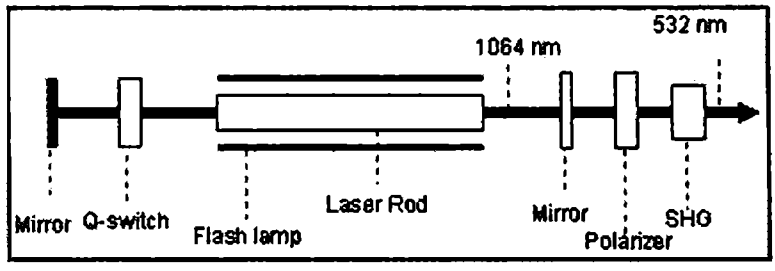

Figure 3.9. Schematic diagram of Nd:YAG Laser used in the Z scan setup.

2. Focusing Lens

Here a plano convex fused silica lens (Laser quality) having focal length 25 cm is placed in the path of the laser beam for focusing the beam on to the sample. The plano convex lens produces a spatial variation in the intensity along which the sample is to be translated.

3. Beam Splitters

Laser from the source is passed through a number of beam splitters to get the required energy. The beam splitters are arranged in some geometrical order so as to reflect laser beam to the successive reflectors. The reflecting surface of each beam splitter was adjusted to be at 45^0 to the laser beam so that only 4% of incident energy is reflected. This arrangement

ensured the laser energy to be incident on to the target and to the reference probe in the required order.

4. Automized Rj-7620 Energy ratiometer

Using two probe heads D_1 and D_2 of the Energy ratiometer, the incident and transmitted energies can be measured. The specifications of the probes of the energy ratiometer used are shown in table 1. These probes are connected to the energymeter, which is automated using LabVIEW. The ratio D_2/D_1 is directly available from the energymeter. The energy ratiometer measures the reference as well as transmitted signals simultaneously.

PD1-RjP 765 Silicon Probe	Maximum energy -2 μJ Dimension -18 ×4cm Detector configuration –flat Maximum peak power density-5 W/cm^2
PD2-RjP-734 Pyroelectric Probe	Maximum energy-2 J Dimension -22.5× 6 cm Detector configuration – cavity Maximum peak power density-1Mw/cm^2

Table 1. The specification of the probes.

The proper communication of the instrument and the PC is achieved by NI LAB VIEW 7.1 through the GPIB interface bus. The acquired data saved as an excel document is again read to a sub programme

file for fitting the experimental data to the theoretical equations. Proper fitting of the data will give the value of the nonlinear refractive index and nonlinear absorption coefficient. The front panel for automating the energy ratiometer is shown in figure 3.10.

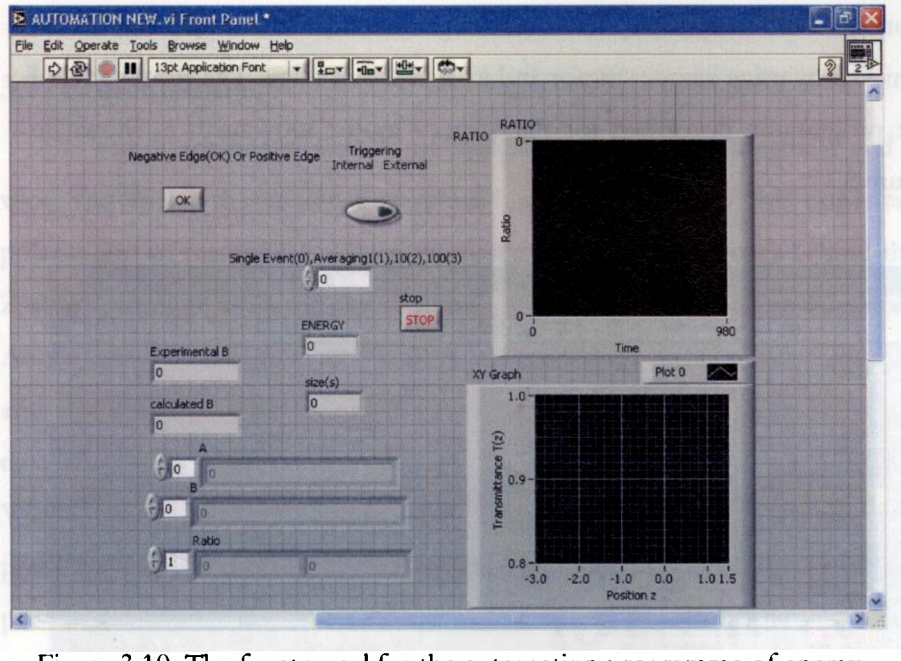

Figure 3.10. The front panel for the automation programme of energy ratiometer.

5. Automated micro stepper

The microstepping motion of the translation stage in the focused region of the lens (varying intensity region) is very significant to get error less data. The pulse width of the laser source used is very narrow of the

order of 6ns and the frequency of the pulsed laser is 10Hz. The nonlinear response induced by the high peak power of the laser pulses is ultrafast that requires an ultrafast data acquisition for the detection. Also sample motion should be highly precise of the order of microns and reproducible such that the output signal measured will be highly accurate while the microstepping motion of the sample cell. The microstep motion of the sample cell can be achieved by using stepper motor and its translation stage. The front panel of the programme developed for the stepper motor movement is shown in figure 3.11.

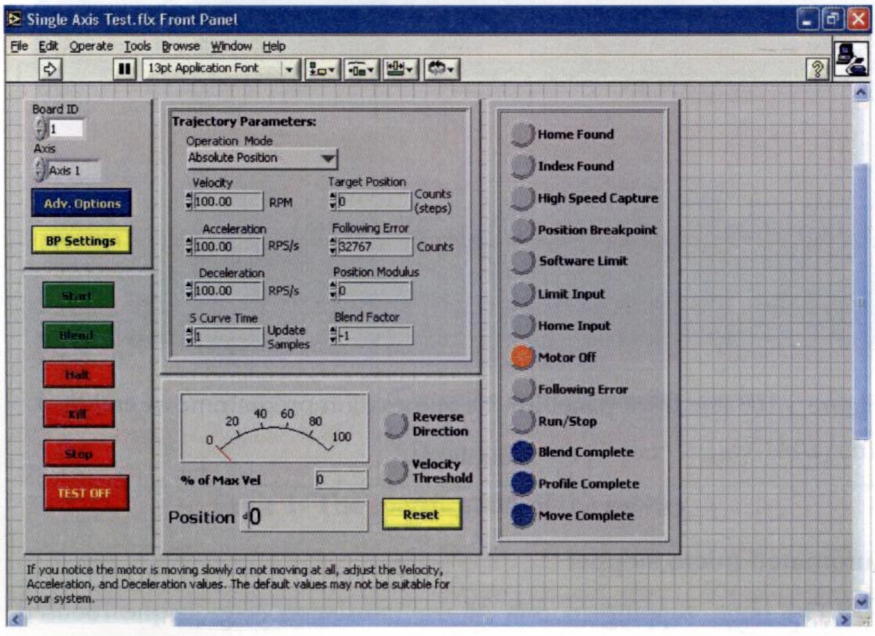

Figure 3.11. The front panel for the automation programme of stepper motor.

The microstep motion is achieved by using NI PCI 7332 card in conjugation with UMI 7764. The stepper motor driver unit attached to the UMI 7764 is properly designed to match the NI product.

The fabricated Z-scan setup enables the direct estimation of the nonlinear coefficients of the samples in colloidal as well as in thin film form.

3.7. Conclusions

The fundamental aspects of optical nonlinearity in materials and a wide variety of the material properties arising out from the nonlinear polarisation of materials has been discussed in detail. The theory behind the Z-scan technique used for the nonlinear optical studies has been discussed. An automated Z-scan setup for the evaluation of the nonlinear absorption and refraction was fabricated. The data acquisition and the analysis of the data were made quite easy by automising the entire setup. Here the LAB VIEW programming tools and devices such as NI PCI 7332, UMI 7764 provides better communication between the instruments and PC. This provides microstep motion of the sample cell and thereby getting very fast and error free data acquisition compared to manual data acquisition. The graphical programming tool is used in the calculation and curve fitting of our application. The interfacing and automation saves lots of time and even can measure the full set of data in few minutes.

3.8. References

1. Y. R. Shen, The Principles of Nonlinear Optics, Wiley, New York (1984)
2. P. A. Franken., A. E. Hill, C. W. Peters and G. Weinreich, Phys. Rev. Lett. **7** 118 (1961)
3. S. D. Coomber, C. D. Cameron, J. R. Hughes, D. T. Sheerin, C. W. Slinger, M. A. Smith and M. Stanley, Proc. SPIE **4457** 9 (2001)
4. H. Wang', X. Yi, S. Chen and X. Fu, Sensors and Actuators A: Physical **122** 108 (2005)
5. K. C. Chin, A. Gohel, W. Z. Chen, H. I. Elim, W. Ji, G. L. Chong, C. H. Sowand A. T. S. Wee, Chem. Phys. Lett. **409** 85 (2005)
6. R. Liu, Y. Shu, G. Zhang, J. Sun, X. Xing, B. Pi, J. Yao, Z. Wang and J. Xu, Opt. Quant. Electron. **39** 1207 (2007)
7. S. H. Park, R. A. Morgan, Y. Z. Hu, M. Lindberg, S. W. Koch and N. Peyghambarian, J. Opt. Soc. Am. B **7** 2097(1990)
8. J. A. Miragliotta and J. Hokins, APL Techn. Digest. **16** 348 (1995)
9. M. J. Weber, D. Milam and W. L. Smith, Opt. Eng. **17** 463 (1978)
10. J. M. Bass, P. A. Pranken, A. E. Hill, C.W. Peters and G. Weinrich, Phys. Rev. Lett. **8** 18 (1962)
11. A. Flusberg, T. Mossberg, and S. R. Hartmann Phys. Rev. Lett. **38**, 59 (1977)
12. R. W. Terhune, P. D. Maker and C. M. Savage, Phys. Rev. Lett. **8** 404 (1962)

13. M. Bass, P. A. Franken, J. F. Ward and G. Weinreich, Phys. Rev. Lett. **9** 446 (1962)
14. J. A. Giordmaine and R. C. Miller, Phys. Rev. Lett. **14** 973 (1965)
15. G. Eckhardt, R. W. Hellwarth, F. J. McClung, S. E. Schwarz and D. Weiner, Phys. Rev. Lett. **9** 455 (1962)
16. A. Chugreev, A. Nazarkin, A. Abdolvand, J. Nold, A. Podlipensky and P. S. J. Russell, Opt. Expr. **17** 8822 (2009)
17. A. S. Pine Phys. Rev. **149** 113 (1966)
18. Y. R. Shen and N. Bloembergen Phys. Rev. **137** A1787 (1965)
19. Sundar and R. E. Newnham, Ferroelectrics. **135** 431 (1992)
20. R. Y. Chiao, C. H. Townes and B. P. Stoicheff, Phys. Rev. Lett. **12** 592 (1964)
21. P. L. Kelley, Phys. Rev. Lett. **16** 384 (1966)
22. E. Cumberbatch, J. Inst. Maths Applics. **6** 250 (1970)
23. R. Y. Chiao, T. K. Gustafson and P. L. Kelley, Topics in Appl.Phys. **114** 129(2009)
24. C. E. Max and J. Arons, Phys. Rev. Lett. **33** 209(1974)
25. I. D. Abella, N. A. Kurnit and S. R. Hartmann, Phys. Rev. **141** 391(1966)
26. S. L. McCall and E. L. Hahn, Phys. Rev. Lett. **18** 908 (1967)
27. G. B. Hocker and C. L. Tang, Phys. Rev. **184** 356(1969)
28. A. Javan, W. R. Bennett and D. R. Herriott, Phys. Rev. Lett. **6** 106(1961)
29. W. Dietel, E. Dopel and D. Kuhlke, Sov. J. Quant. Electron. **12** 668 (1982)

30. J. A. Aust, K. J. Malone, D. L. Veasey and N. A. Sanford, Opt. Lett. **19** 1849 (1994)
31. W. Kaiser and C.G.B. Garrett, Phys. Rev. Lett. **7** 229 (1961)
32. J. M. Ralston and R. K. Chang, Phys. Rev. B **2** 1858 (1970)
33. P. D. Southgate and D. S. Hall, Appl. Phys. Lett. **18** 456 (1971)
34. W. J. Jones and B. P. Stoicheff, Phys. Rev. Lett. **13** 657 (1964)
35. A.Owyoung, IEEE J.Quant. Electron. **14** 192 (1978)
36. R. E. Teets, F. V. Kowalski, W. T. Hill, N. Carlson, T. W. Hansch, SPIE Laser Spectrosc. **113** 80 (1977)
37. B. Y. Zeldovich, V. I. Popovichev, V. V. Ragulskii and F. S. Faizullov, Pisma Zh. Eksp. Teor. Fiz. **15** 160 (1972)
38. R. W. Hellwarth, IEEE J.Quant. Electron. **QE-15** 101 (1979)
39. R. L. Sutherland, Handbook of nonlinear optics, Second edition, Marcel Dekker, USA (2003)
40. J. C. Maxwell, Royal Society Transactions **CLV** 459 (1865)
41. E. G. Sauter, Nonlinear optics, John Wiley & Sons Inc, New York (1996)
42. Y. R. Shen, The principles of nonlinear optics, John Wiley and Sons, New york (1991)
43. Y. P. Svirko and N. I. Zheludev, Polarization of Light in Nonlinear Optics, John Wiley & Sons, Chichester (1998)
44. A. Yariv, Optical Electronics in Modern Communications, Oxford University Press, New York (1997)

45. G. L. Wood and E. J. Sharp, Nonlinear Optics, (Eds) R. E. Fisher and W. J. Smith, McGraw Hill Inc., New York (1994)
46. R. A. Fisher (Ed.) Optical Phase Conjugation, Academic press, New York (1983)
47. M. A. Foster, J. M. Dudley, B. Kibler, Q. Cao, D. Lee, R. Trebino and A. L. Gaeta , Appl. Phys. B: Lasers and Optics **81**, 363 (2005)
48. P. Dong and A. G. Kirk , Phys. Rev. Lett. **93** 133901 (2004)
49. D. J. Williams, P. Prasad, Introduction to nonlinear optical effects in molecules and polymers, Wiley, New York (1991)
50. P. Weinberger, Phil. Mag. Lett. **88** 897 (2008)
51. G. P. Agrawal and N. Olsson, IEEE J. Quant. Electron. **25** 2297 (1989)
52. R. W. Boyd, Nonlinear optics, Second edition, Elsevier, Singapore (2003)
53. J. N. Bloembergen and Y. R. Shen, Phys. Rev. **133** 37 (1964)
54. P. A. Franken and J. F. Ward, Rev. Mod. Phys. **35** 23 (1963)
55. E. Cumberbatch, J. Inst. Maths Applics **6** 250 (1970)
56. A. L. Gaeta, Phys. Rev. Lett. **84** 3582 (2000)
57. P. L. Kelley, Phys. Rev. Lett. **15** 1005 (1965)
58. A. T. Young, Appl. Opt. **20** 533 (1981)
59. C. V. Raman and K. S. Krishnan, Nature **121** 3048 (1928)
60. G. Mayer, Ann Phys. **9** 273 (1931)
61. W. Kaiser and C. G. B. Garrett, Phys. Rev. Lett. **7** 229 (1961)
62. C. L. Wang and C. L. Pan, Jpn. J. Appl. Phys. **33** L1607 (1994)
63. R. Paschotta and U. Keller, Appl. Phys. B **73** 653 (2001)

64. B. Kohler, V. V. Yakovlev, K. R. Wilson, J. Squier, K. W. DeLong and R. Trebino, Opt. Lett. **20** 483(1995)

65. M. J. Damzen,V. I. Vlad, V. Babin, V. Mocofanescu, Stimulated Brillouin scattering: fundamentals and applications, Institute of Physics, Great Britain (2003)

66. Y. Aoki and K. Tajima, J. Opt. Soc. Am. B **5** 358 (1988)

67. F. Benabid, J. C. Knight, G. Antonopoulos and P. S. J. Russell, Science **298** 399 (2002)

68. K. Keita, R. Frey, P. Delaye, D. Dolfi, J. P. Huignard and G. Roosen, Opt. Commun. **263** 300 (2006)

69. M. Nunoshita, Y. Nomura, T. Matsui and T. Nakayama, Opt. Lett. **4** 27 (1979)

70. K. R. Cooper, J. Elster, M. Jones and K.G. Kelly, IEEE Systems Readiness Technology Conference 847 (2001)

71. J. R. Isidro, A. K. Mairaj, V. Pruneri, D. W. Hewak, M. C. Netti and J. J. Baumberg, J. Non-Crystal. Solids **317** 241 (2003)

72. L. W. Tutt and T. F. Boggess, P. Quant. Electron. **17** 299 (1993)

73. J. E. Ehrlich, X. L. Wu, I. Y. S. Lee, Z. Y . Hu, H. Rockel, S. R. Marder and J. W. Perry, Opt. Lett. **22** 1843 (1997)

74. K. P. Unnikrishnan, V. P. N. Nampoori, V. Ramakrishnan, M. Umadevi and C. P. G. Vallabhan, J. Phys. D: Appl. Phys. **36** 1242 (2003)

75. S. S. Kubakaddi and B. G. Mulimani, J. Phys. C: Solid State Phys. **18** 6647 (1985)

76. B. L. Justus, Z. H. Kafafi and A. L. Huston, Opt. Lett. **18** 1603(1993)

77. S. R. Mishra, H. S. Rawat, M. P. Joshi and S. C. Mehendale, J. Phys. B: At. Mol. Opt. Phys. **27** L157 (1994)

78. M. Sheik-Bahae, A. A. Said and E. W. Van Stryland, Opt. Lett. **14** 955 (1989)

79. M. J. Weber, D. Milam and W. L. Smith, Opt. Eng. **17** 463 (1978)

80. M. J. Moran, C. Y. She and R. L. Carman, IEEE J.Quant.Elecron. **QE-11** 259(1975)

81. S. R. Friberg and P. W. Smith, IEEE J. Quantum Electron. **QE-23** 2089(1987)

82. R. Adair, L. L. Chase and S. A. Payne, J. Opt. Soc. Am. B **4** 875 (1987)

83. A. Owyoung, IEEE J. Quant. Electron. **QE-9** 1064 (1973)

84. W. E. Williams, M. J. Soileau and E. W. Van Stryland, Opt. Commun. **SO** 256 (1984)

85. D. Weaire, B. S. Wherrett, D. A. B. Miller and S. D. Smith, Opt. Lett. **4** 331 (1974)

86. J. D. Gaskill, Linear Systems Fourier Trunsforms and Oprics, Wiley, New York (1978)

87. E. W. Van Stryland, M. A. Woodall, H. Vanherzeele and M. J. Soileau, Opt. Lett. **10** 490 (1985)

88. J. A. Hermann, J. Opt. Soc. Am. B **1** 729 (1984)

Chapter 4

Linear and nonlinear optical properties of luminescent ZnO nanoparticles embedded in PMMA matrix

4.1. Introduction

Zinc oxide is a wide direct band gap (~ 3.37 eV) semiconductor that has tremendous potentials for blue-ultraviolet light emitters and detectors, transparent high-power electronics and piezoelectric transducers. The low threshold for optical pumping and large exciton binding energy (~ 60 MeV) allow lasing action in ZnO to be reached at extremely low pumping power at room temperature. Recently, ultrafast carrier dynamics in nanostructured ZnO [1, 2] and huge nonlinear refraction and absorption in ZnO thin films have been observed [3]. Ultrafast all-optical switching devices are the key component for next generation broadband optical networks. The implementation of such devices requires materials with low linear and nonlinear losses, high Kerr-type refractive nonlinearities and response times of a few picoseconds or less [4]. To search for materials which meet the above requirements, it has been suggested to target at semiconductors with their band gap at least twice the photon energy used ($E_g > 2E_{photon}$) avoiding optical absorption due to one or two-photon transitions [5-6]. In this regard, wide-gap semiconductors are a suitable candidate; and ZnO has been recently reported to be one of the promising candidates [7].

Nonlinear absorbers can be used as optical limiters, which have a linear transmission up to a threshold input flounce I_{th} and the value of I_{th} may vary in different materials. If the input fluence is increased above the I_{th}, the transmittance remains a constant. The nonlinear absorption in ZnO originates from the so called multi photon absorption processes of which

two photon absorption is the significant mechanism at laser wavelength 532nm. Two-photon absorption is an instantaneous nonlinearity in which, an electron absorbs two photons at approximately the same time (or within less than a nanosecond) and achieves an excited state that corresponds to the sum of the energy of the incident photons. The present study deals with absorptive as well as refractive nonlinearity of ZnO nanoparticles embedded in poly methyl methacrylate (PMMA) matrix.

4.2. Experimental

ZnO nanoparticles were prepared at room temperature by wet chemical route without any capping agents [9], using 0.1 mol of zinc acetate and varying concentration of NaOH (0.025M to 0.2M) in methanol and stirred for 2 hours. The chemical reaction involved is as follows:

$$Zn(CH_3COO)_2 2H_2O + 2NaOH \rightarrow ZnO + 2(CH_3COO).Na+3H_2O$$

The size of the nanoparticles was verified by transmission electron microscopy (TEM). It was not possible to filter out the nanoparticles prepared at the lower concentration of NaOH in the reaction mixture because of their smaller size. The concentrations of the ZnO nanoparticles in the resulting colloidal solution were found by atomic absorption spectroscopy (AAS). A part of the colloidal solution was filtered out to get fine ZnO powder for the X–ray diffraction (XRD) studies. The XRD patterns of the ZnO powder obtained at higher concentrations of NaOH in the reaction mixture were taken using Rigaku DMAX-C X-ray diffractometer. 2 grams of PMMA was mixed with 10 ml of chloroform and

was stirred for 1 hour. 3ml of the ZnO solution is added drop wise to the PMMA solution (10ml) and stirred again for one hour. The resulting viscous solution was spin coated on glass plate at a rotation speed of 1500rpm so as to get a thin film of thickness 1μm. The UV-visible absorption spectra of the as prepared ZnO colloids and ZnO: PMMA thin films were recorded using Jasco V 570 spectrophotometer.

The nonlinear optical properties were analyzed using single beam Z-scan technique. The experimental setup for the nonlinear study is shown in figure 4.1.

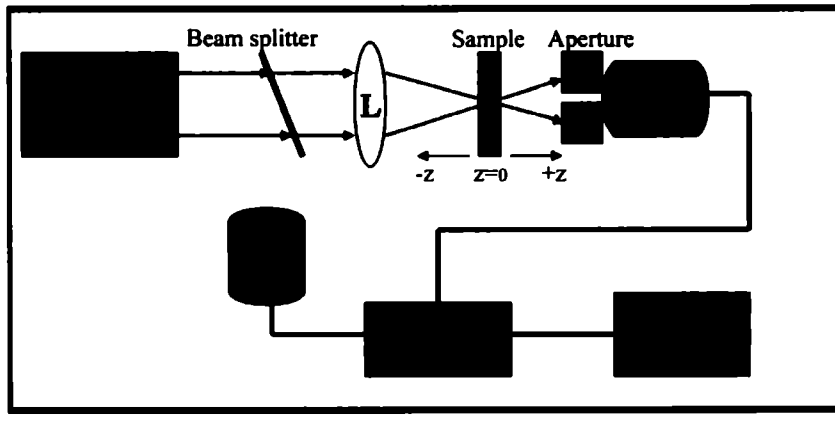

Figure 4.1. Schematic of closed aperture Z-scan setup.

The experimental setup consists of Nd:YAG laser working at 532nm operating at a repetition rate of 10Hz which function as the light source. The incident beam is splitted into two, one is taken as the reference beam and the other beam is allowed to transmit through the sample. The laser

beam was focused using a lens of focal length 25cm on to the sample. The sample was translated in the spatially varying intensity region on either side (-z to +z) of the focal point (z=0) using the translation stage of an automated stepper motor. The reference laser fluence, transmitted fluence and ratio between them were measured using the probes D1 and D2 of an automated energy ratio meter (RJ-7620 energy ratio meter) simultaneously for different positions of z. The dependence of incident laser fluence on the nonlinear absorption and nonlinear refraction were analyzed using open (without aperture) and closed aperture (with aperture) Z-scan techniques respectively.

4.3. Results and discussions

The XRD pattern (Figure 4.2) of ZnO synthesized by wet chemical method has large full width at half maximum (FWHM) compared to the bulk commercial ZnO which confirms the formation of ZnO nanoparticles. The FWHM shows a gradual increase with decrease in concentration of the NaOH in the reaction mixture indicating decrease in particle size. The ZnO nanoparticles produced by the wet chemical route has a thin passivation layer of $Zn(OH)_2$. The oxygen is being supplied by the NaOH. The increase in the concentration of NaOH increases the dissolved oxygen, which promotes the growth of ZnO. Thus increasing the concentration of NaOH will increase the growth of ZnO and agglomeration enhances the size of ZnO.

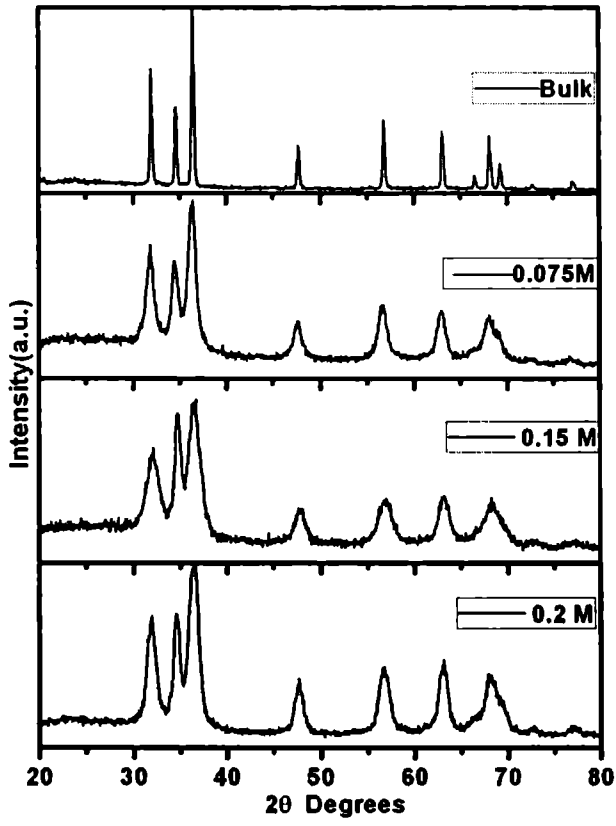

Figure 4.2. XRD pattern of bulk ZnO and the ZnO nanoparticles prepared at various NaOH concentrations.

The high resolution TEM (HRTEM) image of ZnO nanoparticles prepared with 0.075M of NaOH is shown in figure 4.3. The selected area electron diffraction (SAED) pattern of ZnO nanoparticles prepared at 0.075M (the inset of figure 4.3(b)) exhibits a concentric diffused ring pattern due to the nanocrystalline nature of ZnO [10]. TEM analysis of the ZnO

reveals the formation of hexagonal nanoparticle with size as 6 nm. Atomic scale images of ZnO nanoparticles prepared with 0.075M in the reaction mixture (figure 4.3(b) shows parallel lines of atoms at regular intervals of 0.28nm which coincides the d spacing corresponding to (100) planes of ZnO. The d values obtained from the SAED confirms the formation of (102) and (103) planes of ZnO.

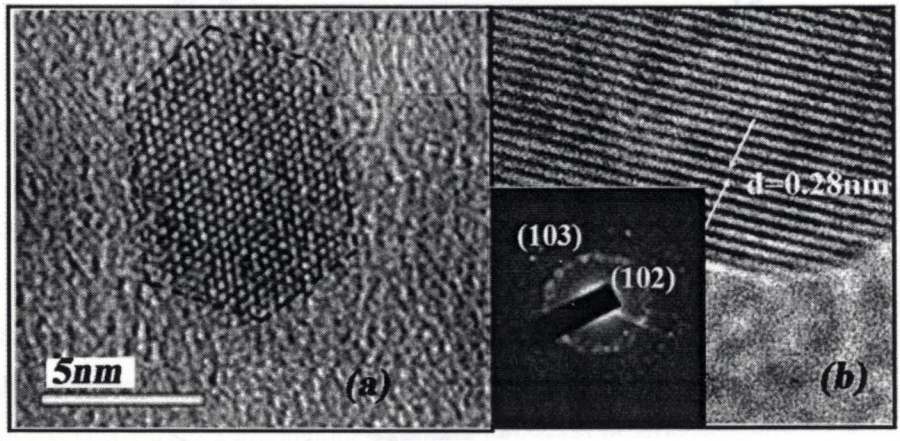

Figure 4.3 (a) HRTEM image of ZnO nanoparticles prepared at 0.075 M NaOH and (b) HRTEM images of ZnO nanoparticles prepared at 0.075 M showing parallel lines of atoms at regular intervals (inset shows SAED pattern).

Figure 4.4(a) shows the TEM image of the ZnO nanoparticles prepared at 0.2M NaOH showing an average particle size of 10nm ; and figure 4.4(b) shows the HRTEM image showing parallel lines of atoms: the interplanar spacing observed d=0.28nm corresponds to the (100) plane of

ZnO. The inset of figure 4.4(b) shows the SAED pattern showing the (102) and (100) planes of ZnO.

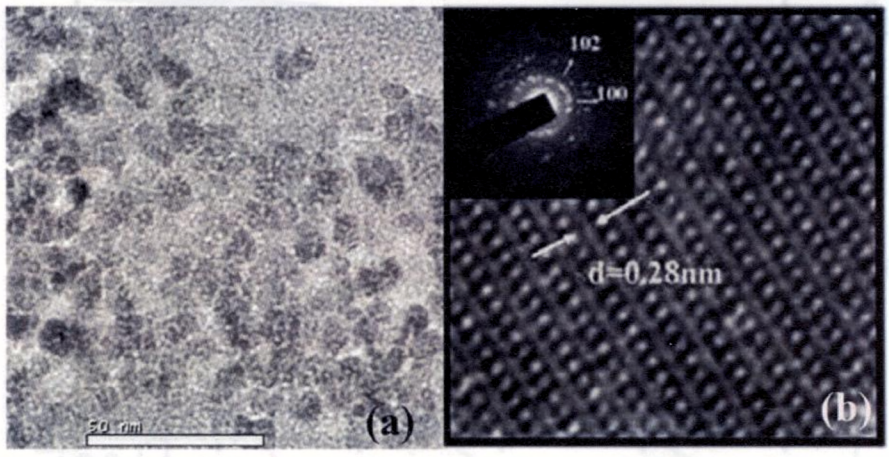

Figure 4.4 (a) TEM and (b) HRTEM images of ZnO nanoparticles prepared at 0.2M NaOH showing parallel lines of atoms at regular intervals (inset shows SAED pattern).

The transmission spectrum of the ZnO:PMMA films are compared with that of pure PMMA film (figure 4.5). It shows the transparency of the ZnO:PMMA film is above 60% in the visible region. Inset of the figure 4.5 shows the photograph of the ZnO:PMMA thin films with the writing beneath it.

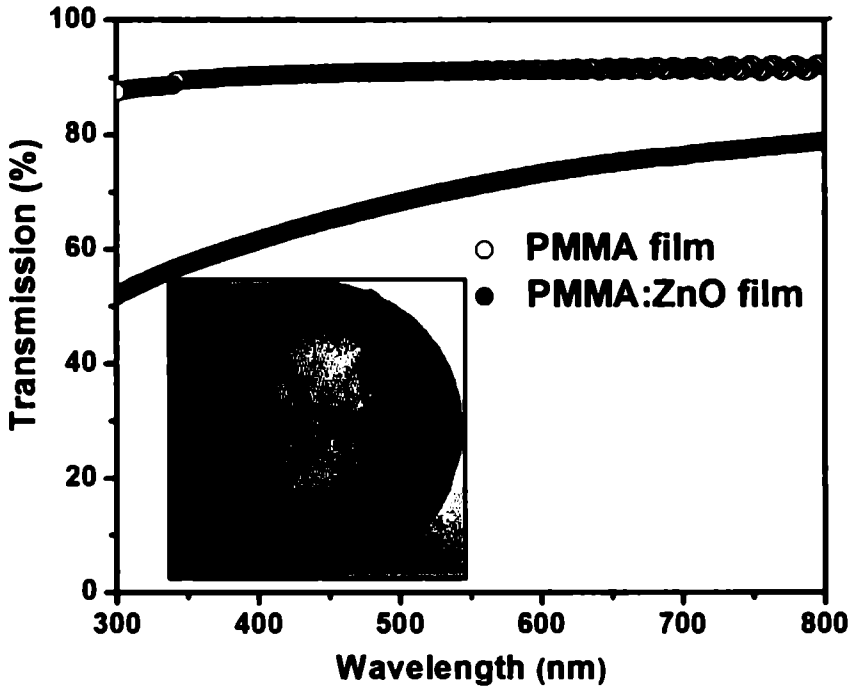

Figure 4.5. The transmission spectra of ZnO:PMMA and pure PMMA thin films (inset shows the photograph of ZnO:PMMA films with the writing beneath the film).

The UV-visible absorption spectra of the ZnO nanoparticles in methanol are shown in figure 4.6. The absorption in the ZnO above λ=370nm corresponds to the band-to-band transition. An increase in the band gap with decrease in particle size is observed which is attributed to the quantum size effect [11]. The band gap of ZnO nanoparticles prepared with various NaOH concentration increases as the concentration of NaOH

(figure 4.7) decreases in the reaction mixture. Second peaks at 420nm are sub–band transition due to the interstitial zinc and zinc vacancy [12].

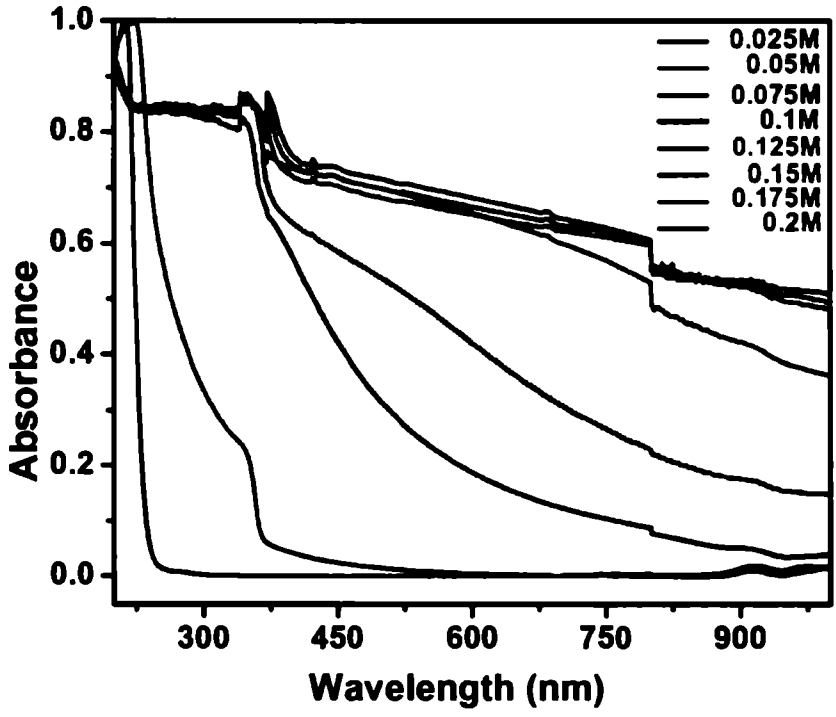

Figure 4.6. UV-visible absorption spectra of ZnO colloidal solution prepared at various NaOH concentrations.

The average particle size can be deduced from the absorption spectra using eqn.(4.1). Here the pronounced dependence of the band gap on the size of ZnO nanocrystals is used to determine the particle size [13]. The band gap is calculated from the point of inflection of the first derivative

curve of the absorption spectra. The difference in the value of band gap of the ZnO nanoparticles with respect to bulk ZnO, ΔE_g is found. From the ΔE_g, the particle size, d, is determined [13] using eqn.(4.1),

$$\Delta E_g = 100(18.1d^2 + 41.4d - 0.8)^{-1} \quad (4.1)$$

The particle size shows a progressive decrease from 10nm to 2.9nm with the decrease in concentration of NaOH from 0.2M to 0.025M (figure 4.7).

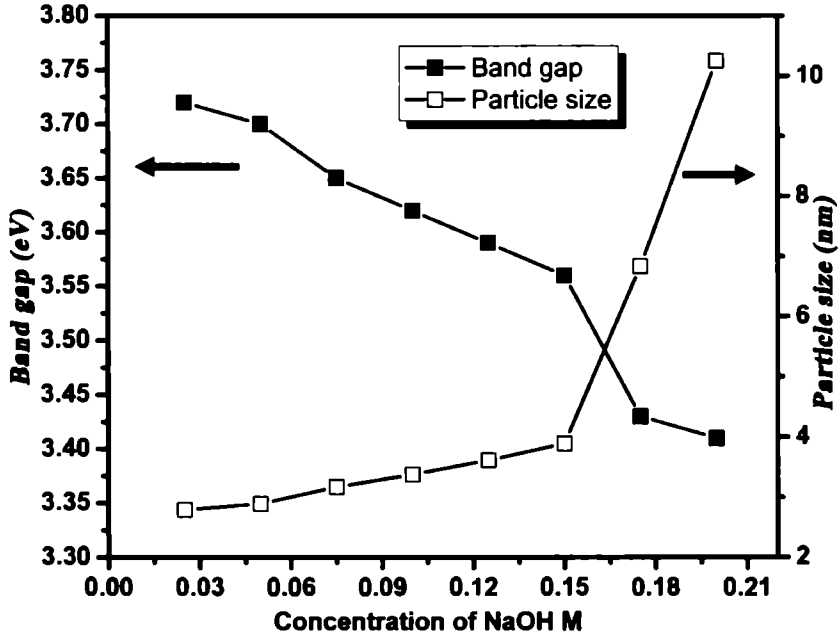

Figure 4.7. Dependence of band gap and particle size of ZnO nanoparticle on the NaOH concentration in the reaction mixture.

The figure 4.8 shows that the concentration of the ZnO nanoparticles synthesized decreases with increase of the concentration of NaOH in the reaction mixture. Therefore the lower concentration of ZnO nanoparticles results in lower absorption at higher wavelengths in larger sized nanoparticles.

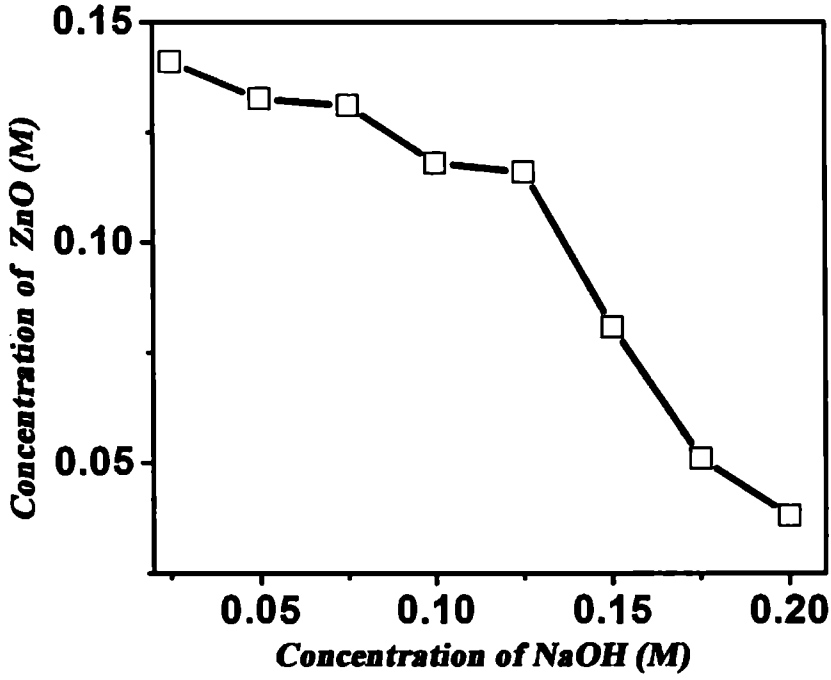

Figure 4.8. Variation in the concentration of ZnO nanoparticles produced at various NaOH concentrations.

Generally the PL spectra of ZnO contains one emission peak in the UV region attributed to the free excitons and one or more emission peaks in

the visible region which is attributed to the defects in ZnO. The PL spectra of ZnO nanoparticles shown in figure 4.9 have emission bands in the UV and visible regions for excitation at 325 nm. Efficient UV emission near band edge is attributed to free exciton emission with high electronic density of states, which shift to higher energies due to the reduction in nanoparticle size as the NaOH concentration in the reaction mixture is decreased. As the particle size decreases, due to the quantum confinement, the energy levels of the conduction and valence bands shift apart, giving rise to a blue shift in the PL exciton emission [14]. The emission in the visible region is related to the defects in the ZnO [15]. The green emission at 532nm is commonly attributed to oxygen interstitial [16]. The energy levels involved in the PL emission are shown in the inset of figure 4.9. Blue emissions at 468nm correspond to the electron transition from the shallow donor level of zinc interstitials to the valence band [17]. Therefore the blue emission would be originating from the electron transition from the bottom of the conduction band to an acceptor level (caused by Zn vacancy) [18].

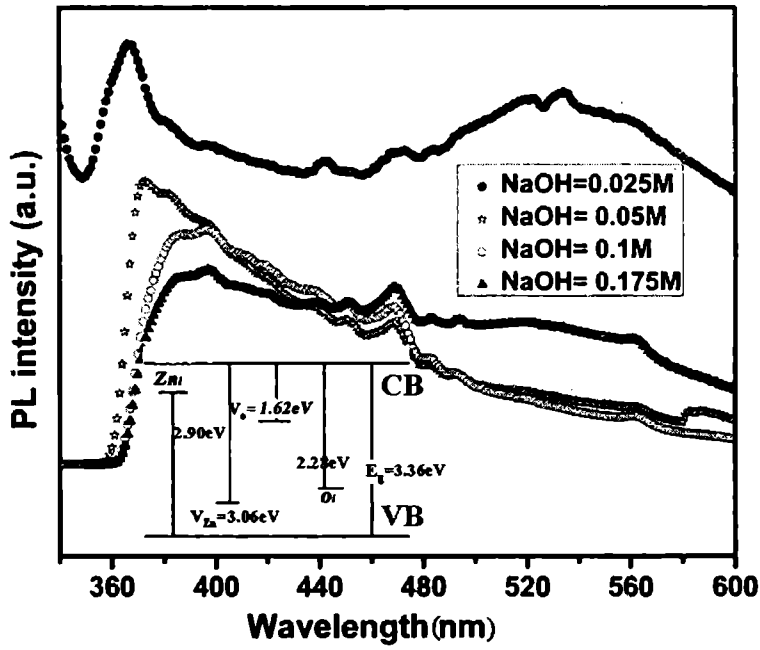

Figure 4.9. PL emission spectra of ZnO:Na nanoparticles prepared at various concentration of NaOH ((inset shows the energy level and transition of PL emission in ZnO, where Zn_i ,O_i, V_o, V_{Zn} represents zinc interstitial , oxygen interstitial , oxygen vacancy and zinc vacancy respectively).

Optical nonlinearities of ZnO:PMMA films were measured using single beam Z-scan technique. Figure 4.10 gives the open aperture Z-scan traces of ZnO:PMMA films (which contains ZnO nanoparticles having different particle sizes and hence different band gap) at laser irradiance of 0.325J/cm^2 which shows that the samples can be best used for optical limiting applications. That means all films show a decrease in transmission with increase in the input laser fluence.

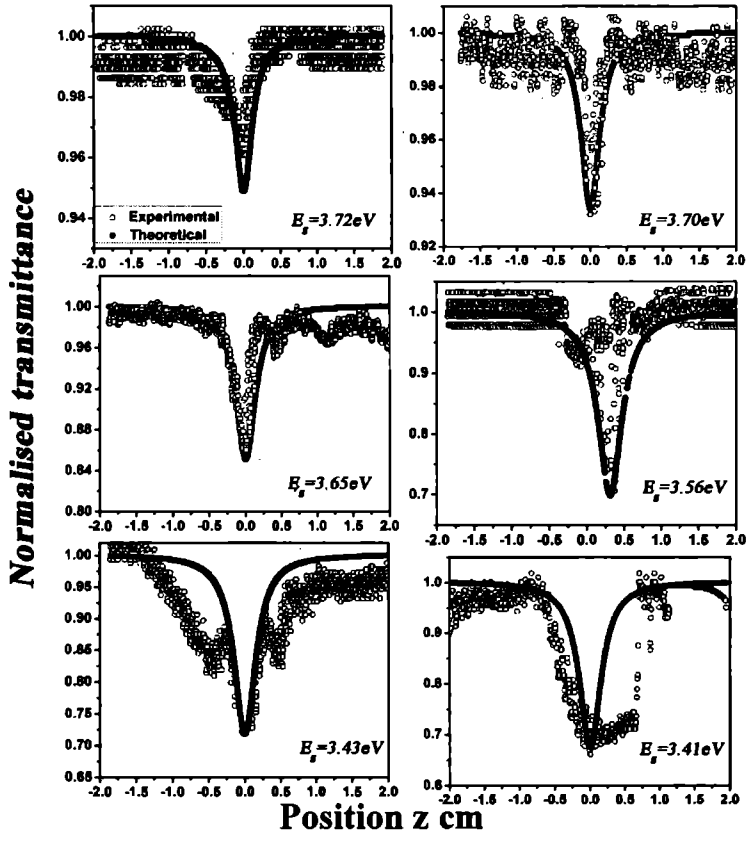

Figure 4.10. Open aperture Z-scan traces of the ZnO:PMMA films containing ZnO nanoparticles having different band gap (E_g) at laser irradiance of 0.325J/cm^2.

Here the optical limiting curve fits to a two photon absorption transition between the valence and conduction band given by the theoretical eqn.(4.2) using Shake Bahae formalism,

$$T(z,S=1)=\frac{1}{\sqrt{\pi}q_0(z,0)}.\int \ln\left[1+q_0(z,0)e^{-\tau^2}\right]d\tau \qquad (4.2)$$

where $q_o(z,0)=\beta I_0 L_{eff}$ and β is the two photon absorption coefficient, L_{eff} is given by $\frac{\left(1-e^{-\alpha L}\right)}{\alpha}$ where L is the sample length, α is the linear absorption coefficient I_0 is the incident irradiance at z=0 [8].

From the open aperture Z-scan curves, it is found that as the band gap decreases (increase in particle size), the rate of two photon absorption increases which is attributed to an inverse proportionality between β and third power of band gap E_g^3 [19] and enhancement in the nonlinear susceptibility due to enhanced oscillator strength with particle size [20]. Hence the dip in the open aperture curve increases with increase in particle size such that, the observed increase in the limiting efficiency with increase in the particle size (decrease in band gap) resulted. The value of the nonlinear absorption coefficient β taken using Shake Bahae eqn.(4.2) ranges from 21cm/GW to 682cm/GW as the band gap decreases from 3.72eV to 3.41eV. It is also found that the experimental curves deviate from the theoretical equations using Shake Bahae formalism for thin films containing larger sized nanoparticles (E_g=3.43eV and E_g=3.41eV) prepared at larger NaOH concentration. The nanoparticles with E_g=3.43eV show a shift from reverse saturable absorption (RSA) to saturable absorption (SA) and again back to RSA behaviour which is a fifth order nonlinear process [21]. In larger nanoparticles, there is chance for two photon absorption induced free carrier absorption [22]. This leads to broadening of the open aperture curve

in particles prepared with larger concentration of NaOH. However detailed studies are needed to evaluate the exact phenomena behind the curve broadening.

Figure 4.11 gives the closed aperture Z-scan curves at laser irradiance of 0.325J/cm^2.

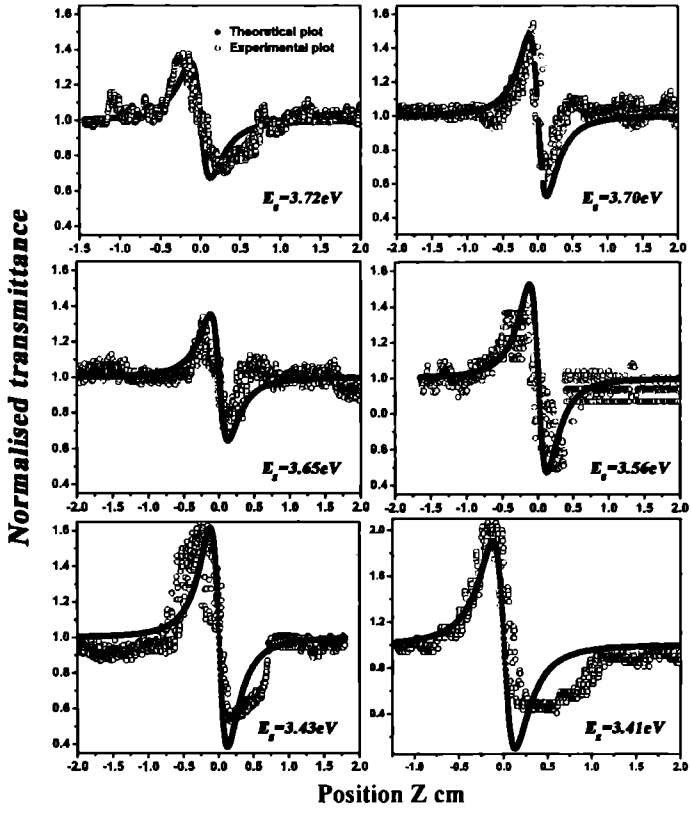

Figure 4.11. Closed aperture Z-scan traces of the ZnO: PMMA films containing ZnO nanoparticles having different band gap (E_g) at laser irradiance of 0.325J/cm^2.

Since in materials having both refractive and absorptive nonlinearity closed aperture measurements have contribution from both. So the closed aperture Z-scan data of these samples are divided with the open aperture data in order to eliminate the effect of nonlinear absorption and the resulting curves are fitted with the theoretical equation for pure nonlinear refraction eqn.(4.3) and the value of the nonlinear refractive index γ corresponding to best theoretical fit is found. The aperture linear transmittance $S = 1 - e^{\left(\frac{-2r_a^2}{w_a^2}\right)}$ is taken as S=0.35 in this case.

The on axis phase shift at the focus $\Delta\phi_0$ can be obtained through the best theoretical fit from the normalized closed aperture transmittance [8, 23]. The theoretical equation for the normalized Z-scan transmittance $T(z,\Delta\phi_0)$ is given by eqn.(4.3),

$$T(z,\Delta\phi_0) \approx [1 - \frac{4\Delta\phi_0 x}{(x^2+9)(x^2+1)}] \tag{4.3}$$

where $x = \frac{z}{z_0}$ and $\Delta\phi_0$ =+ve and $\Delta\phi_0$ =-ve respectively for self focussing and self defocusing type refractive nonlinearity.

The nonlinear refractive index can be calculated from the following eqns. (4.4) and (4.5),

$$\gamma = \frac{\lambda\Delta\phi_0}{2L_{eff}I_0} \tag{4.4}$$

$$n_2(esu) = \frac{cn_0\gamma}{40\pi} m^2/W \tag{4.5}$$

The peak to valley shape of the curves indicates a negative value of refractive index. The deviation of the experimental closed aperture curve from the theoretical plot is attributed to the small variation in the Guassian shape of the laser pulse. Obviously from figure 4.11, the thin films containing larger sized nanoparticles (E_g=3.43eV and E_g=3.41eV) shows very large nonlinear phase change $\Delta\phi_0$ causing the experimental curves to deviate from the Shake Bahae eqn. (4.3). This larger phase change may be due to two photon generated free carrier refraction in higher sized nanoparticles which is a fifth order nonlinear process [24]. However detailed analysis may be required in order to exactly determine which mechanism is responsible for the discrepancy in the shape of the closed aperture curve. The energy loss of the incident laser pulses due to Fresnel reflection by the surfaces of ZnO:PMMA film in the Z-scan analysis is not considered [25].

The value of the nonlinear absorption cross section (σ_{TPA}) is related to nonlinear absorption coefficient (β) [26] as given by eqn. (4.6),

$$\sigma_{TPA} = \frac{\omega\beta h}{2\pi N} \tag{4.6}$$

where N is the concentration of the ZnO molecules per cm^3 and $\frac{h\omega}{2\pi}$ is the exciting photon energy. The cross section σ_{TPA} is expressed in Geopert Mayer units where 1 GM = 10^{-50} cm^4 s $phot^{-1}$ mol^{-1}. The variation of the nonlinear absorption cross section with particle size is plotted in figure 4.12. Obviously the nonlinear absorption cross section is found to increase with increase in the particle size (decrease in band gap).

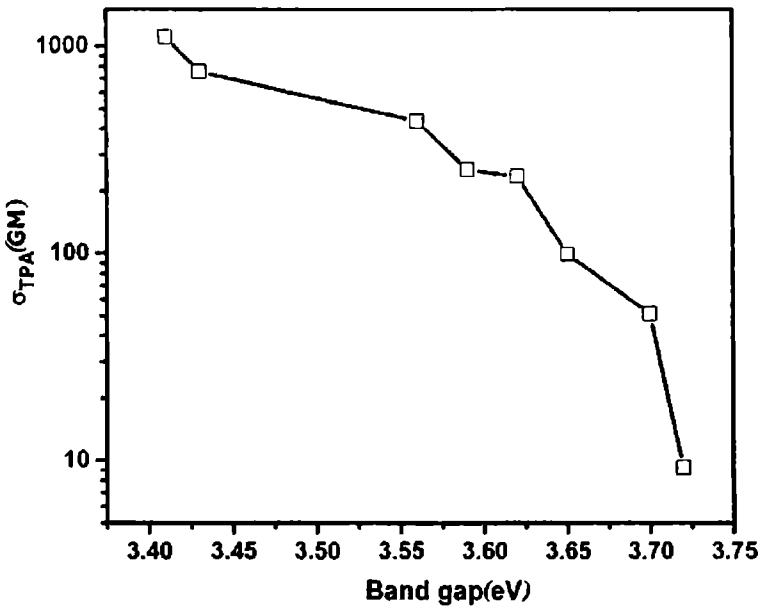

Figure 4.12. The two photon absorption cross section versus the band gap of the ZnO nanoparticles.

It is observed that the efficiency of nonlinear refraction increases with decrease in band gap or increase in the particle size. The enhancement in the nonlinear refractive index with increase in particle size is attributed to the size dependent enhancement of the oscillator strength of the coherently generated excitons [26, 27]. Confinement of the excitons in the ZnO nanoparticle leads to the enhancement of oscillator strength per nanoparticle by a factor $\frac{R^3}{a_b^3}$ where R is the radius of the nanoparticle and a_B is the exciton Bohr radius. The value of n_2 is found to be varying from -0.47

$\times 10^{-7}$esu to -4.159×10^{-7}esu when the band gap varies from 3.72eV to 3.41eV. The variation of the particle size, band gap, concentration, TPA coefficient and TPA cross section of ZnO with NaOH concentration in the reaction mixture is shown in the table 4.1.

Concentration of NaOH (M)	Particle size (nm)	Band gap (eV)	Concentration of ZnO (M)	β (cm/GW)	σ_{TPA} (GM)
0.025	2.79	3.72	0.141	21.1	9.28
0.05	2.89	3.7	0.133	109.3	51.1
0.075	3.17	3.65	0.131	210.7	99.6
0.1	3.37	3.62	0.118	448.5	236
0.125	3.61	3.59	0.116	475.8	254
0.15	3.81	3.56	0.081	567	436
0.175	6.83	3.43	0.051	622	755
0.2	10.25	3.41	0.038	682	1110

Table 4.1. Variation of the particle size, band gap, concentration, TPA coefficient and TPA cross section of ZnO nanoparticles with NaOH concentration in the reaction mixture.

Therefore the high value of nonlinear coefficients enables the use of ZnO:PMMA as a potential nanocomposite material for the development of nonlinear optical devices with a relatively small limiting threshold. The mechanical properties of the polymer films enable its use for device fabrication as compared to ZnO nanoparticles dispersed in a solution. The nanoparticles in solution are unstable and settle down with ageing, the

quantum dots embedded in PMMA matrix are extra stable and hence stable optical devices can be fabricated.

4.4. Conclusions

ZnO nanoparticles embedded in PMMA matrix are prepared by wet chemical synthesis. The band gap of the samples shows a decrease with increase in concentration of NaOH in the reaction mixture indicating an increase in particle size. The photoluminescence spectra of the ZnO colloids show strong UV emission attributed to exciton emission and the strong green and blue emissions attributed to the defect emission in the ZnO. The optical absorptive nonlinearity of the ZnO:PMMA thin films are analyzed using open aperture Z-scan technique which shows optical limiting type nonlinearity which is due to the two photon absorption in ZnO. Broadening of the open aperture curve is observed in particles prepared with larger concentration of NaOH. This deviation from the theoretical curve of two photon process in ZnO:PMMA films containing larger sized nanoparticles is attributed to two photon absorption induced free carrier absorption. The efficiency of nonlinear absorption is found to increase with increase in the band gap. The nonlinear refraction in the ZnO:PMMA shows a self-defocusing type; ie, a negative value of nonlinear refractive index (n_2). The value of nonlinear absorption coefficient as well as refractive index are found to be increasing with increase in particle size. The enhancement in the n_2 and β is attributed to the enhanced oscillator strength in bigger nanoparticles. The mechanical properties of the polymer films enable its use for device

fabrication as compared to ZnO quantum dots dispersed in a solution. Stability of the nanoparticles embedded in the PMMA matrix is more as compared to the ZnO nanoparticles dispersed in solution.

4.5. References

1. J. C. Johnson, K. P. Knutsen, H. Q. Yan, M. Law, Y. F. Zhang, P. D. Yang and R. J. Saykally, Nano Lett. **4** 197 (2004)
2. C. K. Sun, S. Z. Sun, K. H. Lin, K. Y. J. Zhang, H. L. Liu, S. C. Liu and J. J. Wu, Appl. Phys. Lett. **87** 23106 (2005)
3. J. H. Lin, Y. J. Chen, H. Y. Lin and W. F. Hsieh, J. Appl. Phys. **97** 33526 (2005)
4. U. Ozgur, Y. I. Alivov, C. Liu, A. Teke, M. A. Reshchikov, S. Dogan, V. Avrutin, S. J. Cho and H.Morkoc, J. Appl. Phys. **98** 41301 (2005)
5. A. Villeneuve, C. C. Yang, P. G. J. Wigley, G. I. Stegeman, J. S. Aitchison and C. N. Ironside, Appl. Phys. Lett. **61** 147 (1992)
6. C. C. Yang, A. Villeneuve, G. I. Stegeman and J. S. Aitchison, Opt. Lett. **17** 710 (1992)
7. A. Major, F. Yoshino, J. S. Aitchison, P. W. E. Smith, E. Sorokin and I. T. Sorokina, Appl. Phys. Lett. **85** 4606 (2004)
8. M. S. Bahae, A. A. Said, T. Wei, D. J. Hagan and E. W. Van Stryland, IEEE J. Quant. Electron. **26** 760 (1990)
9. B. Vinitha, K. Manzoor, R. S. Ajimsha, P. M. Aneesh and M. K. Jayaraj, Synthesis and Reactivity in Inorganic, Metal-Organic, and Nano-Metal Chemistry **38** 126 (2008)

10. P. E. J. Flewitt and R. K. Wild, Physical methods for material characterization, 2nd edn, IOP Publicating ltd, Philadelphia (2003)
11. S. Furukawa and T. Miyasato, Phys. Rev. B **38** 5726 (1988)
12. X. M. Fan, J. S. Lian, L. Zhao and Y. H. Liu, Appl. Surf. Sci. **252** 420 (2005)
13. R. Viswanatha, S. Sapra, B. Satpati, P. V. Satyam, B. N. Dev and D. D. Sharma, J. Mater. Chem. **14** 661 (2004)
14. K. F. Lin , H. M. Cheng, H. C. Hsu , L. J. Lin and W. F. Hsieh, Chem. Phys. Lett. **409** 208 (2005)
15. S. H. Jeong, J. Kim and B. T. Lee, J. Phys. D: Appl. Phys. **36** 201 (2003)
16. J. Bang, H. Yang and P. H. Holloway, Nanotechnology **17** 973 (2006)
17. D. H. Zhang, Z. Y. Xue and Q. P.Wang, J. Phys. D: Appl. Phys. **35** 2837 (2002)
18. N. Zhaoyuan and L. Huoquan, Plasma Sci. Tech. **7** 2665 (2005)
19. L. W. Tutt and T. F. Boggess, Prog. Quanta Electr. **17** 299 (1993)
20. E. Hanamura, Phys. Rev. B **42** 1724 (1990)
21. P.Premkiran, D.R .Reddy, B.G. Maiya, A.K. Dharmadhikari, G.R. Kumar and D.N Rao, Opt. Commun. **252** 150 (2005)
22. X. J. Zhang, W. Ji and S. H. Tang , J. Opt. Soc. Am. B **14** 1951 (1997)
23. J. Zheng, Y. Guo, X. Li, G. Zhang and W. Chen, J. Opt. A: Pure Appl. Opt. **8** 835 (2006)
24. X. Zhang, H. Fang, S. Tang and W. Ji, Appl. Phys. B **65** 549 (1997)
25. E. Hecht, Optics, 4th edn., Addison Wesley, Eugene (2002)

26. S. S. Chunosova, V. A. Svetlichnyi, Y. P. Meshalk, Quant. Electron. **35** 415 (2005)

27. W. Zhang, H. Wang, K. S. Wong, Z. K. Tang , G. K. L. Wong and J. Ravinder, Appl. Phys. Lett. **85** 1601 (2004)

28. S. Sapra and D. D. Sharma, Phys. Rev. B **69** 125304 (2004)

Chapter 5

Ultrafast optical nonlinearity of luminescent ZnS:Cu nanoparticles embedded in PVA matrix

5.1. Introduction

Semiconductor nanocrystals have attracted widespread attention owing to their distinct optical and electronic properties that can be tuned by the quantum size effect. When the particle size is reduced below the Bohr exciton radius these particles show a quantum confinement effect due to localization of charge carriers, so that they are called as quantum dots. Quantum dots are considered [1] to be very relevant candidates for optoelectronic devices of the future due to their nonlinear optical properties, increased quantum efficiency for luminescence, etc. Several attempts have been made in order to improve the photoluminescence performance of nanocrystals for many applications, including flat-panel displays, photoluminescent or electroluminescent devices, infrared windows and solar cells [2–5].

ZnS is a typical wide-gap II–VI semiconductor with an energy gap of 3.7eV [6]. Since the early 1980s, considerable research work on ZnS nanocolloids and their optical properties has been reported [7, 8]. Bhargava *et al* [9] gave the first report on the luminescence properties of Mn doped ZnS nanocrystals that were synthesised through a room temperature chemical process. Since then, a few reports have appeared investigating the photoluminescence properties of Mn doped ZnS nanocrystals [10] and Cu doped ZnS nanocrystals [11] through various techniques. Doping of ZnS nanoparticles by transition metal ions, e.g. Mn^{2+} [12, 13], Cu^{2+} [14, 15] and rare earth ions, e.g. Eu^{2+} [16, 17] have been successfully carried out by

techniques such as thermal evaporation, sol gel processing, co-precipitation, and micro emulsification.

In the case of nanosized ZnS, the photoluminescence properties are still controversial. Blue and green luminescence emission bands have often been observed together in the same sample, such as at 420nm and 520nm by Lee *et al* [15] and at 460nm and 507nm by Xu *et al* [17]. On the other hand, a single emission peak has been reported at 480nm by Khosravi *et al* [14] while Huang *et al* observed a single emission peak at 415nm [18]. Recently, Bol *et al* reported a red emission peak at 600nm in ZnS:Cu nanoparticles and assigned it to the recombination of deeply trapped electron with Cu^{2+} [19]. Therefore the role of dopant concentration on optical properties of doped semiconductor nanoparticles is very important from the view points of basic physics as well as practical application. In the present work, we have synthesised ZnS:Cu nanoparticles and studied the influence of copper in widening the band gap thereby enhancing the photoluminescence and nonlinear optical properties of ZnS nanoparticles.

5.2. Experimental

ZnS:Cu nanoparticles were prepared at room temperature by wet chemical route without any capping agents, using 0.1 mol of zinc chloride and 0.07M Na_2S. The doping concentration of Cu was varied from 1 to 3 atomic weight percentage. The reaction mixture in aqueous solution was stirred for 1.5 hours. The chemical reaction involved is as follows,

$$(1\text{-}x)ZnCl_2 + Na_2S + xCuCl_2 \rightarrow Zn_{(1-x)}Cu_xS + 2NaCl$$

The photoluminescence spectra of the as prepared colloidal solutions were recorded using flourimeter. The ZnS:Cu colloidal solution was filtered to get fine ZnS:Cu powder for the X–ray diffraction (XRD) studies and diffused reflectance spectroscopy (DRS). The XRD patterns were recorded using Rigaku DMAX-C X-ray diffractometer. The diffused reflectance spectra of the ZnS:Cu powders were measured using JASCO V570 spectrophotometer. The sizes of the nanoparticles were verified by transmission electron microscopy (TEM). ZnS:Cu poly vinyl alcohol nanocomposite film fabricated by spin coating was used for nonlinear optical studies. 4 gms of poly vinyl alcohol (PVA) was mixed with 50 ml of water and was stirred until it dissolves homogenously. 1.6 gm of the ZnS:Cu powder is added to the PVA solution (5ml) and stirred again for one hour. The resulting viscous solution was spin coated on a glass plate at a rotation speed of 1000rpm so as to get a thin film. The nonlinear absorption of the nanoparticle embedded polymeric thin films was analyzed using open aperture Z-scan technique employing ultrafast laser pulses of 100fs duration at 800nm from a Ti:Saphire laser.

5.3. Results and discussion

The XRD pattern (Figure 5.1) of pure ZnS and ZnS:Cu powder synthesized by wet chemical method exhibits a higher full width at half maximum (FWHM) compared to the bulk commercial ZnS, which indicates the formation of nanoparticles. The patterns of all the powder samples indicate the formation of ZnS phase with the cubic zinc blende (sphalerite)

structure. The prominent peaks due to (200) (θ=33.15°, d=2.70A°) and (222) (θ=58.353°, *d*=1.56 A°) planes were observed in the XRD pattern. A splitting of the (200) peak occurs on Cu doping, which is due to the latuce deformation produced with the addition of Cu.

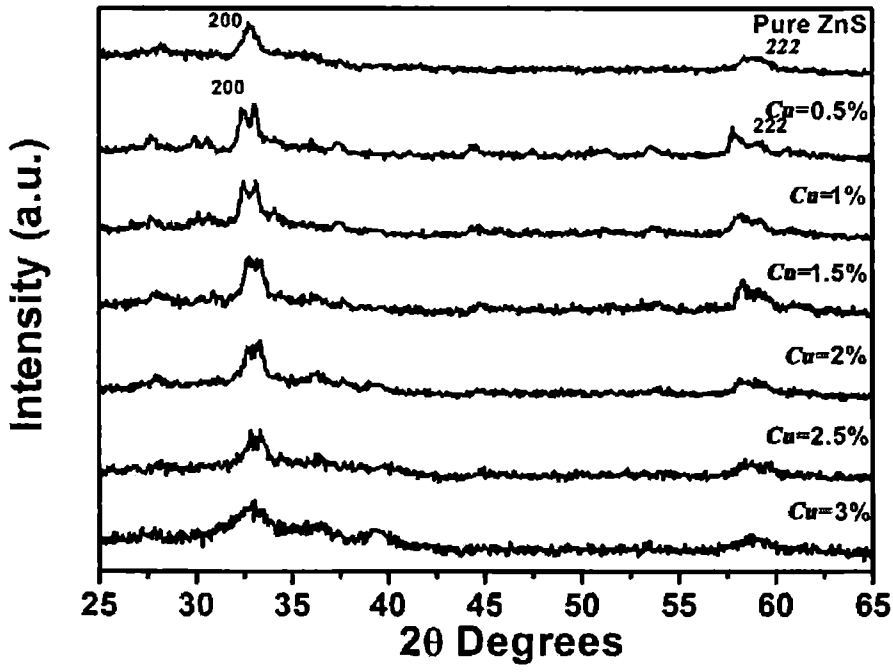

Figure 5.1. The XRD pattern of the pure and copper doped ZnS powder.

The high resolution TEM (HRTEM) image and selected area electron diffraction (SAED) pattern of ZnS:Cu nanoparticles with x=0.01 is shown in figure 5.2(a) and 5.2(b). The SAED exhibits a concentric diffused ring pattern due to the nanocrystalline nature of ZnS:Cu [20]. TEM analysis of the ZnS:Cu reveals the formation of nanoparticle with size 6 nm.

HRTEM shows parallel lines of atoms at regular intervals of $2.7A^0$ which coincides with the d spacing corresponding to the (200) planes of ZnS. The d values obtained from the SAED confirm the formation of (200) and (222) planes of ZnS.

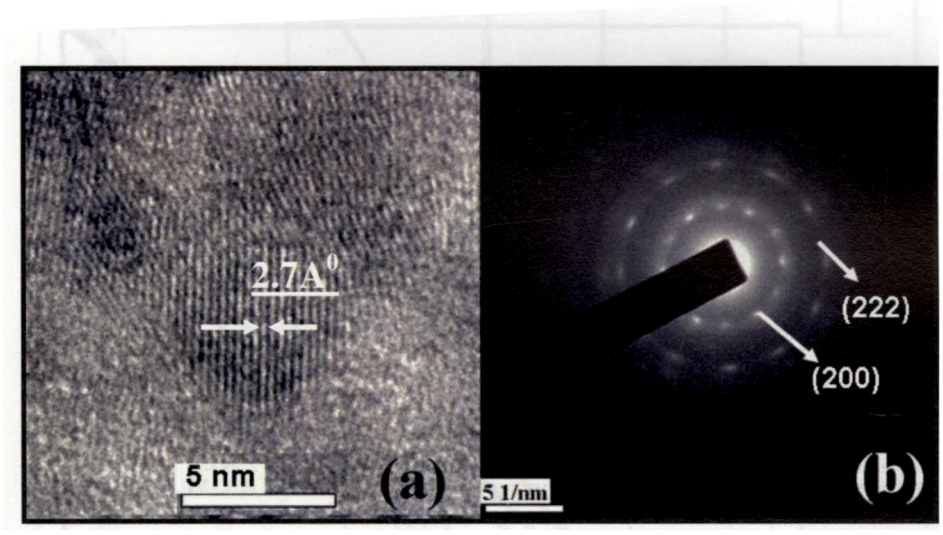

Figure 5.2. The HRTEM and SAED pattern of the ZnS:Cu nanoparticles with x=0.01.

The band gap for the ZnS:Cu nanoparticles is found from the Kubelka-Munk plots as shown in figure 5.3. Compared to the band gap of bulk sphalerite ZnS (3.67eV) [21], the synthesised ZnS:Cu nanoparticles displayed an increase in the band gap which indicates the formation of the nanocrystals. Also a systematic increase in the band gap (3.88eV to 4.25eV) with increase in the copper doping concentration is observed which is attributed to the shifting apart of the valence and conduction bands, due to

the formation of impurity levels in between. This kind of increase in band gap with increase in the copper doping concentration has been reported by Manzoor *et al* [22].

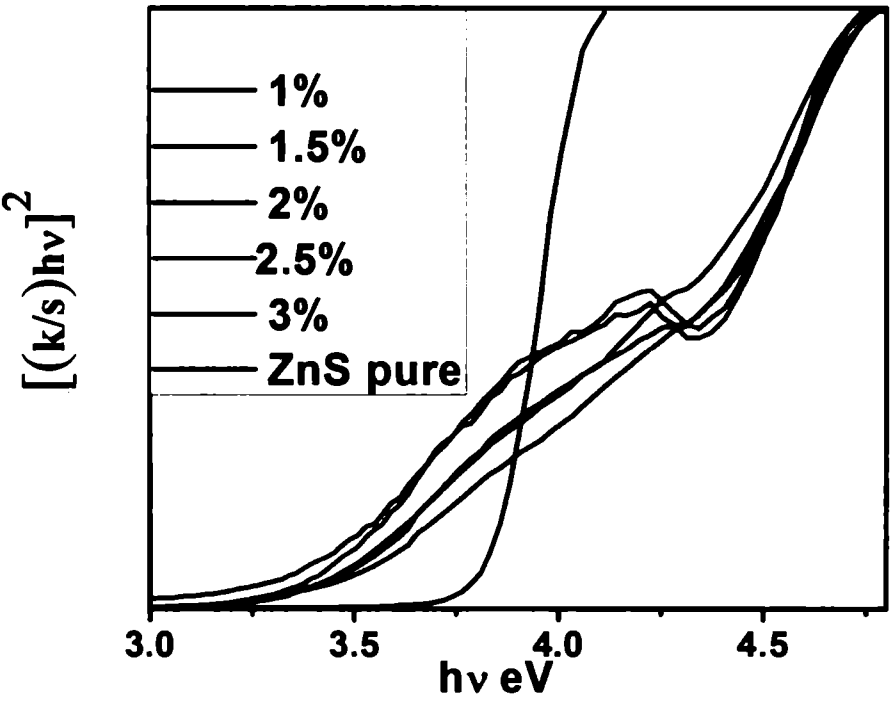

Figure 5.3. The Kubelka-Munk plots reduced from the diffused reflectance spectra.

Figure 5.4 schematically illustrates the band gap widening associated with Cu^{2+} doping, and the electronic transitions involved in the excitation and emission processes.

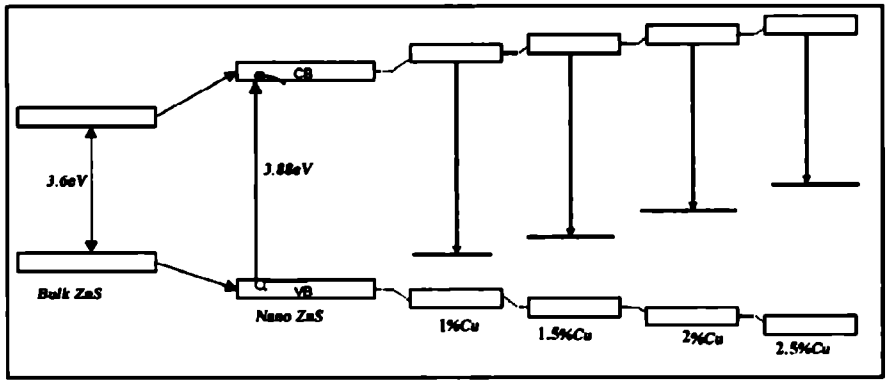

Figure 5.4. Schematic diagram showing the band gap widening in Cu doped ZnS nanoparticles.

The photoluminescence emission of the pure ZnS nanoparticles is shown in figure 5.5 and inset shows the PL excitation spectra. The undoped ZnS shows excitation peak at 318nm corresponding to the band-to-band electronic excitation. PL emission from the pure ZnS (λ_{ex}=318nm) shows a blue emission peak at 434nm which is attributed to the sulphur vacancies. For low concentrations of sulfide ions during precipitation, the ZnS nanoparticles formed will have a large number of sulfur vacancies $(V_S)^{2+}$ [22]. Bearing a charge of 2^+, the V_S sites can effectively trap excited electrons from the conduction band and act as a doubly ionized donor by forming a shallow energy level below the conduction band (CB) edge. Subsequent electron–hole (e–h) recombinations at the valence band lead to blue emissions, referred to as 'self-activated' emission in nanosized ZnS.

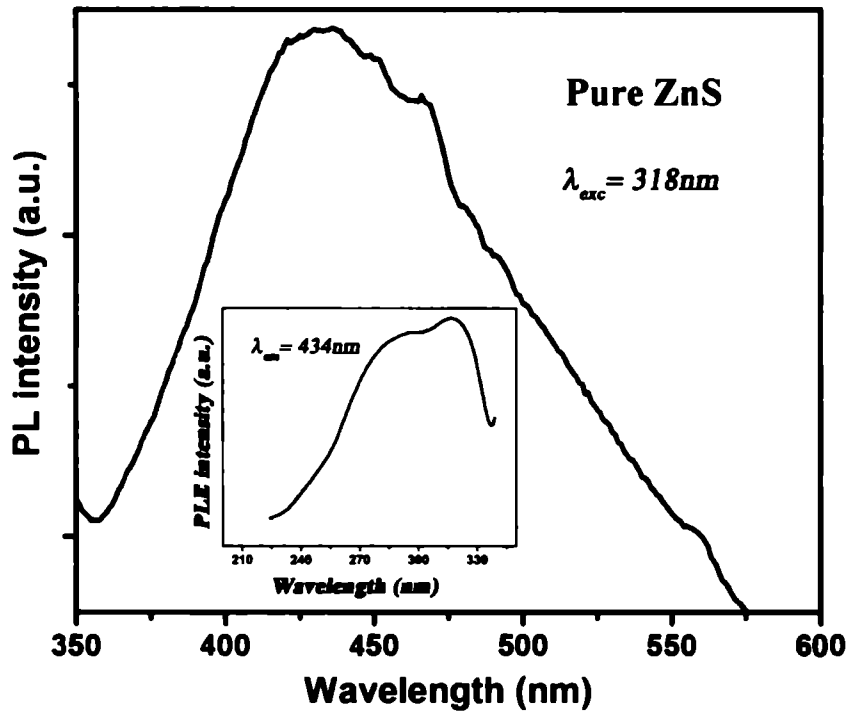

Figure 5.5. The photoluminescence emission spectra of pure ZnS (Inset shows the corresponding excitation spectra).

In doped nanoparticles a larger numbers of dopant centers are situated near the surface than in the interiors, and therefore nanoparticles are expected to have better luminescent emission efficiencies compared to their bulk counterparts. The photoluminescence emission of the ZnS:Cu nanoparticles is shown in figure 5.6. The green photoluminescence emission (λ_{ex}=375nm) arises from the recombination between the shallow donor level (sulphur vacancy) and the t_2 level of Cu^{2+}.

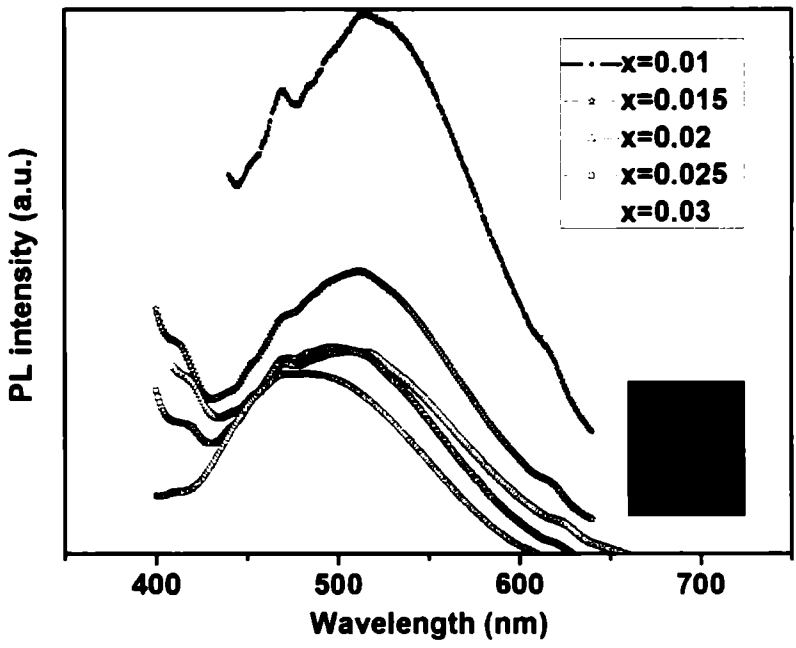

Figure 5.6. PL emission of Cu doped ZnS nanocolloids (Inset shows the green luminescence from ZnS:Cu nanocolloids).

With the incorporation of Cu^{2+} pairs, the V_S-related 434 nm peak is completely quenched at the expense of green emissions, indicating the formation of impurity-related new energy levels within the band-gap of nanoparticles. The PL emission maxima shows a blue shift in wavelength with increase in the dopant percentage indicating widening in the separation between the copper acceptor levels and the V_S donor levels; which also supports the widening of band gap with increase in the copper doping.

When the doping concentration is increased, the luminescence intensity observed to be diminished which is caused by the formation of CuS, though the XRD measurement did not detect the existence of the copper sulfide phase [23, 24]. The reason for the reduced emission is that the formation of CuS particles will effectively reduce the number of Cu^{2+} optically active luminescencent centers in ZnS nanoparticles. The formation of CuS can be detected with the change in colour observed for the powder from white to grey when the Cu doping percentage is increased. The schematic energy level diagram of ZnS:Cu nanoparticles and the mechanism of PL emission is depicted in Fig. 5.7.

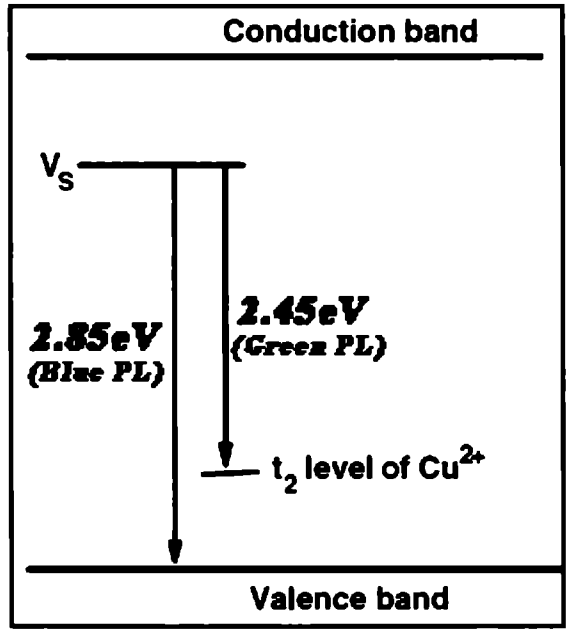

Figure 5.7. Schematic energy level diagram showing the emission mechanism in ZnS:Cu nanoparticles.

The excitation spectra of ZnS:Cu nanophosphors recorded for the green emission (Figure 5.8) also reveal a new excitation band at 375 nm, indicating that, characteristic intra-band gap electronic transitions are associated with Cu^{2+} substitution for Zn (Cu_{Zn}). As the Cu doping percentage is increased a blue shift in the excitation peak is observed. This suggests widening in the band gap in ZnS nanoparticles doped with higher Cu^{2+} concentrations.

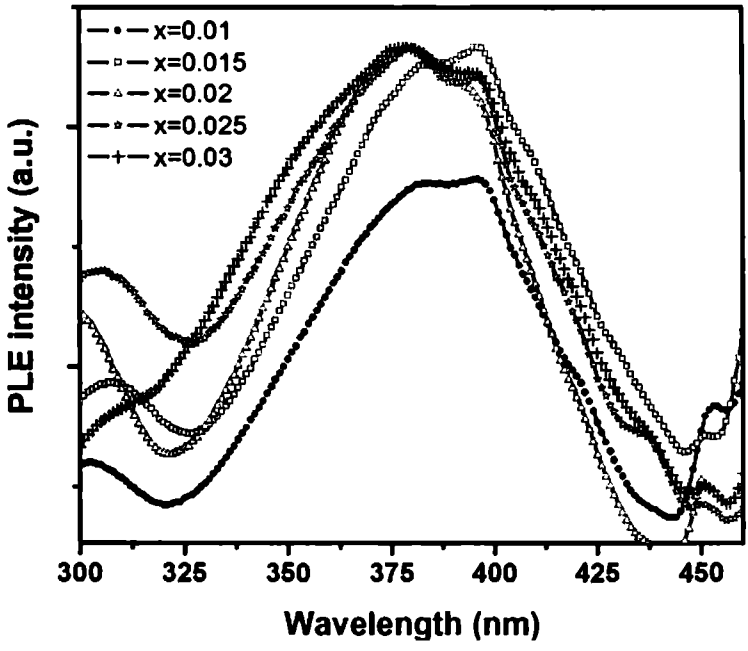

Figure 5.8. The PL excitation spectra of the Cu doped ZnS nanocolloids.

The open aperture *Z*-scan traces taken using ultrafast (100fs) laser pulses at 800nm at an average energy of 17 μJ are shown in figure 5.9(a).

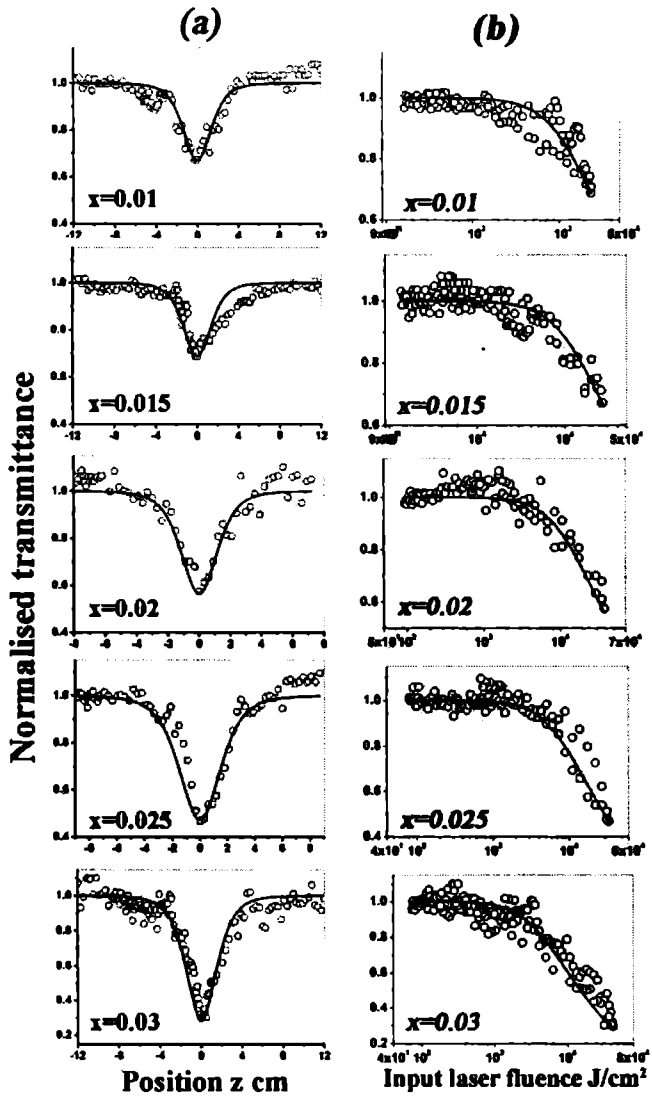

Figure 5.9. Ultrafast (a) open aperture Z-scan traces and (b) optical limiting plots of copper doped (Cu At% varied from 0.01 to 0.03) ZnS nanoparticles.

Figure 5.9(a) clearly shows reverse saturable absorption (RSA) type nonlinearity. Figure 5.9(b) shows the corresponding optical limiting plots. All the samples show a reduction in the transmission with increase in the input laser fluence. The open circles denote experimental data points whereas the solid lines are the theoretical fits. This reduction in transmission at 800nm (1.52eV) is attributed to a three photon absorption process since absorption across the band gap takes place only through the absorption of three photons simultaneously or in multiple steps. The experimental data points fit well to a three photon absorption process as governed by the equation (5.1),

$$T(z) = \frac{(1-R^2)\exp(-\alpha L)}{\sqrt{\pi}\, p_0} \int_{-\infty}^{\infty} \ln\left[\sqrt{1+p_0^2(-2\tau^2)} + p_0 \exp(-\tau^2)\right] d\tau \qquad (5.1)$$

where T is the net transmission of the sample, R is the Fresnel reflection coefficient at the air-sample interface (In our case negligible reflection is occurring and hence R is taken to be zero), α is the linear absorption coefficient, and L is the sample length. p_0 is given by $p_0 = \sqrt{2\gamma(1-R)^2 I_0^2 L_{eff}}$ where γ is the three-photon absorption coefficient, I_0 is the incident intensity and L_{eff} is given by $[1-\exp(-2\alpha L)]/2\alpha$. By numerically fitting the experimental data to eqn.(5.1), the three photon absorption coefficient (γ) can be calculated. The three photon absorption coefficient γ is found to increase with the doping concentration as shown in figure 5.10.

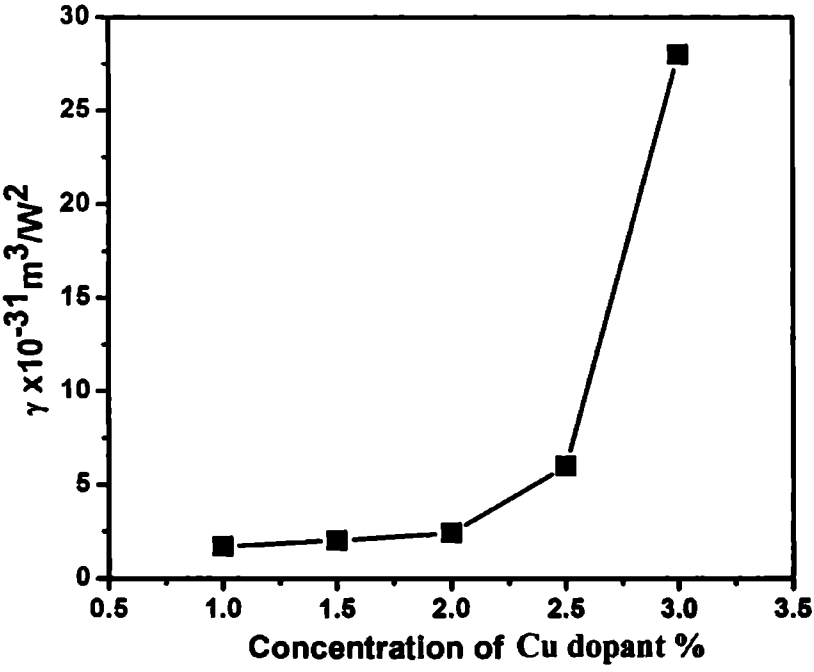

Figure 5.10. Variation of the three photon absorption coefficient γ with the dopant concentration.

Frequency-degenerate three photon absorption is a process wherein three photons, whose energies are the same, are absorbed by the nanoparticle simultaneously through two virtual states to reach the excited state which is strongly band gap dependent. The frequency-degenerate three photon absorption coefficient has been found to decrease with increase in the band gap of the undoped quantum dots (inversely proportional to the 7^{th} power of band gap) as reported earlier [25]. However in the present case, both the band gap (figure 5.3) and the three photon absorption coefficient

(figure 5.10) are found to increase with increase in Cu concentration and therefore the increase in the nonlinear absorption cross section cannot be attributed to the decrease in band gap.

Thus the band gap relation model suggested for frequency-degenerate 3PA in undoped quantum dots is not strictly applicable for doped nanoparticles. This indicates that the relevant mechanism for nonlinear absorption is not the frequency-degenerate three photon absorption occurring in a single step, as expected for undoped quantum dots. The main reason for the reduction in transmission may be the enhancement of three photon absorption by multi step transitions [26]. The intra band gap defect levels (Cu^{2+}) play an intermediary role in enhancing the multi step transitions. These states could mediate multi step excitation processes, which might lead to apparently high value for the 3PA cross section in doped nanocrystals. The density of states is largely dependent on the amount of doping and is increased considerably if a significant amount of dopants is introduced. As the density of the defect levels increases the 3PA cross section will be enhanced thereby increasing the rate of multi step transition enhanced three photon absorption. Therefore the nonlinear absorption enhancement at 800nm in ZnS:Cu with the increase in copper doping may be due to the multi step transition favoured three photon absorption process.

Thus the present experiments show that Cu doped ZnS nanoparticles are efficient ultrafast optical limiting material and when embedded into a PVA matrix it can be a potential device offering protection

from ultrafast laser pulses. The polymer matrix also offers flexibility and mechanical strength.

5.4. Conclusions

ZnS:Cu nanoparticles have been prepared through the wet chemical route in aqueous media. The XRD patterns indicate the formation of ZnS nanoparticles with the cubic zinc blende (Sphalerite) structure. The ZnS:Cu nanoparticles display a systematic increase in the band gap with increase in the copper doping concentration. Green photoluminescence emission is observed in ZnS:Cu which arises from transitions between the sulphur vacancy donor levels and the copper acceptor levels. The PL emission peak and PL excitation peak show a blue shift with increase in the dopant percentage, indicating a widening in the band gap. The open aperture Z-scan traces of the ZnS:Cu nanoparticles embedded in PVA matrix shows a reduction in transmission at higher laser intensities which is attributed to three photon absorption. The reduction in transmission is stronger with increase in the dopant concentration. This increase in the value of the nonlinear absorption coefficient with dopant concentration is due to the enhancement in the density of intermediate defect levels, which plays a significant role in strengthening three photon absorption. Thus Cu doped ZnS nanoparticles in a polymer matrix is found to be a promising candidate for optical limiting applications in the ultrafast time domain.

5.5. References

1. Y. Wang and N. Herron, J. Phys. Chem. **95** 525 (1991)
2. M. Jayalakshmi and M. M. Rao, J. Power Sources **157** 624 (2006)
3. B. Julian, J. Planelles, E. Cordoncillo, P. Escribano, P. Aschehoug, C. Sanchez, B. Viana and F. Pelle, J. Mater. Chem. **16** 4612 (2006)
4. N. Charvet, P. Reiss, A. Roget, A. Dupuis, D. Grunwald, S. Carayon, F. Chandezon and T. Livache, J. Mater. Chem. **14** 2638 (2004)
5. S. Song and Q. Gao, J. Appl. Phys. **99** 106107 (2006)
6. Y. W. Jun, Y. Y. Jung and J. Cheon, J. Am. Chem. Soc. **124** 615 (2002)
7. L. E. Brus, IEEE J. Quant. Electron. **22** (1986) 1909
8. A. Henglein, Electrochemistry II, edited by E. Steckhan, Top. Curr. Chem. **143** Springer, Berlin (1988)
9. R. N. Bhargava, D. Gallagher, X. Hong and A. Nurmikko, Phys. Rev. Lett. **72** 416 (1994)
10. K. Sooklal, B. S. Cullum, S. M. Angel and C. J. Murhy, J. Phys. Chem. **100** 4551 (1996)
11. P. Yang, C. Song, M. Lu, G. Zhou, Z. Yang, D. Xu and D. Yuan, J. Phys. Chem. Solids **63** 639 (2002)
12. B. Y. Geng, L. D. Zhang, G. Z. Wang, T. Xie, Y. G. Zhang and G. W. Meng, Appl. Phys. Lett. **84** 2157 (2004)
13. B. Bhattacharjee, D. Ganguli, K. Iakoubovskii, A. Stesmans and S. Chaudhuri, Bull. Mater. Sci. **25** 175 (2002)
14. A. A. Khosravi, M. Kundu, L. Jatwa, S. K. Deshpande, U. A. Bhagwat, M. Sastry and S. K. Kulkarni, Appl. Phys. Lett. **67** 2702 (1995)

15. S. Lee, D. Song, D. Kim, J. Lee, S. Kim, I. Y. Park and Y. D. Choi, Mater. Lett. **58** 342 (2004)

16. W. Chen, J. O. Malm, V. Zwiller, Y. Huang, S. Liu, R. Wallenberg, J. O. Bovin and L. Samuelson, Phys. Rev. B **61** 11021 (2000)

17. S. J. Xu, S. J. Chua, B. Liu, L. M. Gan, C. H. Chew and G. Q. Xu, Appl. Phys. Lett. **73** 478 (1998)

18. J. Huang, Y. Yang, S. Xue, B. Yang, S. Liu, and J. Shen, Appl. Phys. Lett. **70** 2335 (1997)

19. A. A. Bol, J. Ferwerda, J. A. Bergwerff and A. Meijerink, J. Lumin. **99** 325 (2002)

20. P. E. J. Flewitt and R. K. Wild, Physical Methods for Material Characterization, 2nd edn, IOP Publicating ltd, Philadelphia (2003)

21. S. Shinoya and W. M. Yen, Phosphor Handbook, CRC Press, Washington DC (1999)

22. K. Manzoor, S. R.Vadera, N. Kumar and T. R. N. Kutty, Mater. Chem. Phys. **82** 718 (2003)

23. W. Q. Peng, G. W. Cong, S. C. Qu, Z. G. Wang, Opt. Mater. **29** 313 (2006)

24. H. Bang, S. Morishima, J. Sawahata, J. Seo, M. Takiguchi, M. Tsunemi, K. Akimoto and M. Nomura, Appl. Phys. Lett. **85** 227 (2004)

25. J. U. Kang, A.Villeneuve, M. S. Bahae, G. I. Stegeman, K. A. Hemyari, J. S. Aitchison and C. N. Ironside, Appl. Phys. Lett. **65** 147 (1994)

26. X. B. Feng, G. C. Xing and W. Ji, J. Opt. A: Pure Appl. Opt. **11** 024004 (2009)

Chapter 6

Linear and nonlinear optical characterization of gold and silver nanoparticles prepared by liquid phase pulsed laser ablation

6.1. Introduction

Metal nanoparticles occupy a marvelous field of research interest in the nonlinear optics due to their remarkable properties of Mie resonances [1] and quantum size effects [2]. Nanoparticle metal colloidal solutions of the noble metals (copper, silver and gold) exhibit a very intense colour which is absent in the bulk materials as well as for the individual atoms. This colouration is due to the collective oscillation of the free conduction electrons induced by the interacting electromagnetic fields [3-6]. These resonances are called surface plasmon resonances (SPR). Mie theory and Maxwell Garnet theory [7] explain the SPR band in terms of higher moment oscillations and particle size [8]. It has been proved that the electrical and optical properties are strongly dependent on size and shape of the nanoparticles [9]. A simulation based on quasi-static, scattering and local field theory has been developed to describe the optical properties of gold nanospheres and numerical calculations show that both intensity and wavelength maximum of the absorption, light scattering and fluorescence emission are sensitive to the dielectric constant of the surrounding medium [10].

A number of methods have been proposed to control the size and shape of nanoclusters including chemical reduction, photolysis of metal salts and ultrasonic reduction. However these chemical reduction methods [11-13] produce byproducts which contaminates and affect the stability of the clusters. Ablation of solid targets in liquid media [14] to produce

nanoparticles is advantageous over other methods like the thermal decomposition and ion exchange methods employed for the preparation of solid-state composite materials, due to its simplicity. Nano and femto second pulsed laser ablation of metal nanoclusters are reported in various solvents, water, ethanol and toluene [14-16]. The resulting solution would consist only the colloids and solvent, no byproducts of metal would be present.

In this chapter we report nanosecond ablation of gold and silver targets in deionised water and the dependence of laser fluence and ablation time on optical properties of the nanoclusters. The nonlinear optical properties such as nonlinear refraction and nonlinear absorption are also studied using single beam Z-scan technique [17]. Metal nanoparticles have been suggested for applications in nonlinear optics for the last decade due to the enhanced third order susceptibility of metal nanoclusters and metal nanocomposites [18-21] near the SPR. The large optical nonlinearity near the SPR can be explained on the basis of local field enhancement inside the nanoparticle [22, 23]. At the SPR position, the electric field inside the particle is much larger than the applied electric field. The ratio of the electric field inside the particle to the applied field is called the local field factor, $f(\omega)$. For a spherical particle with a radius very small compared to the wavelength of light, the local field factor is given by eqn.(6.1) [24, 25],

$$E_l = \frac{3\varepsilon_h}{\varepsilon_m + 2\varepsilon_h} E_0 = fE_0 \qquad (6.1)$$

where ε_h is the dielectric constant of the host medium, ε_m is the complex dielectric constant of the metal, E_l is the local field developed inside the nanoparticles and E_0 is the incident field. The local field factor becomes large when the real part of the denominator ($\varepsilon_m+2\varepsilon_h$) goes to zero. Even when the inherent χ^3_m of the metal inside the particle is very low, because of the local field enhancement, the χ^3_{eff} could be very large.

Aqueous metal nanocolloids may undergo a partial sedimentation and this may affect the stability of optical nonlinearity [26]. In a device point of view these metal nanocrystals can be embedded in suitable dielectric host matrix so as to achieve better stability compared to colloidal solution. If the dielectric matrix used offer ease of flexibility, it will be an additional advantage in the device fabrication point of view. Hence a polymer matrix will do better compared to any other dielectric media like silica, TiO_2 etc [27]. The gold and silver nanoparticles showing better nonlinearity are embedded in a stable polymer matrix so as to yield ease of flexibility as well as long term stability for the devices as compared to the metal nanocolloids. The optical nonlinearity of polymer embedded Au and Ag nanocrystals are analyzed using single beam Z-scan technique.

6.2. Experimental

Second harmonics of Nd:YAG laser (532nm) operating at a repetition rate of 10Hz was focused on to high purity gold and silver target immersed in 15 ml deionized water. Keeping the ablation time the same (1 hour), the laser fluence was varied from 1.2J/cm^2 to 3.8J/cm^2. The UV-

visible absorption spectra of the as prepared gold and silver nanocluster solutions were recorded using JASCO V570 spectrophotometer. The UV-visible absorption spectra of the silver colloidal solutions were taken after 5days and after 15 days of synthesis in order to study the effect of ageing. In order to analyse the influence of duration of ablation on the properties of silver nanoparticles, another set of the silver colloidal solutions in 15ml water were prepared using third harmonics (355nm) and fourth harmonics (266nm) of Nd:YAG laser source keeping the incident fluence the same ($1.2J/cm^2$) and varying the laser ablation time from 1 hour, 2 hour and 3 hour.

The sizes of the nanoparticles were analyzed by transmission electron microscopy (TEM). The experimental procedure followed for the synthesis of nanocrystal embedded polymer films is described below. 2 gms of poly vinyl alcohol was mixed with 20ml water solution and stirred well for one hour at a temperature 50^0C. To this viscous fluid 15ml of Au/water was added drop wise and again stirred for 2 hours at room temperature. For thorough mixing of Au nanocrystals in the PVA matrix, the resultant viscous colloidal solution was subjected to ultrasonic agitation for 15 minutes. Soon after the agitation, 3ml of both the Au/PVA was spin coated on a glass plate at 1000rpm so as to get a thin uniform film of thickness 1μm in which Au nanocrystals were embedded inside the dielectric host matrix. Following the same procedure for the fabrication of Au/PVA film, the Ag nanocrystals were also embedded in PVA matrix so as to produce Ag/PVA film.

The nonlinear absorption and nonlinear refraction of the samples were analyzed using the single beam Z-scan technique. Second harmonics of Nd:YAG laser (532 nm, pulse width 6-7ns) having a repetition rate of 10 Hz was used as the source for the nonlinear optical studies.

6.3. Results and discussions

The mechanism of nano particle growth during liquid phase pulsed laser ablation can be explained using the model presented by Mafune *et al* [29]. According to this, while the plume expands in the media like water, small polar molecules of water create an electrical bilayer around the nanoparticles [30]. In these solvents, the OH group on the gold nanoparticles generates surface charge and an electrical bilayer is formed. The electrostatic repulsion between the gold nanoparticles prevents further growth and results in stable clusters.

6.3.1. Gold nanoparticles by LP-PLA

The gold nanoparticles in the size range 2-99nm is expected to have that the position of the maximum optical absorption between 520-580nm [28]. Figure 6.1 shows the absorption spectra obtained for the samples prepared at different laser fluences varying from 1.2J/cm^2 to 3.8J/cm^2. The UV-visible absorption spectra of the samples show strong surface plasmon resonance peaks only in the visible region (518nm – 530nm), a property shown by spherical Au nanoparticles as proposed by Mie theory. For non spherical particles such as nanorods, additional plasmon modes at a higher wavelength (800nm) corresponding to the longitudinal mode of oscillation

appears in addition to the transverse mode of oscillation (around 520nm) of the free electron cloud [31]. The presence of a single plasmon peak in the lower wavelength proposes a spherical shape to the Au nanocrystals.

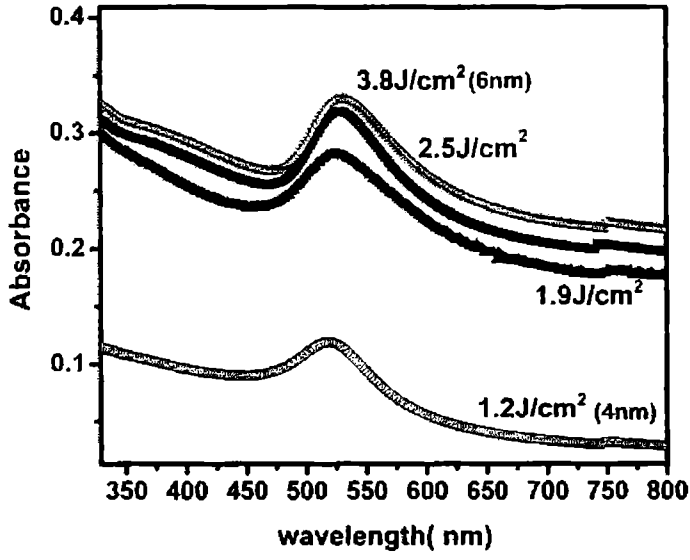

Figure 6.1. UV-visible absorption spectra of Au nanoclusters prepared at different laser fluences.

A red shift in the absorption maxima from 518 nm to 530 nm indicates an increase in particle size [22]. When size of the particle increases, light cannot polarize the nanoparticle homogenously since in larger clusters localization of the d band electrons increases the screening of the ions by surface electrons thereby reducing the polarizability near the surface and retardation effect lead to the excitation of higher order modes [31]. This is

regarded as an extrinsic size effect. This leads to a red shift in the SPR peak with increase in nanoparticle size. The amplitude of the SPR peak is found to increase with increase in the ablation fluence which is attributed to the increase in the number of gold nanoparticles in water. The broadening of the absorption band with a decrease in particle size is observed which is attributed to the increased damping known as Landau damping [6]. As long as the particles are apart there will be no contribution to the observed broadening, but when the volume fraction of Au nanoparticles increases inter particle interaction comes in to play.

The dependence of the absorption cross section of plasmon resonance on the particle size and the surrounding dielectric media as proposed by the Drude model for the spherical metal nanoparticle can be used in the simulation so as to find out the particle size. The model consists of a sphere of radius R in a suspending medium. The nanosphere has a dielectric function ε_1, and the embedding medium has dielectric function ε_2. It is important to note that, $\varepsilon_1=\varepsilon_{1r}+i\varepsilon_{1i}$ can have real and imaginary frequency-dependent components. In Drude model, the frequency dependent complex dielectric constant can then be written as [32],

$$\varepsilon(\omega)=\varepsilon_r+i\varepsilon_i=\varepsilon_b(\omega)-\frac{\frac{\omega_p^2}{\omega^2}}{1+\frac{1}{\omega^2\tau^2}}+i\frac{\frac{\omega_p^2}{\omega^2}}{\omega\tau(1+\frac{1}{\omega^2\tau^2})} \qquad (6.2)$$

where $\varepsilon_b(\omega)$ is the dielectric function of bulk metal which is due to interband transition, ω_p denotes the plasmon frequency of the bulk metal, τ

is the relaxation time and ω is the frequency of electromagnetic wave. The absorption cross-section is given as follows,

$$\sigma_{abs} = \frac{24\pi^2 R^3 \varepsilon_{li} \varepsilon_2}{\lambda[(\varepsilon_{1r} + 2\varepsilon_2)^2 + \varepsilon_{li}^2]} \tag{6.3}$$

The simulation and the experimental plots obtained for the nanoparticles prepared at a laser fluence 1.2J/cm^2 and 3.8J/cm^2 are shown in figure 6.2(a) and 6.2(b) respectively. The particle sizes calculated from the simulation analysis are 4nm and 6nm respectively for nanoparticles prepared at 1.2J/cm^2 and 3.8J/cm^2 ablation fluences.

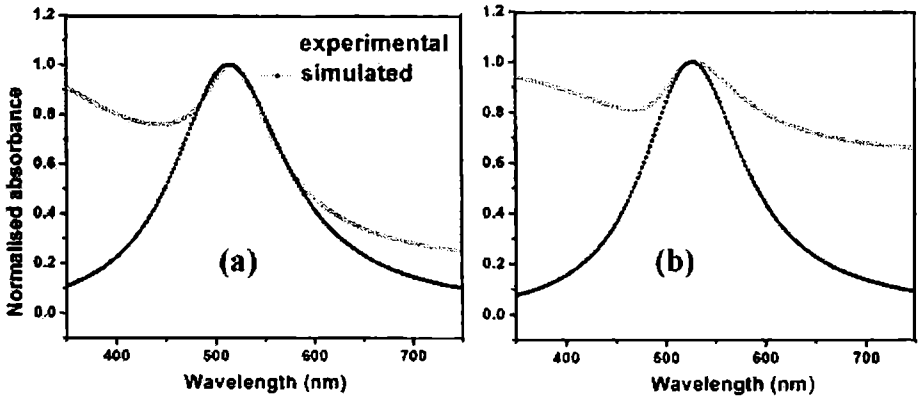

Figure 6.2. Experimental and simulated absorption spectra of nanoparticles of different size (a) 4nm (b) 6nm.

The TEM and size histogram of the nanoparticles prepared at 1.2J/cm^2 and 3.8J/cm^2 are shown in figure 6.3. The TEM image shows gold nanoparticles distributed uniformly in the aqueous media confirming the

spherical shape to the nanoparticles as observed in the UV-visible absorption spectra. The average particle size of the Au nanoclusters are confirmed to be to be 4nm and 6nm for laser fluences 1.2J/cm^2 and 3.8J/cm^2 respectively which is exactly similar to the values obtained from simulating the absorption spectra. TEM analysis shows almost similar particle size (4nm) can be created at a much lower laser fluence 1.2J/cm^2 as compared to the higher laser fluence of 60J/cm^2 as reported by Kabashin *et al* using the femtosecond laser ablation [14].

The high resolution TEM (HRTEM) and selected area electron diffraction (SAED) pattern of the nanoparticles prepared at 1.2J/cm^2 and 3.8J/cm^2 are shown in figure 6.4. The d values obtained from SAED pattern matches well with the (220), (200) and (400) planes of gold. The HRTEM shows the atomic planes where the d spacing observed is 2.35A^0 that corresponds to the (111) plane of gold.

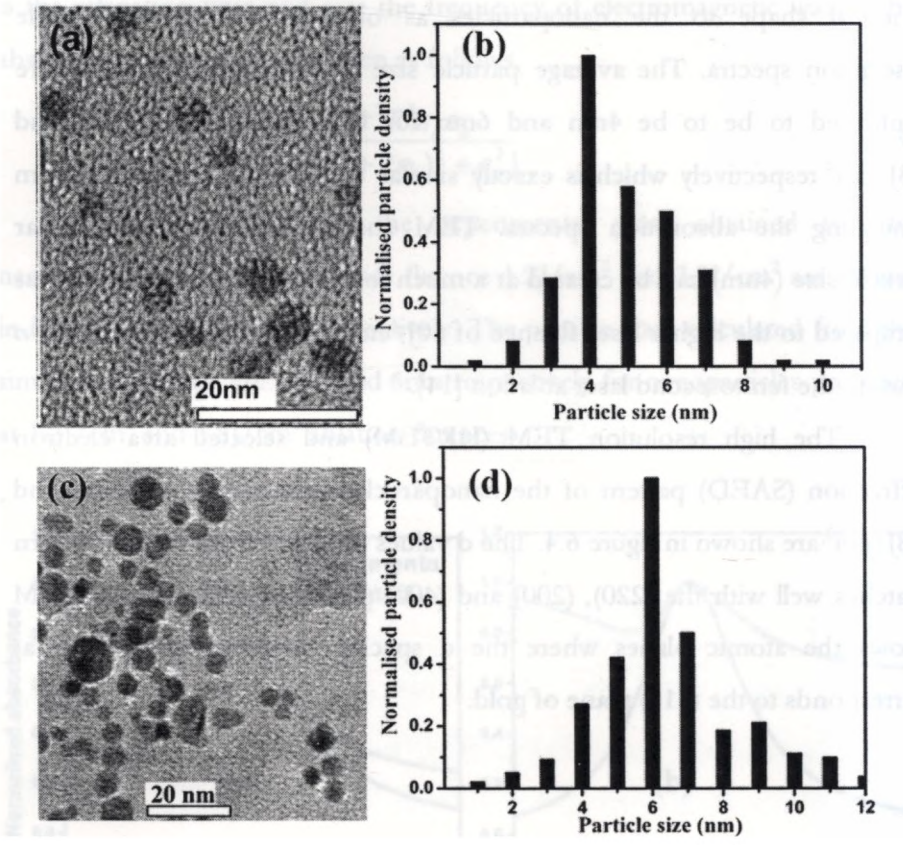

Figure 6.3. TEM (a, c) and size histogram (b, d) of Au nanoclusters prepared at 1.2 J/cm^2 (top row) and 3.8 J/cm^2 (bottom row).

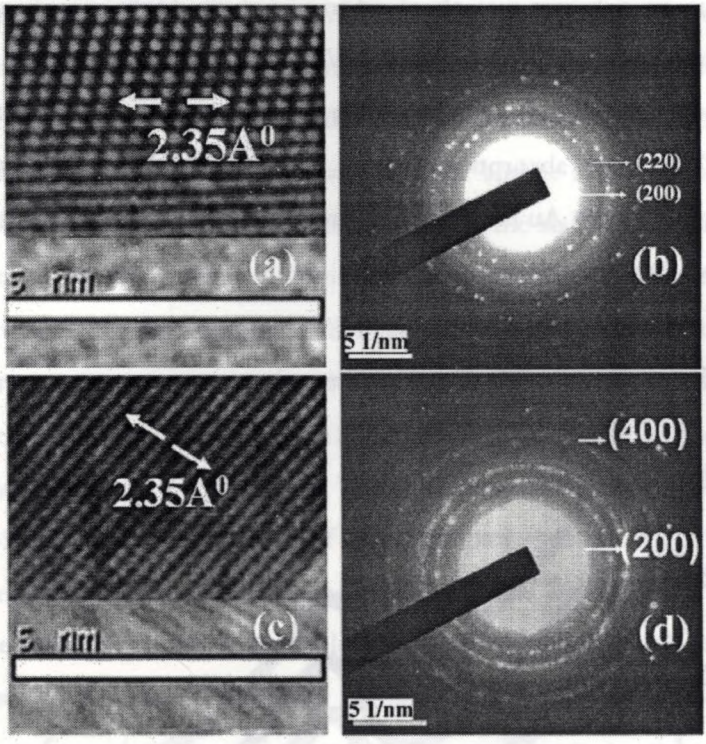

Figure 6.4. HRTEM (a, c) and SAED (b, d) of Au nanoclusters prepared at 1.2 J/cm^2 (top row) and 3.8 J/cm^2 (bottom row).

Au nanoclusters in water prepared at fixed laser fluence of 1.9J/cm^2 for different durations 1 hour, 2 hour and 3 hour show SPR peak at the same position 520nm (Figure 6.5) indicating an almost constant size of the nanoparticles irrespective of the duration of ablation. It has been reported in the literature that during the growth of nanoparticles with nanosecond lasers, a reduction in particle size will be observed due to the efficient radiation absorption by the previously ablated particles [15]. No such a

reduction in particle size was observed in our study. Only an enhancement in the absorbance is observed in the UV-visible spectrum which is due to the increased nanoparticle density of the samples with increase in ablation duration. Therefore absorption spectra indicate an almost constant size (around 4nm) for the Au nanoparticles prepared at 1.9J/cm^2 independent of the ablation duration.

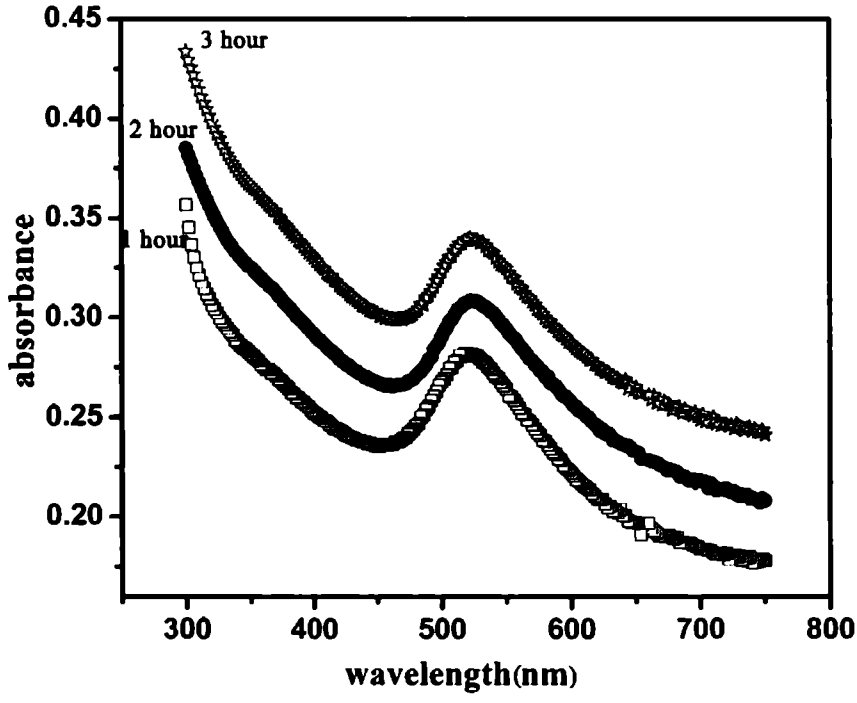

Figure 6.5. UV-visible absorption spectra of Au nanoclusters prepared at a laser fluence of 1.9J/cm^2 for different ablation duration.

In the case of noble metal nanoparticles, the optical properties are due to the d and outermost s-p conduction electrons. In band calculations the outermost d and s electrons of the constituent atoms must be treated as leading to six bands: five of them are fairly flat and lie a few eV below the Fermi level, they are usually denoted as d bands, the sixth one being almost free electron like, ie roughly parabolic with an effective mass close to that of free electron. This last band is called s-p band or conduction band. To induce a transition between the d-bands and the conduction band, the photon energy $\hbar\omega$ has to be larger than a gap of energy $\hbar\omega_g$. In the case of gold, this gap energy ($\hbar\omega_g$) is 1.7eV. These inter band transitions explain the colour of bulk gold. In the case of metal colloids there is one absorption band due to surface plasmon resonance, for gold $\hbar\omega_s$ corresponds to 2.3eV. Since the inter band and surface plasmon absorptions in Au NPs situates very close to the excitation energy 532nm (2.33eV) optical excitation will lead to surface plasmon and inter band contributions to the nonlinear response at 532nm.

The conduction electrons contribution as a whole is called intra band. The susceptibility induced by the intra band transitions is an electric dipole one and it is attributed to the confinement of the free electrons. It is therefore strongly particle size dependent, varying as a^{-3} when particle size $a<<a_0$ where a_0 is a parameter related to the Fermi energy and dephasing time of the conduction electrons [10]. In the case of gold and for the 532nm light the value of a_0 is found to be ~13.6nm.

The optical absorptive nonlinearities are measured by open aperture Z-scan technique at an irradiance value I_0=0.325J/cm^2. The experimentally obtained curve in the present study (Figure 6.6) is of reverse saturable absorption type where the transmittance falls down with increasing incident laser fluence. The solid line in figure 6.6 represents the theoretical fitting to the experimentally obtained data points.

The mechanism of nonlinear absorption can be explained as follows. When excited at 532nm (2.33eV), the electrons in the filled d band of gold will be excited to the unoccupied states in the conduction band due to inter band transitions. Plasmonic absorption happens from the ground sate of the conduction band to the excited state of the conduction band thus generating a number of free carriers in the excited state of the conduction band. A part of the free electrons will be pumped even to higher energy levels in the conduction band causing free carrier absorption.

Thus a major contribution to the origin of nonlinear absorption in gold nanoparticles is attributed to the intra band excitations from the plasmon band to the free carrier band and subsequent free carrier absorption. Since the probability for intra band transition is particle size dependent proportional to a^3, the intra band contribution will be maximum in smaller sized nanoparticles leading to much efficient nonlinear absorption. Thus the origin of nonlinear absorption in gold nanoparticles is attributed to inter band, plasmonic and free carrier absorption.

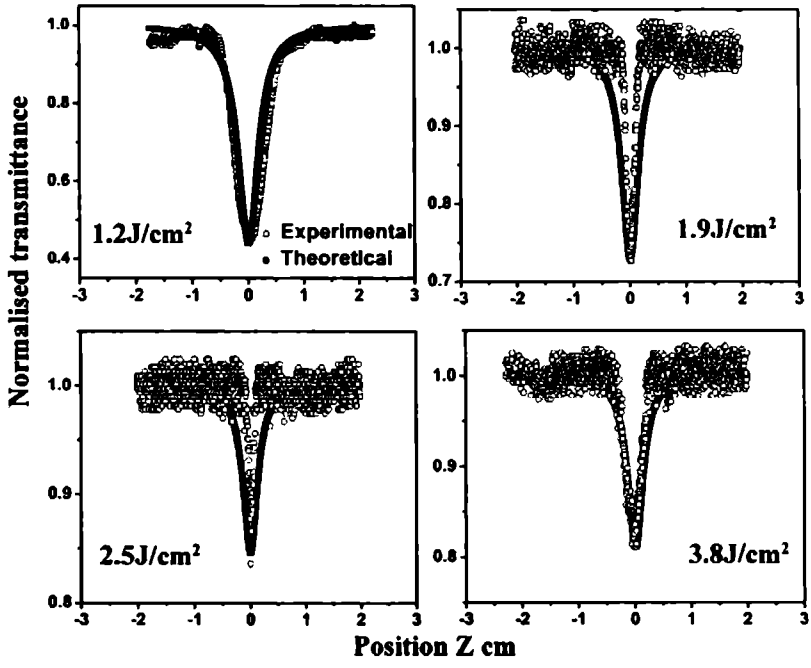

Figure 6.6. Open aperture Z-scan traces of gold nanoparticles prepared at various laser ablation fluences.

Experimental data fit well with the theoretical eqn.(6.4) for normalized transmittance T(z, S=1) corresponding to nonlinear absorption [19],

$$T(z,S=1)=\frac{1}{\sqrt{\pi}q_0(z,0)}.\int \ln\left[1+q_0(z,0)e^{-r^2}\right]d\tau \qquad (6.4)$$

where $q_o(z,0)=\beta I_0 L_{eff}$ and β is the nonlinear absorption coefficient, L_{eff} is given by $\frac{\left(1-e^{-\alpha L}\right)}{\alpha}$ where L is the sample length, α linear absorption coefficient I_0 is the incident intensity. The experimental data points are fitted

with the theoretical eqn.(6.4) with β taken as the fitting parameter and the value of β corresponding to the best theoretical fit is taken. The optical absorptive nonlinearities of the samples prepared at lowest ($1.2J/cm^2$, 4nm) and highest ($3.8J/cm^2$, 6nm) laser ablation energy shows that a better absorptive nonlinearity is obtained for smallest nanoparticles (4nm). The nonlinear absorption coefficient β corresponding to 4nm and 6nm are 4.737×10^{-10} m/W and 4.37×10^{-11} m/W respectively; ie a decrease in the value of β with increase in size of nanoparticles. The optical limiting plots corresponding to 4nm and 6nm is shown in figure 6.7 which clearly shows the reduction in transmission as the size of the nanoparticles decreases.

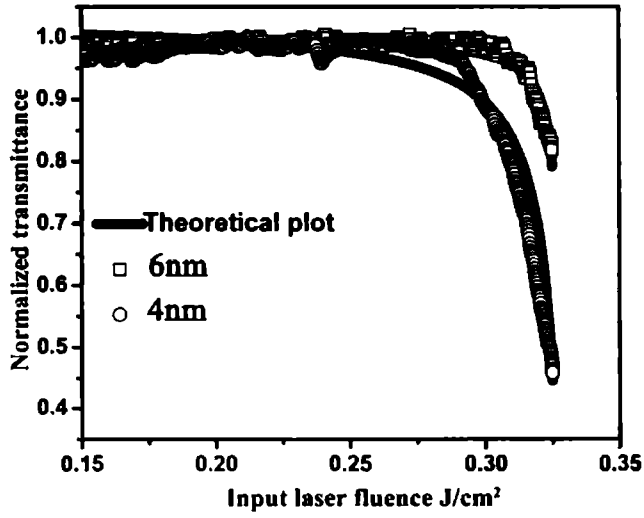

Figure 6.7. Optical limiting characteristic of the Au nanoclusters of particle size 4nm and 6nm (the solid line represents theoretical fitting to the experimental data).

The $Im(\chi^{(3)})$, χ_I^3 is related to the nonlinear absorption coefficient β through the following eqn.(6.5),

$$\chi_I^3 = \frac{n_0^2 \lambda c \beta}{48\pi^3}(esu) \qquad (6.5)$$

where λ and c are the wavelength of incident laser beam (532nm) and velocity of light in vacuum respectively. The value of χ_I^3 is calculated to be 0.757×10^{-10}esu and 0.0698×10^{-10}esu respectively for 4nm and 6nm Au nanoparticles. Hence these Au nanoclusters found valuable application for optical limiting device fabrications. The values of the λ_{SPR}, particle size, β and χ_I^3 corresponding to the Au nanoparticles prepared at different laser ablation fluence value are shown in table 6.1.

Laser fluence (J/cm^2)	**λ_{SPR} (nm)**	**TPA coefficient β (cm/GW)**	**$Im(\chi^{(3)})$ χ_I^3 (esu)**
1.2	**518**	**47.37**	**0.757×10^{-10}**
1.9	**521**	**7.9**	**0.126×10^{-10}**
2.5	**526**	**5.94**	**0.0933×10^{-10}**
3.8	**530**	**4.37**	**0.0698×10^{-10}**

Table 6.1. The variation of λ_{SPR}, β and χ_I^3 with laser ablation fluence of Au colloids.

The Au nanoclusters in water show good nonlinear refraction which is attributed to the self defocusing effect in the sample. Self defocusing has

electronic (population lens) and thermal (thermal lens) contributions. Electronic contribution arises from the induced polarization due to the population redistribution between the ground and excited conduction band states (intra band transition) [35]. Higher nonlinear refraction in smaller nanoparticles is due to particle size dependent enhancement in the oscillator strength associated with intra band electronic transitions. The thermal lens contribution arises from the excited hot electrons (electrons with higher energy than Fermi energy). They got thermalized by dissipating the excess energy through scattering processes [33]. The excess thermal energy increases the surrounding temperature and generates a temperature gradient. This temperature gradient leads to a variation in refractive index, which is called a thermal lens [34].

The closed aperture transmittance $T(z,\Delta\phi_0)$ is related to the on axis phase shift at the focus $\Delta\phi_0$ by [17] eqn.(6.6),

$$T(z,\Delta\phi_0) \approx [1-\frac{4\Delta\phi_0 x}{(x^2+9)(x^2+1)}] \tag{6.6}$$

where $x=\frac{z}{z_0}$.

and $\Delta\phi_0$ is related to the nonlinear refractive index γ through eqn.(6.7),

$$\gamma=\frac{\lambda\Delta\phi_0}{2L_{eff}I_0} \tag{6.7}$$

Therefore fitting the closed aperture data with theoretical eqn.(6.6) (where γ is taken as the fitting parameter) yields the value of nonlinear

refractive index γ. The nonlinear refractive index γ and the real part of third order optical nonlinear susceptibility χ_R^3 can be given by the eqn.(6.8),

$$\chi_R^3 = \frac{n_0 n_2}{3\pi} = \frac{n_0^2 c\gamma}{120\pi^2}(esu) \qquad (6.8)$$

where n_0 is the linear refractive index of the sample (for gold n_0=0.47), ε_0 is the permittivity of free space and c is the velocity of light in vacuum.

The typical closed aperture curves for the Au nanoclusters of sizes 4nm and 6nm are shown in figure 6.8(a) and 6.8(b) respectively. The nonlinear refractive index γ is found to be $-2.421\times10^{-15}m^2/W$ and $-1.115\times10^{-15}m^2/W$ respectively for the nanoparticles of 4nm and 6nm size. The χ_R^3 is calculated to be -38.37×10^{-10}esu and -4.07×10^{-10}esu respectively for 4nm and 6nm nanoparticles. The enhancement in the χ_R^3 in lower sized nanoparticles originates from the size dependent enhancement in the local electric field inside the nanoparticle. The size dependence in the real part of nonlinear susceptibility χ_R^3 indicates the contribution from the intra band transitions in the conduction band.

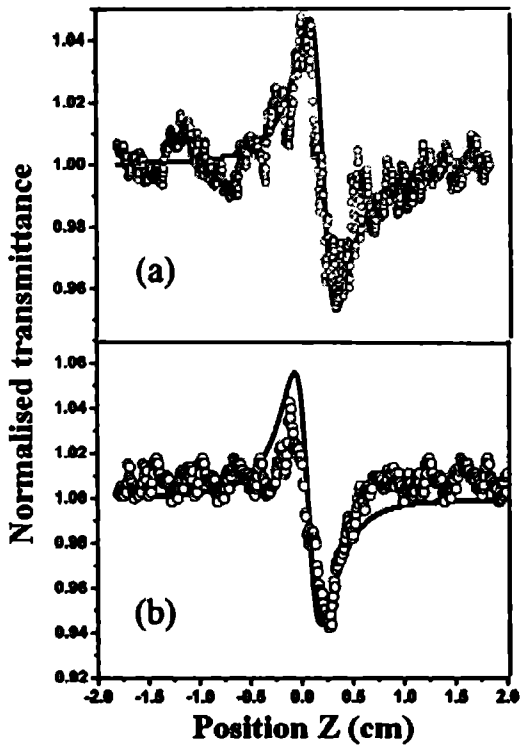

Figure 6.8. Closed aperture Z-scan traces of the Au nanoclusters of particle size (a) 6nm and (b) 4nm.

For nonlinear optical applications, it will be better to incorporate the nanoparticles immobilized in a suitable matrix like polymer or glass. The ease of flexibility that the polymer matrix offers as compared to a rigid fragile matrix like glass makes it best to incorporate Au nanoparticles in polymer matrix for fabricating devices. Lower size (4nm) nanoparticles having high value of γ as well as β are embedded inside the poly vinyl alcohol (PVA) matrix so as to achieve a stable optical limiting device.

The UV-visible absorption spectra of the Au/PVA film as well as pure PVA film are shown in figure 6.9, which show the presence of strong SPR bands peaked at 520nm indicating the incorporation of Au NPs in the matrix. A slight shift (2nm) in the SPR compared to the colloidal solution in water is due to a change in the dielectric constant of the medium used. Inset of the figure 6.9 show the photograph of the Au/PVA thin film with the writing beneath it.

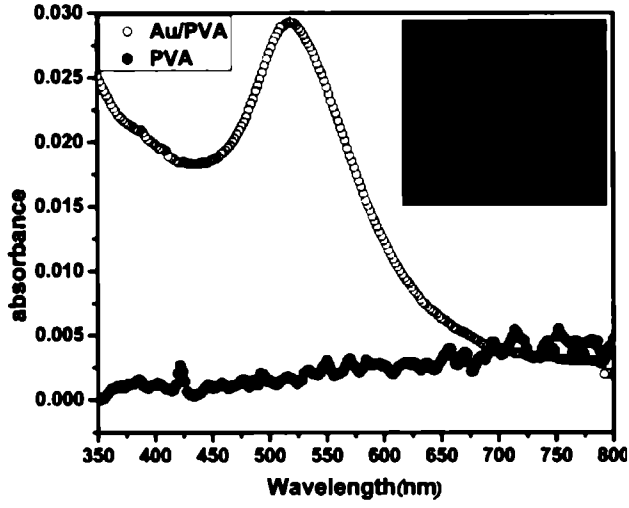

Figure 6.9. UV-visible absorption spectra of Au/PVA films (inset shows the photo of Au/PVA film).

The open as well as closed aperture Z-scan traces of the Au/PVA films are recorded using Z-scan technique. Figure 6.10(a) shows the optical limiting curve of Au/PVA films where as figure 6.10(b) gives the closed aperture curve showing negative refractive index type nonlinearity. The

optical limiting property of Au nanocrystals in polymer film is similar to the Au colloids but the nonlinear refraction in Au/PVA is found to be better compared to the Au/water colloidal solution. The deviation of the experimental plots from the theoretical fit may be attributed to the contribution from thermally induced nonlinear scattering produced by the generated hot plasma in the solid polymer matrix [36].

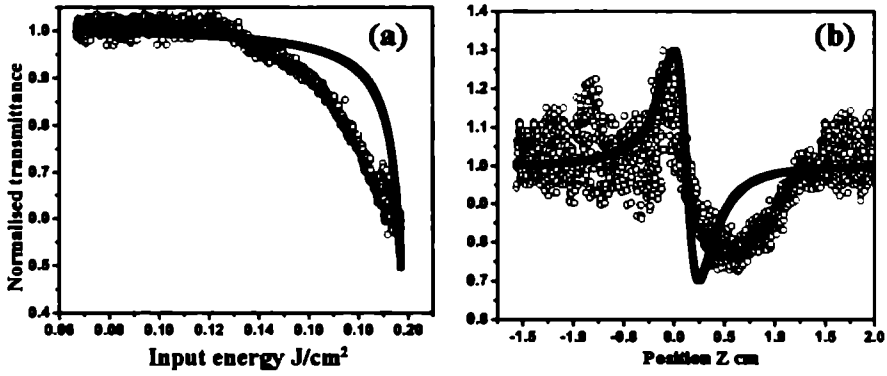

Figure 6.10. (a) The optical limiting and (b) self defocusing curve of Au nanocrystals in PVA matrix.

The nonlinear refraction may contain electronic as well as thermal contributions. However the enhancement in the refractive index may be attributed to thermally induced lensing in the Au/PVA as compared to the Au/water colloidal solution. Thermal lensing arises from the excited hot electrons which are thermalized by dissipating the excess heat energy through scattering process [33]. The excess thermal energy increases the surrounding temperature and generates a temperature gradient which leads to a variation in refractive index which is called a thermal lens [34]. Phase

shift (0) suffered by incident laser beam as a result of thermal lensing is given by,

$$\theta \alpha dS/dT$$

But for liquid samples $\frac{ds}{dT} = \frac{dn}{dT}$, where as in solid sample $\frac{ds}{dT}$ involves contribution from $\frac{dn}{dT}$, end phase curvature and thermal stress [35]. Larger expansion of the hotter centre compared to the cooler edge of the solid sample leads to an end face curvature contribution and the fact is that the cooler part of the sample prevents the expansion of its hotter centre generating a thermal stress. Hence the induced phase shift in a solid sample will be higher as compared to a liquid sample. This may be the reason for the enhanced nonlinear refractive index in the thin film sample. However detailed analysis may be required in order to completely determine the exact phenomena behind the high value of nonlinear refraction shown by the Au nanocrystals in polymer matrix.

The value of the nonlinear absorption coefficient as well as refractive index is better compared to those reported earlier in Au colloids as well as in Au thin films [36-38]. Therefore the optical limiting efficiency as well as self defocusing nature observed in our work is much better compared to earlier reports. Hence the Au/PVA film is found to be a suitable material for nonlinear optical applications involving optical limiting and self defocusing. The Au nanocrystals will be very stable inside the polymer matrix and will work efficiently for long term applications.

Figure 6.12(a) and figure 6.12(b) shows the HRTEM images of the silver nanoparticles prepared at 1.2J/cm^2 and 3.8J/cm^2 respectively, the size of the silver nanoparticles are found to be 4nm and 6nm respectively. Figure 6.12(c) and figure 6.12(d) gives the selected area electron diffraction (SAED) pattern of silver nanoparticles showing the (111) and (200) planes of silver.

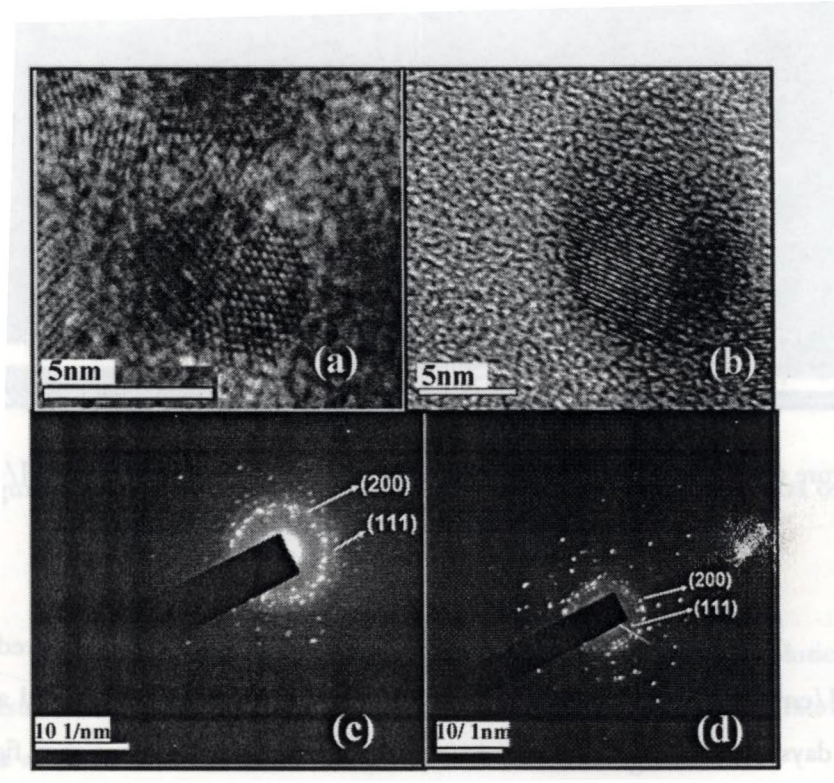

Figure 6.12. The TEM image of nanoparticles prepared at (a) 1.2J/cm^2 and (b) 3.8J/cm^2 (c) SAED pattern of nanoparticles prepared at 1.2J/cm^2 and (d) 3.8J/cm^2.

Figure 6.13(a) and figure 6.13(b) show HRTEM images showing parallel lines of atoms of the silver nanoparticles prepared at 1.2J/cm^2 and 3.8J/cm^2 respectively where the observed inter planar spacing 2.35A^0 is in well agreement with (111) plane of silver.

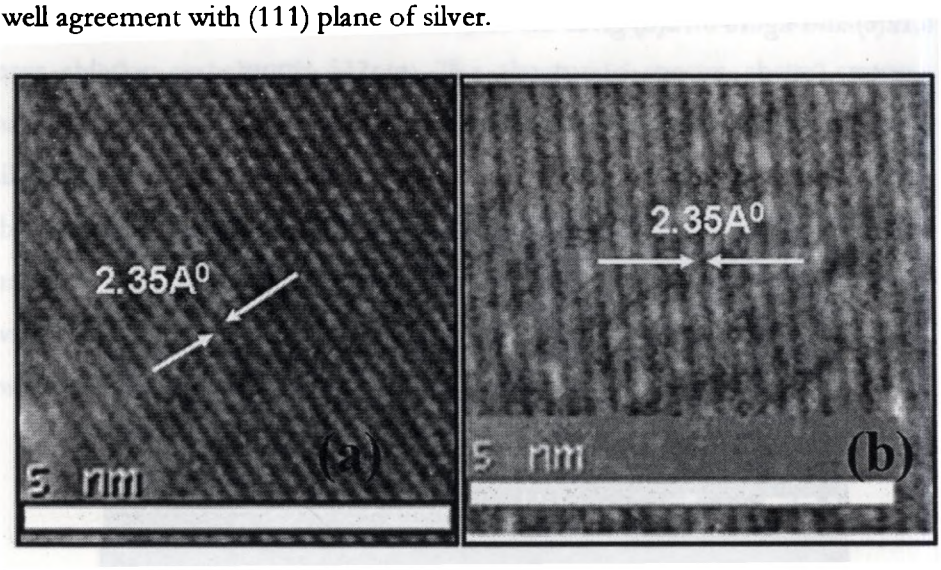

Figure 6.13. HRTEM images of silver nanoparticles prepared at (a) 1.2J/cm^2 and (b) 3.8J/cm^2 showing parallel lines of atoms.

The absorption spectra of the colloidal solutions prepared at 1.2J/cm^2 and 3.8J/cm^2 taken just after the synthesis, after 5 days and after 15 days are shown in figure 6.14(a) and 6.14(b) respectively. From figure 6.14(a) and 6.14(b), it is found that the SPR band is diminished after 15days for the nanoparticles prepared at ablation fluence 3.8J/cm^2 (7nm) where as the SPR band is present even after 15days for nanoparticles prepared at ablation fluence 1.2J/cm^2 (4nm). It shows the extra stability of silver

nanoparticles prepared at lower ablation fluence. This fast decay of SPR band of silver nanoparticles prepared at 3.8J/cm^2 is attributed to the increased nanoparticle concentration and particle size for the colloidal solutions prepared at higher laser fluence, which lead to the agglomeration of the nanoparticles in the colloidal solution.

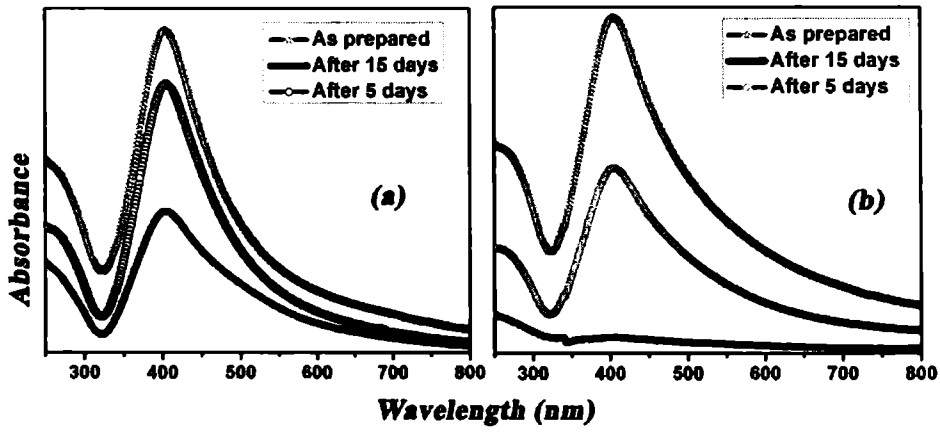

Figure 6.14. The effect of ageing on the UV-visible absorption spectra of silver nanoparticles prepared at (a) 1.2 J/cm^2 and (b) 3.8 J/cm^2.

The open aperture Z-scan plots for silver colloidal solutions (measured with Nd:YAG laser at 532nm operating at a repetition rate of 10Hz at a laser irradiance I_0=0.521 J/cm^2) are shown in figure 6.15.

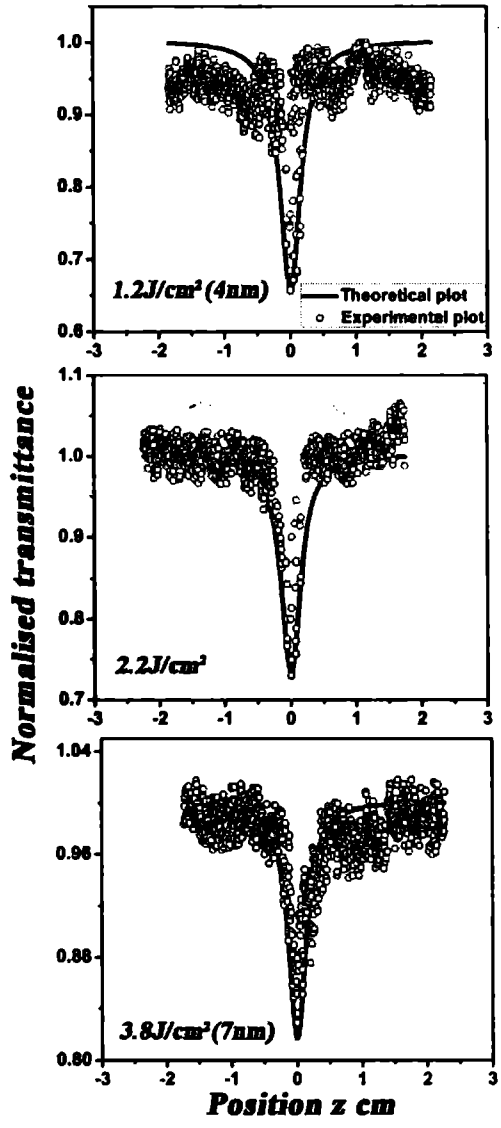

Figure 6.15. Open aperture Z-scan curves of silver nanoparticles prepared at 532nm for various laser ablation fluence.

Figure 6.12(a) and figure 6.12(b) shows the HRTEM images of the silver nanoparticles prepared at 1.2J/cm^2 and 3.8J/cm^2 respectively, the size of the silver nanoparticles are found to be 4nm and 6nm respectively. Figure 6.12(c) and figure 6.12(d) gives the selected area electron diffraction (SAED) pattern of silver nanoparticles showing the (111) and (200) planes of silver.

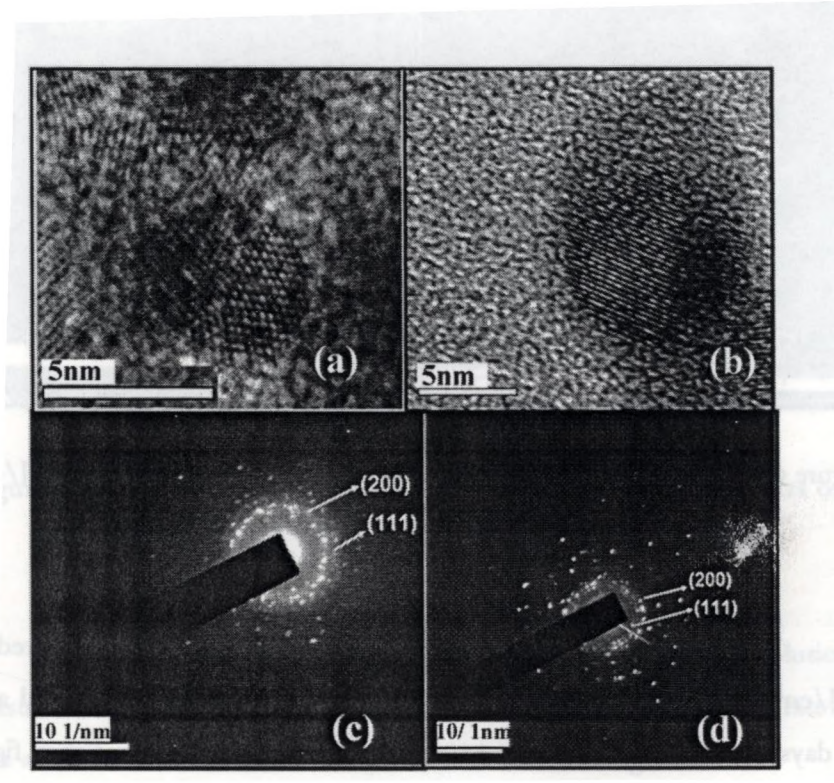

Figure 6.12. The TEM image of nanoparticles prepared at (a) 1.2J/cm^2 and (b) 3.8J/cm^2 (c) SAED pattern of nanoparticles prepared at 1.2J/cm^2 and (d) 3.8J/cm^2.

Figure 6.13(a) and figure 6.13(b) show HRTEM images showing parallel lines of atoms of the silver nanoparticles prepared at 1.2J/cm^2 and 3.8J/cm^2 respectively where the observed inter planar spacing 2.35A^0 is in well agreement with (111) plane of silver.

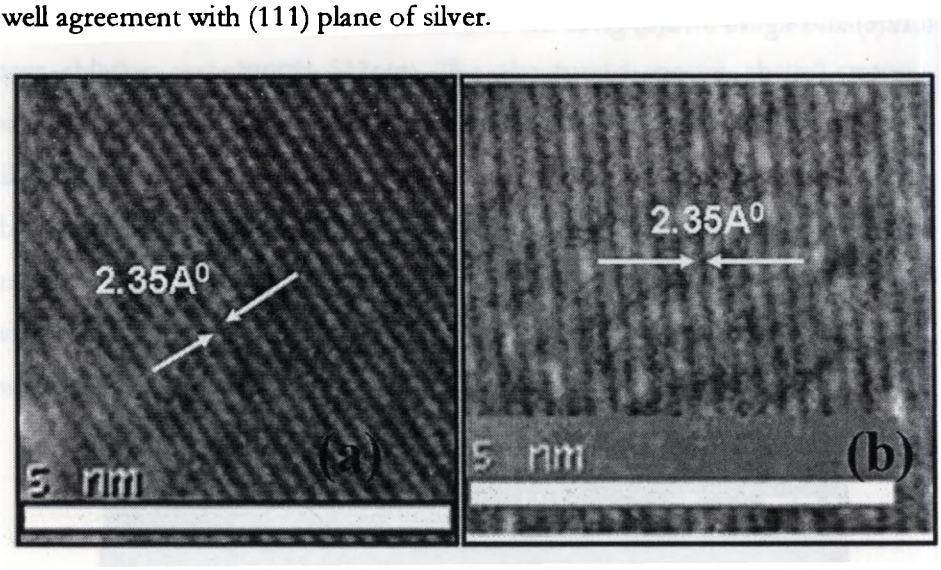

Figure 6.13. HRTEM images of silver nanoparticles prepared at (a) 1.2J/cm^2 and (b) 3.8J/cm^2 showing parallel lines of atoms.

The absorption spectra of the colloidal solutions prepared at 1.2J/cm^2 and 3.8J/cm^2 taken just after the synthesis, after 5 days and after 15 days are shown in figure 6.14(a) and 6.14(b) respectively. From figure 6.14(a) and 6.14(b), it is found that the SPR band is diminished after 15days for the nanoparticles prepared at ablation fluence 3.8J/cm^2 (7nm) where as the SPR band is present even after 15days for nanoparticles prepared at ablation fluence 1.2J/cm^2 (4nm). It shows the extra stability of silver

nanoparticles prepared at lower ablation fluence. This fast decay of SPR band of silver nanoparticles prepared at 3.8J/cm^2 is attributed to the increased nanoparticle concentration and particle size for the colloidal solutions prepared at higher laser fluence, which lead to the agglomeration of the nanoparticles in the colloidal solution.

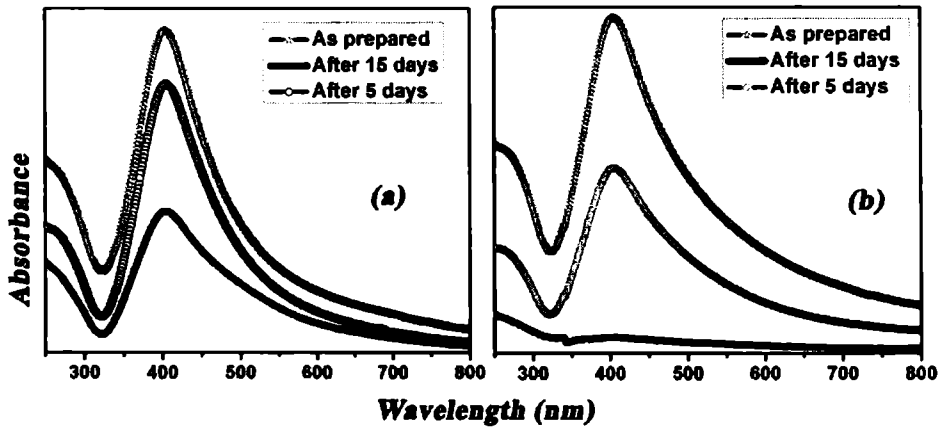

Figure 6.14. The effect of ageing on the UV-visible absorption spectra of silver nanoparticles prepared at (a) 1.2 J/cm^2 and (b) 3.8 J/cm^2.

The open aperture Z-scan plots for silver colloidal solutions (measured with Nd:YAG laser at 532nm operating at a repetition rate of 10Hz at a laser irradiance I_0=0.521 J/cm^2) are shown in figure 6.15.

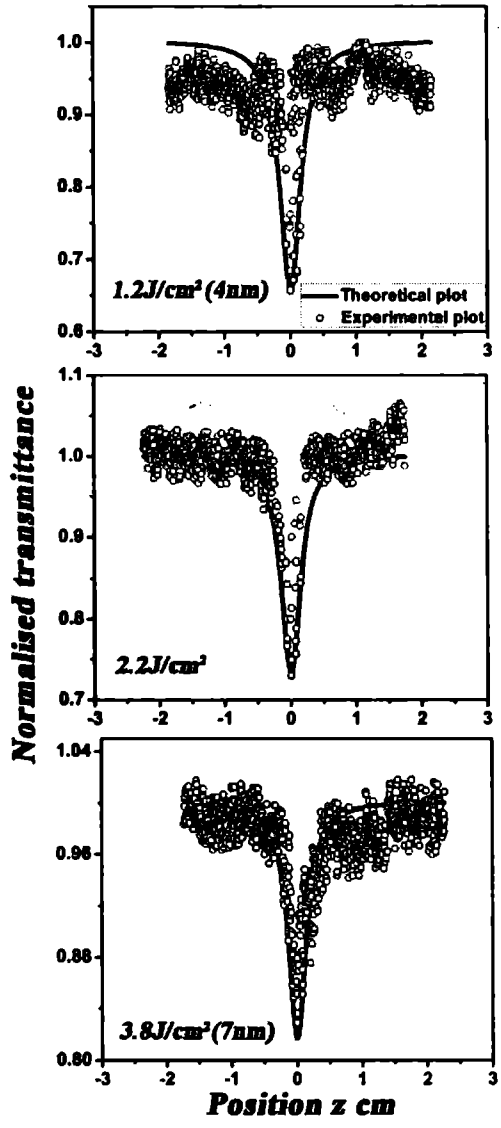

Figure 6.15. Open aperture Z-scan curves of silver nanoparticles prepared at 532nm for various laser ablation fluence.

The experimentally obtained curve in the present study (Figure 6.15) is of optical limiting type where the transmittance falls down with increasing incident laser fluence. When excited at 532nm (2.33eV), the electrons in the filled d band of silver will be excited to the unoccupied states in the conduction band due to inter band transitions. The excitation energy needed for the direct inter band transition in silver is 4eV and hence this transition cannot be achieved by single photon absorption (2.33eV). Hence the nonlinear absorption at 532nm will be occurred by two-photon absorption (TPA) between the filled d band and unoccupied conduction band.

A decrease in the limiting efficiency with increase in the size of nanoparticles is observed from figure 6.15. This can be explained as follows. The TPA excited electrons are free carriers possessing whole spectra of energies kinetic as well as potential which may lead to transient absorption due to free carrier absorption (FCA). A part of the excited electrons will be pumped even to higher energy levels causing excited state absorption (Intra band transition) which is particle size dependent varying as a^{-3}. Thus the efficiency of free carrier absorption will be greater in smaller silver nanoparticles. The size dependence in the nonlinear absorption coefficient indicates the contribution from the intra band transitions in the conduction band. Thus the origin of nonlinear absorption in silver nanoparticles is attributed to two-photon absorption followed by free carrier absorption. Experimental data fit well with the theoretical eqn.(6.4) for normalized transmittance T(z, S=1) corresponding to a nonlinear absorption process [40]. The value of β obtained for the Ag nanoparticles of particle sizes 4nm

and 7nm are 8.173 cm/GW and 2.015 cm/GW respectively which shows that a better absorptive nonlinearity is obtained for smallest nanoparticles (4nm) produced at laser ablation fluence 1.2J/cm^2.

The Im($\chi^{(3)}$), χ_I^3 is related to the nonlinear absorption coefficient β through the following eqn.(6.5), (here in our case the value of n_0 =1.45). And the values of χ_I^3 are calculated to be 18.18×10^{-12} esu and 4.55×10^{-12} esu respectively for 4nm and 7nm Ag nanoparticles. Hence these Ag nanoclusters found valuable application for optical limiting device fabrications. The values of the λ_{SPR}, β and χ_I^3 corresponding to the Ag nanoparticles prepared at different laser fluences are shown in table 6.2.

Laser fluence (J/cm^2)	**λ_{SPR} (nm)**	**β(cm/GW)**	**χ_I^3 (esu)**
1.2	**403**	**8.173**	**18.448×10^{-12}**
2.2	**404**	**4.042**	**9.123×10^{-12}**
3.8	**406**	**2.015**	**4.55×10^{-12}**

Table 6.2. The variation of λ_{SPR}, β and χ_I^3 with laser ablation fluence of Ag colloids.

The smallest silver nanoparticles (4nm) showing maximum nonlinear absorption is embedded in poly vinyl alcohol matrix (PVA) for the fabrication of a solid optical limiting device. The UV-visible spectra of the Ag/PVA and pure PVA film are shown in figure 6.16; the SPR peak at 407nm for Ag/PVA indicates the presence of silver nanoparticles.

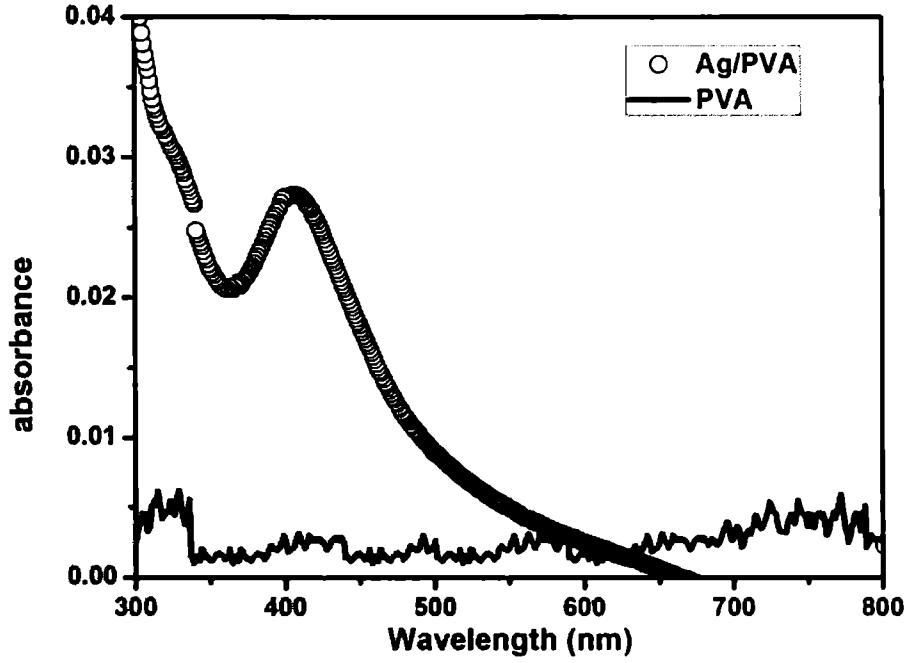

Figure 6.16. The UV-visible absorption spectra of Ag/PVA film.

The open aperture Z-scan traces of the Ag/PVA film showing good nonlinear absorption is given in figure 6.17. Ag nanocrystals in polymer film display almost the same limiting efficiency as the Ag/water colloidal solution which can be used effectively for the fabrication eye protection goggles for laser operators and for protecting sensors attached to laser optics.

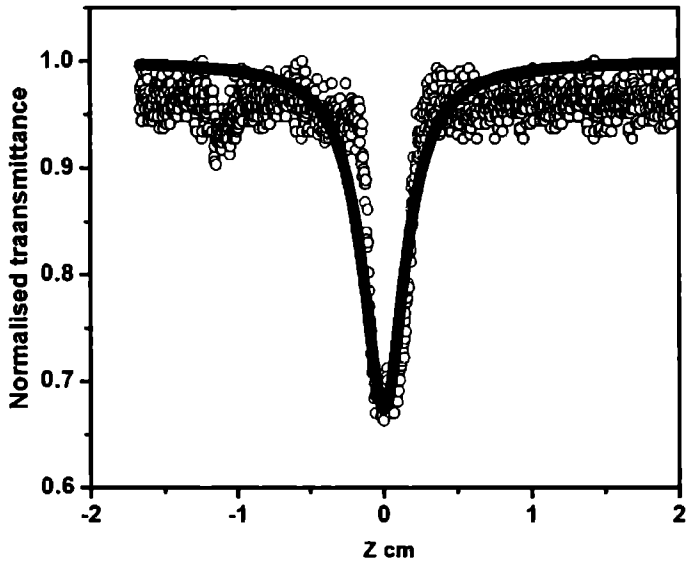

Figure 6.17. Open aperture Z-scan traces of the Ag/PVA film.

(b). Silver nanoparticles prepared at 266 and 355nm

The UV-visible absorption spectra of the Ag nanoparticles prepared at incident laser wavelength 355nm and 266nm at a fixed laser fluence 1.2J/cm^2 for different ablation durations are shown in figure 6.18(a) and 6.18(b) respectively. In both cases the amplitude of the SPR peak is found to increase with increase in the duration of laser ablation which is attributed to the increase in number of silver nanoparticles in water. Figures 6.18(a) and 6.18(b) shows that the SPR peak blue shifts with increase in the duration of laser ablation. This can be attributed to a reduction in particle size due to the efficient radiation absorption by the previously ablated particles [41].

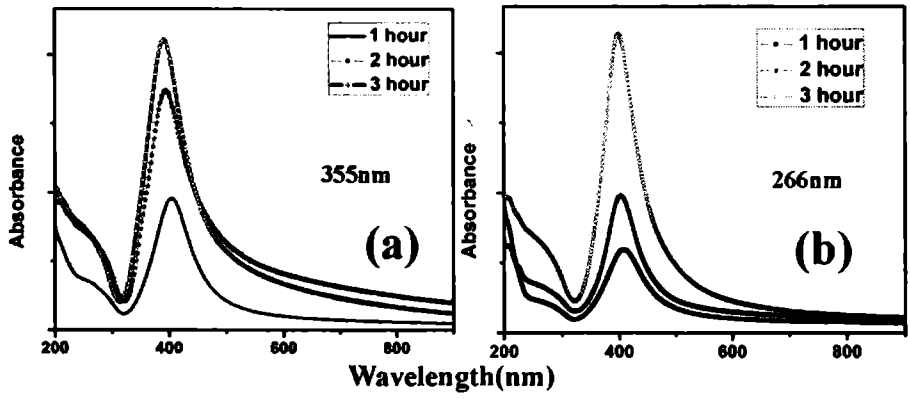

Figure 6.18. UV-visible absorption spectra of silver nanoparticles prepared for different durations at laser wavelength (a) 355nm (b) 266nm at a laser ablation fluence 1.2J/cm^2.

The TEM image of the silver colloids produced at 266nm for 1 hour and 3 hour duration is shown in figure 6.19(a) and 6.19(b). It confirms the reduction in the average particle size and a more homogenous size distribution with increase in the laser ablation duration. Inset of figure 6.19(a) shows the HRTEM image of the silver nanoparticles produced at 1 hour duration which shows parallel lines of atoms at a separation of 2.35A^0 corresponding to the (111) plane of silver.

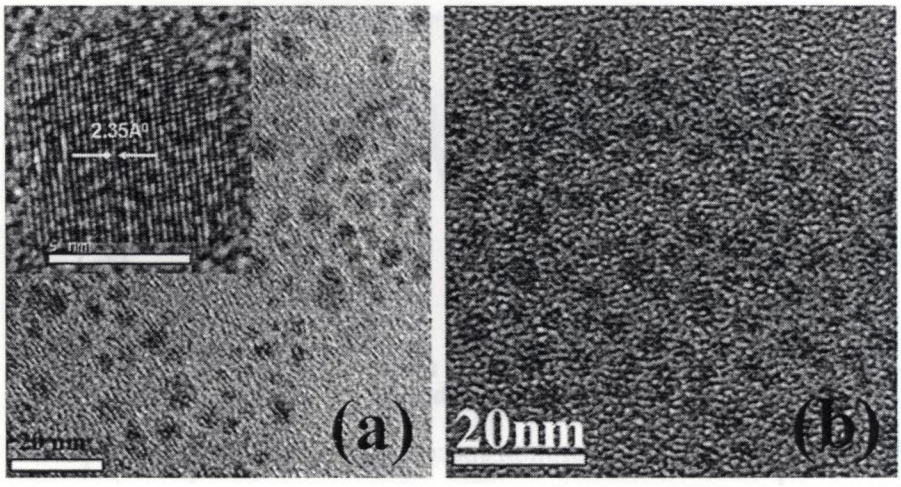

Figure 6.19. TEM image of the silver nanoparticles prepared at ablation fluence 1.2J/cm^2 for ablation duration (a) 1 hour (b) 3 hour (inset shows HRTEM image of silver nanoparticles).

6.4. Conclusions

Gold and silver nanoparticles of different sizes are produced by laser ablation of gold and silver target in deionised water. An increase in nanoparticle size is observed with increasing laser ablation fluence. The absorption spectrum of the nanocolloids is red shifted in wavelength with increase in particle size. The silver nanoparticles prepared at higher laser fluence are found to be less stable as compared to those prepared at lower laser fluence. The optical absorptive nonlinearity of the Au and Ag nanoclusters shows an optical limiting type nonlinearity which finds application in the fabrication of optical limiting devices. It is found that the efficiency of limiting increases with decrease in particle size. The nonlinear

refraction of Au nanoclusters shows negative refractive index value indicating self defocusing type nonlinearity. Both the real and imaginary parts of nonlinear susceptibility are found to be increasing with decrease in particle size which is attributed to the size dependent enhancement in the oscillator strength in the nanoparticle. Stable and flexible nonlinear device is fabricated by incorporating the Au and Ag nanocrystals showing better nonlinearity in a poly vinyl alcohol matrix. The enhancement in the nonlinear refractive index for the Au nanocrystals in polymer matrix as compared to Au nanocrystals in water is attributed to the thermal effects arising in the solid film. For fixed laser ablation fluence, the size of the silver nanoparticles decreases with increase of the duration of ablation due to the effective radiation absorption by the previously ablated particles.

6.5. References

1. M. Kerker, The Scattering of light and other electromagnetic radiation, Academic, New York (1969)
2. U. Kreibig and M. Vollmer, Optical properties of metal clusters, Springer-Verlag, New York (1995)
3. A. Cottey, J. Phys. C: Solid State Phys. **4** 1734 (1971)
4. G. C. Papavassiliou, Prog. Solid State Chem. **12** 185 (1979)
5. B. S. Yilbas, R. Davies, Z. Yilbas and A. Koc, Pramana **34** 473 (1990)
6. C. F. Bohren and D. R. Huffman, Absorption and Scattering of Light by Small Particles, Wiley, New York (1983)
7. M. Garnet and J. C. Philos, Trans. R. Soc. London **203** 385 (1904)

8. Y. Xia and N. J. Halas, MRS Bull. **30** 338 (2005)
9. P. Mulvaney, Langmuir **12** 788 (1996)
10. F. Hache, D. Ricard, C. Flytzanis and U. Kriebig, Appl. Phys. A **47** 347 (1988)
11. M. T. Reetz, M .Winter and B. Tesche, Chem. Commun. 147 (1997)
12. F. Favier, E. M. Walter, M. P. Zach, T. Benter and R. M. Penner, Science **293** 2227 (2001)
13. J. Hu, T. W. Odom and C. M. Lieber, Acc. Chem. Res. **32** 435 (1999)
14. A. V. Kabashin and M. Meunier, J. Appl. Phys. **94** 7941 (2003)
15. R. M. Tilaki, A. Irajizad and S. M. Mahadevi, Appl. Phys. A **84** 215 (2006)
16. A.Vincenzo, A. R. Gian, P. Stefano and M. Moreno, J. Phys. Chem. B **109** 23125 (2005)
17. M. S. Bahae, A. A. Said and E. W. Van Stryland, Opt. Lett. **14** 955 (1989)
18. Y. Hamanaka, K. Fukuta, A. Nakamura, L. M. Liz-Marzan and P. Mulvaney, Appl. Phys. Lett. **84** 4938 (2004)
19. M. Ballesteros, J. Solis, R. Serna and C. N. Afonso, Appl. Phys. Lett. **74** 2791 (1999)
20. S. W. Lu, U. Sohling, M. Mennig and H. Schmidt, Nanotechnology **13** 669 (2002)
21. L. Francois, M. Mostafavi, J. Belloni, J. F. Delouis, J. Delaire and P. Feneyrou, J. Phys. Chem. B **104** 6133 (2000)

22. B. Karthikeyan, J. Thomas and R. Philip, Chem. Phys. Lett. **414** 346 (2005)

23. N. Pinçon, B. Palpant, D. Prot, E. Charron and S. Debrus, The Eur. Phys. J. D **19** 395 (2002)

24. D. Ricard, P. H. Roussignol and C. H. R. Flytzanis, Opt. Lett. **10** 511 (1985)

25. F. Hache, J. Opt. Soc. Am. B **3** 1647 (1986)

26. V. A. Karavanskii, A.V. Simakin, V. I. Krasovskii and P. V. Ivanchenko, Quant. Electron. **34** 644 (2004)

27. N. Venkatram, R. S. S. Kumar, D. N. Rao, S. K. Medda, S. De and G. De, J. Nanosci. Nanotech. **6** 1990 (2006)

28. G. Fu, W. Cai, Y. Gan and J. Jia, Chem. Phys. Lett. **385** 15 (2004)

29. F. Mafune, J. Y. Kohno, Y. Takeda, T. Kondow and H. Sawabe, J. Phys. Chem. B. **104** 9111 (2000)

30. J. Turkevich, P. C. Stevenson and J. Hillier, J. Discuss. Faraday Soc. **11** 55 (1951)

31. S. Link and M. A. E. Sayed, Ann. Rev. Phys. Chem. **54** 331 (2003)

32. R. D. Averitt, D. Sarkar and N. J. Halas, Phys. Rev. Lett. **78** 4217 (1997)

33. J. Y. Bigot, V. Halte, J. C. Merle and A. Daunois, Chem. Phys. **251** 181 (2000)

34. J. P. Gordon, R. C. C. Leite, R. S. Moor, S. P. S. Porto and J. R. Whinnery, J. Appl. Phys. **36** 3 (1965)

35. C. Jacinto, D. N. Messias, A. A. Andrade, S. M. Lima, M. L. Baesso and T. Catunda, J. Non-Cryst. Solids **352** 3582 (2006)

36. R. A. Ganeev and A. I. Ryasnyansky, Appl. Phys. B **84** 295 (2006)
37. D. D. Smith, Y. Yoon, R. W. Boyd, J. K. Campbell, L. A. Baker and R. M. Crooks, J. Appl. Phys. **86** 6200 (1999)
38. R. F. Souza, M. A. R. C. Alencar, E. C. D. Silva, M. R. Meneghetti and J. M. Hickmann, Appl. Phys. Lett. **92** 201902 (2008)
39. B. Fei, Z. X. Zheng, W. Z. Hua, W. Qiang, H. Hao, X. J. Jun, Chin. Phys. Lett. **25** 4463 (2008)
40. M. Sheik-Bahae, A. A. Said and E. W. Van Stryland, Opt. Lett. **14** 955 (1989)
41. R. M. Tilaki, A. Irajizad and S. M. Mahadevi, Appl. Phys. A **84** 215 (2006)

Chapter 7

Linear and nonlinear optical properties of gold nanoparticle attached MWCNTs

7.1. Introduction

The search for potential optical limiters for the protection of sensors from intense laser pulses have motivated many researchers to examine new nanomaterials which exhibit superior optical limiting properties. There exists a very interesting member of carbon family, carbon nanotubes (CNTs) which are widely accepted as a superior material for potential optical limiting applications [1–4]. CNTs have attracted considerable attention because of their unique structure, which have various electronic and optical applications. These tubes are found in two types of structures: single walled carbon nanotubes (SWCNTs) and multiwalled carbon nanotubes (MWCNTs). SWCNT is made of single graphitic cylinder while there are many coaxial graphitic cylinders for each MWCNT. Each cylinder may be visualized as the conformal mapping of a two dimensional honeycomb lattice onto its surface. Earlier studies show that MWCNTs, which are made up of multilayers of graphene sheets that can be rolled into the shape of a hollow cylinder, are noble candidates for broadband optical limiting from the visible to the infrared region [5, 6]. The optical limiting action was observed also in SWCNTs that are made of one layer of a graphene sheet [7].

Noble metal colloids or nanoparticles such as gold (Au) and silver (Ag) nanoparticles are known to possess large nonlinear optical properties. Their optical properties have also been actively studied by picosecond and femtosecond lasers in the surface plasmon absorption (SPA) region [8–10].

A broadband optical limiter based on gold and silver coated MWCNTs has been reported earlier [11].

Recently, research efforts have been devoted to the fabrication of gold nanoparticle supported on the surface of CNTs [12-17]. In fact the main hurdle faced while the fabrication of CNTs attached with gold nanoparticles (Au-NPs) is that most of the preparation techniques either need pre-treatment of pristine CNTs, such as oxidation by strong oxidizing acid or functionalization with surfactant or polyelectrolyte, or need some special instruments and tedious procedures [18-21]. The Au-NPs produced using these technique have a broad particle size distribution. Therefore, the synthesis and attachment of very small and homogenously distributed Au-NPs to the surface of CNTs, especially through a simple and cost-effective route still remains a crisis.

In the present work, gold nanoparticles (Au-NPs) have been grown by liquid phase pulsed laser ablation (LP-PLA) of pure gold target in water. The nanoparticles synthesised in water through laser ablation do not require any additional capping agents or stabilizers and they are very stable for months. A simple method has been used here to directly attach Au-NPs with high dispersivity to the walls of CNTs without using any surfactant or polyelectrolyte to functionalize the CNTs [22]. In the adopted method, when the hydrophobic CNTs were immersed into a colloidal suspension of Au-NPs, a small amount of ethanol was also added into the colloidal Au solution so as to reduce the interfacial tension between CNTs and water, thereby enhancing their wettability in aqueous solution containing Au-NPs.

7.2. Experimental

7.2.1. Preparation of highly dispersed Au-NPs in aqueous media

Third harmonics of Nd:YAG laser (355nm) operating at a repetition rate of 10Hz was focused on to a high purity gold target immersed in 15 ml deionized water. Keeping the ablation fluence the same ($1.2J/cm^2$), Au-NPs in water with various concentrations were prepared by varying the duration of laser ablation from 1 hour to 3 hour. The UV-visible absorption spectra of the as prepared nano colloidal solutions were recorded using JASCO V570 spectrophotometer in the wavelength region 200-1000nm. The concentration of the Au colloids prepared at various ablation durations is measured using inductively coupled plasma atomic emission spectroscopy (ICP-AES) analysis. The size of the nano particles were analyzed by transmission electron microscopy (TEM).

7.2.2. Preparation of carbon nanotubes with attached Au-NPs

Commercial, heat-treated MWCNTs devoid of metal or organic impurities were obtained from Chengdu Organic Chemicals Co. Ltd. The CNTs have diameters of 15–20 nm and length in the range of 20μm. The purity of the MWCNTs is checked using Micro-Raman scattering experiments which is performed with a Horiba Jobin Yvon LabRam HR system at a spatial resolution of 2 mm in a backscattering configuration. The 514.5nm line of Argon ion laser was used for excitation. The Micro-Raman studies will also give us average inner diameter of the MWCNT. De-ionized (DI) water was used for preparing all the aqueous solutions. In order to attach the Au-NPs to the walls of CNT the following procedure was followed. In this typical procedure, a measured amount of CNT (50.3 mg) was added to 10 mL of

the as-prepared gold suspension in water. About 5 mL ethanol was added immediately under continuous stirring for 12 hrs. The pink colour that is characteristic of gold colloids began to fade with time, which is presumably due to the attachment of the Au-NPs on to the surface of CNT. Thus, both surface modification and attachment were accomplished in one step. The black solid after the 12 hour stirring was separated by filtering and then dried overnight in an oven at 50^0 C. Part of this powder has been used for the X-ray diffraction (XRD) and TEM analysis to confirm the attachment of Au-NPs to the surface of MWCNTs. TEM images were recorded at an accelerating voltage of 200 kV using JEOL TEM. XRD pattern was recorded using Rigaku model X-ray diffractometer with Cu K_α radiation (λ = 0.15418 nm).

The MWCNTs with attached Au-NPs (MWCNT/Au) has to be embedded in polymer solid matrix for the ease of fabrication of optical limiter. For that 5 gms of poly vinyl alcohol (PVA) was added in 50 ml water and stirred thoroughly such that the PVA dissolved completely and homogenously. 0.03 gms of MWCNT/Au was weighed and added to 5 ml of PVA solution. The resulting viscous solution was stirred well for 1 hour such that the powder was dispersed uniformly in the PVA matrix. The viscous solution was then spin coated at a speed of 1000 rpm on a clean glass plate and dried. Thus MWCNT/Au embedded in polymer matrix was obtained which can be used as the sample material for the nonlinear optical studies using the Z-scan setup. For a comparison, a thin film of pure MWCNT (0.03 gm) in PVA was also prepared in the same way discussed

above. Second harmonics of Nd:YAG laser (532 nm, pulse width 6-7ns) having a repetition rate of 10 Hz was used as the light source for the nonlinear optical studies using open aperture Z-scan technique.

7.3. Results and Discussions

The Raman spectra of pure MWCNT (figure 7.1) shows three peaks at 1339cm^{-1}, 1566cm^{-1}, 2678cm^{-1}. The band at 1339 cm^{-1} is due to disorder in the graphene layers caused by sp^3 bonding (the "D" band) [23, 24]. This D-band gives the contribution of amorphous carbon in the sample [25]. The G band at 1566cm^{-1} is an intrinsic feature of a carbon nanotube that is closely related to vibrations in all sp^2 carbon material [26]. The second order D band at 2678cm^{-1}, which is due to second order Raman scattering is also confirmed the sample was carbon nanotube [27]. Absence of any additional Raman peaks proves that the MWCNTs used are completely pure and are devoid of any metal or organic impurities.

The ratio of integrated intensities of the D and G bands, I_D/I_G, is one of the most informative parameters in Raman spectroscopy of carbon materials and has been used extensively to calculate the in plane sp^2 crystallite size, L_a, in disordered carbon materials [28]. L_a is determined from the following general formula,

$$L_a(nm) = \frac{560}{E_L^4}\left(\frac{I_D}{I_G}\right)^{-1} \qquad (7.1)$$

where E_L is the laser energy and here for Argon Ion laser E_L = 2.41399eV. And for our sample we got I_D = 173 and I_G = 179 leading to a crystalline size equal to 17.07nm.

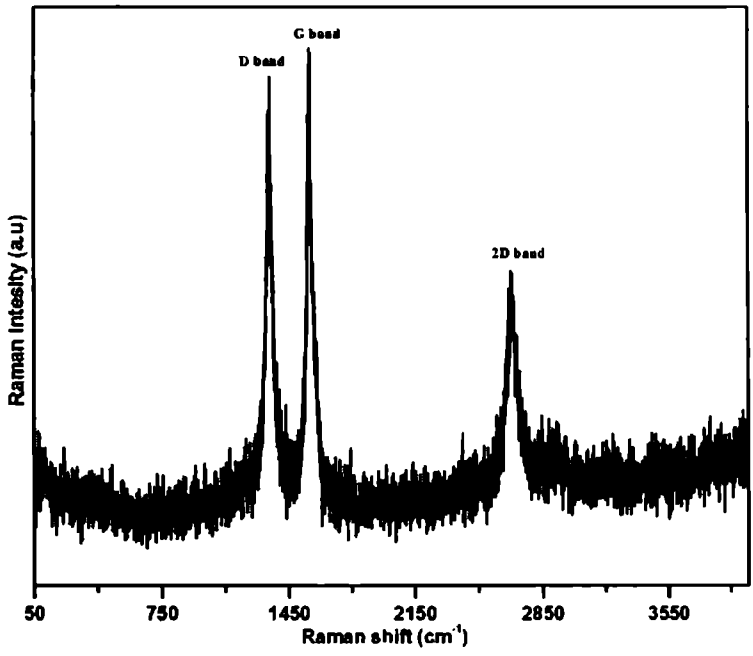

Figure 7.1. Raman spectra of pure MWCNT.

The ICP-AES analysis shows that the concentration of the Au in the colloid is found to increase with increase in the duration of laser ablation. The concentration of the colloids prepared at laser ablation durations 1hr, 2hr and 3hr are 3.45ppm, 4.25ppm and 7.65ppm respectively. The UV-visible spectra (figure 7.2) shows strong surface plasmon resonance (SPR) band peaking at 520nm indicating the presence of Au-NPs.

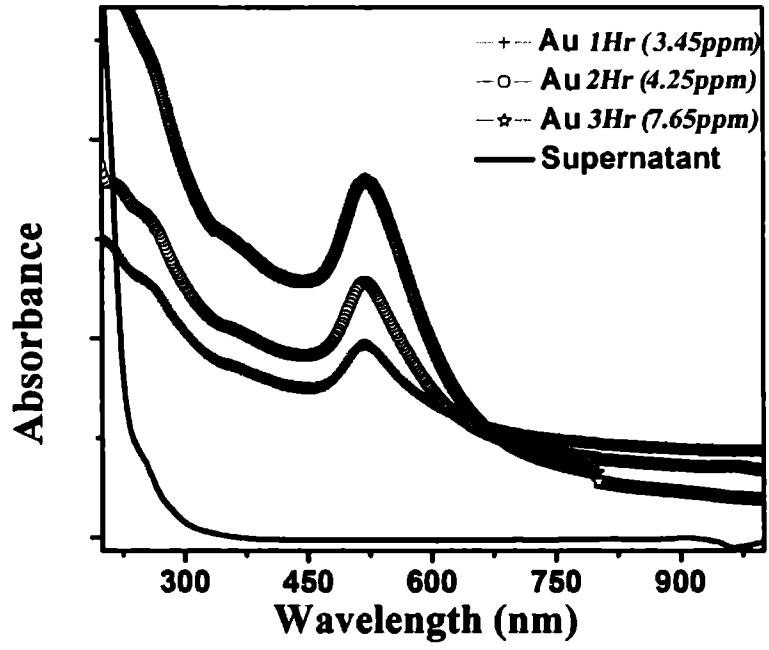

Figure 7.2. The UV-visible absorption spectra of gold nanocolloids in water and the supernatant solution after filtration.

The amplitude of the SPR peak is increasing gradually with increase of the duration of laser ablation indicating the increase in the concentration of the Au-NPs in the colloidal solution as observed from the ICP-AES analysis. The plasmon peak remains at almost the same wavelength which shows that the particle size remains unchanged with different ablation duration. The UV-visible absorption spectra of the supernatant solution after the filtration of the MWCNT/Au black powder is also shown in the figure 7.2. It is observed that the UV-visible spectra of the supernatant

solution do not show any SPR band in the visible region that indicates the absence of the Au-NPs in the supernatant solution. It means that entire Au-NPs in the colloidal solution have been loaded on to the walls of the MWCNT.

The trial for attaching Au-NPs on to the walls of hydrophobic CNT is based on the concept that addition of ethanol will reduce the interfacial tension between the walls of the CNTs and water and hence it will modify the wettability of CNTs [29]. As received MWCNT powder exhibited very poor dispersibility in water media [30]. The use of ethanol and other short-chain alcohols to reduce the interfacial tension between a hydrophobic domain and water has been well explained earlier [31-33]. More specifically, from a molecular point of view, short-chain alcohols behave as surfactants, in that they possess both hydrophilic (hydroxyl group) and hydrophobic (alkyl group) moieties. In an aqueous suspension of CNTs, it is therefore conceivable that the added ethanol molecules will be adsorbed onto the CNT walls through their alkyl groups, thus altering the interactions among the CNTs. The adsorbed ethanol molecules would then reduce the hydrophobic attraction among the CNTs, making it easier for them to disperse in an aqueous medium. A direct consequence of adding the ethanol is an increase in the interfacial area between water and the CNTs.

The mechanism of attachment of the Au-NPs to the surface of the MWCNTs can be explained as follows. As pointed out by Reincke *et al* [32], adsorption of Au-NPs on an oil/water interface is primarily driven by the reduction of interfacial free energy. Similarly, in our case, the adsorption of

Au-NPs on the CNT/water interface is caused by the system's tendency to seek a lower free energy. The adsorbed ethanol molecules will provide specific attachment sites to the Au NPs. As said above, the added ethanol molecules will be adsorbed onto the CNT walls through their alkyl groups, and they link to the water layer around the Au NPs through the hydroxyl group thus adsorbing the NPs on its surface. Since the attachment is based on the concept of electrostatic interaction, short chain alcohols work well rather than the alcohols with long chains.

The XRD pattern of pure MWCNT and MWCNT/Au is shown in figure 7.3. The XRD shows the main peak at $2\theta=26.7^0$ which corresponds to the (002) plane and the small peak at 43.6^0 corresponds to (101) plane of the MWCNT. The XRD pattern of the CNTs is similar to that of graphite though the main peak (002) is much weaker and broadened, indicating that the hexagonal ring structure of graphene sheets remain unchanged in the CNTs. The very small shift of the (002) reflection from $2\theta= 26.2^0$ for pure MWCNT to 26.7^0 for the MWCNT/Au is observed which may be attributed to the very small change in the microstructure of MWCNTs due to ethanol addition. The etching by OH radicals and deposition of C radicals on the surface of CNTs are considered to be responsible for the modification of the MWCNT structures. The observation of a very small peak at 38.8^0 corresponds to (111) plane of the Au-NPs attached to the walls of MWCNTs indicating that the deposited Au-NPs are small face centred cubic Au crystallites.

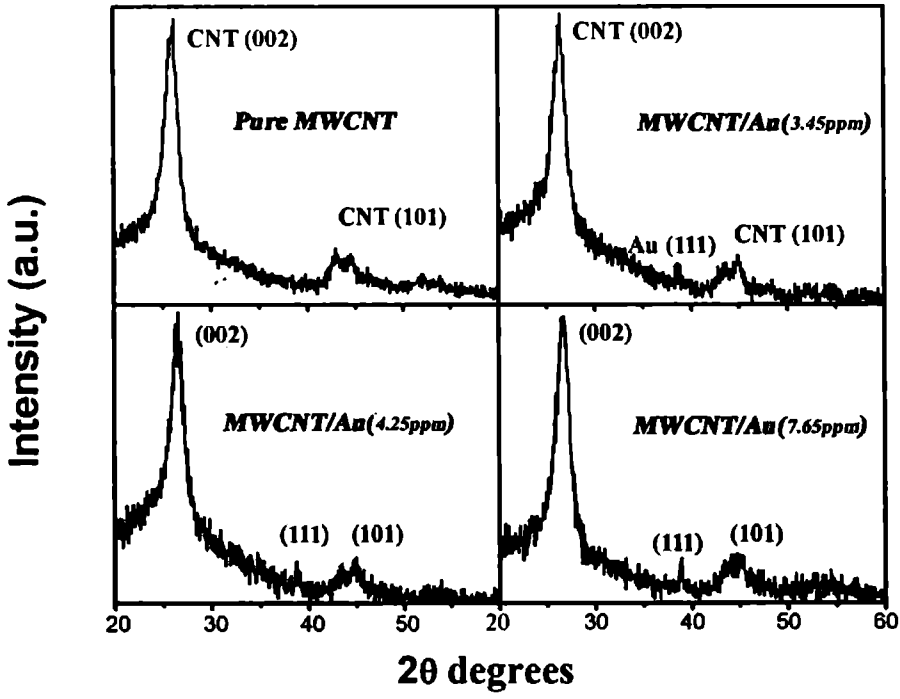

Figure 7.3. The XRD pattern of pure MWCNT and MWCNT with attached Au-NPs.

The TEM image and size histogram of the Au-NPs in water produced at laser ablation energy 1.2J/cm^2 for 1 hour duration is shown in figure 7.4(a) and 7.4(b) respectively which shows average size of Au-NPs to be 7nm. The high resolution TEM (HRTEM) (inset of figure 7.4(a)) shows parallel lines of atoms with interatomic spacing 2.35A^0 that corresponds to (111) plane of gold. Inset of figure 7.4(b) shows the selected area electron

diffraction (SAED) pattern which corresponds to atomic planes (111) and (220) of gold.

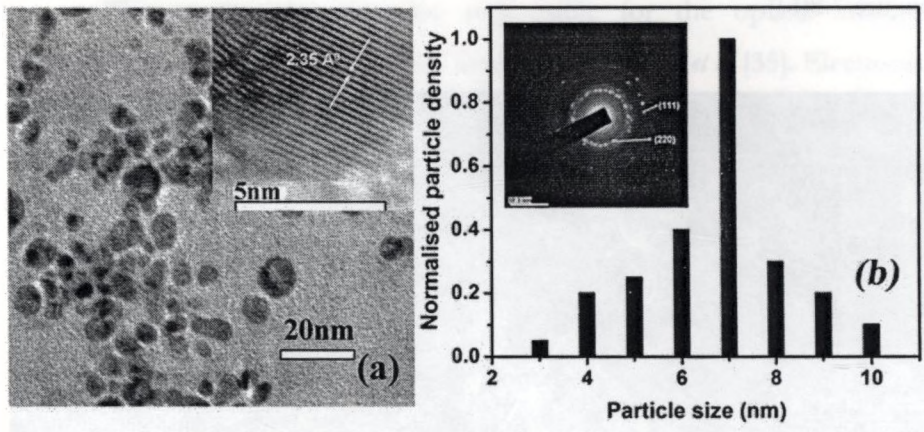

Figure 7.4(a). The TEM image, HRTEM (inset) and (b) size histogram, SAED (inset) of Au-NPs grown by LP-PLA.

The TEM and HRTEM pattern of the MWCNT/Au are shown in figure 7.5(a) and 7.5(b) respectively. From TEM studies it is observed that the outer diameter of the MWCNT is around 15.6nm quite close to the value obtained from the Micro-Raman studies. TEM characterization confirms that all the Au-NPs were attached to the CNT walls. The attached Au-NPs have a narrow size distribution and are finely dispersed. From the TEM images of the MWCNT/Au, we can see the Au-NPs as dark spots on the CNT surface. Thus it can be noted that the hydrophobic CNT could be decorated uniformly with desired loading ratios of Au-NPs. Figure 7.5(b) shows the HRTEM image of MWCNT/Au, showing parallel lines of atoms.

The interplanar spacing of MWCNT as seen from figure 7.5(b) is 3.47A^0 which corresponds to (002) plane of MWCNT. The interplanar spacing of Au-NPs is found to be 2.35A^0, which corresponds to (111) plane of gold (Figure 7.5(b)).

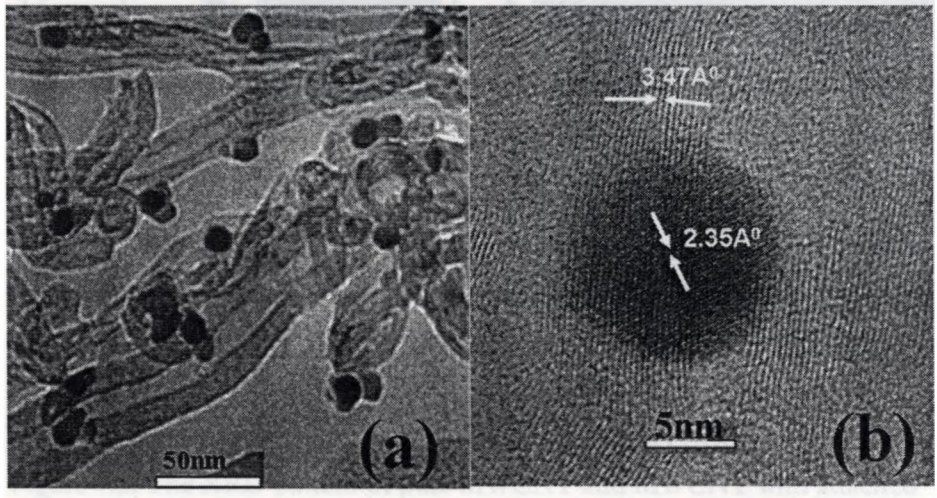

Figure 7.5. (a) TEM and (b) HRTEM image of MWCNT with attached Au-NPs.

The optical limiting characteristics of thin films containing pure MWCNTs as well as those with attached Au-NPs (containing different loading ratios of NPs) in PVA matrix has been taken by the automated Z-scan setup [34]. Second harmonics of Nd: YAG laser (532 nm, pulse width 6-7ns) having a repetition rate of 10 Hz was used as the light source for the nonlinear optical studies. The optical limiting plots (taken at laser irradiance I_0=0.15J/cm^2) of thin films containing pure MWCNTs and MWCNT/Au in

a PVA matrix are shown in figure 7.6. All films show an optical limiting type nonlinearity; that means a decrease in transmission with increase in the input laser fluence.

The mechanisms that are responsible for the optical limiting phenomena in MWCNTs have been investigated by Sun *et al* [35]. Electronic structure study of the CNTs done by Chen *et al* [6] shows that the CNTs have a lower work function, lower electron binding energy and stronger plasma excitation. Broadband OL with MWCNTs embedded in polymethyl methacrylate films has been reported by Sun *et al* [1]. The limiting response appearing in our case suggests that the optical limiting property may mainly result from another mechanism, i.e., nonlinear scattering [36-38]. In this process, heating due to the presence of the laser pulses can lead to vaporization and ionization of carbon particles or nanotubes (avalanche ionization), and then form rapidly expanding microplasmas in solid host polymer matrix. In return, these microplasmas strongly scatter light from the transmitted beam direction, leading to the decrease in the measured transmitted light energy.

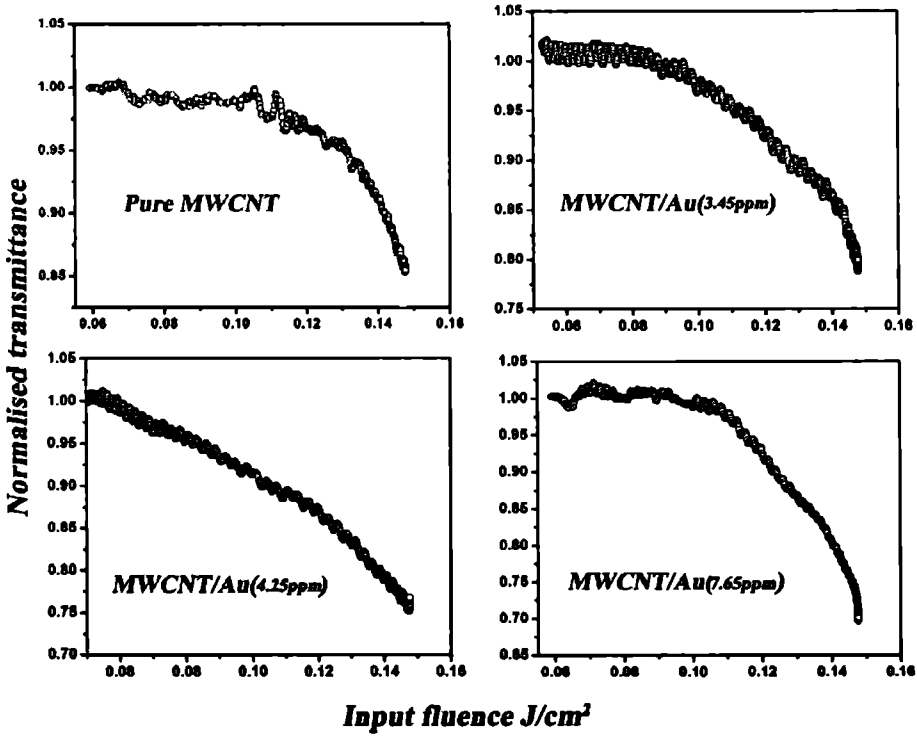

Figure 7.6. The optical limiting plots of the thin films containing pure MWCNT and MWCNT/Au in PVA matrix with different concentration of Au-NPs.

An increase in the optical limiting property has been observed (Figure 7.6) with increasing the gold loading ratio on the surface of MWCNTs. We propose that this improvement of the optical limiting performances in MWCNT/Au is mainly due to nonlinear scattering properties resulting from the surface plasmon absorption (SPA) processes in the Au NPs at 532 nm. This SPA band is due to the electromagnetic field-

induced collective oscillations of the conduction electrons in states near the Fermi level, known as surface plasmons. The photon energy absorbed will expand the metal particles into a micro plasma state in the sub-nanosecond range, inducing a scattering centre [10]. These micro plasma scattering centres around the metal particles result in a strong nonlinear scattering effect. As the density of the Au-NPs on the surface of the MWCNT increases, the SPA cross section increases, thus enhancing the related nonlinear scattering. Also there may be another contribution from free-carrier absorption of Au-NPs as reported earlier [39].

Thus MWCNTs with attached Au-NPs found excellent application as an OL material with high stability and durability. They can be effectively used for the fabrication of eye protecting goggles for the laser operators and sensor protecting boxes. The ease of flexibility and high mechanical strength that the polymer host matrix offers will help in molding the devices of any desired shapes depending on our application side. Also when the nanocolloids are embedded inside polymeric matrices the chance for interparticle interaction leading to the agglomeration of the NPs will not be there keeping the properties of the device the same and hence the device will be an efficient, functional and stable performer for long term applications.

7.4. Conclusions

Au-NPs produced by LP-PLA in water were directly attached to the walls of MWCNTs with high homogeneity and dispersivity. Both XRD and TEM characterization showed that Au-NPs distributed uniformly on the

walls of MWCNTs. The MWCNTs attached with Au-NPs show good optical limiting which is attributed to the nonlinear scattering. An increase in the optical limiting property has been observed with increasing the concentration of Au-NPs which have contribution from the nonlinear absorption caused by the SPA processes at 532nm in Au NPs. Thus highly stable and flexible optical limiting device has been fabricated using MWCNTs with attached Au-NPs in a polymer matrix.

7.5. References

1. X. Sun, R. Q. Yu, G. Q. Xu, T. S. A. Hor and W. Ji, Appl. Phys. Lett. **73** 3632 (1998)
2. J. E. Riggs, D. B. Walker, D. L. Carroll and Y. P. Sun, J. Phys. Chem. B **104** 7071 (2000)
3. L. Liu, S. Zhang, T. Hu, Z. X. Guo, C. Ye, L. Dai and D. Zhu, Chem. Phys. Lett. **359** 191 (2002)
4. L. Vivien, D. Riehl, P. Lanon, F. Hache and E. Anglaret, Opt. Lett. **26** 223 (2002)
5. S. R. Mishra, H. S. Rawat, S. C. Mehendale, K. C. Rustagi and A. K. Sood, Chem. Phys. Lett. **317** 510 (2000)
6. P. Chen, X. Wu, X. Sun, J. Lin, W. Ji and K. L. Tan, Phys. Rev. Lett. **82** 2548 (1999)
7. L. Vivien, E. Anglaret, D. Richl, F. Bacou, C. Journet, C. Goze, M. Andrieux, M. Brunet, F. Lafonta, P. Bernier and F. Hache, Chem. Phys. Lett. **307** 317 (1999)

8. M. Y. Han, W. Huang, C. H. Chew, L. M. Gan, X. J. Zhang and W. Ji, J. Phys. Chem. B **102** 1884 (1998)
9. P. V. Kamat, M. Flumiani and G. V. Hartland, J. Phys. Chem. B **102** 3123 (1998)
10. L. Francois, M. Mostafavi, J. Belloni, J. Delouis, J. Delaire and P. Feneyrou, J. Phys. Chem. B **104** 6133 (2000)
11. K. C. Chin, A. Gohel, W. Z. Chen, H. I. Elim, W. Ji, G. L. Chong, C. H. Sow and A. T. S. Wee, Chem. Phys. Lett. **409** 85 (2005)
12. B. Xue, P. Chen, Q. Hong, J. Y. Lin and K. L. Tan, J. Mater. Chem. **11** 2378 (2001)
13. A. V. Ellis, K. Vijayamohanan, R. Goswami, N. Chakrapani, L. S. Ramanathan, P. M. Ajayan and G. Ramanath, Nano Lett. **3** 279 (2003)
14. V. Georgakilas, D. Gournis, V. Tzitzios, L. Pasquato, D. M. Guldie and M. Prato, J. Mater. Chem. **17** 2679 (2007)
15. X. Hu, T. Wang, L. Wang, S. J. Guo and S. Dong, Langmuir. **23** 6353 (2007)
16. P. Santhosh, A. Gopalan and K. P. Lee, J. Catal. **238** 177 (2006)
17. T. Sainsbury, J. Stolarczyk and D. Fitzmaurice, J. Phys. Chem. B **109** 16310 (2005)
18. X. Hu, T. Wang, X. Qu and S. Dong, J. Phys. Chem. B. **110** 853 (2006)
19. M. A. C. Duarte and L. M. Liz-Marzan, J. Mater. Chem. **16** 22 (2006)
20. M. S. Raghuveer, S. Agrawal, N. Bishop and G. Ramanath, Chem. Mater. **18** 1390 (2006)
21. L. Q. Jiang and L. Gao, Carbon **41** 2923 (2003)

22. H. C. Choi, M. Shim, S. Bangsaruntip and H. J. Dai, J. Am. Chem. Soc. **124** 9058 (2002)

23. A. Mierczynska, J. Friedrich, H. E. Maneck, G. Boiteux J. K. Jeszka, CEJC, **2** 363 (2004)

24. J. T. McCann, B. Lim, R.Ostermann, M. Rycenga, M. Marquez and Y. Xia, Nano Lett. **7** 8 (2007)

25. A. A. Puretzky, H. Schittenhelm, X. Fan, M. J. Lance, L. F. Allard Jr. and D. B. Geohegan, Phys. Rev. B **65** 245425 (2002)

26. F. Zhang, C. Mihoc, F. Ahmed, C. Lathe and E. Burkel, Chem. Phys. Lett. (2011)

27. S. Gupta and Y. Ding, The Open Spectroscopy Journal, **2** 40 (2008)

28. N. Soin, S. S. Roy, S. C. Rayb and J. A. McLaughlin, J. Raman Spectrosc. **41** 1227 (2010)

29. H. V. Ly and M. L. Longo, Biophys. J. **87** 1013 (2004)

30. N. T. Huy, A. Maeda, D. T. Uyen, D. T. Trang, M. Sasai and T. Shiono, Acta Tropica **101** 130 (2007)

31. S. S. Andrade, D. Rabelo, V. K. Garg, A. C. Oliveira, P. C. Morais, J. Magn. Mater. **289** 25 (2005)

32. F. Reincke, S. G. Hickey, W. K. Kegel and D. Vanmaekelbergh, Angew Chem. Int. Ed. **43** 458 (2004)

33. P. Cheng, D. Li, Z. Yuan, Y. Zou and D. Yang, Mater. Chem. Phys. **111** 271 (2008)

34. M. S. Bahae, A. A. Said, and E. W. Van Stryland, Opt. Lett., **14** 955 (1989).

35. X. Sun, Y. Xiong, P. Chen, J. Lin, W. Ji, J. H. Lim, S. Yang, D. J. Hagan and E.W. Van Stryland, Appl. Opt. **39** 12 (2000)

36. K. Mansour, M. J. Soileau and E. W. Van Stryland, J. Opt. Soc. Am. B **9** 1100 (1992)

37. K. M. Nashold and D. P. Walter, J. Opt. Soc. Am. **12** 1228 (1995)

38. R. Goedert, R. Becker, A. Clements and T. Whittaker, J. Opt. Soc. Am. B **15** 1442 (1998)

39. R. Sreeja, P. M. Aneesh, A. Aravind, R. Reshmi, R. Philip and M .K. Jayaraj, J. Electrochem. Soc. **156** 167 (2009).

Chapter 8

Summary and scope for future work

8.1. Summary

Development of nonlinear optical devices having ultrafast nonlinearity is a very relevant field of research which finds applications in optical limiting. The demand for protection of eyes of laser operators and various types of optical sensors attached to the laser optics systems from laser pulses has resulted in search for optical limiting devices. In order to prevent the accidental entrance of the laser pulses in to the eyes, the laser operators must use goggles which are transparent at low intensity of light but non-transparent towards high intensity of light. Since the optical limiting devices are transparent at low intensity of light but non-transparent towards high intensity of light, they can be effectively used as a preventor of the laser pulses.

In the present study, we have succeeded in fabricating nanostructures based polymeric nonlinear optical limiting devices. The most striking character of our method is that the excellent compatibility between NPs and polymers is obtained via modifying the surface of the NPs to ensure the homogeneous distribution of NPs in the polymer matrix. The existence of the polymer network can stabilize the NPs, which act as cross-linking points. The structure of such NP/polymer composite network can stabilize the NPs for a long term, which is important for the protection of their function. The high device flexibility will render them to be actively used in any desired shapes. These superior optical limiting devices may be used as eye protection goggles or as protectors of sensors.

A completely automized Z-scan setup for the nonlinear optical characterization was fabricated in the laboratory. The automized setup made the data acquisition and data analysis quite easy. A better communication between the instruments and PC was achieved by the use of the LAB VIEW programming tools in conjugation with devices such as NI PCI 7332, UMI 7764. The micro step motion of the sample cell enabled to acquire very fast and error free data compared to manual data acquisition. The interfacing and automation saved lots of time and even could measure the full set of data in a few minutes.

The next step was the fabrication of the flexible nonlinear optical device having good mechanical strength based on metal and semiconductor nanostructures encapsulated polymeric optical limiting devices. All the devices gave comparatively good optical limiting characteristics and a few among them give good self defocusing type refractive nonlinearity.

ZnO nanoparticles in the present investigation were synthesized by room temperature wet chemical methods. The size of the quantum dots were tuned by varying the concentration of the NaOH in the precursor solution. The size of the nanoparticles was found to be increasing with increase in the concentration of the NaOH as observed from the broadening of the XRD spectra and blue shift in the absorption edge in the UV-visible absorption spectra and then confirmed by the TEM analysis. The nonlinear optical studies show an optical limiting type absorptive nonlinearity and self defocusing type refractive nonlinearity. The nonlinear absorption was due to the two photon absorption in ZnO. The values of

nonlinear absorption coefficient β as well as refractive index n_2 are found to be increasing with increase in particle size. The enhancement in the n_2 and β is attributed to the enhanced oscillator strength in bigger nanoparticles. The ZnO nanoparticles are very stable inside the polymer matrix and will work efficiently for long term optical applications.

ZnS:Cu nanoparticles were prepared by chemical route in aqueous media. ZnS nanoparticles with the sphalerite structure were formed as observed from the XRD pattern and as confirmed from the TEM characterization. The ZnS:Cu nanoparticles displayed a regular increase in the band gap with increase in the copper doping concentration. Copper doped ZnS samples showed green luminescence which resulted from the transition between the sulphur vacancy donor levels and the copper acceptor levels. These ZnS:Cu nanoparticles were embedded in PVA matrix and the Z-scan analysis performed with Ti-Sapphire laser (800nm with pulse width of 100 fs) showed a reduction in transmission which was due to three photon absorption process occurring in multiple steps. An increase in the value of the nonlinear absorption coefficient with increase in the doping concentration was found which was due to the increase in the density of intermediate defect levels which played a supplementary role in the enhancement of the rate of multi step transition enhanced three photon absorption. These Cu doped ZnS nanoparticles in the polymer matrix could be used as an effective sample material for optical limiting device fabrications at slightly different laser wavelengths.

Nanoparticles of gold and silver were synthesized by LP-PLA in water media by varying the laser ablation fluence using second harmonic of Nd:YAG laser at 532nm. The size of the Au and Ag nanoclusters was found to be increasing with increase in the ablation fluence as observed from the UV-visible absorption spectra and TEM studies. The silver nanoparticles prepared at higher laser fluence were found to be less stable as compared to those prepared at lower laser fluence. The optical limiting efficiency of Au and Ag nanoparticles increased with decrease in the nanoparticles size which is due to the size dependent enhancement in the oscillator strength in the nanoparticles associated with the intra band contribution to the nonlinear absorption. The Au nanoparticles showed self focusing type refractive nonlinearity. The lower sized Au and Ag nanoparticles showing maximum nonlinearity were embedded in PVA matrix and casted into thin film having approximate thickness of 1μm by spin coating. Such nanoparticles embedded polymeric films showing very good optical limiting were used for fabricating flexible limiting device having good mechanical strength. Also in the case of silver nanoparticles, it was observed that when the duration of ablation was increased keeping the incident laser fluence fixed, the size of the nanoparticles was decreased which was attributed to the efficient radiation absorption by the previously ablated nanoparticles.

Gold nanoparticles were successfully attached on to the surface of MWCNT's. Synthesis and attachment of homogenously distributed Au-NPs on to the surface of CNTs, especially through a simple and cost-effective route without using any surfactant or polyelectrolyte to functionalize the

CNT's was introduced. Au nanoparticles of different concentrations were synthesized by LP-PLA in deionised water using third harmonic of Nd:YAG laser source by varying the duration of ablation keeping the laser fluence constant and minimum. A low value of laser fluence was maintained to obtain smallest sized nanoparticles. The attachment was achieved by the addition of a small amount of ethanol into MWCNT added Au colloidal solution in order to decrease the interfacial tension between the hydrophobic MWCNT and water. Au-NPs were distributed uniformly on the walls of MWCNT's as found from the XRD and as confirmed from the TEM studies. Au-nanoparticles attached MWCNTs were embedded in PVA films. The films showed optical limiting nature, which was attributed to the nonlinear scattering in MWCNTs. An increase in the optical limiting property was observed with increasing the concentration of Au-NPs on the surface of MWCNTs which was due to the additional contribution from the nonlinear absorption caused by the SPA processes at 532nm in Au-NPs. Thus highly stable and flexible optical limiting device was fabricated using MWCNTs with attached Au-NPs in a polymer matrix.

8.2. Scope for future studies

8.2.1. Fabrication of eye protection goggles and sensor protecting boxes based on in-situ polymerized nanoparticles

As regarding the protection of sensors attached to the lasers, sensors should be kept in boxes made up of these optical limiting materials. In a device and industrial point of view, we should use materials with high

mechanical strength and ease of flexibility so that they can be moulded easily into any shape needed for the application. The development of optical limiters based on metal and semiconductor nanoparticles incorporated into the polymer matrix via insitu polymerization can improve the performance of the optical limiter. The insitu polymerization will diminish the minute chance of agglomeration inside the polymer matrix and loss of transparency and thus keeps the stability and functionality of the device well; even though the chance of agglomeration is not relevant for ultrafine nanoparticles below 10nm. Subsequently they are molded into desired shape for making laser preventing goggles and sensor protecting boxes. For this purpose we can prepare the nanoparticles of gold [1], silver [2] and ZnO [3] embedded in the polymer matrix through in-situ polymerization tools.

8.2.2. Luminescent ZnS quantum dots for the cancer cell attachment

One of the most exciting applications of nanotechnology in medicine is the use of luminescent quantum dots (QDs) for bio-medical imaging [4]. Further, quantum dots can be made very effective for targeted imaging by attaching them with disease specific ligands such as proteins, vitamins, monoclonal antibodies and peptides. Despite the fact that there have been significant developments in anti cancer technology such as radiotherapy, chemotherapy and hormone therapy, cancer still remains as one of the leading cause of death all over the world. In all these methods, normal cells are also destroyed along with the tumor cells since the cell killing is proportional to the region of exposure [5, 6]. This lack of tumor

specific treatment is one of the main hurdles of the current cancer treatment technology.

An ideal solution to these limitations is to deliver a biologically effective concentration of anti cancer agents with high specificity. Luminescent quantum dot (QD) based on doped zinc sulfide (ZnS), conjugated with a cancer-targeting ligand, folic acid (FA), is presented as a promising bio-friendly system for targeted cancer imaging [7]. Folic acid has specific attachment to the cancer cells due to the presence of the Folate Receptor (FR) alpha protein [8], which is more prominent in the cancer cells such as FR positive human nasopharryngeal epidermoid carcinoma, KB cells as compared to the normal cells. Folate Receptor alpha protein is encoded by the FOLR1 gene [9]. The FR, a tumor associated glycosyl phosphatidylinositol anchored protein, can actively internalize bound folates and folate conjugated compounds via receptor-mediated endocytosis [10, 11]. The protein encoded by this gene is a member of the Folate Receptor (FOLR) family. The members of this family has a special affinity to folic acid and for several reduced folic acid derivatives.

Luminescent centers in doped QDs could be excited using bio-friendly visible light >400 nm by directly populating the dopant centers, leading to bright emission. Specific attachment of Folic acid attached ZnS quantum dots synthesized through wet-chemical route to the FR+ cancer cell line has been reported earlier [7]. However these chemical methods produce byproducts, which contaminates and affect the stability of the nanoparticles and as regarding biological applications only contamination

free nanoparticles have real relevance. It is very tedious to synthesise extra stable nanoparticles with extremely small size using the chemical route. In therapeutic applications of the nanoparticles, kidney can filter only those nanoparticles with extremely small size after the specified cancer targeting is achieved. In this situation the safe and practically simple methods like laser ablation of solid targets [12] has been introduced which produces homogenous dispersion of extremely small sized nanoparticles devoid of impurities with maximum stability in a transparent aqueous media.

Luminescent ZnS:Cu nanoparticles can be prepared by liquid phase pulsed laser ablation technique (LP-PLA) in water media. As synthesised nanoparticles can be attached to folic acid after the preparation and these ZnS:Cu nanoparticles will show green luminescence under UV illumination. The cytotoxicity of bare and FA conjugated QDs can be tested. The attachment of the nanoparticles to the cancer cells may be checked by fluorescence microscopy where in ZnS:Cu nanoparticles will show specific luminescence in the green region. Hence it will be easy for tracing out the cancer cells from the normal cells, and thus the drug delivery becomes quite easy thereby the cancer cells may be destroyed without affecting the normal cells.

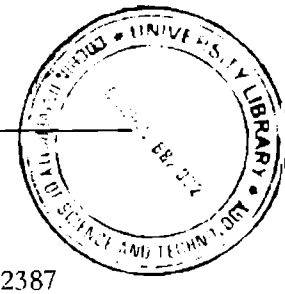

8.3. References

1. S. Porel, S. Singh and T. P. Radhakrishnan, Chem. Commun. 2387 (2005)
2. S. Porel, S. Singh, S. S. Harsha, D. N. Rao and T. P. Radhakrishnan, Chem. Mater. **17** 9 (2005)
3. J. W. Shim, J. W. Kim, S. H. Han, I. S. Chang, H. K. Kim, H. H. Kang, O. S. Lee and K. D. Suh, Colloids and Surfaces A: Physicochem. Eng. Aspects **207** 105 (2002)
4. T. Jamiesona, R. Bakhshia, D. Petrovaa, R. Pococka, M. Imanib, A. M. Seifalian, Biomater. **28** 4717 (2007)
5. L. H. Reddy, J. Pharmacol. **57** 1231 (2005)
6. S. Jaracz, J.Chen, L. V. Kuznetsova, I. Ojima, Bioorg. Med. Chem. **13** 5043 (2005)
7. K. Manzoor, S. Johny, D. Thomas, S. Setua, D. Menon and S. Nair, Nanotechnology **20** 065102 (2009)
8. C. P. Leamon, J. A. Reddy, Adv. Drug Delivery Rev. **56** 1127 (2004)
9. I. G. Campbell, T. A. Jones, W. D. Foulkes and J. Trowsdale, Cancer Res. **51** 5329 (1991)
10. B. A. Kamen and A. Capdevila, Proc. Natl. Acad. Sci. **83** 5983 (1986)
11. C. P. Leamon and P. S. Low, J. Biol. Chem. **88** 5572(1991)
12. J. Zheng, Z. Zheng, W. Gong, X. Hu, W. Gao, X. Ren and H. Zhao, Chem. Phys. Lett. **465** 275 (2008)